Spectroscopic and catalytic investigations of V_xO_y/SBA-15 and magnesium vanadate model catalysts for selective propene oxidation

vorgelegt von
Diplom-Chemikerin
Anke Walter
aus Berlin

Von der Fakultät II - Mathematik und Naturwissenschaften
der Technischen Universität Berlin
zur Erlangung des akademischen Grades
Doktor der Naturwissenschaften
Dr.rer.nat.

genehmigte Dissertation

Promotionsausschuss:
Vorsitzender: Prof. Dr. Thomas Friedrich, TU Berlin
1. Berichter: Prof. Dr. Thorsten Ressler, TU Berlin
2. Berichter: Prof. Dr. Christian Hess, TU Darmstadt

Tag der wissenschaftlichen Aussprache: 26.10.2011

Berlin 2011
D 83

Abstract

The objective of the present work was elucidating structure-activity relationships concerning the individual role of vanadium sites in selective propene oxidation. Two suitable vanadium oxide model catalyst systems were employed: vanadium oxides supported on SBA-15, "V_xO_y/SBA-15", and various magnesium vanadate phases. Detailed investigations on the preparation, thermal stability, structure, and structural evolution under reducing and propene oxidizing condition were conducted. Various *in situ* methods were used, *e.g.* UV-Vis-DRS, X-ray absorption spectroscopy, Raman spectroscopy and X-ray powder diffraction. These were combined with online MS gas phase analysis. Catalytic characterization of the model catalysts was performed using quantitative GC gas phase analysis.

In a first investigation magnesium vanadate phases, $Mg_3V_{10}O_{28}{\cdot}28H_2O$, MgV_2O_6, monoclinic and triclinic $Mg_2V_2O_7$, and $Mg_3V_2O_8$, were prepared and compared with V_2O_5. Besides $Mg_3V_{10}O_{28}{\cdot}28H_2O$ all oxides were stable enough to be used for reaction tests. No significant structural changes or reduction of the bulk phase during propene oxidation occurred for the magnesium vanadates up to 673 K. Conversely, V_2O_5 was reduced to VO_2(B) under reaction conditions and V_4O_9 was formed as intermediate phase. Catalytic performance of the magnesium vanadates was lower compared to that of V_2O_5. The highest propene conversions were measured for monoclinic $Mg_2V_2O_7$. Only marginal differences in selectivity towards oxygenated products such as acrolein were observed for the different magnesium vanadate phases. Compared to V_2O_5, total oxidation was increased while mainly acrolein was formed as partial oxidation product. *In situ* UV-Vis-DRS revealed that the catalytic performance correlated with the reducibility of the magnesium vanadate catalysts.

Second part, Emphasis of the present work, was placed on the investigation of selective propene oxidation over V_xO_y/SBA-15 model catalysts. Preparation of highly disperse V_xO_y/SBA-15 samples without formation of V_2O_5 during the preparation process was possible using a grafting anion exchange method. Three different V_xO_y/SBA-15 samples with vanadium loadings in the range of 1.4 wt%-7.7 wt% (0.3 V/nm^2 – 2.4 V/nm^2) were synthesized. A hydrated state of V_xO_y/SBA-15 was present at ambient temperatures of 300 K in humid atmospheres. The hydrated state consisted of polymerized vanadium oxide units with square pyramidal coordination of the vanadium centers. Thermal treatment in oxygen and water saturated atmospheres resulted in dehydration, loss of coordinated water, and the direct formation of the dehydrated state of V_xO_y/SBA-15 above 440 K. The dehydrated state of V_xO_y/SBA-15 was described by an ordered arrangement of dimeric vanadium oxide units with tetrahedral coordination of the vanadium centers. *In situ* spectroscopic measurements revealed that the dehydrated V_xO_y/SBA-15 structure corresponds to the vanadium oxide structure during selective propene oxidation. Formation of additional V-O-Si bonds to the support during catalytic reaction was deduced. Moreover, catalytic reaction in propene and oxygen lowered the reducibility of the vanadium centers in V_xO_y/SBA-15 using propene as reducing agent. Vanadium loading had only minor impact on the catalytic performance of V_xO_y/SBA-15. Besides formation of CO_2 and CO mainly formation of acrolein, propionaldehyde, acetaldehyde and acetic acid was observed. No significant change in product selectivites was observed compared to V_2O_5 reference. Hence, similar active vanadium oxides centers may be present on V_xO_y/SBA-15 and bulk V_2O_5. Conversely to V_2O_5, the average vanadium valence of V_xO_y/SBA-15 was V^{5+} during propene oxidation independent of the initial oxygen to propene ratio. Dynamic investigations in changing reducing and catalytic condition and a reaction order of zero for oxygen during propene oxidation showed that V_xO_y/SBA-15 exhibited a fast re-oxidation of the vanadium centers during propene oxidation.

Zusammenfassung

Das Ziel dieser Arbeit war die Erstellung von geeigneten Struktur-Aktivitäts-Beziehungen von Vanadiumzentren in der selektiven Oxidation von Propen. Dafür wurden zwei Modelsysteme auf Basis von Vanadiumoxiden untersucht: Auf SBA-15 geträgerte Vanadiumoxide, "V_xO_y/SBA-15", und verschiedene Magnesiumvanadat-Phasen. Diverse analytische Methoden wurden genutzt, um die Präparation, die Vanadiumoxid-Struktur, und die Entwicklung der Vanadiumoxid-Struktur unter reduzierenden und Propen-oxidierenden Bedingungen zu verfolgen. Es wurden unter anderem *in situ* UV-Vis-DRS, Röntgenabsorptionsmessungen, Raman-Messungen, sowie Röntgendiffraktionsmessungen angewendet. Gleichzeitig wurde die Zusammensetzung der Gasphasen mittels online Massenspektrometrie untersucht. Zusätzlich erfolgte eine quantitative katalytische Charakterisierung der Modell-Katalysatoren mittels Gaschromatographie.

Im ersten Teil der Arbeit wurden Magnesiumvanadat-Phasen hergestellt: $Mg_3V_{10}O_{28}\cdot 28H_2O$, MgV_2O_6, monoklines und triklines $Mg_2V_2O_7$, sowie $Mg_3V_2O_8$. Diese wurden mit V_2O_5 verglichen. Außer $Mg_3V_{10}O_{28}\cdot 28H_2O$ waren alle untersuchten Oxide thermisch stabil und konnten für Reaktionstests verwendet werden. Für die untersuchten Magnesiumvanadat-Phasen wurde keine Reduktion unterhalb von 673 K beobachtet. Im Gegensatz dazu wurde V_2O_5 zu VO_2(B) unter katalytischen Bedingungen reduziert. V_4O_9 wurde als Zwischenphase gebildet. Die gemessene katalytische Aktivität der Magnesiumvanadat-Phasen war deutlich niedriger als die von V_2O_5. Innerhalb der Magnesiumvanadat-Phasen zeigte monoklines $Mg_2V_2O_7$ die höchste Aktivität. Die gemessenen Produktselektivitäten zwischen den Magnesiumvanadat-Phasen unterschieden sich nur geringfügig. Gegenüber V_2O_5 fand eine erhöhte Totaloxidation von Propen statt. Weiterhin wurde hauptsächlich Acrolein als Partialoxidations Produkt von Propen gebildet. *In situ* UV-Vis-DRS Messungen zeigten, dass die katalytische Aktivität der Magnesiumvanadat-Phasen mit der Reduzierbarkeit der Vanadiumzentren korrelierte.

Im zweiten Teil, dem Mittelpunkt dieser Arbeit, wurden V_xO_y/SBA-15 Modell Katalysatoren für die selektive Oxidation von Propen untersucht. Die Herstellung von hoch dispersen Vanadiumoxid-Strukturen auf dem SBA-15 Träger, ohne die Bildung von kristallinen V_2O_5-Phasen, war mittels einer speziellen Ionen-Austausch Prozedur möglich. Es wurden drei Proben mit Vanadium-Beladungen im Bereich von 1.4 wt%-7.7 wt% (0.3 V/nm^2 – 2.4 V/nm^2) hergestellt. Bei niedrigen Temperaturen von 300 K und in wassergesättigten Atmosphären lag eine hydratisierte Phase von V_xO_y/SBA-15 vor. Die Vanadiumoxid-Struktur der hydratisierten Phase besteht aus kondensierten Vanadiumoxideinheiten mit quadratisch planarer Koordination der Vanadiumzentren. Thermische Behandlung in sauerstoffhaltigen Atmosphären führte zu einer Dehydratation der hydratisierten Phase. Für Temperaturen höher 440 K bildete sich die dehydratisierte Struktur von V_xO_y/SBA-15 unter der Abspaltung von koordiniertem Wasser aus. Die Vandiumoxid-Struktur der dehydratisierten Phase konnte durch eine regelmäßige Anordnung von benachbarten dimeren Vanadiumoxideinheiten beschrieben werden. Dabei sind die Vanadiumzentren in der dehydratisierten Phase tetraedisch koordiniert. *In situ* spektroskopische Messungen haben gezeigt, dass die dehydratisierte Phase der Vanadiumoxid-Phase unter katalytischen Bedingungen entspricht. Während der Propenoxidation bilden sich zusätzliche V-O-Si-Bindungen aus. Weiter ändert sich die Reduzierbarkeit der Vanadiumzentren in V_xO_y/SBA-15, nachdem diese katalytischen Reaktionsbedingungen ausgesetzt waren. Die Vanadiumbeladung hatte nur einen geringen Einfluss auf die katalytischen Eigenschaften von V_xO_y/SBA-15. Neben der Bildung von CO_2 und CO wurde die Bildung von Acrolein, Propionaldehyd, Acetaldehyd und Essigsäure beobachtet. Gegenüber einer V_2O_5 Referenz wurden nur geringe Unterschiede in den gemessene Selektivitäten der Reaktionsprodukte der Propenoxidation festgestellt. Daher wird vermutet, dass sowohl auf V_xO_y/SBA-15 als auch auf V_2O_5 ähnliche aktive Zentren auf der Oberfläche vorliegen müssen. Im Gegensatz zu V_2O_5 war die mittlere Vanadiumvalenz +5 während der Oxidation von Propen. Untersuchungen mit wechselnden reduzierenden und oxidierenden Gasatmosphären und eine Reaktionsordnung nullter Ordnung für Sauerstoff zeigten, dass eine schnelle Re-Oxidation der Vanadiumzentren während der Propenoxidation stattfindet.

Danksagung

Zunächst bedanke ich mich bei den drei Gutachtern dieser Arbeit: Prof. Dr. Thorsten Ressler für die interessante wissenschaftliche Fragestellung, die exzellente fachliche Betreuung, die mit dieser Arbeit verbunden war, und stete Diskussionsbereitschaft während meiner Promotionszeit. Bei Prof. Dr. Christian Hess bedanke ich mich für seine Unterstützung, die Möglichkeit zur Durchführung von *in situ* Raman Experimenten in seinem Arbeitskreis, hilfreiche Diskussionen und die Übernahme des Zweitgutachtens. Prof. Dr. Thomas Friedrich danke ich für die Übernahme des Prüfungsvorsitzes.

Herrn Dr. Jan Dirk Epping danke ich für Durchführung und Auswertung der Festkörper NMR Messungen. Dr. Jörg Thielemann danke ich für die Durchführung und Unterstützung bei den *in situ* Raman Messungen. Für die Aufnahme der Elektronenmikroskopbilder danke ich den Mitarbeitern des ZELMI an der TU Berlin. Herrn Harald Link möchte ich für die durchgeführten ICP-OES Messungen danken. Dr. Elisabeth Irran danke ich für die Aufnahme und Hilfe bei der Auswertung der Einkristall-Röntgenmessungen.

Semiha Schwarz danke ich für Unterstützung bei der Synthese von SBA-15 und V_xO_y/SBA-15 und die vielen TG Messungen. Weiter bedanke ich mich bei ihr auch für die herzliche Atmosphäre und die vielen nicht fachlichen Gespräche, die das Arbeiten so angenehm gemacht haben. Bei Dr. Astrid Jürgensen bedanke ich mich für die Aufnahme der zahlreichen Diffraktogramme und die durchgeführten RFA Messungen, sowie für ihre Unermüdlichkeit beim Korrekturlesen dieser Arbeit. Auch allen weiteren Mitgliedern des Arbeitskreises danke ich, die stets Diskussionsbereitschaft gezeigt haben und mich bei der Durchführung der zahlreichen Messungen auf vielfältige Weise unterstützt haben: Dr. Thomas Christoph Rödel, Alexander Hahn, Dr. Anne Dennstedt, Gregor Koch, Juliane Scholz, Alexander Müller, Rafael Zubrzycki, und Sigrid Imme. Ich danke auch Mateusz Jastak, Jacek Kozuch und Udo Dorn, die mich im Rahmen ihrer Praktika während der Synthese der Magnesiumvanadate und Vanadium-Referenzen unterstützt haben. Weiter möchte ich mich auch bei Alper Ünal und Dr. Ingo Piotrowski bedanken für ihre hilfreichen Ratschläge zur Synthese. Auch allen weiteren Mitgliedern des Instituts für Chemie der TU Berlin, die diese Arbeit unterstützt haben und nicht weiter namentlich genannt sind, danke ich.

Besonders bedanke ich mich auch bei DESY und dem Hasylab in Hamburg und ANKA in Karlsruhe für die Erteilung von Messzeit und die finanzielle Unterstützung. Weiter bedanke ich mich bei der Deutschen Forschungsgemeinschaft (DFG) und dem Beirat der Zentralen Frauenbeauftragten der TU Berlin für die finanzielle Unterstützung.

Stephan Rau und meiner Familie danke ich für den Rückhalt und die stete Motivation zu dieser Arbeit.

Contents

Part II Spectroscopic and catalytic investigations of V_xO_y/SBA 15 model catalysts for selective propene oxidation

1 Introduction

1.1 Motivation

Heterogeneously catalyzed reactions play a fundamental role in the production of fuels and a wide range of chemical products. Approximately 60% of industrial chemicals and intermediates are produced via selectively catalyzed oxidation reactions [1]. One important industrial process is the selective oxidation of propene towards acrolein and acrylic acid (3.7 million tons per year [2]). The major production process is a two stage reaction using propene as feedstock [3]. First, propene is oxidized to acrolein using bismuth molybdate based catalysts. Second, acrolein is oxidized to acrylic acid using molybdenum based oxide catalysts mixed with other transition metals such as vanadium and tungsten. The total yield of acrylic acid of this process is 87% [3]. Increasing the total yield of industrial processes, like the production of acrylic acid, is of great interest because natural resources like crude oil are saved and costs are lowered. Therefore, new catalysts with improved activity and high selectivity towards the desired products are sought.

Industrial research is mostly based on chemical intuition and “trial and error” methods which involve testing of a large number of catalysts. Another approach in research is a rational catalyst design [4] that involves a deeper understanding of the complexity of active catalysts. In addition to catalytic testing, the objective of these studies is to elucidate the properties of well chosen model catalysts. Properties like chemical composition, electronic structure, coordination of metal sites, and surface and bulk structures are investigated. The aim is to derive structure-activity relationships that enlighten how the catalytic performance correlates with these properties. Furthermore, this knowledge is used to develop new and improved model catalysts. However, the required structure-activity relationships are not sufficiently understood for the majority of heterogeneous catalysts.

The development of new catalysts that use propane instead of propene as initial feed for the acrylic acid synthesis [3,5,6] attracted much attention in the past decades. Highly active mixed metal oxide catalysts for the direct oxidation of propane to acrylic acid exhibit complex structures and compositions, *e.g.* Mo, V, W, Te, and Nb oxides [4,5,6]. With respect to structure-activity relationships, it is crucial to understand how structure and individual metal sites influence the catalytic performance. However, changing the composition of these active mixed metal oxides will mostly induce a change in the structure as well. Therefore, the superior catalytic performance of these active bulk mixed metal oxides cannot be assigned unambiguously to the functionality of individual metal centers or particular structure motifs. Hence, it is difficult to distinguish between chemical and structural complexity. In order to reduce the number of variables that affect the catalytic performance, suitable model systems exhibiting a lower complexity are sought [7]. Two approaches seem feasible. Model systems with either plain composition and structural variety [8,9], or model systems exhibiting structural invariance and a suitable

compositional variety [10] are promisingly. Binary metal oxides constitute rather simple model systems for the former case. The present work focused on vanadium oxides as binary metal oxides.

Although a huge structural variety exists among binary vanadium oxides [11] V_2O_5 was found to be the only stable binary V^{5+} oxide. Therefore, two approaches for vanadium oxide based model catalysts were chosen in the present work. In a first approach, ternary vanadium oxides were sought as model catalysts to extend the range of available bulk vanadium oxides. Magnesium vanadates were chosen because no additional possibly active "metal sites" are introduced. Furthermore, magnesium vanadate systems exhibit a variety of structural motifs (octahedral and tetrahedral coordination of V^{5+}), which makes them very suitable as structural model systems. In a second approach, silica supported vanadium oxides were chosen as model systems. Supporting metal oxides on silica may enable the stabilization of particular metal structures that are not stable and, thus, not available under *in situ* conditions otherwise. It was shown recently that hexagonal MoO_3 supported on mesoporous silica (SBA-15) is stabilized up to 773 K under reaction conditions [8]. Furthermore, silica supports exhibit a large surface area, no activity for catalytic reactions, and rather weak interactions with the supported metal oxides. In addition to bulk model systems, supported metal oxide catalysts exhibit high dispersions and an improved surface to bulk ratio. Hence, the need for differentiating between bulk and surface structures is avoided.

Both model systems chosen were previously investigated in the selective oxidation of propane to propene [5,12,13,14]. However, few investigations addressed the selective oxidation of propene towards acrolein. Here, selective oxidation of propene was chosen as model reaction because many Mo [7-10] or V [15,16] mixed transition metal oxide model systems are active for this reaction. Understanding the correlations of structure and reactivity of these simple "binary" model systems with different metal sites, thus, may help to understand the complexity of highly active mixed transition metal catalysts.

1.2 Vanadium oxides in catalysis

Only 3-5% of the vanadium consumption is due to the use of vanadium compounds in catalysis [17,18]. Vanadium is mainly used as alloying element in the steel and metal industry. Nevertheless, vanadium based oxide catalysts, mainly V_2O_5, play an important role in selective oxidation reactions. Some important chemical processes that are based on vanadium containing metal oxide catalysts are summarized in ***Table 1-1***.

Table 1-1: Commercially important selective oxidations with catalysts containing vanadium [18,19].

Industrial process	Catalyst material	World production 2002 product (Mt/y)
Oxidation of SO_2 to SO_3, production of sulfuric acid	V_2O_5	> 100
Selective reduction NH_3 to NO_x	$V_2O_5/WO_3/TiO_2$	-
Oxidation of benzene to maleic anhydride	V_2O_5	1.4
Oxidation of butane to maleic anhydride	V,P oxides	
Oxidation of naphthalene to phthalic anhydride	V,Mo oxides and V-K oxides on SiO_2	2.2
Oxidation of o-xylene to phthalic anhydride	V,Ti oxides	
Oxidation of acrolein to acrylic acid	V,Mo,W oxides	3.8
Oxidation of methacrolein to methacrylic acid	V,Mo,W oxides	2.4

1.3 Supported vanadium oxides in catalysis

Supported vanadium oxides constitute model systems that are employed for the elucidation of fundamental knowledge on structure and reactivity of many heterogeneous oxidation reactions. The most important reactions discussed are the selective oxidation of methanol [20,21,22,23] and methane [24,25,26,27] to formaldehyde and the oxidative dehydrogenation of propane to propene [12,28,29]. Typical supports are SiO_2, Al_2O_3, ZrO_2, TiO_2, and Nb_2O_5 [16,30]. In the past decades many investigations were performed that concern the impact of the respective support material on the structure of the supported vanadium oxide phase and the catalytic performance. However, fundamental aspects concerning the vanadium oxide structure and the reactivity of supported vanadium oxide catalysts are still discussed intensively in the literature. A general introduction into the main topics discussed is provided by reviews from Wachs *et al.* [30], Keller *et al.* [18], and Muyalert *et al.* [31]. A brief summary of the proposed vanadium oxide structures of V_xO_y/SiO_2 catalysts under various conditions will be given below. ***Figure 1-1*** depicts the vanadium oxide structures present on silica supports that are proposed and discussed in the literature. The structure of V_xO_y/SiO_2 catalysts depends mainly on the vanadium oxide dispersion (***Figure 1-1***). Crystalline V_2O_5 is present at high vanadium coverages. The vanadium coverage where a monolayer of disperse vanadium oxide structures is achieved is well below the theoretical maximum monolayer coverage (7-8 V/nm^2) [30]. This is in contrast to other support materials like Al_2O_3. The maximum dispersion that can be obtained without the formation of detectable V_2O_5 crystallites is approximately 2.5 V/nm^2 and is typically reported for mesoporous silica supports with high surface areas such as SBA-15 or MCM materials [23,31,32].

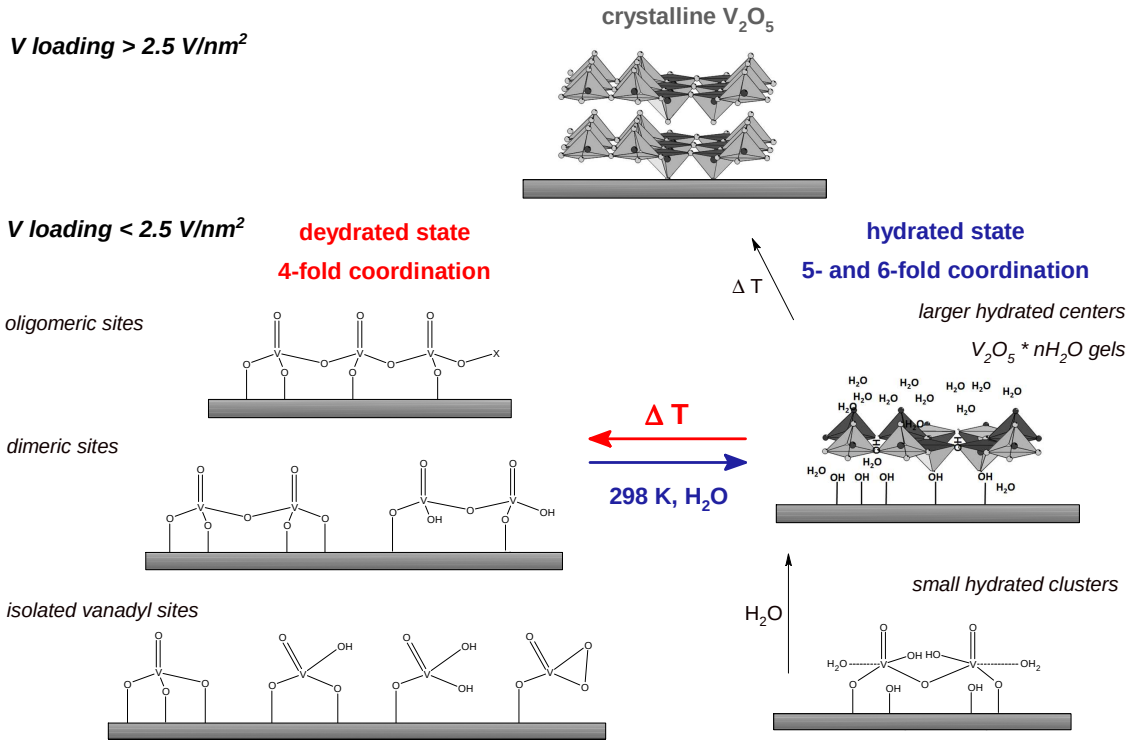

Figure 1-1: Main structural configurations of the vanadium oxide phase on silica supports discussed in literature.

First attempts to characterize the structure of highly dispersed vanadium oxide phases on SiO_2 were reported by Hanke *et al.* [33] in 1975. They proposed that after thermal treatment of V_xO_y/SiO_2 samples chainlike vanadium oxide species with tetrahedral coordination of the vanadium centers form on SiO_2. These vanadium species are transformed reversibly into octahedrally coordinated vanadium centers in the presence of water at ambient temperature. The described tetrahedral structure corresponds to the dehydrated state, and the octahedral structure corresponds to the hydrated state, according to the literature [31]. Since the early 1990's the number of publications that address the structure of the disperse vanadium oxide phases present on V_xO_y/SiO_2 catalysts increased significantly (***Figure 1-2***). This is ascribed to the development and the improvement of *in situ* spectroscopic methods such as Raman spectroscopy, UV-Vis-DRS, EPR, NMR, XAS, IR spectroscopy, and XPS that are mainly used to characterize V_xO_y/SiO_2 samples.

The hydrated state is proposed to consist of small square pyramidal [34] or pseudo octrahedral [35] coordinated vanadium centers (***Figure 1-1, right***). With increasing coordination of water to the hydrated vanadium oxide phase Xie *et al.* [34] reported the formation of V_2O_5*nH_2O gels that transform into V_2O_5 clusters during thermal treatment. Conversely, other authors assumed a reversible transformation of the highly dispersed hydrated state into the dehydrated state and vice versa for V_xO_y/SiO_2 samples [35].

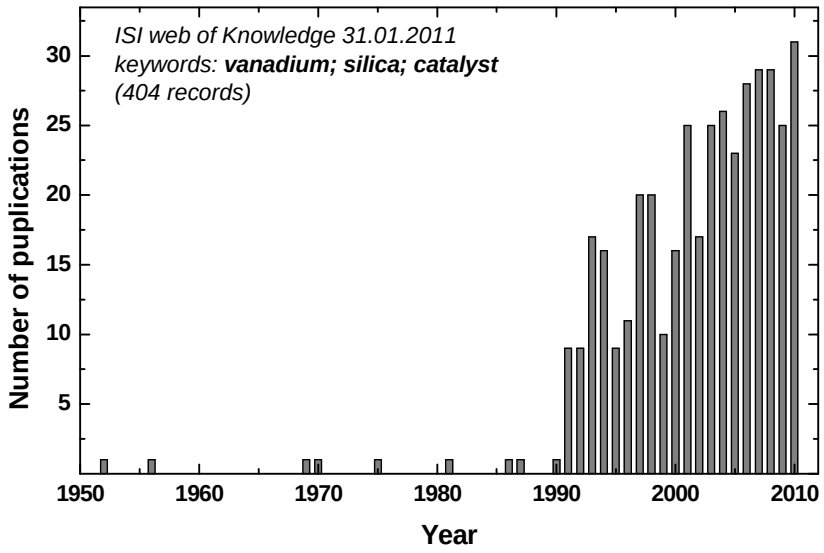

Figure 1-2: The number of papers that are found in the ISI web of Knowledge database using the keywords vanadium, silica, and catalyst [36].

All reports that discuss the structure of the highly dispersed dehydrated state propose that tetrahedrally coordinated vanadium centers are present on the silica support (***Figure 1-1, left***). However, structure, connectivity, and bonding of the tetrahedral units to the SiO_2 support are still under debate [37,38,39]. Mainly isolated "VO_4" structures are reported for the dehydrated state of V_xO_y/SiO_2. These isolated vanadium oxide sites can be attached via three Si-O-V bonds to the silica support [39]. Launay *et al.* [26] and others [24] concluded from the presence of V-OH groups in the dehydrated state that only two bonds to the support are present. Keller *et al.* [37] proposed "umbrella models" in which the isolated "VO_4" centers have either two V-OH bonds or a peroxo group (V-O_2). In contrast to reports that propose isolated vanadium oxides as the major phase in the dehydrated state, the formation of dimeric or chainlike V_xO_y structures with tetrahedral coordination of the vanadium centers was discussed. Schraml-Marth *et al.* [40] concluded that isolated vanadium centers will be present only at very low vanadium loadings. They reported the formation of dimeric units or chains with V-O-V bonds for medium vanadium loadings. The formation of the V-O-V bond was explained by a lack of "sterically suitable" Si-OH groups that are needed to form V-O-Si bonds [40]. Very recently, Hess *et al.* concluded on the basis of XAS [41], NEXAFS [42,43], and IR spectroscopy (using NO as probe molecule) [44] investigations that similar dimeric vanadium centers are present on SBA-15. Based on the results of Raman measurements, Hess *et al.* [38] proposed that the dimeric $[V_2O_7]_x$ units exhibit V-OH groups.

The dehydrated state is often assumed to be the active vanadium oxide phase under catalytic conditions. The role of V-O-support, V=O, V-OH, V-O_2, and V-O-V bonds in the catalytic mechanism (*e.g.* H abstraction from the organic reactant) is still under discussion. Bell [21] and others [16] proposed that the V-O-support bond plays a fundamental role in the selective oxidation of methanol to formaldehyde and other reactions. They assign the low activity (TOF) of V_xO_y/SiO_2 compared to other support materials (Al_2O_3, ZrO_2, TiO_2, Ta_2O_5, CeO_2, and Nb_2O_5) to the "high electronegativity of the Si cations" [16].

Conversely, calculations by Rosanska *et al.* [45] showed that a reaction mechanism involving vanadyl groups (V=O) or peroxo groups (V-O_2) is also feasible in the ODP of propane. No differences between isolated and dimeric V_xO_y/support species were determined by Rosanska *et al.* [45]. V-O-V bonds were proposed to be irrelevant for the selective oxidation of hydrocarbons because no increase of the TOF was observed with increasing vanadium loading (V-O-V bonds) [31]. However, the results of the vanadium oxide structure in the dehydrated state of V_xO_y/SiO_2 reported in the literature are very ambiguous. With respect to structure activity relationships more detailed knowledge on the structure of supported V_xO_y/SiO_2 will be required to reveal the active vanadium oxide phase under catalytic conditions.

More detailed introductions concerning the topic of the respective chapter and to the magnesium vanadate system will be provided in front of each chapter.

1.4 Outline of the work

The objective of the present work was the investigation of suitable vanadium oxide model systems for the selective oxidation of propene to acrolein. In addition to V_2O_5, magnesium vanadate systems and silica supported vanadium oxide catalysts with different vanadium loading were chosen as model catalysts. Prior to investigating the catalysts under catalytic conditions, a detailed characterization of the vanadium oxide structures was performed. The focus of this work was on supported vanadium oxide catalysts denoted as V_xO_y/SBA-15. A brief outline of the work is given below.

Part I ***(Chapter 2) Magnesium vanadates and V_2O_5 are discussed as model catalysts for the selective oxidation of propene.***

Magnesium vanadate phases ($Mg_3V_{10}O_{28}\cdot 28H_2O$, $Mg_2V_2O_7$, MgV_2O_6, and $Mg_3V_2O_8$) with different structural motifs were synthesized. The structural evolution of thermally stable maganesium vanadates and V_2O_5 under oxidizing, reducing, and propene oxidation conditions was investigated *in situ* using UV-Vis-DRS, XAS, and XRD. In addition, the catalytic performance during propene oxidation was determined in a fixed bed reactor. Correlations of reducibility and the vanadium oxide structure with the catalytic performance are described.

Part II ***(Chapter 3-9) SBA-15 supported vanadium oxides are discussed as model catalysts for the selective oxidation of propene.***

Chapter 3: A short introduction to the fundamentals of X-ray absorption spectroscopy and UV-Vis-DR spectroscopy is given. Furthermore, the experimental details about the preparation of SBA-15 and V_xO_y/SBA-15 and the various measurements performed are described.

Chapter 4: Three different preparation methods were evaluated for the preparation of supported vanadium oxide catalysts. During preparation the evolution of the vanadium oxide structure was monitored using spectroscopic methods. The SBA-15 support was characterized with XRD, physisorption measurements, and electron microscopy. Three vanadium loadings in the range of 1.4-7.7 wt% V (0.3-2.4 V/nm^2) were chosen for further structural and catalytic characterization.

Chapter 5: Elucidation of the hydrated and dehydrated vanadium oxide structure present on SBA-15 was performed using UV-Vis-DRS and XAS spectroscopy. Theoretical model structures which were suitable to describe the experimental data were employed.

Chapter 6: Hydration and dehydration processes of the vanadium oxide structure were investigated *in situ* using various spectroscopic methods. In addition, the dehydration of the SBA-15 support was investigated. Aging effects and re-dispersion of crystalline V_2O_5 species to disperse vanadium oxide species were observed. The impact of water on the dehydration process was probed.

Chapter 7: The evolution of the structure of V_xO_y/SBA-15 catalysts and the composition of the gas phase were investigated *in situ* under propene oxidation conditions. Reliable catalytic results were obtained from measurements in a laboratory fixed bed reactor. The catalytic performance during propene oxidation was investigated as a function of thermal treatment and vanadium loading.

Chapter 8: Reducibility in propene and re-oxidation of V_xO_y/SBA-15 in oxygen and under catalytic conditions was followed by *in situ* UV-Vis-DRS and XAS. Changing interactions of the vanadium oxide phase and the SiO_2 support were observed as a result of the catalytic reaction in propene and oxygen.

Chapter 9: General conclusions that were deduced from the V_xO_y/SBA-15 model system with respect to structure activity relationships are provided.

Part I

Spectroscopic and catalytic investigations of magnesium vanadate model catalysts and V_2O_5 for selective propene oxidation

2 *Magnesium vanadate model systems and V_2O_5 during selective propene oxidation*

2.1 Introduction

Vanadium based mixed transition metal oxide catalysts play an important role in selective oxidation catalysis of light alkanes and alkenes with gas phase oxygen [5,162,46]. However, the most active and selective catalysts for such reactions exhibit complex structures and compositions, *e.g.* Mo/V/(Sb,Te)/Nb/O catalysts [5,14,46]. For the development of improved catalysts it is essential to understand the specific role of vanadium in oxidation catalysis. Besides 'trial and error' approaches model system based studies are employed. The latter allow disentangling of the individual effects of chemical composition, coordination, and electronic structure of the transition metal oxide. The focus of the present work was to investigate the influence of structural motifs on the catalytic behavior of vanadium oxides. Selective oxidation of propene was chosen as model reaction because many Mo [47] or V [16,48] mixed transition metal oxide model systems are active for this reaction. Finding correlations between these model systems may help to understand the complexity of highly active mixed transition metal catalysts.

Here, vanadium oxide based model systems exhibiting an average vanadium valence of V^{5+} were employed. Only V_2O_5 was found as stable binary V^{5+} oxide. Therefore ternary vanadium oxides were sought to extent the range of available oxides. In order to avoid the introduction of a second "possibly active" metal atom (Fe, Cr, Zn, Pb, Cu,…) alkali and alkali earth vanadates were preferred. However, most alkali (Na, K) orthovanadates are sensitive towards hydration which makes them unsuitable. Furthermore, alkali earth vanadates tend to form carbonates which may be stable and may not decompose at reaction temperatures [49,50]. Typical carbonate decomposition temperatures are 1098 K for $CaCO_3$ and 1723 K for $BaCO_3$. Only $MgCO_3$ decomposes at a lower temperature of 623 K. Therefore, different magnesium vanadate phases were synthesized as ternary vanadium oxide phases. Magnesium vanadate systems exhibit a variety of structural motifs (octahedral and tetrahedral coordination of V^{5+}) which makes them very suitable as structural model systems.

Reports on the catalytic performance of magnesium vanadates in propene oxidation are rarely found in literature [51,52]. Supported vanadium oxide and magnesium vanadate catalysts are mostly used for oxidative dehydrogenation (ODH) of light alkanes. In this field, activity and selectivity of vanadium oxide catalysts is still a controversial issue [53]. A summary of the concepts is provided by Centi *et al.* [14] and Bettahar *et al.* [5]. The influence of geometry between the vanadium oxide unit and the hydrocarbon [54], the redox properties [55,56,57,58], and other aspects are reviewed. For the selective propene oxidation similar correlations as found for the ODH of propane may be present.

V_2O_5 was measured in addition to the magnesium vanadates. V_2O_5 is often used as a reference compound. It is active but less selective for propene oxidation and other reactions like the ODH of propane [51,58,59]. Haber *et al.* [60] and other authors discussed the catalytic behavior of V_2O_5 on the basis of theoretical calculations and *in situ* measurements. They proposed V_6O_{13} and V_4O_9 intermediates to be present under reducing and catalytic conditions [60,61,62,63]. In contrast, Yamazaki *et al.* [64] and Holdago *et al.* [65] only detected V_4O_9 phases under sulfur and H_2S oxidizing conditions. The important role of the nature and the valence of reduced vanadium oxide phases in oxidation catalysis of V_2O_5 was shown by Ballarini *et al.* for the ODH reaction [59]. However, a detailed knowledge of structure activity correlations under *in situ* propene oxidizing conditions remains scarce. Hence, a detailed *in situ* analysis was performed to investigate the kind of binary vanadium oxide phase present under catalytic propene oxidation.

2.2 Experimental

2.2.1 Sample preparation

$Mg_3V_2O_8$ (magnesium orthovanadate), MgV_2O_6 (magnesium metavanadate) and $Mg_2V_2O_7$ (magnesium pyrovanadate) where synthesized according to Delmon *et al.* [55] via a citrate method. $Mg(NO_3)_2{\cdot}6H_2O$ (Fluka, 99 %) and NH_4VO_3 (Fluka, 99 %) were used as metal precursors in the concentrations required for the desired Mg/V ratio. The salts were dissolved in 500 ml water. The mixture was heated at 363 K for 2 h until a clear yellow solution was obtained. After cooling to 300 K 2 ml of 65% HNO_3 were added to avoid precipitation. Subsequently, citric acid (three negative charges per molecule, Roth 99.5%) was added to neutralize the positive charges of Mg^{2+} and V^{5+}. Water was removed by evaporation in two steps to avoid the formation of NO_x gases (200 mbar and 343 K; 30 mbar and 363 K). The resulting amorphous solid was calcined in two steps: 18 h at 653 K and 6-8.5 h at 823-1023 K either in a muffle furnace or an open tube furnace depending on the resulting phase (***Table 2-1***). Calcination of the precursor was performed in several batches due to the small size of the crucibles. Batches exhibiting the same structural characteristics were mixed and homogenized.

$Mg_3V_{10}O_{28}{\cdot}28H_2O$ (magnesium decavanadate) was synthesized according to Iida and Ozeki [66]. V_2O_5 (3.64 g / 20.1 mmol) was dissolved in 450 ml of a H_2O_2/H_2O mixture (50 ml 30% H_2O_2 and 400 ml H_2O) resulting in a red solution. Afterwards a solution of $Mg(CH_3COO)_2{\cdot}4H_2O$ (2.68 g / 12.50 mmol) in 15 ml water was added and the color of the mixture changed to orange. The amount of water was slowly reduced by evaporation (363 K, 30-40 mbar, 15 h) to 100 ml. Acetone was added drop wise to the remaining solution (100 ml, 30 min). The resulting precipitate was filtered, washed with acetone, and dried under reduced pressure. The solid phase was recrystallized by dissolving the powder in a few ml of water and then storing the solution in a closed bottle in the refrigerator. Deep orange crystals were obtained.

V_2O_5 (vanadiumpentoxide) was used as purchased (Alfa Aesar 99.8%). Phase purity was confirmed by XRD. The V_2O_5 structure proposed by Enjalbert *et al.* [140] matched the experimental XRD pattern and was used for structure refinement.

All samples were stored under ambient conditions (298 K, air).

Table 2-1: Preparation details of the synthesized magnesium vanadate samples.

Magnesium vanadate phase	Furnace type	Crucible	Temperature [K] ; Time second step [h]
$Mg_3V_2O_8$	muffle and tube furnace	ceramic, quartz	1023; 6
m-$Mg_2V_2O_7$ (Batch A)	muffle furnace	ceramic	923 ; 6
m-$Mg_2V_2O_7$ (Batch B)	muffle furnace	ceramic with cover	823-923; 8.5
t-$Mg_2V_2O_7$	tube furnace	quartz	1023 ; 6
MgV_2O_6 (Batch C)	muffle furnace	ceramic	923 ; 6
MgV_2O_6 (Batch D)	tube furnace	quartz	923 ; 6

2.2.2 Powder X-ray diffraction (XRD)

Ex situ XRD measurements were carried out on an X'Pert PRO MPD diffractometer (θ-θ geometry), using Cu K alpha radiation and a solid-state multi-channel PIXcel® detector. Wide angle scans ($5° \leq 2\theta \leq 90°$, variable slits) were collected in reflection mode. The sample was prepared on a silicon sample holder. Data analysis was performed using the software package Topas 3 and Diffrac Plus Evaluation 2003 (Bruker AXS). For phase identification a phase analysis was performed using the PDF and ICSD databases. To verify the structures found a refinement was performed using a fundamental parameter approach. Only the cell parameters (a,b,c,α,β,γ) of the corresponding theoretical structures, a background function, and the size and strain parameters were refined. *In situ* XRD measurements were conducted on a STOE diffractometer (θ-θ Mode) using an Anton Paar *in situ* cell. Thermal stability tests were conducted in 20% O_2 in He (total flow 100 ml/min) in a temperature range from 293 K to 773 K. Reaction tests were performed in 5% propene and 5% O_2 in He in the temperature range from 323 K to 673 K (5 K/min, total flow 56 ml/min). The gas phase composition at the cell outlet was continuously monitored using a non-calibrated mass spectrometer in a multiple ion detection mode (Pfeiffer Omnistar). Phase analysis was performed using the WinXPOW software package (STOE). After reaction all samples were measured *ex situ* (see above).

2.2.3 UV-Vis Diffuse reflectance spectroscopy (UV-Vis-DRS) measurements

UV-Vis-DRS measurements were conducted in a Jasco-V670 UV-VIS-NIR spectrometer using an *ex situ* integration sphere and a Praying Mantis™ *in situ* cell (Harrick Scientific Products, Inc.). MgO (ABCR) was used as reflectance standard. To avoid sintering effects the samples were diluted with MgO for *in situ* measurements. Thermal stability tests were conducted in 20% O_2 and He (total flow 50 ml/min) in a temperature range from 293 K to 657 K using a heating rate of 4 K/min. Reaction tests were performed in

5% propene and 5% O_2 in He in the temperature range from 293 K to 657 K (4 K/min, total flow 40 ml/min). The gas atmosphere was analyzed using a non-calibrated mass spectrometer in a multiple ion detection mode (Pfeiffer Omnistar). A linear correction ($T_{sample} = 0.85\ T_{holder} + 2$ [°C]) was applied to the sample holder temperature which was obtained by a separate measurement using a thermocouple placed in the sample powder bed.

2.2.4 X-ray absorption spectroscopy (XAS)

Ex situ transmission XAS experiments at the V K edge (5.465 keV) were performed at the XAS beamline C at *HASYLAB* using a Si (111) double crystal monochromator. Powders were pressed with a force of 1 ton into a 13 mm diameter pellet resulting in an edge jump at the V K edge of $\Delta\mu_x \sim 1$. X-ray absorption fine structure (XAFS) analysis was performed using the software package WinXAS v3.2 [91]. Background subtraction and normalization were carried out by fitting a linear polynomial to the pre-edge and a 3rd degree polynomial to the post-edge region of an absorption spectrum, respectively. The extended X-ray absorption fine structure (EXAFS) $\chi(k)$ was extracted by using cubic splines to obtain a smooth atomic background $\chi(k)$. The $FT(\chi(k)*k^3)$, often referred to as pseudo radial distribution function, was calculated by Fourier transformation of the k^3-weighted experimental $\chi(k)$ function, multiplied by a Bessel window, into R space.

2.2.5 Quantitative catalysis measurements

Quantitative catalysis measurements were performed using either the UV-Vis-DR *in situ* cell or a fixed bed laboratory reactor connected to an online gas chromatography system (Varian CP-3800) and a non calibrated mass spectrometer (Pfeiffer Omnistar). Hydrocarbons and oxygenated reaction products were analyzed using a Carbowax 52CB capillary column connected to an Al_2O_3/MAPD capillary column or a fused silica restriction (25 m x 0.32 mm) each connected to a flame ionization detector (FID). Reactant gas flow rates of oxygen, propene, and helium were adjusted through separate mass flow controllers to a total flow of 40 ml/min. A mixture of 5% propene and 5% oxygen in He was used for catalytic tests in the range of 295-683 K. Boron nitride (Alfa Aesar, 99.5 %) was used as diluent.

2.3 Results and discussion

2.3.1 Ex situ structural characterization of prepared samples

The synthesized samples were investigated using X-ray powder diffraction (XRD) for phase identification and structure refinement. ***Figure 2-1*** shows the detected XRD powder pattern of the phases obtained together with the theoretical pattern from structure refinement (***Appendix, 10.8***). For $Mg_3V_2O_8$ [67] and MgV_2O_6 [68] only a single phase was detected. For $Mg_2V_2O_7$ a monoclinic [69] and a triclinic [139] phase were synthesized depending on the calcination temperature and furnace type (***Table 2-1***). Each phase was obtained with a phase purity of more than 95 wt%.

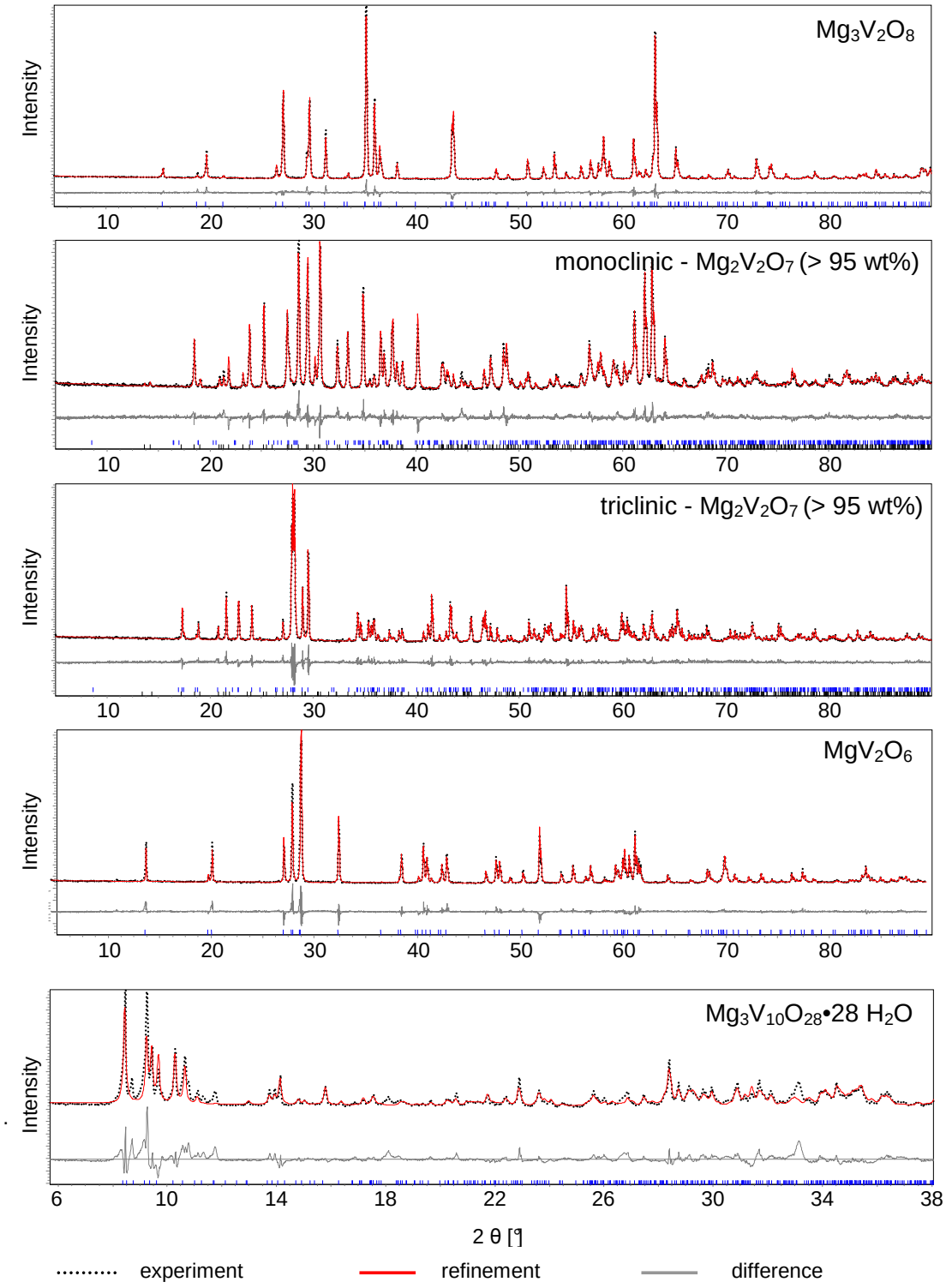

Figure 2-1: Experimental Cu Kα XRD powder patterns of the synthesized magnesium vanadate phases (dotted black) together with the XRD structure refinement of the corresponding phase (solid red) and the differential plot (solid grey).

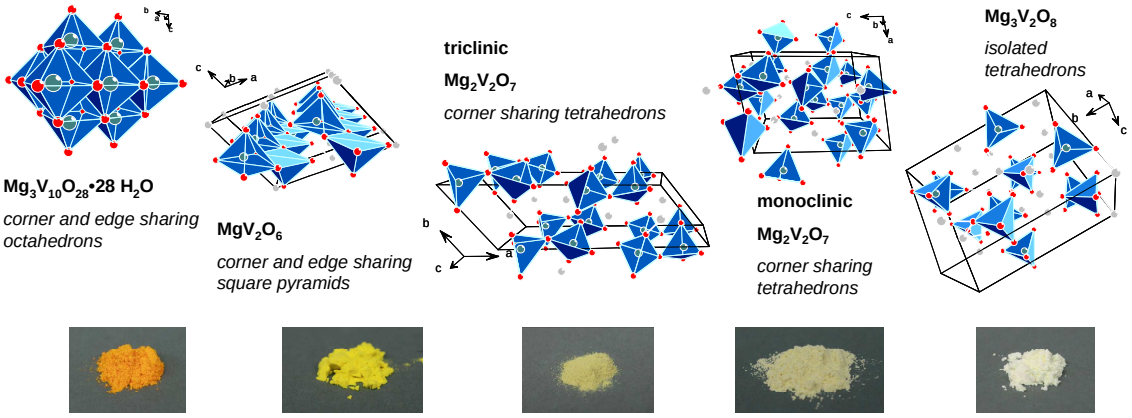

Figure 2-2: Structure motifs of the magnesium vanadate phases and the color of the respective powder.

For the magnesium decavandate a phase refinement of the powder pattern was not satisfactory. However, single crystal analysis (data not reported here) yielded the same $Mg_3V_{10}O_{28}{\cdot}28H_2O$ structure as reported by Iida *et al.* [66]. The observed deviations are explained by different crystal water content due to grinding of the sample. A representation of the synthesized magnesium vanadate phases together with a picture of the colored powders is depicted in ***Figure 2-2***. In addition to the XRD patterns, XAS spectra of all samples were recorded. XAS is more sensitive to changes in the local structure and permits a more detailed determination of average valence, coordination, and structural disorder of the absorbing vanadium center. All three characteristics might change during reaction. The XANES and EXAFS spectra are shown in ***Figure 2-3***. Comparison of position, height, and area of the observed pre-edge peaks as reported by Wong *et al.* [131], indicated that all samples and the V_2O_5 reference had an average valence of +5. UV-Vis diffuse reflectance spectroscopy (UV-Vis-DRS) is more sensitive towards partial reduction processes than XAS or XRD.

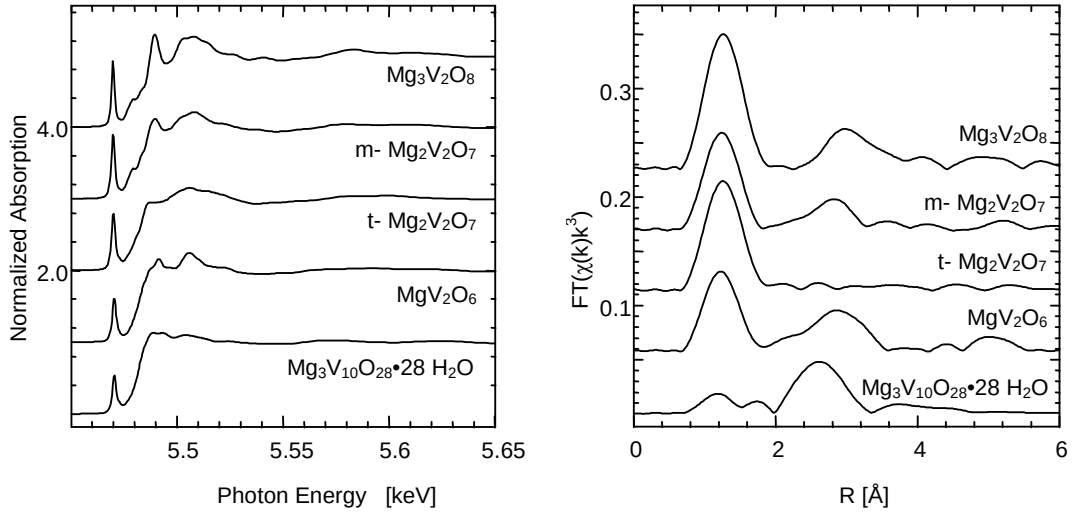

Figure 2-3: V K edge XANES (right) and Fourier transformed $\chi(k)*k^3$ (left) of the as prepared magnesium vanadates.

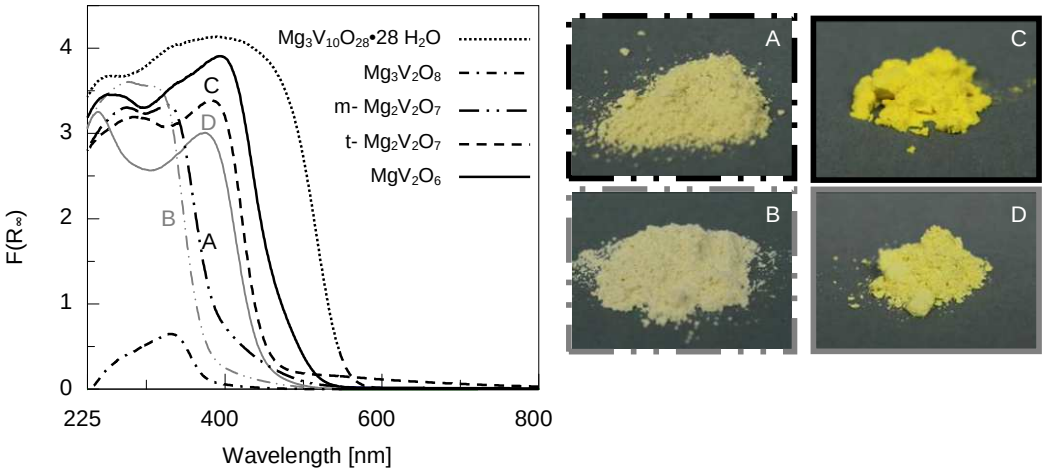

Figure 2-4 Left: UV-Vis-DR absorption spectra of the as-prepared magnesium vanadate phases and differrent sample batches (Table 2-1). Right: picture of the different colored samples batches of the monoclinic $Mg_2V_2O_7$ phase (A,B) and MgV_2O_6 (C,D) phase (lines are the same as on the left side).

The UV-Vis-DR spectra of all samples are shown in ***Figure 2-4***. Only LMCT transitions were visible which are located at wavelengths lower than 600 nm. Vanadium valences of V^{4+}, V^{3+} would generate intervalence and d-d transitions at longer wavelengths. The absence of such bands matched the average valence of V^{+5} observed in XAS. Differences between the respective sample batches considerably affected the UV-Vis-DR spectra. As shown in ***Figure 2-4, right*** different sample batches of the prepared MgV_2O_6 and m-$Mg_2V_2O_7$ did not have the same color. To gain information about the electronic structure, UV-Vis edge energies [99,100,127] and low energy LMCT band positions were determined. The differences in E_g value and the low energy LMCT band position (***Table 2-2***) between the samples batches was ~ 0.2 eV. This was more than the deviations achieved by simple dilution of the sample with the reflectance standard (< 0.1 eV). In XAS a damped XANES and EXAFS were observed for samples A and C compared to sample B and D (***Figure 2-4, right***). XRD structure refinement resulted in poor residuals (GOF, R_{Bragg}) for sample C (***Figure 2-4, right***).

Table 2-2: UV-Vis edge energies (E_g) and low energy LMCT band positions extracted from UV-Vis-DR spectra in Figure 2-4.

Sample	Low energy LMCT [nm]	Low energy LMCT [eV]	E_g [eV]
$Mg_3V_2O_8$	336	3.73	3.44
m-$Mg_2V_2O_7$ (Batch A)	330	3.76	3.29
m-$Mg_2V_2O_7$ (Batch B)	315	3.92	3.47
MgV_2O_6 (Batch D)	376	3.30	2.90
MgV_2O_6 (Batch C)	396	3.13	2.73
t-$Mg_2V_2O_7$	385	3.22	2.85
$Mg_3V_{10}O_{28}$·28 H_2O	~ 400	~ 3.1	2.35

Apparently, structural disorder in the samples had a pronounced effect on the UV-Vis-DR spectra and thus an unambiguous assignment of the structures in the spectra was difficult. Therefore, UV-Vis-DR spectroscopy was used to follow changes during temperature programmed reactions qualitatively and was combined with XRD and XAS analysis of the samples before and after reaction.

Structural stability of the magnesium vanadate phases in oxygen containing atmosphere at elevated temperatures was tested using *in situ* XRD and *in situ* UV-Vis-DRS (20% O_2, 300-773 K). Apart from $Mg_3V_{10}O_{28}\cdot 28H_2O$ all phases and reference V_2O_5 were stable. The magnesium decavanadate decomposed to V_2O_5 and MgV_2O_6 as shown in ***Figure 2-5***. Water was released in three endothermic steps (the first one (298-320 K) not shown in ***Figure 2-5***). During the second (320-450 K) and third water (450-500 K) releasing step the detected reflexes decreased strongly in the XRD pattern. Apparently, this water stabilized the tertiary structure between the different decavanadate units [70]. Above 600 K crystalline V_2O_5 and MgV_2O_6 phases were formed by exothermic decomposition. Due to its low thermal stability $Mg_3V_{10}O_{28}\cdot 28\ H_2O$ was not used for further experiments. During thermal treatment of all other phases in the *in situ* UV-Vis-DR cell only a reversible red shift of the UV-Vis edge energy E_g (0.10 – 0.25 eV) was observed without any structural changes.

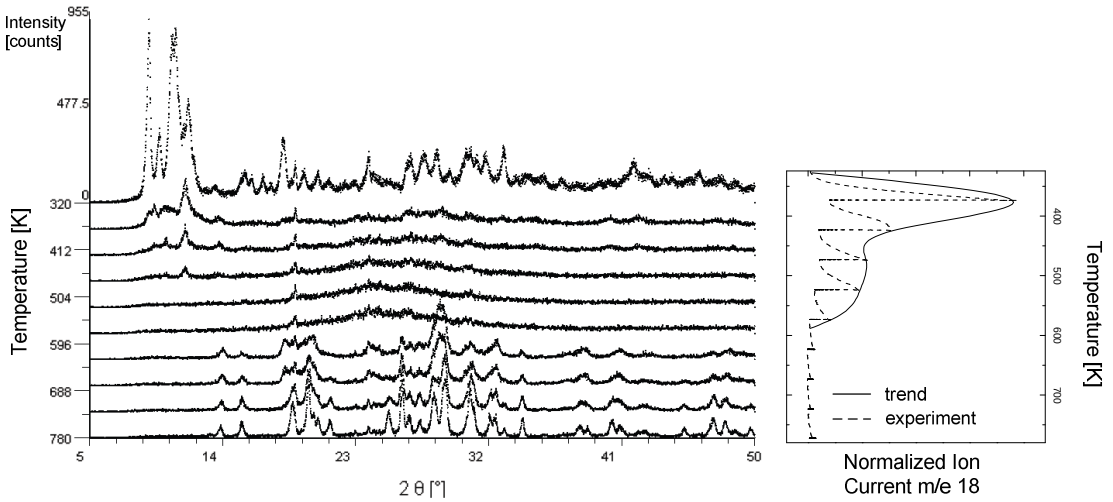

Figure 2-5: Evolution of Cu Kα XRD patterns during thermal treatment of $Mg_3V_{10}O_{28}\cdot 28H_2O$ (323-773 K, 20% O_2 in He) together with the ion current (H_2O) measured during *in situ* XRD.

2.3.2 Structure and reactivity of V_2O_5 and m-$Mg_2V_2O_7$ under catalytic conditions

The structural characterization of the magnesium vanadate phases and V_2O_5 (as active V^{+5} reference) during selective propene oxidation was conducted *in situ* using XRD and UV-Vis-DRS combined with online gas phase analysis. For quantitative analysis of the reaction gas mixture a gas chromatograph was used. Because of the long measurement times of ~ 22 min the gas phase was also monitored and analyzed qualitatively by a non-calibrated mass spectrometer to gain sufficient time resolution. During the temperature programmed reaction none of the magnesium vanadate phases showed any significant structural changes in the XRD measurements. Therefore, only m-$Mg_2V_2O_7$ and V_2O_5 will be compared

and discussed in detail. *In situ* XRD patterns of both samples are depicted in ***Figure 2-6***. As mentioned before no additional phases were detected during measurement of m-$Mg_2V_2O_7$. This is in contrast to the V_2O_5 reference sample (***Figure 2-6, right***). The initial V_2O_5 (space group *Pmmn* [140]) phase was reduced to VO_2(B) (space group *C*12/*m*1 [71]) at temperatures above 623 K. The mixed valence phase V_4O_9 [64] was observed as intermediate phase. In contrast, for the reduction in hydrogen V_6O_{13} was reported as the main intermediate phase [72]. Yamazaki *et al.* described this metastable $(V^{4+}O)_2V^{5+}{}_2O_7$ phase (V_4O_9) as an orthorhombic *Cmcm* structure. V_4O_9 was detected during the reduction of V_2O_5 into VO_2(B) with sulfur. Yamazaki *et al.* [64] assumed a different reaction mechanism because no V_6O_{13} was detected. They concluded that during the reduction of V_2O_5 to V_4O_9 oxygen point defects are formed while the transformation of V_2O_5 into V_6O_{13} proceeds via shearing of the structure.

According to the data from the vanadium oxide phase diagram the formation of a reduced vanadium oxide phase at 673 K would only be expected thermodynamically at low oxygen content (equilibrium pressure $p(O_2) < 1$ Pa) [73,74]. Thus, the presence of reduced vanadium oxide phases was not expected under reaction conditions ($p(O_2) \sim 5$ kPa). However, the phase diagram only considers the oxygen pressure dependence of the binary vanadium oxide system at thermodynamic equilibrium and neglects the reducing potential of the reactants (propene, CO). Due to the long residence times in the *in situ* XRD cell, very high oxygen conversions (> 99%, 650-673 K) were detected. This caused increased total oxidation and the formation of CO. Therefore, the formation of reduced vanadium oxide phases appears likely. For the magnesium vanadate system the oxygen equilibrium pressures where a reduction into the Mg_2VO_4 or MgV_2O_4 phases and MgO is thermodynamically favorable are much lower than for V_2O_5 ($p(O_2) < 1$ Pa). According to the magnesium vanadate phase diagram calculated by Kijima *et al.* [73] this oxygen equilibrium pressure is approximately $8 \cdot 10^{-10}$ Pa (673 K). Apparently, no reduction of the bulk phases seemed feasible concerning the low oxygen conversions detected in the employed temperature range during the *in situ* XRD experiments (***Figure 2-6, left***).

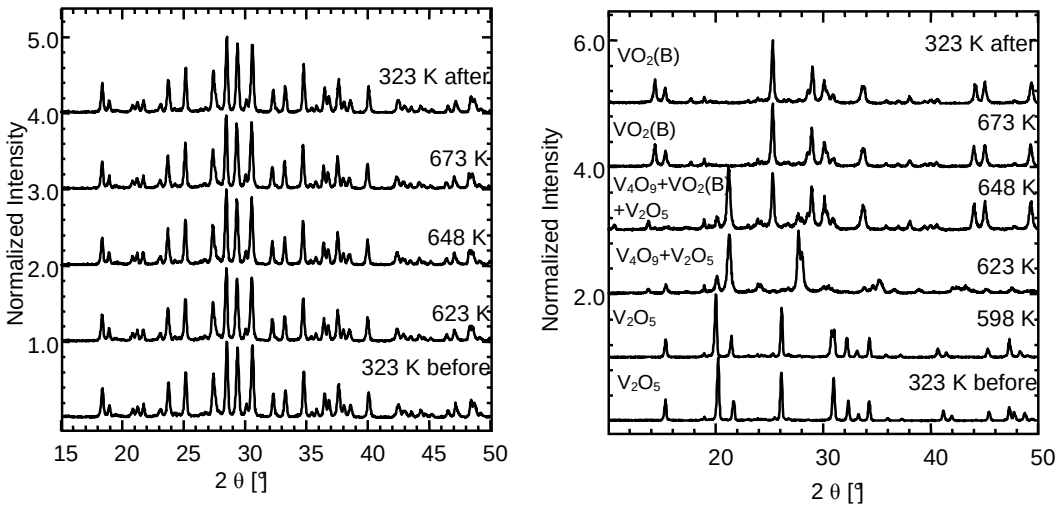

Figure 2-6: Selected *in situ* powder pattern during treatment in 5% propene and 5% oxygen in He (temperature range from 300 K to 673 K) of monoclinic $Mg_2V_2O_7$ (left) and V_2O_5 (right); the diffraction at ~18.9 °2θ originates from the sample holder.

UV-Vis-DRS measurements were conducted in addition to XRD measurements. The spectra of V_2O_5 and m-$Mg_2V_2O_7$ before and after reaction under propene oxidizing conditions from 298 K to 653 K are shown in ***Figure 2-7*** together with the corresponding V K edge XANES spectra. For V_2O_5 the XANES changed significantly. The pre-edge peak decreased and the edge energy shifted to a lower value which indicates reduction of the sample. This reduction was observed as a prolonged absorption region in the UV-Vis-DR spectrum (500-2500 nm). XRD analysis after reaction showed a mixture of V_2O_5, V_4O_9, and VO_2 phases. Thus, the observed absorption bands > 500 nm were ascribed to a mixture of d-d and intervalence charge transfer transitions originating from the reduced V^{4+} oxidation state. Similar to the XRD results no distinct changes were detected in the XANES spectra of the m-$Mg_2V_2O_7$ phase. Small absorption bands between 500 nm and 1000 nm occurred in the UV-Vis-DR spectra of m-$Mg_2V_2O_7$ samples after propene oxidation. These bands were attributed to small fractions of reduced magnesium vanadate phases present at the surface. An overall reduction of the magnesium vanadate phases is not very likely considering the phase diagram [73], as discussed above. However, UV-Vis-DRS spectroscopy is much more sensitive towards partial reduction than XRD and XAS. Furthermore, reduction and re-oxidation kinetics of the involved vanadium centers during the oxidation of propene play an important role [162]. Thus, the reduction step of the involved vanadium oxide center may be slower than the re-oxidation step of this center during propene oxidation. This would cause partially reduced vanadium centers on the surface during the propene oxidation.

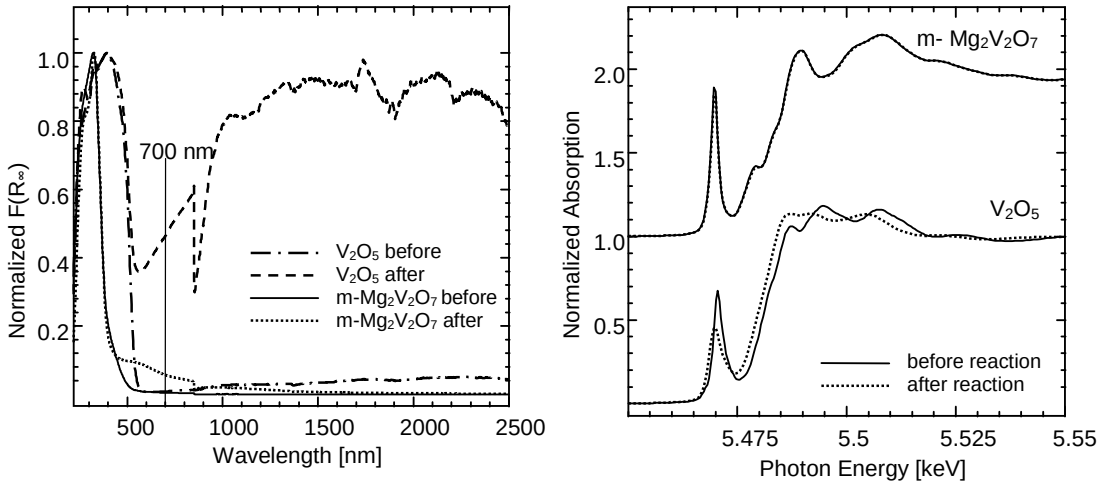

Figure 2-7: UV-Vis-DR absorption spectra (left) and V K edge XANES spectra (right) of monoclinic $Mg_2V_2O_7$ and V_2O_5 before and after treatment in 5% propene and 5% oxygen in He (temperature range from 300 K to 653 K); glitch at 850 nm originates from detector change.

In order to compare the reduction process of all magnesium vanadates the intensity at 700 nm relative to the normalized absorption maximum in the applied temperature range is depicted in ***Figure 2-8, left***. The wavelength at 700 nm was chosen because it is in the range where d-d absorption bands are located. Thus, it is representative for reduced vanadium species. Moreover, the wavelength of 700 nm is located before the wavelength of detector change (850 nm) in the UV-Vis instrument. In the spectra of the two pyrovanadate phases (m- and t-$Mg_2V_2O_7$) a small increase in the intensity at 700 nm was detected. It was assumed that these phases were slightly reduced under catalytic conditions. Comparing the evolution of

the gas phase of m-$Mg_2V_2O_7$ and V_2O_5, the formation of oxidation products (water, carbon dioxide, acrolein) was observed above 570 K for both samples (***Figure 2-8, right***). Apparently, the onset of acrolein formation for V_2O_5 coincidences with the increase in absorption at 700 nm and the appearance of the V_4O_9 phase in the XRD pattern. Interestingly, a significant decrease of acrolein and increase of water and CO_2 in the gas phase was observed above 635 K. Comparing this with the detected structural transformations in XRD (***Figure 2-6, right***) it was assumed that apart from V_4O_9 formation a further reduction towards VO_2(B) occurred. The formation of VO_2(B) seemed to increase the rate of total oxidation of propene.

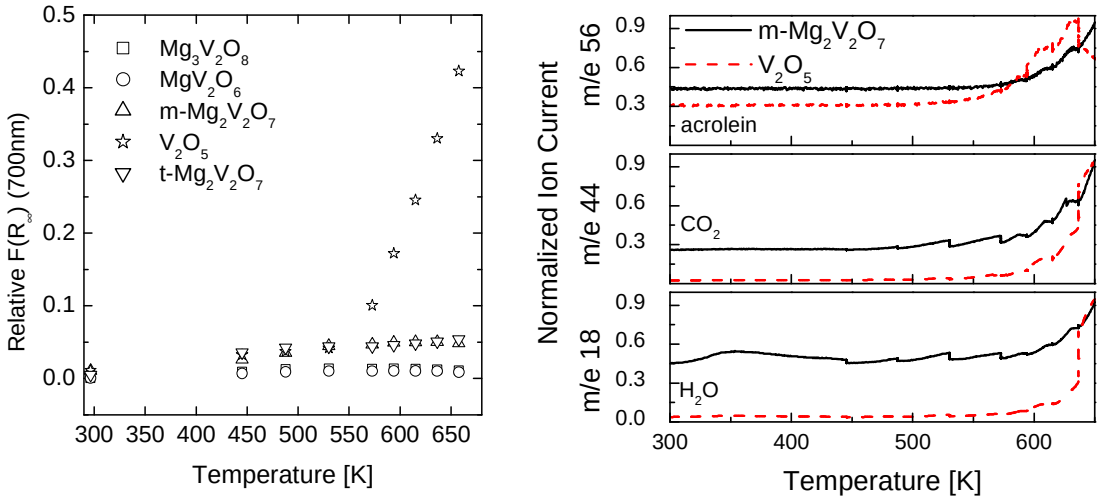

Figure 2-8 Left: Evolution of relative absorption at 700 nm (compared to maximum intensity in the respective spectrum) of the UV-Vis-DR absorption spectra of magnesium vanadate phases and V_2O_5. Right: evolution ion currents (CO_2, water and acrolein) measured during *in situ* UV-Vis-DR studies (thermal treatment in 5% propene and 5% oxygen in He).

2.3.3 Catalytic performance of the magnesium vanadates and V_2O_5

Compared to V_2O_5 all magnesium vanadate samples showed differential conversions (~ 1%). Moreover, quantitative measurements were conducted in a laboratory fixed bed reactor at 673-684 K (***Table 2-3***) which allowed the use of a larger sample mass to increase the conversion. Comparing the conversions of the magnesium vanadate phases, different activities were detected. Taking the rate of propene conversion per gram catalyst as indicator for the activity, the following dependence was found: V_2O_5 >> m-$Mg_2V_2O_7$ > MgV_2O_6 > $Mg_3V_2O_8$ >> t-$Mg_2V_2O_7$ (no activity). A comparison of the measured selectivities could only be made qualitatively because no isoconversional conditions were achieved. Compared to V_2O_5, $Mg_3V_2O_8$ exhibited a low conversion and similar amounts of total oxidation products (CO, CO_2; ***Figure 2-9, right***). For the two other phases the amounts of total oxidation products were slightly higher than that of V_2O_5. The detected amounts of partial oxidation products (oxygenates) were comparable for the m-$Mg_2V_2O_7$ and $Mg_3V_2O_8$ samples.

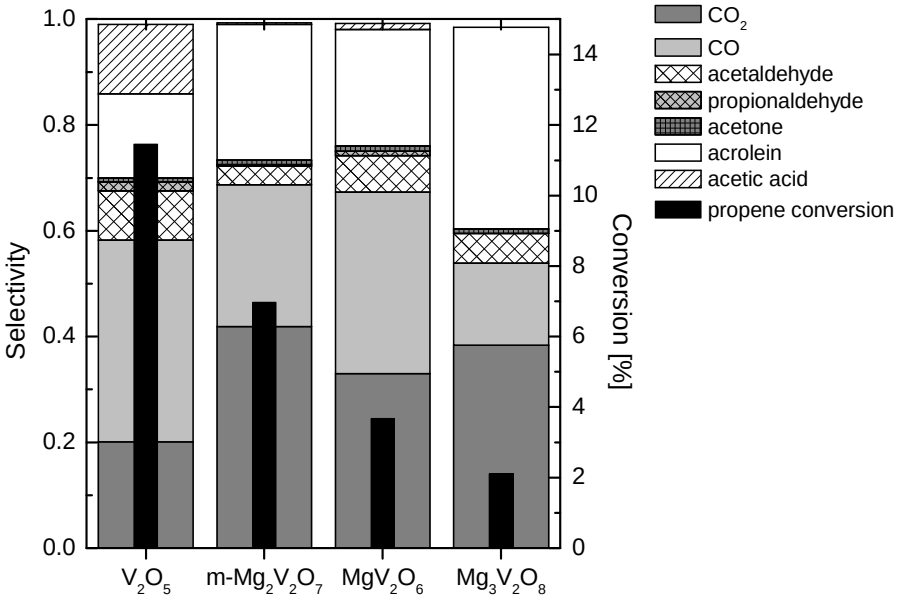

Figure 2-9: Propene conversion and selectivity of the magnesium vanadate phases and V_2O_5 in 5% propene and 5% oxygen in He at 673-683 K

Acrolein was formed as the main product (~ 83% of the oxygenates) followed by acetaldehyde (~ 12% of the oxygenates). Propionaldehyde, acetone and acetic acid were detected as minor components. For the MgV_2O_6 phase the acrolein formation was lower (~ 69% of the oxygenates) and the formation of other partial oxidation products was slightly higher. Hence, a lower selectivity towards acrolein formation was ascribed to this phase. For V_2O_5 the selectivity towards acrolein was lower (~ 38% of the oxygenates) and significant amounts of partial degradation products such as acetic acid (~ 32% of the oxygenates) were detected.

Table 2-3: Catalytic performance of the magnesium vanadate phases compared to V_2O_5 during the selective oxidation of propene (40 ml/min 5% O_2 and 5% propene in He).

Sample	Fixed bed laboratory reactor			*in situ* UV-Vis-DRS cell		
	mass [mg]	$X_{propene}$ [%] 673 K	rate 673 K $\left[\frac{\mu mol_{propene}}{g_{catalyst} \cdot s}\right]$	mass [mg]	$X_{propene}$ [%] 658 K	rate 658 K $\left[\frac{\mu mol_{propene}}{g_{catalyst} \cdot s}\right]$
$Mg_3V_2O_8$	94	< 2	< 0.3	35	0.8	0.3
m-$Mg_2V_2O_7$	91	7	1.1	43	0.7	0.2
t-$Mg_2V_2O_7$	92	--	--	61	1.1	0.3
MgV_2O_6	94	4	0.6	56	0.9	0.2
V_2O_5	20	11	8.2	59	12	2.9

2.3.4 Structural evolution of V_2O_5 and m-$Mg_2V_2O_7$ under reductive conditions

A common explanation of activities and selectivities of magnesium vanadates in the ODH of propane is the difference in their reduction behavior [55,57]. Here, temperature-programmed reduction (TPR) in propene (298-673 K, 5% propene in 95% He) was used to investigate possible correlations between catalytic performance and reducibility of magnesium vanadates and V_2O_5. Comparable to the results obtained under catalytic conditions almost no reduced phases were detected in the XRD patterns of the magnesium vanadate phases (***Figure 2-10, left***). Only at 673 K a small increase in the intensity of the diffractions around 35 °2θ and 43 °2θ was observed. These diffractions may be attributed to MgO [75] and Mg_2VO_4 [76] which were formed from reduction of m-$Mg_2V_2O_7$ [73]. Due to the low intensity and the proximity of the characteristic diffractions of all phases, a more detailed analysis was not feasible. In the XRD patterns of the other magnesium vanadate phases after reduction at 673 K these diffractions were not identified. Conversely, V_2O_5 was reduced to V_2O_3 in several steps (***Figure 2-10, right***). Above 523 K the V_4O_9 phase was formed, which transformed into VO_2(B) above 598 K. Around 648 K VO_2(B) was further reduced to V_2O_3 via the formation of other VO_2 phases. Similar to the results obtained under catalytic conditions the formation of the reduced phases was explained by the p(O_2) - T phase diagram [73] and the high reduction potential of propene and CO.

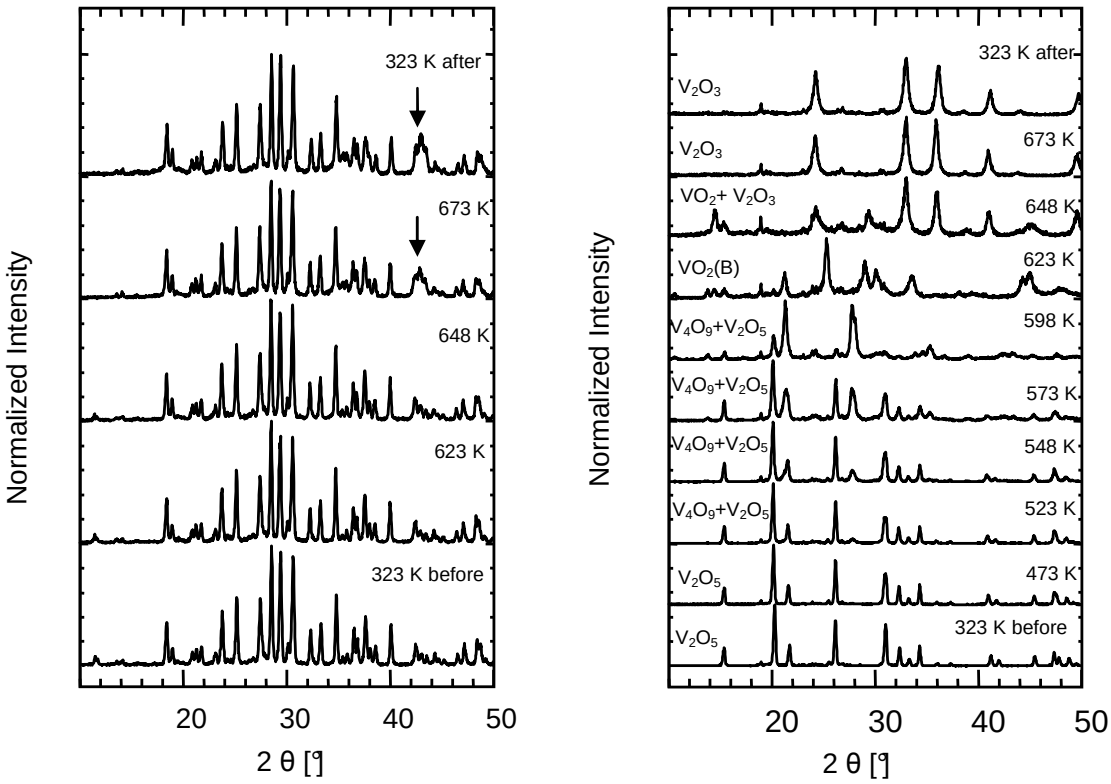

Figure 2-10: Selected *in situ* powder pattern during treatment in 5% propene in He (temperature range from 300 K to 673 K) of monoclinic $Mg_2V_2O_7$ (left) and V_2O_5 (right); the diffraction at ~18.9 °2θ originates from the sample holder.

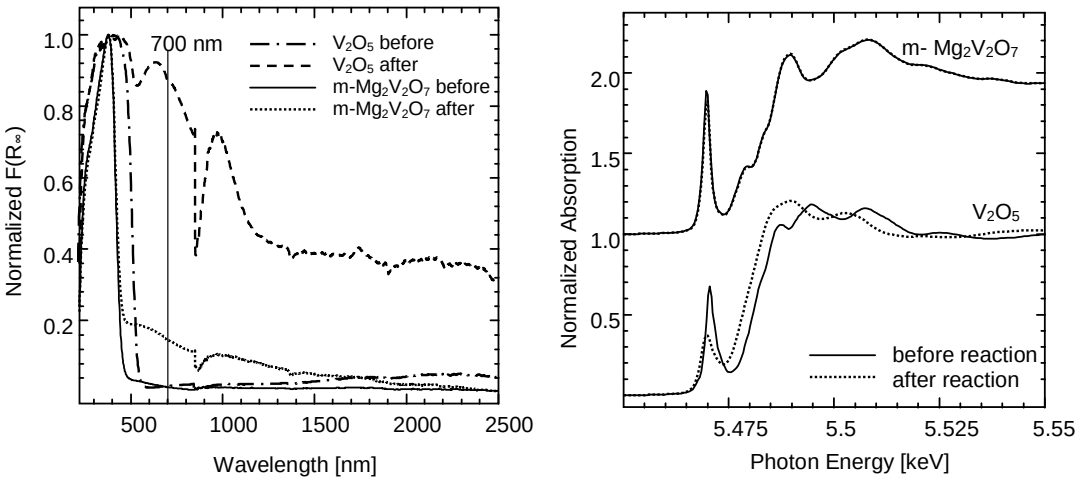

Figure 2-11: UV-Vis-DR absorption spectra (left) and V K edge XANES spectra (right) of monoclinic $Mg_2V_2O_7$ and V_2O_5 before and after treatment in 5% propene in He (temperature range from 300 K to 653 K); glitch at 850 nm originates from detector change.

The UV-Vis-DR and XAS spectra of V_2O_5 and m-$Mg_2V_2O_7$ before and after the reaction with propene (298-653 K, 5% propene in 95% He) are shown in ***Figure 2-11***. As expected from the XRD analysis strong absorption bands above 500 nm were measured for V_2O_5 after the reaction. These were assigned to the reduced vanadium oxide phases V_2O_3, VO_2 (different phases), and V_4O_9. From the position and height of the strongly decreased pre-edge peak in the V K edge XANES spectra of V_2O_5, the average valence was estimated to be ~ V^{4+} after the reaction. For the m-$Mg_2V_2O_7$ phase the V K edge XANES spectra did not change significantly during propene TPR. Only a small decrease of the pre-edge peak was noticeable. Apparently, the average valence remained V^{5+}. The UV-Vis-DR spectra showed a more pronounced reduction of the m-$Mg_2V_2O_7$ phase (***Figure 2-11, left***). The evolution of the relative absorption at 700 nm during TPR with propene in the range from 298-653 K for all magnesium vanadates and V_2O_5 is presented in ***Figure 2-12, left***.

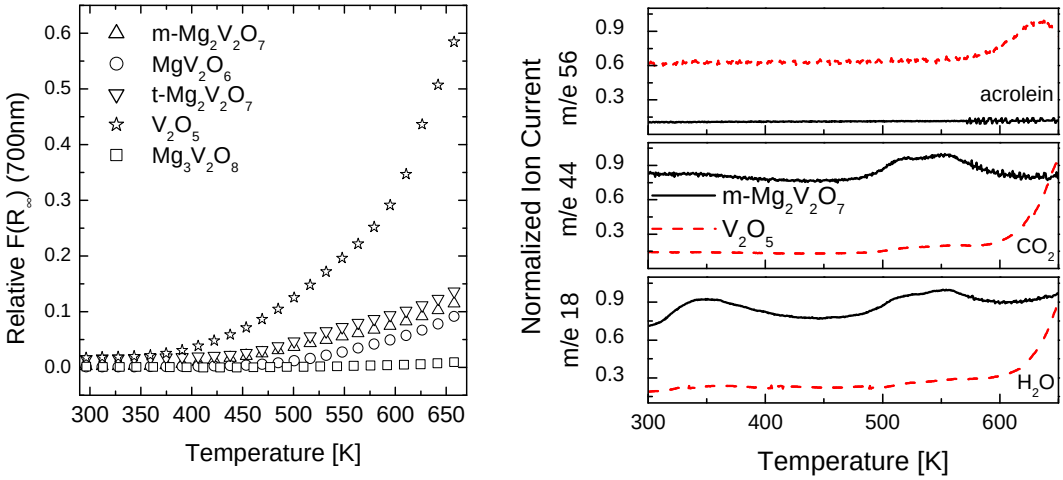

Figure 2-12 Left: Evolution of the relative absorption at 700 nm (compared to the maximum intensity in the respective spectrum) in the UV-Vis-DR absorption spectra of the magnesium vanadate phases and V_2O_5. Right: Evolution of the ion currents (CO_2, water and acrolein) measured during *in situ* UV-Vis-DR studies (thermal treatment in 5% propene in He).

Except for the $Mg_3V_2O_8$ phase all samples showed an increased absorption and, thus, reduction at elevated temperatures above 400-450 K. Relative to the maximum absorption peak the increase of absorption at 700 nm followed the order V_2O_5 >> t-$Mg_2V_2O_7$, m-$Mg_2V_2O_7$ > MgV_2O_6 > $Mg_3V_2O_8$ (no increase). For V_2O_5 above 600 K the slope of the curve increased in agreement with the detection of VO_2 in the XRD pattern. This increase correlated with an enhanced formation of water, CO_2, and acrolein. Hence, different reaction kinetics may be present when V^{5+} is fully reduced to V^{4+}. The evolution of the gas phase during TPR of V_2O_5 and m-$Mg_2V_2O_7$ is depicted in ***Figure 2-12, right***. For V_2O_5 two steps were observed in the formation of water and CO_2. The first step occurred between 520 K and 600 K and correlated with the formation of V_4O_9. The second step occurred between 600 K and 653 K, in agreement with the formation of V^{4+} and V^{3+} phases detected in the XRD pattern (***Figure 2-10, right***). Increased formation of acrolein was only detected during the second step. For m-$Mg_2V_2O_7$ several steps occurred in the formation of water (m/e 18). The first step between 300 K and 400 K was ascribed to dehydration processes. Above 450 K a second step was accompanied by the formation of CO_2 (m/e 44). Afterwards the signal for m/e 18 and 44 slightly increased. The CO_2 formed may be due to carbonates, which formed during storage of the samples under ambient conditions.

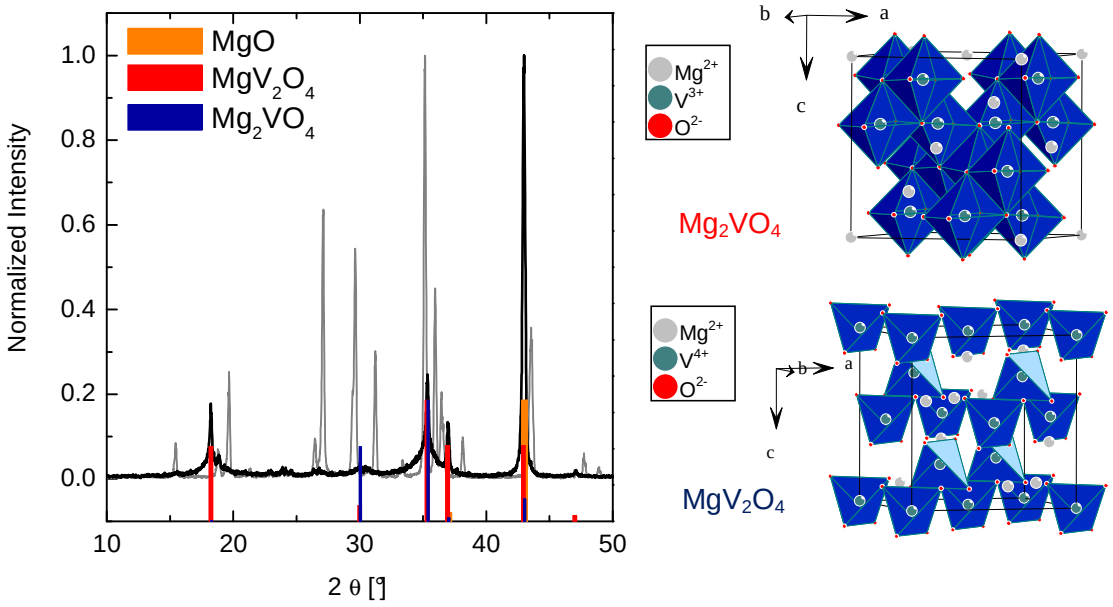

Figure 2-13: The XRD powder pattern of $Mg_3V_2O_8$ before (grey) and after (black) treatment in 5% propene in He (300-773 K) together with the structure motif of the possible $Mg_{2-x}V_{1+x}O_4$ spinel type phases.

To reveal the formation of reduced magnesium vanadate phases as predicted from the chemical potential diagram [73], $Mg_3V_2O_8$ was reduced at temperatures higher than the reaction temperature of 673 K. The XRD patterns before and after reduction at 773 K are shown in ***Figure 2-13***. New phases were detected (> 748 K), which were assigned to MgO [75] and MgV_2O_4 [77]. Mg_2VO_4 [76] (***Figure 2-13***) and MgV_2O_4 form together with $Mg_3V_2O_8$ spinel type $Mg_{2-x}V_{1+x}O_4$ phases. Hence, the formation of these reduced magnesium vanadate phases under reductive conditions was likely.

2.3.5 *Correlations of structure, reducibility, and catalytic activity of V_2O_5*

The presence of reduced vanadium phases during catalytic propene oxidation was shown for V_2O_5. In contrast to the literature [64], here a V_4O_9 phase was mainly detected at lower temperatures of 593- 648 K (instead of V_6O_{13}). The V_4O_9 phase was further reduced towards VO_2(B) at higher temperatures of 648-673 K (***Figure 2-6, right; Figure 2-10, right***). Formation of VO_2(B) was accompanied by an increased oxygen conversion and a decreased formation of partial oxidation products (***Figure 2-8, right***). During reduction in hydrogen V_6O_{13} was observed as mixed valence vanadium oxide phase [78]. This can be explained via a shearing of the V_2O_5 structure through the formation of oxygen defects [60,71]. In contrast to propene, hydrogen is much smaller and more likely to diffuse into the bulk structure of V_2O_5. Thus, the different intermediate structures during reduction in hydrogen or propene may be explained by the nature of the reducing agent. The observed V_4O_9 is not the same V_4O_9 phase reported to be formed by shearing of the V_2O_5 structure [61,62,65,79]. The main difference to that phase was the (202) diffraction at ~ 20.2 °2θ. Unfortunately, this diffraction was not easily distinguishable from the (001) diffraction of the V_2O_5 structure (~ 20.3 °2θ). In the XRD pattern in ***Figure 2-10*** (598 K) residuals of approximately 16 wt% V_2O_5 may be present next to V_4O_9. Nevertheless, the V_4O_9 structure reported by Yamazaki *et al.* [64] was used here, because it was verified by structure refinement of the proposed structure to the experimental powder pattern (***Figure 10-9, appendix***). For the other reported V_4O_9 structure [79] only an indexed file was found in the PDF databases. A representation of the vanadium oxide phases formed during reduction and propene oxidation is depicted in ***Figure 2-14***. Yamazaki *et al.* [64] discussed that the structure of V_4O_9 is similar to $(VO)_2P_2O_7$ structures which are active in many oxidation reactions [162]. Hence, it has to be investigated if a specific influence of the proposed structure motifs in this structure (V^{5+} tetrahedrons and V^{4+} / V^{5+} square pyramids and octahedrons) accounts for the catalytic activity of V_2O_5. Alternately, the formation of V^{4+} centers together with oxygen defects and mobile bulk oxygen may be responsible. However, the formation of V_4O_9 coincides with the formation of reaction products during *in situ* UV-Vis-DR measurements (***Figure 2-8***). This leads to the conclusion that V_2O_5 is not the catalytically relevant vanadium oxide structure under selective propene oxidizing conditions. Moreover, the role of lower vanadium valences of binary vanadium oxides in the reaction processes of propene oxidation has to be investigated in more detail.

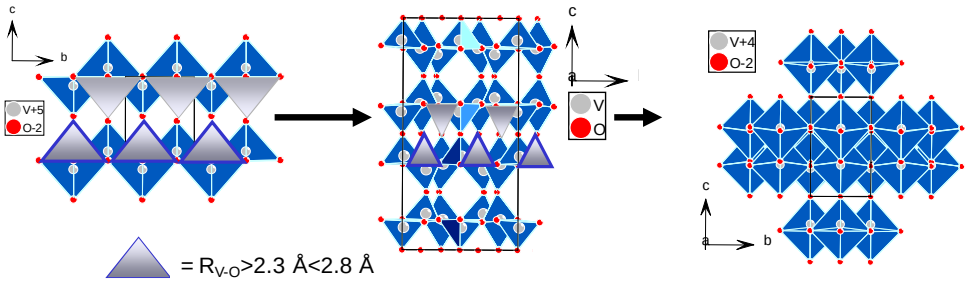

Figure 2-14: (100) plane of the phases formed during the reduction and oxidation of V_2O_5 in the presence of propene at elevated temperatures (left: V_2O_5 *Pmmn* [140]; middle: V_4O_9 *Cmcm* [64]; right: VO_2(B) *C*12/*m*1 [71]); triangles indicate location of distorted octahedrons with V-O distances between 2.3 Å and 2.8 Å.

2.3.6 Correlations of structure, reducibility, and catalytic activity of the magnesium vanadate system

The *in situ* experiments indicated that the structure activity correlations of the magnesium vanadate systems are different from V_2O_5 during the selective oxidation of propene in the employed temperature range studied here. Compared to V_2O_5 the bulk structures of the magnesium vanadates were stable under reducing and propene oxidizing conditions. Only for m-$Mg_2V_2O_7$ a slight reduction was detected at 673 K in the XRD pattern (***Figure 2-10***). Deep reduction of the bulk phase was only observed at temperatures which were higher than the temperature of catalytic propene oxidation at 673 K (***Figure 2-13***). However, on the surface slight reduction was observed in UV-Vis-DRS of all magnesium vanadate phases (***Figure 2-8, Figure 2-12***). For non stoichiometric magnesium vanadate phases under reducing conditions (propane) Burrows *et al.* [80] observed the formation of spinel type $Mg_{2-x}V_{1+x}O_4$ phases on the surface of the catalysts. Thus, such structures may be present on the surface including the fact that these structures were formed under reducing conditions at elevated temperatures (> 748 K, ***Figure 2-13***). Except for the t-$Mg_2V_2O_7$ phase, magnesium vanadate phases with higher degree of reduction (***Figure 2-12***) also showed the higher propene conversion (***Figure 2-9***). Thus, similar to the ODH of propane the activity may be correlated to the reducibility and the lability of surface anions as proposed by Volta *et al.* [81] for the oxidative dehydrogenation of alkanes.

Otherwise, concerning the t-$Mg_2V_2O_7$ phase there seems to be a more complex correlation between the magnesium vanadate phases and catalytic activity. UV-Vis-DRS showed that the t-$Mg_2V_2O_7$ phase had the same reducibility as the m-$Mg_2V_2O_7$ phase but no activity was observed in the catalytic experiments (***Figure 2-10, Figure 2-12***). A similar decrease of activity between those two phases was observed by Sugiyama *et al.* [57] during the ODH of propane. A noticeable difference between the anion structures of both pyrovanadate phases are very short V-V distances of 3.3 Å in the t-$Mg_2V_2O_7$ phase [139]. This causes a higher distortion of the $V_2O_7^{4-}$ dimers. Moreover, there are vanadium oxygen distances between 2 Å - 3 Å which implies a higher connectivity of the $V_2O_7^{4-}$ units than dimers. The $V_2O_7^{4-}$ units seem to form distorted chains (***Figure 2-15***). As these chains are not formed via corner sharing tetrahedrons like in the structure of metavanadates (NH_3VO_4), the oxygen atoms are strongly coordinated by the vanadium atom. These vanadium centers in t-$Mg_2V_2O_7$ may interact differently with the gas phase propene and oxygen molecules which adsorb on the surface. Thus, a deeper understanding of the catalytic behavior of those two phases will provide a more profound knowledge of the underlying reaction mechanism.

Comparison of the activity and the selectivity of the other magnesium vanadate phases showed that the same amounts of products were observed for $Mg_3V_2O_8$ and the m-$Mg_2V_2O_7$ phase. For the m-$Mg_2V_2O_7$ phase higher conversions were detected. Hence, the same catalytically active vanadium centers have to be present in both samples. However, due to the lower reducibility and lower vanadium to magnesium content a lower amount of these centers were present in the $Mg_3V_2O_8$ under catalytic conditions. For the MgV_2O_6 phase a lower conversion and a decreased formation of acrolein among the oxygenated products was detected. This structure and a higher amount of vanadium in the oxide may allow a different

coordination of the reactants on the surface. Furthermore, other oxidizing species (more electrophilic O^- than nucleophilic O^{2-} [162]) may have formed which are reacting with the propene molecule. Examples of such distinct differences between the various magnesium vanadate phases are not yet found in literature for the reaction with propene. Solonsa *et al.* [51] detected the formation of acrolein solely for the MgV_2O_6 and the m-$Mg_2V_2O_7$ phase.

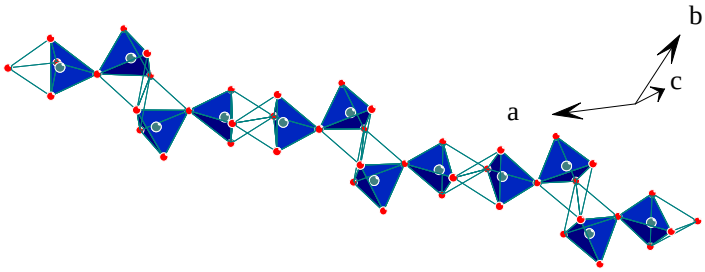

Figure 2-15: Scheme of the triclinic $Mg_2V_2O_7$ structure (lines indicate connections between tetrahedral $V_2O_7^{4-}$ units when the first V-O coordination sphere is extended from 2.3 Å to 3Å).

2.3.7 Comparison of the magnesium vanadate system and V_2O_5

Similar to the binary vanadium oxide system (V_2O_5) the catalytic activity of the ternary magnesium vanadate system seemed to be correlated with the reducibility of the vanadium oxide species. Conversely, if the selectivites of the reaction products were compared more differences were detected between the magnesium vanadates and V_2O_5. Especially m-$Mg_2V_2O_7$ and $Mg_3V_2O_8$ exhibited an increased total oxidation of propene compared to V_2O_5. This was explained by the enhanced basicity of the surface due to the Mg content in the samples. In general, propene (considered as basic molecule) will be more readily adsorbed at acidic centers than at basic centers and oxygenated reaction products (organic acids and aldehydes) will adsorb more strongly on basic surfaces. Thus, through the stronger adsorption of the oxygenated reaction products consecutive reactions such as total oxidation seemed to be favored on magnesium vanadate catalysts. The same concept was used to interpret their superior performance compared to V_2O_5 in the ODH of propane. However, this concept explains only the formation of CO_2 and CO. Comparison of the amounts of oxygenated reaction products showed a significantly higher selectivity towards acrolein for the magnesium vanadate phases (69% - 83% of the oxygenates) than for V_2O_5 (~ 32% of the oxygenates). For V_2O_5 an increased formation of partial degradation products was detected (acetic acid, acetaldehyde). Thus, a different nature of the oxygen species may be present on the surface. According to general concepts [162], electrophilic oxygen (O^-) is proposed to be less selective than nucleophilic oxygen (O^{2-}). Similar to the concepts reviewed by Gryzybowska *et al.* [162] the oxygen species present may be correlated with the re-oxidation mechanism of the metal oxide during catalysis. Therefore, a low re-oxidation rate of the reduced vanadium species may be present on the binary vanadium oxide causes a higher amount of unselective O^-.

2.4 Summary

Various ternary magnesium vanadate phases were synthesized and tested for the selective oxidation of propene. Consistent with the results during ODH of propane the reactivity was correlated with the reducibility of the surface of the respective magnesium vanadate phase. The reactivity followed the order monoclinic $Mg_2V_2O_7$ > MgV_2O_6 > $Mg_3V_2O_8$. Only the triclinic $Mg_2V_2O_7$ showed no activity for the selective oxidation of propene. The different magnesium vanadate phases showed only marginal differences in the selectivities towards oxygenated products such as acrolein. Compared to measurements perfomed with V_2O_5 total oxidation was increased but among the partial oxidation products mainly acrolein was formed. The overall activity of the magnesium vanadate phases was significantly lower than that of the reference V_2O_5. In contrast to the magnesium vanadate system, a bulk reduction was observed for V_2O_5 during the selective oxidation of propene. With the onset of catalytic activity, formation of the mixed valence phase V_4O_9 was observed. V_4O_9 was further reduced to VO_2(B) at elevated temperatures. Apparently, the measured activities and selectivities of the ternary magnesium vanadate and the binary vanadium oxide system indicated that, apart from the reducibility of the vanadium oxide phases, different catalytic mechanisms may apply. In summary, the results presented here confirm the suitability of these vanadium oxides as model systems for studying the influence of vanadium in selective propene oxidation. The formation of reduced phases for both binary and ternary systems is subject of further investigation.

PART II

Spectroscopic and catalytic investigations of V_xO_y/SBA-15 model catalysts for selective propene oxidation

3 Fundamentals and experimental details

3.1 Catalyst preparation

Mesoporous silica SBA-15 was prepared according to literature procedures [82,83]. 1.0 g poly(ethylene glycol)-block-poly(propylene glycol)-block-poly(ethylene glycol) triblock copolymer (Aldrich, pluronic, P-123) was dissolved in 60.5 ml water and 3.3 ml concentrated H_2SO_4 at 323 K in a water bath. After drop wise addition of 2.3 g tetraethyl orthosilicate (TEOS), the reaction mixture was stirred for 24 h at 323 K. The resulting suspension was heated in a closed bottle to 381 K for 24 h. The resulting white powder was filtered and washed with deionized water and dried at 353 K for 72 h. The dry powder was calcined at 453 K for 4 h and for 12 h at 823 K.

The *ammonium decavanadate precursor* was prepared as follows [84]. 1 g NH_4VO_3 was dissolved in 33 ml water and heated to 343 K for 24 h. The remainder was filtered off and 1.4 ml 50% acetic acid was added drop wise to the resulting yellow solution. After addition of 26.5 ml ethanol the deep orange solution was cooled with a mixture of 1:1 acetone and dry ice. The resulting orange powder was filtered and washed with 1 ml ethanol and 2 ml diethyl ether. Structure and phase purity were confirmed by single crystal XRD analysis and X-ray powder diffraction (data not shown here).

Functionalized SBA-15 was prepared via a grafting ion exchange method described by Hess *et al.* [32]. SBA-15 was heated in vacuum for 24 h and afterwards functionalized by adding 3-aminopropyltriethoxysilane (APTES) to a suspension of SBA-15 in toluene (1 ml APTES : 15 ml toluene: 1 g SBA-15). The suspension was stirred under reflux for 24 h. After distilling off the solvent, the content was washed with diethyl ether and afterwards filtered and washed in a Soxhlet apparatus with diethyl ether for 24 h and then dried at room temperature for 72 h. The dry powder was stirred in 0.3 M HCl for 12 hours. The content was filtered again, washed with water and dried in air overnight (functionalized SBA-15). Vanadium oxide supported on SBA-15 was prepared by adding appropriate amounts of ammonium decavanadate to a suspension of functionalized SBA-15 in water and stirring under ambient conditions for 12 h. After filtration and washing with water the resulting powder was dried at 323 K for 2 h and calcined at 823 K for 12 hours. In comparison to the samples prepared by the grafting ion exchange method two samples were prepared by incipient wetness and wet impregnation method. For the *incipient wetness SBA-15* 69 mg of ammonium decavanadate were dissolved in 1 ml water and added drop wise to 1 g SBA-15 powder. After each addition the powder was homogenized and dried under ambient conditions. The resulting powder was calcined at 823 K for 12 hours. For *wet impregnation SBA-15* 10 g NH_4VO_3 (Fluka, 99%) were dissolved in 450 ml water. After addition of 5 g SBA-15 the mixture was stirred at 343 K for 17 h. The suspension was filtered hot and the resulting powder was dried for 1 h at 323 K. The powder was heated to 773 K (rate 1 K/min) and calcined for 3 h. The samples were stored under ambient conditions (298 K, air).

3.2 Catalyst characterization

3.2.1 X-ray absorption spectroscopy (XAS)

3.2.1.1 Fundamentals

X-rays are able to penetrate condensed matter. After passing through the matter the intensity of the incident light (I_0) is attenuated, which can be expressed by Lambert's law ($I = I_0 \exp(-\mu d)$). The attenuation depends on the sample thickness (d) and the linear absorption coefficient (μ). The absorption coefficient, expressed as mass absorption coefficient, refers to the density of a material. The dependence of the (mass) absorption coefficient on the energy of the incident light and the atomic number (Z) of the absorbing material causes a smooth decay of the absorption coefficient. However, if the energy of the incident light reaches the specific binding energy (E_B) of tightly bound core electrons (1s, 2s, 2p levels) these electrons will be excited to empty states above the Fermi level (***Figure 3-1, left***). At this energy a sharp rise in absorption will be detected, which is denoted as the absorption edge. The absorption edge is element specific and termed after the ground state of the electron (1s, 2s, 2 $p_{1/2}$, $2p_{3/2}$) as K, L_I, L_{II}, or L_{III} edge. As a consequence of the absorption process a photoelectron and a core hole at the initial state of the photoelectron are generated. The core hole is refilled by electrons located at higher energy levels. The energy released by this relaxation process can be detected as fluorescence or as Auger and secondary electrons, which are generated. The wavelength of the emitted light or the kinetic energy of the released electrons are element specific.

The photoelectron originating from the absorbing atom will interact with the electron density of adjacent atoms in condensed matter (***Figure 3-1, middle***). The propagation of the photoelectron away from the absorbing atom is considered as a spherical wave with a wavelength $\lambda = 2\pi/k$, with the wavenumber k defined as:

$$k = \sqrt{\left(\frac{8\pi^2 m_e}{h^2}\right)(h\nu - E_B)}\,. \tag{3.1}$$

Where hν is the energy of the incident photon, m_e the mass of the electron and E_B the binding energy of the photoelectron. When the outgoing electron wave reaches neighboring atoms it will be scattered back. The resulting incoming spherical electron wave interferes with the outgoing photoelectron wave. This interference influences the absorption coefficient and thus the measured absorption spectra. The impact of the scattering process of the photoelectron on the absorption coefficient can be explained quantum mechanically. The absorption coefficient is proportional to the transition probability of the excited electron. Within a dipole approximation this transition probability is proportional to a function, which depends on the initial and the final state wavefunction of the exited electron (Fermi's golden rule). The initial state is the localized electron in the core level. The final state wavefunction is dependent on the contribution from the outgoing electron wave and the backscattered electron wave (***Figure 3-1***).

Moreover the core hole in the initial state of the electron influences the final state wave function. These different, energy depended, contributions to the final wavefunction lead to oscillations of the absorption coefficient that can be extracted from the X-ray absorption spectra.

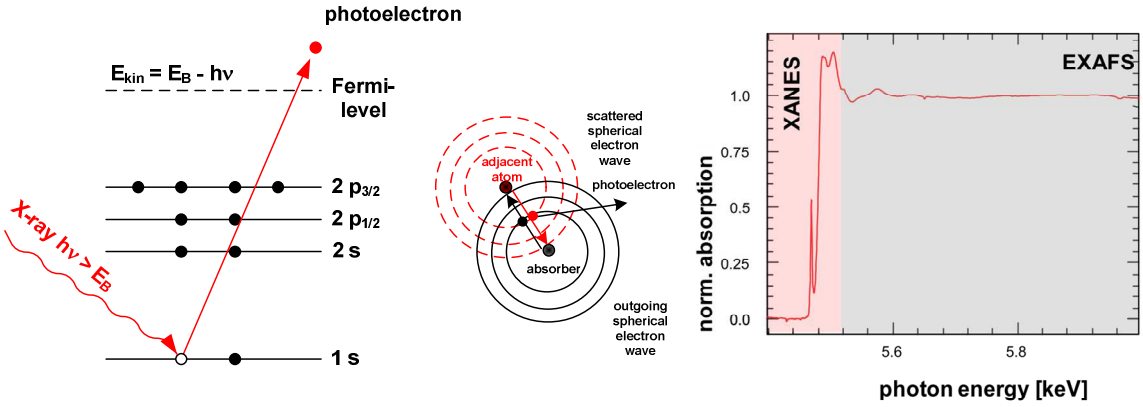

Figure 3-1 Left: excitation process of the photoelectron, middle: scattering process of the photoelectron, right: typical V K edge spectrum.

Typically XAS spectra are recorded in transmission mode. The sample is placed between two ion chambers that measure the intensity of the X-ray radiation. Detection with fluorescence radiation or Auger electrons is also possible in the cases of low element concentration and of light elements surrounded by a strongly absorbing matrix. The spectra are normally recorded from 100 eV before to a few hundred eV after the absorption edge of the analyzed element in the sample. X-ray absorption spectra can be divided into two sections (***Figure 3-1, right***). The X-ray absorption near edge structure (XANES) and the extended X-ray absorption fine structure (EXAFS).

The XANES region is located approximately 50 eV before and after the absorption edge. This region contains information about the electronic properties, *e.g.* the oxidation state, and the local geometry around the absorbing atom. The latter is mostly determined from pre-edge features that are located before the absorption edge. These are caused by dipole and/or quadruple transitions of core electrons into empty or partially filled d states near the Fermi level in transition metal elements. For K edges (1s, ground state) dipole transitions are forbidden (Lapporte's rule) in the case of centrosymmetric configurations. Therefore, very symmetrical octahedrally coordinated absorption centers will not show significant pre-edge features. In contrast, absorption centers in a strongly distorted environment, *e.g.* tetrahedral, allow a mixing of d and p states and will show very intense pre-edge features. For 3d transition metal elements (V, Cr, Mn) the mixing of 3d and 4p states is more likely than for higher d band transition metal elements (Mo, W). After the absorption edge the XANES spectra show specific oscillations, which are either due to transitions to higher unoccupied states or to multiple scattering effects of the photoelectron which is more dominant. Typically this region is used as "fingerprint" region in comparison with the spectra of well characterized references. A theoretical description is more difficult than for the EXAFS region but possible using software codes like Feff 8 [85].

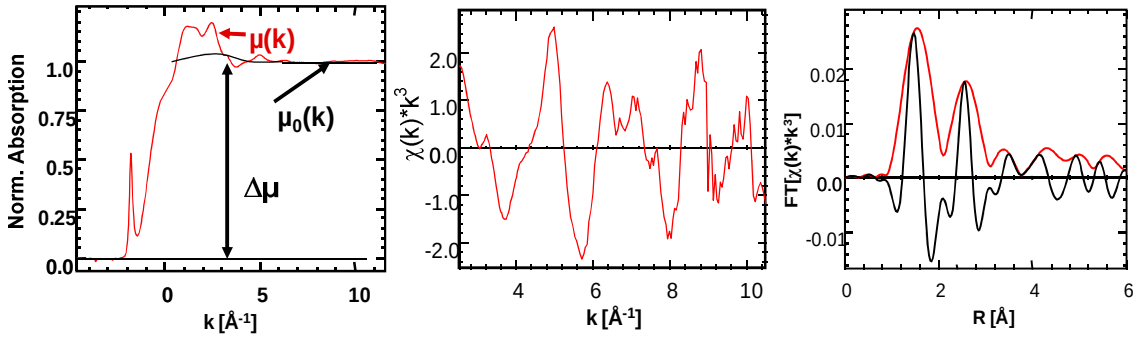

Figure 3-2: XAS data reduction, left: extraction of the χ(k), middle: k^3 weighted χ(k), right: Fourier transformed k^3 weighted χ(k).

The EXAFS region at higher energies is dominated by oscillations of the absorption coefficient caused by scattering of the photoelectron at adjacent atoms. The oscillatory part of the measured absorption coefficient μ(k) can be separated from the atomic absorption of a free atom $\mu_0(k)$ and is denoted as the EXAFS function χ(k):

$$\mu(k) = \mu_0(k) \cdot (1 + \chi(k)) \,. \tag{3.2}$$

The typical steps of XAFS data reduction are depicted in ***Figure 3-2***. For a single scattering event the EXAFS function can be described theoretically by a single scattering plane-wave approximation, which is well described in the literature [86,87]. The EXAFS function of an atom in a compound is the sum of all scattering events caused by the presence of neighboring atoms:

$$\chi(k) = \sum_{j=1}^{j} A_j(k) \sin(2kR_j + \varphi_j(k)) \,, \tag{3.3}$$

with the amplitude

$$A_j(k) = N_j \frac{S_0^2(k) e^{-2R_j/\lambda(k)}}{kR_j^2} e^{-2k^2\sigma_j^2} \cdot F_j(k) \,. \tag{3.4}$$

The term N_j refers to the number of atoms in the j^{th} coordination shell (coordination numbers). The fraction term describes the damping of the signal. The amplitude reduction term, S_0^2, describes the intensity loss due to relaxation effects on the remaining electrons of the absorber atom caused by the core hole. The intensity loss of the spherical electron wave is considered by the term $1/R^2$. The term $\exp(-2R_j/\lambda(k))$ considers the finite lifetime of the core hole. It is determined by the average free path length of the photoelectron. The term $\exp(-2k^2\sigma^2_j)$ describes the influence of static and thermal disorder on the amplitude. It is determined by the disorder parameter σ^2_j. The $F_j(k)$ function considers the specific backscattering power of each element and is strongly dependent on k. Weighting the EXAFS function with k allows emphasizes of light (*e.g.* oxygen, k weight 0) or strong scatterers (*e.g.* platinum, k weight 3). Typically the EXAFS function is Fourier transformed as shown in ***Figure 3-2,right***. The envelope of

the Fourier transformed EXAFS function corresponds to a pseudo radial distribution around the absorbing atom. However, the scattering process causes a phase shift of the electron wave (φ(k), ***Equation 3.3***). Therefore, all distances in the experimental FT(χ(k)*k^3) are shifted by 0.4-0.5 Å to lower values. Software codes like FEFF [88] allow the calculation of theoretical scattering paths from suitable theoretical models. The calculated theoretical parameters of the resulting scattering paths (*e.g.* N, R, σ^2, E_0) can be refined to the experimental XAFS data. This allows the determination of local structure parameters like coordination numbers, distances, and disorder parameters. Modern software codes allow the consideration of more complex scattering processes like multiple scattering [89].

3.2.1.2 Experimental details of XAS

In situ transmission XAS experiments were performed at the V K edge (5.465 keV) at beamlines E4, C, and A1 at the Hamburg Synchrotron Radiation Laboratory, HASYLAB, and at the XAFS beamline at ANKA using a Si (111) double crystal monochromator. The energy range used for V K near edge scans (XANES) and extended XAFS scans (EXAFS) was 5.4-5.7 keV (~ 3 min/scan) and 5.4-6.0 keV (~ 20 min/scan), respectively. For fast measurements QEXAFS scans were performed (5.4-5.8 keV, ~ 2.5 min). For *in situ* and *ex situ* XAFS measurements samples were mixed with BN and PE, respectively, and pressed into self-supporting pellets (5 mm and 13 mm in diameter, respectively). In order to obtain an edge jump, $\Delta\mu_x$, below 1.0 at the V K edge, 2.5 mg of 7.7 wt% and 4.1 wt% V_xO_y/SBA-15 and 3 mg of 1.4 wt% V_xO_y/SBA-15 diluted with BN (~ 15 mg), and 3-6 mg of bulk vanadium oxides (*e.g.* $Mg_3V_2O_8$, MgV_2O_6) diluted with PE or wax (~ 100 mg) were employed. Transmission XAS measurements were performed in an *in situ* cell (***Figure 3-3***) described previously [90]. Dehydration of V_xO_y/SBA-15 was conducted in 20% O_2 and He (total flow 40 ml/min) in a temperature range from 293 K to 623 K or 723 K at a heating rate of 5 K/min and a holding time of typically 30-60 min at 623 K. Reaction tests were performed in 5% propene and 5% O_2 in He in the temperature range from 293 K to 723 K (5 K/min, total flow 30-40 ml/min). The gas atmosphere was analyzed using a noncalibrated mass spectrometer in a multiple ion detection mode (Omnistar from Pfeiffer). *Ex situ* XAFS measurements were performed in He atmosphere at room temperature.

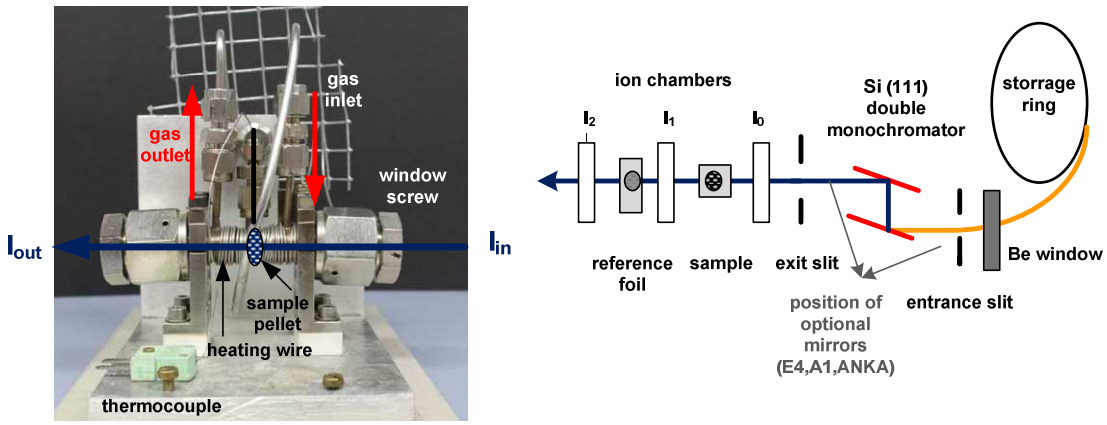

Figure 3-3 Left: *in situ* transmission XAS cell, right: typical configuration of transmission beamlines.

X-ray absorption fine structure (XAFS) analysis was performed using the software package WinXAS v3.2 [91]. Background subtraction and normalization of the extended XAFS scans were carried out by fitting linear polynomials to the pre-edge and 3rd degree polynomials to the post-edge region of an absorption spectrum, respectively. The extended X-ray absorption fine structure (EXAFS) $\chi(k)$ was extracted by using cubic splines to obtain a smooth atomic background $\mu_0(k)$. The FT($\chi(k)*k^3$), often referred to as pseudo radial distribution function, was calculated by Fourier transforming the k^3-weighted experimental $\chi(k)$ function, multiplied by a Bessel window, into R space. EXAFS data analysis was performed using theoretical backscattering phases and amplitudes calculated with the *ab-initio* multiple-scattering code FEFF7 [88]. EXAFS refinements were performed in R space simultaneously to the magnitude and the imaginary part of a Fourier transformed k^3-weighted experimental $\chi(k)$ using the standard EXAFS formula [92]. Structural parameters allowed to vary in the refinement were (i) the disorder parameter σ^2 of selected single-scattering paths assuming a symmetrical pair-distribution function and (ii) distances of selected single-scattering paths. Coordination numbers (CN), E_0 shifts, and the amplitude reduction factor S_0^2 were kept invariant in the final fitting procedures. To ensure the statistical significance of parameters during the fitting procedure correlations of specific parameters were made to reduce the number of free running parameters and to improve the stability of the refinement. The reduction of the parameters was conducted in the following steps. First, the number of independent parameters (N_{ind}) was calculated according to the Nyquist theorem $N_{ind} = 2/\pi * \Delta R * \Delta k + 2$. In all cases the number of free running parameters in the refinements was well below N_{ind}. Second, confidence limits were calculated for each individual parameter. Third, a so-called F test was performed to assess the significance of the effect of additional fitting parameters on the fit residual. The corresponding procedure was adopted from the well-known library “Numerical Recipes in C” [93].

XANES Analysis was performed in using a shorter range of the XAFS scans. Background subtraction and normalization of the XAFS scans were carried out by fitting linear polynomials to the pre-edge and the post-edge regions of an absorption spectrum, 5.40-5.456 and 5.52-5.60 keV, respectively. Peak height and energy position (relative to 5.465 keV) were determined for the point of maximum intensity of the pre-edge feature. The pre-edge peak area and the centroid energy (relative to 5.465 keV) were determined according to a method described by Chaurand *et al.* [94]. In short, the section around the absorption edge (5465 eV) was extracted from the normalized XANES spectra (~ 2 eV before edge, ~ 10-15.0 eV after edge). The background was fitted by an empirically interpolated function, using a cubic spline function with 12 independently adjustable knots. After subtraction of the background the normalized pre-edge feature was fitted using 2-3 pseudo Voigt functions (Gauss/Lorentz factor was fixed to 0.7). The centroid energy was determined from the center of gravity, which is obtained from the area weighted energy positions of the individual pseudo Voigt functions.

3.2.2 UV-Vis Diffuse reflectance spectroscopy measurements

3.2.2.1 Fundamentals

UV-Vis (200-800 nm) and near-infrared (NIR, 800-2500 nm) spectroscopy are used for investigations of electronic transitions of valence electrons, *e.g.*, in transition metal compounds. Electronic excitations of transition metal compounds may arise from metal centered transitions (MC) where the orbitals involved are localized at the absorbing metal center. In the case of vanadium compounds these are mainly due to d-d transitions of vanadium centers in the oxidation states of +4 and +3. These transitions are located at wavelengths higher than 600 nm and are weak for centrosymmetric configurations (octahedral coordination) because they are forbidden according to the Laporte selection rule (Δ l = $\pm$ 1). Metal centered transitions are theoretically well described by Crystal field and Ligand field theory [95,96]. Another class of transitions are charge transfer (CT) transitions. These are theoretical described by the molecular orbital (MO) theory. The molecular orbitals involved are formed by linear combination of metal and ligand orbitals. The transition takes place between an occupied electronic level located on a donor atom to an empty level centered on an acceptor atom. In the case of highly oxidized transition metal oxide compounds (d^0 configuration) mostly ligand-to-metal charge transfer transitions (LMCT) appear. These are due to a transfer of electron density from the oxygen lone pair orbital to an empty t_2 or e state of the d^0 transition metal ion. Mostly these transitions are located at a wavelength lower than 600 nm and are very intense (Laporte-allowed). Charge transfer transitions must be described by molecular orbital theory which makes interpretation more complex than for metal centered transitions. An example for a calculation of the MnO_4^- ion is provided by Woodward *et al.* [97]. Moreover, interpretation of UV-Vis spectra becomes more complex in solid compounds as molecular orbitals tend to overlap and form electronic band structures.

Typically UV-Vis spectra are measured by transmission spectroscopy from liquid phase. According to Lampert-Beer's law quantification can be made by measuring the ratio transmitted light (I_T) to incident light (I_0). The resulting absorbance (A_λ) obtained from the transmission spectrum is proportional to the sample thickness (d), the absorption coefficient (ε_λ), and the analyte concentration ($c_{analyte}$):

$$A_\lambda = -\lg\left(\frac{I_T}{I_0}\right) = \varepsilon_\lambda \cdot c_{analyte} \cdot d \,. \tag{3.5}$$

However, in the solid phase light will normally not be transmitted through the sample. Hence, diffused reflectance spectroscopy (DRS) is used for powdered samples. It is described theoretically by a model developed by Schuster, Kubelka and Munk (denoted as SK or SKM model). In the following, a short introduction will be provided. More detailed descriptions are found in the literature [95,98,99].

Due to the fact that the wavelength of incident light has the same dimensions as the illuminated particles (200-3000 nm) the incident light can be absorbed and scattered from the particles. Scattering is mainly due to specular (regular or mirror like) and diffuse reflectance which is depicted schematically in ***Figure***

3-4. Specular reflectance is dependent on the angle of incidence. In contrast, diffuse reflected light will be scattered in all directions. There are three types of diffuse scattering: (i) single scattering, (ii) multiple scattering and (iii) dependent scattering. The last one is present when phase coherence exists between photons scattered from neighboring centers. It occurs when the average distance between two scattering centers is smaller than 2-3 times the particle diameter, which is the case for the V_xO_y/SiO_2 samples studied here. For a theoretical description of dependent scattering the *Radiative Transfer theory* has to be employed. Schuster, Kubelka, and Munk simplified the solution of this model with the assumptions explained below. In short, the incident light and the scattered light are considered as monochromatic fluxes in (I) and out (J) of the sample bed. These fluxes are connected to apparent absorption (K) and scattering (S) coefficients. These coefficients are related to the diffuse reflected light (remittance or reflectance) of an infinitely thick sample (R_∞) that can be determined experimentally:

$$F(R_\infty) = \frac{(1-R_\infty)^2}{2R_\infty} = \frac{K}{S} \qquad \text{, with } R_\infty \approx R_\infty^{real} = \frac{R_\infty^{sample}}{R_\infty^{ref.}} \tag{3.6}$$

R_∞ cannot be determined directly from spectrometric measurements. Typically the ratio of the remittance of a sample related to the remittance of an ideal white standard reference is measured. White standards are MgO, $BaSO_4$, Spectralon® (special Teflon) or the support material of a supported catalyst.

The SKM model is only valid if some assumptions are made. The incident light has to be diffuse and monochromatic and the scattered light has to be scattered isotropically. Which means that no specular reflection occurs that is also strongly dependent on the absorption of the sample. The sample has to be infinitely thick, which in practice is achieved with 1-5 mm sample thickness. Also, there must not be any fluorescence. The distribution of the absorbing centers has to be homogenous and the concentration of the absorbing centers has to be low ($F(R_\infty) < 1.0$). The latter has to be considered, if DRS is used quantitatively. However, in practice if no quantitative information is needed a better resolution is often achieved for higher $F(R_\infty)$ values. To exclude spectral artifacts like damping of signals or asymmetric signals a comparison with a diluted sample has to be performed.

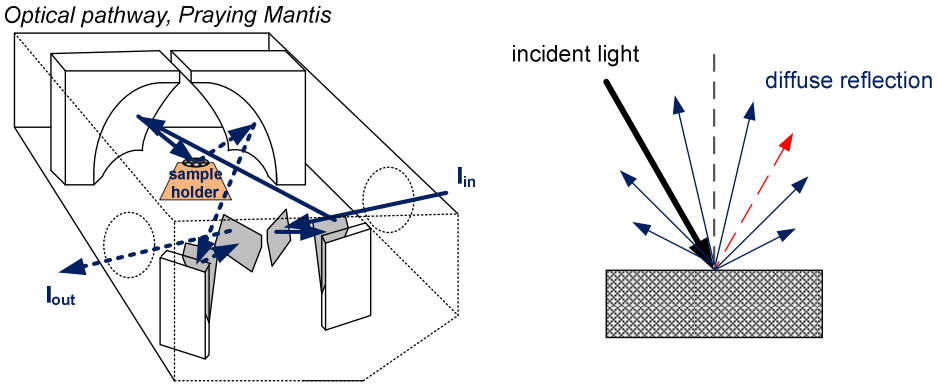

Figure 3-4 Left: Praying Mantis™ set up, right: illustration of specular and diffuse reflection.

Normally diffuse reflectance spectra are measured in additional cells, which are placed into a normal UV-VIS-Spectrometer. All types of measurement cells have in common that they reduce the amount of specular reflection and mainly collect the diffuse reflected light. For *in situ* measurements typically a Praying Mantis™ configuration (Harrick Scientific Products, Inc.) is used, which allows a horizontal placement of the sample bed (***Figure 3-4***). The *in situ* cell is depicted in ***Figure 3-5***. A disadvantage of the Praying Mantis™ configuration is the low performance and high spectral noise in the UV range (200-300 nm) because of the high number of optical mirrors. Furthermore, in the NIR range heat radiation is detectable.

3.2.2.2 Experimental details of UV-Vis-DRS

UV-Vis-DRS measurements were conducted in a Jasco-V670 UV-Vis-NIR spectrometer using an *ex situ* integration sphere or a Praying Mantis™ *in situ* cell (Harrick Scientific Products, Inc.) as depicted in ***Figure 3-5***. MgO (ABCR) or pure SBA-15 were used as reflectance standard. Samples were measured as is or diluted with MgO for bulk vanadium oxides or SBA-15 in the case of V_xO_y/SBA-15 samples. Pretreatment was conducted in 20% O_2 and He (total flow 50 ml/min) in a temperature range from 293 K to 554-626 K using a heating rate of 4 K/min. Reaction tests were performed in 5% propene and 5% O_2 in He in the temperature range from 293 K to 676 K (4 K/min, total flow 40 ml/min). The gas atmosphere was analyzed using a non-calibrated mass spectrometer in a multiple ion detection mode (Pfeiffer Omnistar) and a gas chromatograph (section ***3.3.1***). A linear correction (T_{sample} = 0.80 T_{holder} + 1 [°C]) was applied to the sample holder temperature, which was obtained by a separate measurement using a thermocouple placed in the sample powder bed ***Figure 3-5***.

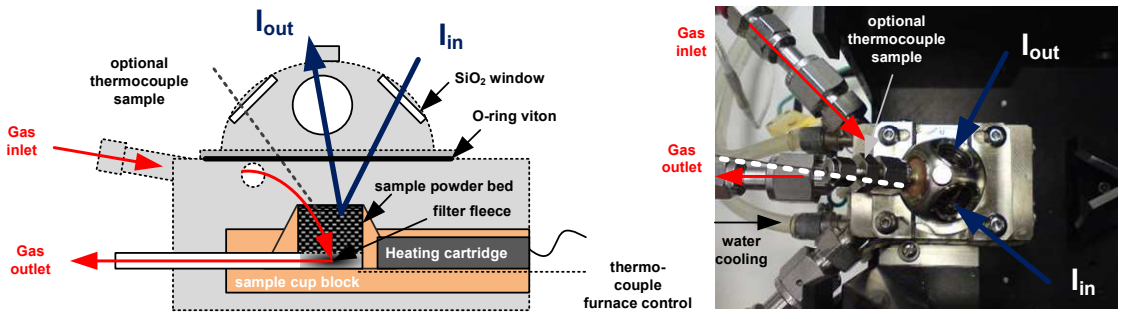

Figure 3-5 Left: schematic drawing of the Praying Mantis™ *in situ* UV-Vis-DR cell, right: picture of the *in situ* UV-Vis-DR cell. The position of the optional thermocouple that was used to determine the sample temperature is marked as dashed line.

Data processing and the conversion of the measured spectra to Kubelka Munk units (denoted as KM or $F(R_\infty)$) were performed using the spectra manger 2.0 software package from Jasco. UV-Vis edge energies (E_g) were determined from the spectra according to the procedure described in the literature [100]. Therefore, the data was plotted as $(F(R_\infty)*h\nu)^2$ versus energy (eV). A linear function was fitted to the first intensity increase in the spectrum. The intersection of this fit line with the abscissa was used as the E_g value. An example is given in ***Figure 3-6***.

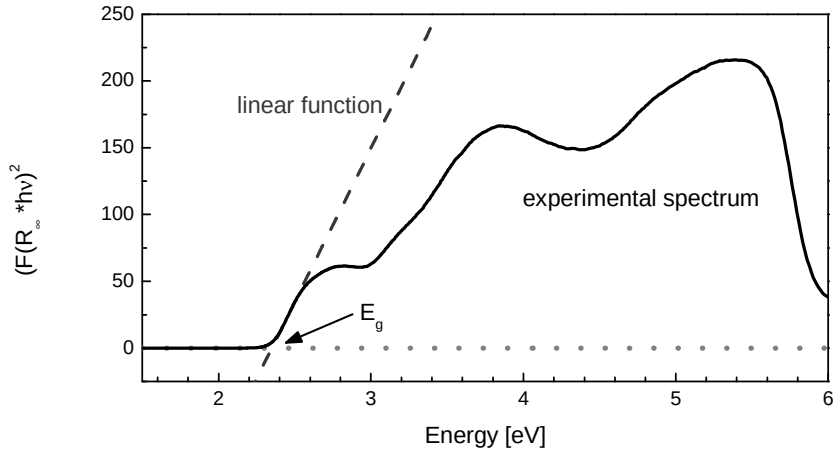

Figure 3-6: Example for the determination of the UV-Vis edge energy E_g of V_2O_5.

3.2.3 Powder X-ray diffraction (XRD)

The XRD measurements were made with an X'Pert PRO MPD diffractometer (θ-θ geometry), using Cu K alpha radiation and a solid-state multi-channel PIXcel® detector. Wide angle scans (5-90 °2θ, step=0.013 °2θ, time=60 s/step, variable slits) were collected in reflection mode. The sample was prepared as a cavity mount using a silicon sample holder. The cavity had a diameter of 15 mm and a depth of ~0.1 mm, and the surface of the holder was cut in such a way that no Si-peaks were detected. To obtain absolute values for the (100) diffraction line of SBA-15 small angle scans (0.4-6.0 °2θ and -0.4-4.0 °2θ, step=0.013 °2θ, time=90 s/step, fixed slits) were collected in transmission mode with the sample spread between two layers of Kapton® foil. For comparison small angle scans (0.4-6.0 °2θ step=0.013 °2θ, time=60 s/step, fixed slits) were collected in reflection mode, which had a better resolution of the higher hkl diffraction lines of SBA-15.

3.2.4 Physisorption measurements

Nitrogen physisorption isotherms were measured at 77 K on a BEL Mini II volumetric sorption analyzer (BEL Japan, Inc.). The SBA-15 samples were outgassed under vacuum for about 20 min at 368 K and 16-20 h at 443 K before starting the measurement. After outgassing, the sample color had turned from orange to a color between white and grey. Data processing was done using the BELMaster V.5.2.3.0 software package. The specific surface area was calculated using the standard Brunauer–Emmett–Teller (BET) method in the relative pressure (p/p_0) range of 0.05–0.20 with a nitrogen area of 0.162 nm^2. The adsorption branch of the isotherm was used to calculate pore size distribution and cumulative pore area according to the method of Barrett, Joyner, and Halenda (BJH) [101].

3.2.5 Elemental analysis

The V content was determined by ICP-OES and X-ray fluorescence analysis (RFA). For ***ICP-OES measurements*** (Jobin Yvon JY 38 Plus) 40-200 mg sample were dissolved in 0.1 M NaOH using a 100 ml volumetric flask (~ 40 mg/L V content). Standard solutions made from V_2O_5 and SBA-15 were used for calibration (20- 60 mg/L V content). ***RFA measurements*** were performed on a PANalytical AXIOS spectrometer (2.4 kW model) equipped with a Rh Kα source, a gas flow detector and a scintillation detector. Samples were prepared as 13 mm pellets (100 mg sample diluted with 100 mg wax). Quantification was performed using a standardless analysis which considered the finite thickness of the sample in the calculation (Super Q 5 software package / PANalytical). ***CHNS Element Analysis*** was performed to determine the nitrogen content after APTES funtionalization and the amount of residual carbon and sulfur content after calcination of SBA-15 and the functionalized SBA-15 samples. For CHNS-measurements a FlashEA 1112 NC Analyzer with CHNS-O configuration (ThermoFinnigan/ ThermoElectron) was used. The relative error was ~ 2%.

3.2.6 Solid state NMR

The solid state ^{29}Si MAS-NMR-measurements were carried out on a Bruker Avance II spectrometer with an external magnetic field of 9.4 T (i.e. a ^{1}H resonance frequency of 400 MHz) and with a Bruker 4 mm double resonance-H-X MAS-probe. The ^{29}Si resonance frequency was 79.46 MHz. Between 2000 and 20000 transients were recorded with a relaxation delay of 30 s. Proton signals were decoupled during the acquisition by applying TPPM (Two Pulse Phase Modulation) decoupling. The ^{29}Si spectra are referenced to TMS (tetramethylsilane) using TKS (Tetrakis(trimethylsilyl)silan) as a secondary reference. Data analysis was performed using the software package DMfit by Massiot *et al.* [102]. Three Gaussian functions were refined to the experimental spectrum of the SBA-15 samples. The NMR shift was determined for the bare SBA-15 sample and fixed in the refinement of the V_xO_y/SBA-15 samples.

Samples treated under reaction atmosphere were prepared in the laboratory reactor and transferred into the air tight sample containers in a moisture free glovebox.

3.2.7 Raman spectroscopy

Ex situ Raman spectra were recorded using a FT-RAMAN spectrometer RFS 100 (Bruker). For excitation a Nd : YAG laser was used (1064 nm, resolution 1 cm^{-1}). The laser power was 100 mW as measured at the position of the sample. Samples were measured in glass containers. For dehydrated V_xO_y/SBA-15 samples the sample containers were heated in a sand bath for 12 h at 673 K in a muffle furnace. Directly after the sample containers were taken out of the hot oven (673K) they were closed by melting to avoid rehydration of the samples.

In situ Raman spectra were measured at the TU Darmstadt. An argon ion laser (Melles Griot) at 514 nm and a helium neon laser at 632 nm were used for excitation. For detection a transmissive spectrometer equipped with a Pelletier CCD detector (Kaiser Optical, HL5R) operated at 233 K was used. The spectral resolution was about 5 cm^{-1}. The laser power was 3 mW for hydrated V_xO_y/SBA-15 samples and 3 and 6 mW for dehydrated V_xO_y/SBA-15 samples as measured at the position of the sample. The powder samples were introduced into a sample holder developed by Hess and Thielemann [103]. The accumulation time for the spectra was typically 33 min. Heating was therefore performed stepwise. Pretreatment and dehydration experiments were conducted in synthetic air (total flow 25-60 ml/min) in a temperature range from 293 K to 623-823 K. Reaction tests were performed in 5% propene and 5% O_2 in N_2 in the temperature range from 293 K to 823 K (total flow 70 ml/min). Gas atmosphere was analyzed using a non-calibrated mass spectrometer in a multiple ion detection mode. For *in situ* experiments V_xO_y/SBA-15 was pressed at 70 MPa and sieved to obtain a particle size between 250 and 355 µm.

3.2.8 Thermal analysis

Thermogravimetric (TG) and Differential thermal analysis (DTA) measurements were conducted using a SSC 5200 from Seiko Instruments. The gas flow through the sample compartment was kept very low to avoid mass transport of the light SBA-15 particles out of the sample container. It was adjusted to 50 ml/min (20% O_2 / 80% N_2). The gas atmosphere was analyzed using a noncalibrated mass spectrometer in a multiple ion detection mode (Omnistar from Pfeiffer). Heating was conducted with a rate of 5 K/min in the range from 303 K to 623 K or 723 K in an aluminum cup. For measurements up to 1173 K a corundum cup was used. To extract the apparent activation energy of the dehydration step of the Kieselgel 60, SBA-15, and V_xO_y/SBA-15 sample heating rates (β) of 2, 4, 6, 8, and 10 K/min were used. Before and after heating the furnace temperature was held for 60 min at 303 K and 623 K, respectively. The apparent activation energy was determined by a method described by Vansant *et al.* [104] for silica samples. The maximum of the DTA curve (temperature, T_{max}) was determined and used to calculate the apparent activation energy for water desorption (E_D) using an Arrhenius type linear plot (***Equation 3.7***).

$$2\ln T_{\max} - \ln \beta = \frac{E_D}{RT_{\max}} + C \tag{3.7}$$

3.2.9 Electron microscopy

Selected samples were measured in a high resolution Hitachi S-4000 scanning electron microscope (SEM) to estimate particle size and distribution. The samples were prepared using a standard sample holder with carbon stickers. The same samples were investigated by transmission electron microscopy (TEM) on a FEI Tecnai G² 20 S-TWIN instrument. The instrument worked with a LaB_6 cathode and a acceleration voltage of 200 kV. An EDX (EDAX) r-TEM SUTW detector (Si(Li)) was used for EDX measurements. Measurements on both instruments were performed by ZELMI (Zentraleinrichtung Elektronenmikroskopie) at the TU Berlin.

3.3 Catalytic characterization

3.3.1 Quantitative measurements – gas chromatography

Quantitative measurements were performed using a laboratory fixed bed reactor or the *in situ* spectroscopic cells connected to a non calibrated mass spectrometer (Omnistar from Pfeiffer) and an online GC system. The double GC-system consisted of two connected Varian CP-3800 gas chromatographs (***Figure 3-7***). A flow chart is depicted in ***Figure 3-7*** and ***Figure 3-8***. Hydrocarbons and partial oxidation products were analyzed with the first Varian CP-3800 using a Carbowax 52CB capillary column (25 m x 0.32 mm) connected via a Deans switch either to an Al_2O_3/MAPD capillary column (25 m x 0.32 mm) or to a fused silica restriction (25 m x 0.32 mm), each connected to a flame ionization detector (FID). Permanent gases (O_2, N_2, CO_2, CO) were separated using a Varian CP-3800 "Permanent Gas Analyzer" with a Hayesep Q (2 m x 1/8") and a Hayesep T packed column (0.5 m x 1/8") as precolumns combined with a back flush by using a 10-fold valve. For separation a Hayesep Q packed column (0.5 m x 1/8") was connected via a molesieve (1.5 m x 1/8") to a thermal conductivity detector (TCD). Sample delivery tubes after the reaction cell outlet, valves, and sample loops where constantly heated to 473 K. Mixtures of 1-5% propene and 2-10% oxygen in helium were used for catalytic tests in the range of 295-770 K. Reactant gas flow rates of oxygen (20% O_2 (4.8) in He (5.0), relative error ± 1%, Linde Gas, Air Liquide), propylene (10% propene (3.5) in He (5.0), relative error ± 1%, Linde Gas) and helium (6.0 Air Liquide) were adjusted through separate mass flow controllers to a total flow of 20-75 ml/min (1013 hPa, 273 K). Independent of the reaction gas flow rate the flow rate through the sample loops was adjusted to 20 ml/min. To ensure reproducibility of the measurements the sample gas flow was stopped for several seconds before injection. The injection of sample gas was performed simultaneously in both gas chromatographs. A scan time of approximately 22 min was achieved.

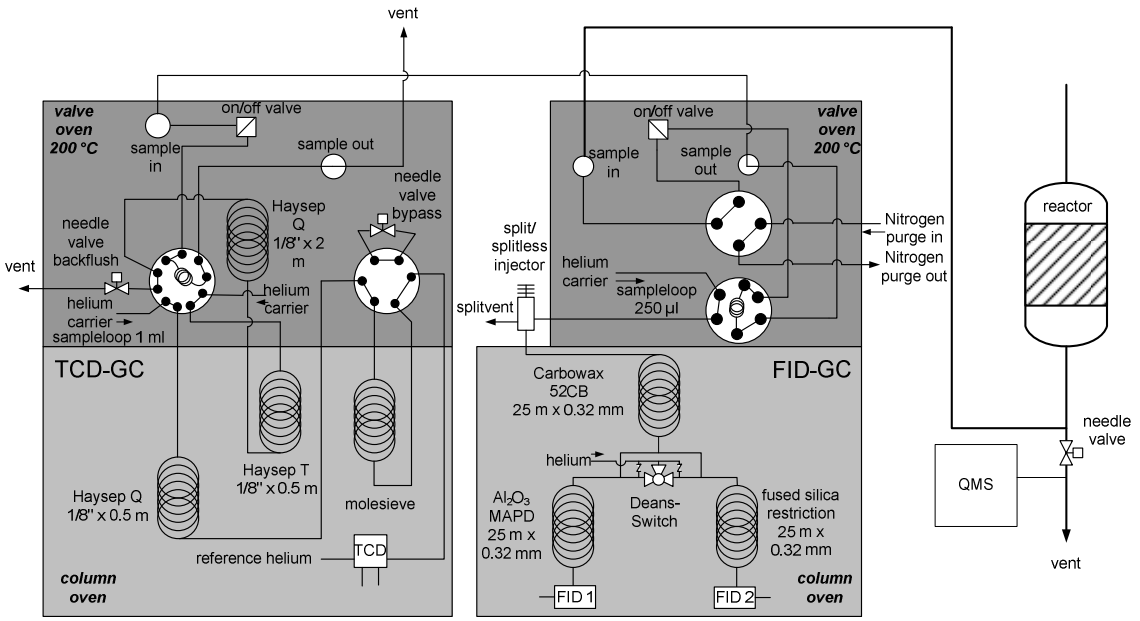

Figure 3-7: Drawing of the used double GC setting.

Pure reaction gases (10% propene or 20% O_2 in He, Linde) were used for calibration. Gas mixtures were employed for the calibration of CO, CO_2, (1 Vol% in He, relative error ± 2%, Linde Gas) and acrolein (0.1 Vol% in He, relative error ± 5%, Linde Gas). All other compounds were calibrated using liquid mixtures, which were injected into the split injector using a 1µl syringe. Each mixture contained known concentrations of a solvent (*e.g.* pentane or MeOH) and a group of oxygenated products such as acids (acrylic acid, propionic acid, acetic acid), aldehydes (acetaldehyde, propione aldehyde, acetone, acrolein) and alcohols (isopropyl alcohol, n-propanol, allylalcohol) together with acrolein in each mixture. The measured retention factor of gas phase acrolein and the ratio of the retention factor of the acrolein standard and the respective analyte in the liquid phase were used to calculate the retention factor of the analyte in the gas phase. Measurement and analysis of the chromatograms was conducted using the Galaxie Software package from Varian.

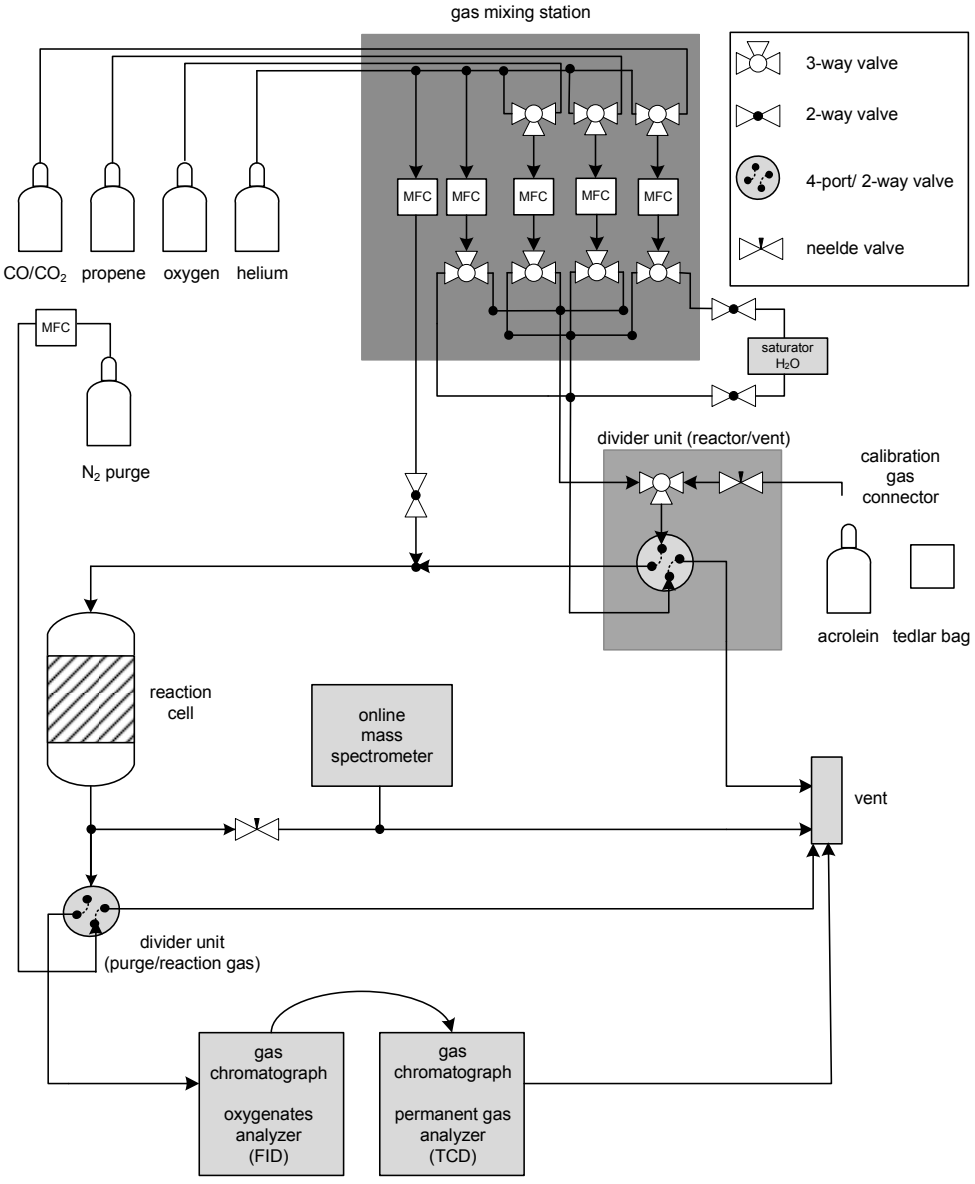

Figure 3-8: Simplified flow chart of the measurement set up used in the laboratory.

3.3.2 *Laboratory fixed bed reactor*

The laboratory fixed bed reactor was made from a SiO_2 tube (30 cm length, 9 mm inner diameter) which was placed vertically in a tube furnace. The sample was placed on a frit (P3 porosity) in the center of the isothermal zone of the furnace (***Figure 3-9***). In addition to the furnace temperature the reactor temperature was recorded using a thermocouple placed next to the reactor tube. Sample mass was 11 mg for 7.7 wt%, 22 mg for 4.1 wt% and, 61 mg for 1.4 wt% V_xO_y/SBA-15. Boron nitride (Alfa Aesar, 200-300 mg) was used for dilution. To ensure differential reaction conditions the reactor was operated at low propene conversion levels.

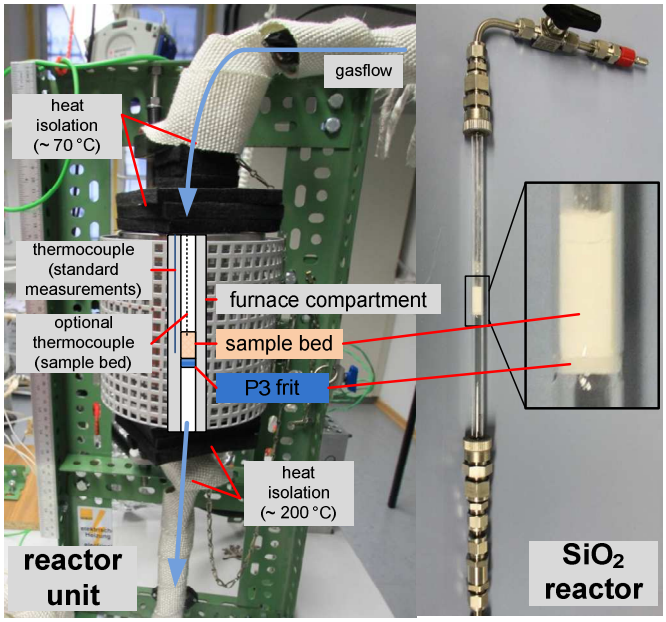

Figure 3-9: Picture of the furnace and reactor used for quantitative measurements.

3.3.3 *Calculation of conversion, selectivity, carbon balance, and reaction rate*

Conversion of propene and selectivity of products were calculated on the basis of mole flows calculated from the measured volume fractions. The calculation of conversion (X) of a key compound (k, propene) and selectivity (S) towards the desired product (p) can be made using the following equations (***3.8, 3.9***) derived from standard text books [105].

$$\text{Conversion}: \quad X_k = \frac{\dot{n}(k)^{in} - \dot{n}(k)^{out}}{\dot{n}(k)^{in}} \tag{3.8}$$

$$\text{Selectivity}: \quad S_P = \frac{\dot{n}(p) - \dot{n}(p)^{in}}{\dot{n}(k)^{in} - \dot{n}(k)} \cdot \frac{|\nu(k)|}{\nu(k)} \tag{3.9}$$

Instead of the mole fraction flow ($\dot{n}$) of a compound (i) the measured volume fractions (Vol%) of the reactants were used for calculation. Both quantities are proportional if the total pressure (open system), total volume, volume flow ($\dot{V}$) and temperature (473 K, GC sample loop) are assumed to be constant during the measurements ($\dot{n}(i) \propto \dot{V}(i) \propto Vol\%(i)$). The equations used for conversion (***3.10***) and carbon balance (***3.11***) are listed below. Carbon balances were higher than 0.95.

Conversion: $$X_k = \frac{Vol\%(k)^{in} - Vol\%(k)^{out}}{Vol\%(k)^{in}} \tag{3.10}$$

Carbon balance:

$$\frac{Vol\%(C)^{out}}{Vol\%(C)^{in}} = \frac{\sum_{x}^{1}(a_{px} \cdot Vol\%(px)^{out}) + Vol\%(CO_2)^{out} + Vol\%(CO)^{out} + 3 \cdot Vol\%(C_3H_6)^{out}}{3 \cdot Vol\%(C_3H_6)^{in}} \tag{3.11}$$

For calculating the selectivity, a detailed knowledge of the reaction network is required for the determination of the stoichiometric factors. However, partial oxidation of propene may proceed over a complex reaction network including consecutive reactions and many side products. Therefore, some simplifications were made for calculating the selectivity. Instead of stoichiometric factors the fraction of carbon atoms in a molecule (a_{pn}) relative to propene (a_k=3) was used. ***Equation 3.12*** was used to ensure the reliability of the selectivities obtained.

$$S_{pn} = \frac{\frac{a_{pn}}{a_k} \cdot \left(Vol\%(pn)^{out} - Vol\%(pn)^{in}\right)}{Vol\%(k)^{in} - Vol\%(k)^{out}} \tag{3.12}$$

$$S_{pn} = \frac{\frac{a_{pn}}{a_k} \cdot Vol\%(pn)}{\sum_{x}^{1}\left(\frac{a_{px}}{a_k} \cdot Vol\%(px)\right)} \tag{3.13}$$

Measurements were only used if reasonable values were calculated for S_{pn} (~ 0.8-1.0). Deviations can be explained by the fact that the analytical GC system used did not permit measuring compounds like formaldehyde or formic acid, which may be formed during the reaction. To ensure comparability of the selectivity obtained all selectivities were calculated using ***Formula 3.13***. The selectivity therein does not refer to the propene conversion but to the sum of all measured reaction products.

Reaction rates for a compound (i) were determined using ***Formula 3.14***. The catalyst mass refers to the total mass of the sample used or to the respective mass (m_{cat}) of the transition metal in the sample (*e.g.* V).

$$r_i = \frac{X_i \cdot Vol\% \cdot \dot{V}}{m_{cat} \cdot V_m \cdot 60} \qquad [r_i] = \frac{mol}{g \cdot s} \tag{3.14}$$

3.3.4 Estimation of mass and heat transport limitations

To ensure that the quantitative gas phase data were determined in a regime of kinetic control, mass transport and heat transport effects were estimated for propene oxidation reactions.

C_3H_6 (g) + 4.5 O_2 (g) → 3 CO_2 (g) + 3 H_2O (g) $\quad \Delta H_R^0$ = -1926 kJ/mol

C_3H_6 (g) + 3 O_2 (g) → 3 CO (g) + 3 H_2O (g) $\quad \Delta H_R^0$ = -1077 kJ/mol

C_3H_6 (g) + O_2 (g) → C_3H_4O (g) + H_2O (g) $\quad \Delta H_R^0$ = -329 kJ/mol

The selective oxidation of propene towards acrolein was chosen as model reaction for the V_xO_y/SBA-15 catalysts. Many side reactions, *e.g.* total oxidation to CO and CO_2 are possible for this reaction. In the case of total oxidation the reaction enthalpy (ΔH_R^0) is much higher than for the oxidation to acrolein. Thus, an increased heat formation will be observed in the case of propene combustion to CO_2. A calculation of the heat that will occur at 10 % propene conversion (assumption that only CO_2 is formed) is shown below. The reaction enthalpies were calculated using the parameters in ***Table 3-1***. The parameters for the mole stream calculation are listed in ***Table 3-2***.

mole stream calculation: $\dot{n} = -Vr = \frac{Vol\% \cdot \dot{V}}{V_m} \cdot X$ (3.15)

heat stream calculation: $\dot{Q} = \dot{n} \cdot \Delta H_R^0 = 17 J / \min$ (3.16)

With the calculated heat stream of 17 J/min the increase of temperature (T) of a 1g material with a heat capacity (C_P) of 1 J/(g*k) can be calculated.

$$\dot{Q} = C_P \cdot \dot{m} \cdot \Delta T \tag{3.17}$$

$$\Delta \dot{T} = \frac{\dot{Q}}{C_P \cdot m} = 17 K / \min . \tag{3.18}$$

That the heat formed can be dissipated by the sample gas stream was inferred from the following calculation. A sample gas stream of 40 ml/min was assumed with an estimated density of 0.5 g/cm^3. Therefore a mass stream of 20 g/min gas is present. The heat capacity (C_p) of the gas was estimated to be 1 J/gK. Considering these values the sample gas stream can dissipate 20 J/min, which is higher than the heat of combustion formed. Thus, heat transport should not disturb the measurements.

Table 3-1: Standard enthalpy of formation ΔH_f^0 for selected compounds in the gas phase.

Compound	ΔH_f^0	Ref.
H_2O (g)	-241.83 kJ/mol	[106]
O_2 (g)	0 kJ/mol	[106]
CO_2 (g)	-393.5 kJ/mol	[106]
CO (g)	-110.5 kJ/mol	[106]
C_3H_6 (g)	-20.4 kJ/mol	[106]
C_3H_4O (g)	-67.0 kJ/mol	[107]

To ensure that no mass transport limitations due to the mesoporous SBA-15 were present, an estimation based on the Weisz-Prater criterion was conducted. The parameters used are listed in ***Table 3-2***.

$$C_{W-P} = L^2 \frac{n+1}{2} \frac{r_{eff} \cdot \rho_{cat}}{D_{eff,propene} \cdot c_{propene}} << 1 \tag{3.19}$$

Given, that the pore diameter d_p of 8 nm is much shorter than the particle length of ~ 50 µm Knudsen diffusion was assumed.

$$D_{eff} \cong D_{Kn} = \frac{\tilde{\nu} d_p}{3}, \tag{3.20}$$

using the average velocity of propene molecules in the gas phase: $\tilde{\nu} = \sqrt{\frac{8 \cdot k_B \cdot T}{\pi \cdot m_{propene}}}$. (3.21)

A resulting Weisz modulus (C_{W-P}) of 0.11 indicates that the reaction proceeds much slower than the propene diffusion into the pores of SBA-15. Thus mass transport effects can be neglected.

Table 3-2: Parameters used to estimate the mass and heat transfer.

Parameter	Value	Description
L	50 µm	particle length
n	1	reaction order
r_{eff} (5 Vol%, 40 ml/min, X=10%)	1.36 mol/(g*s)	effective reaction rate
T	673 K	reaction temperature
m_{propne}	$7*10^{-23}$g	mass of propene molecule
R	8.314 J/(mol*K)	gas constant
k_B	$1.38*10^{-13}$ J/K	Boltzmann constant
d_p	8 nm	pore diameter
$M_{propene}$	42 g/mol	molarmass of propene
D_{Kn} (673 K)	$5*10^{-8}$ m^2/s	Knudsen diffusion of propene in SBA-15
$c_{propene}$ (673 K, 5 Vol%)	$1.36*10^{-6}$ mol/cm^3	propene concentrations
ρ_{cat}	2 g/cm^3	assumed density of SBA-15
V_m	22.414 mol/l	molar volume of an ideal gas
$\dot{n}$ (5 Vol%, 40 ml/min, X=10%)	$9*10^{-6}$ mol/min	mole stream of propene
$\tilde{\nu}$ (673 K)	18.4 m/s	average velocity of propene molecules

4 Comparison of various preparation methods for the synthesis of supported vanadium oxide catalysts

4.1 Introduction

Various methods for the preparation of supported transition metal oxide catalysts are reported in literature. They range from rather simple methods like wet impregnation [8,40] and incipient wetness procedures [37,108] to multi step reactions where the transition metal precursor is chemically bound to the support (silica) [32] before the calcination step. For all preparation methods the formation of disperse vanadium oxide structures for calcined V_xO_y/SiO_2 samples (hydrated and dehydrated state) exhibiting a vanadium density lower than 2.5 V/nm^2 was reported [23,32]. Three typical preparation methods were tested to verify that independent of the preparation method applied the same well dispersed vanadium oxide structures will be present on the SBA-15 support. First, samples were prepared by wet impregnation, which means stirring SBA-15 in an aqueous NH_4VO_3 solution. Second, samples were prepared by incipient wetness using an aqueous $(NH_4)_6V_{10}O_{28}{\cdot}xH_2O$ solution. Third, samples were prepared by a grafting/ion exchange method introduced by Hess *et al.* [32] (***Figure 4-1***). For all samples vanadium coverages below 2.5 V/nm^2 were intended. The structure of the prepared samples were characterized in the calcined (hydrated and dehydrated) and uncalcined state using XRD, XAFS, Raman spectroscopy, and UV-Vis-DRS. Additionally, physisorption, electron microscopy, and small angle XRD measurements were conducted to detect changes in the mesoporous SBA-15 support.

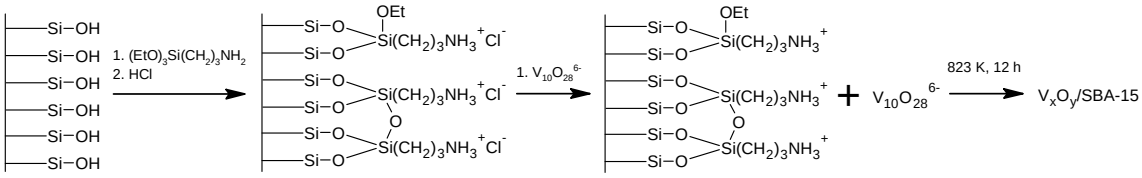

Figure 4-1: Simplified reaction scheme of the APTES grafting and ion exchange ($(NH_4)_6V_{10}O_{28}{\cdot}xH_2O$ precursor) preparation process of V_xO_y/SBA-15 samples.

4.2 Results and discussion

4.2.1 Surface area and vanadium content of the V_xO_y/SBA-15 samples

The results of the vanadium element analysis and the BET surface area determination are listed in ***Table 4-1***. More detailed tables of the physisorption results, small angle XRD, and CHN element analysis are provided in the appendix (***Table 10-1, Table 10-2***). The vanadium dispersion in ***Table 4-1*** was referred to the BET surface area determined for the calcined V_xO_y/SBA-15 samples. A similar V dispersion was

determined on different samples. Therefore, the sample names refer to the vanadium content (ICP) of the samples (*e.g.* 7.7 wt% V_xO_y/SBA-15).

Table 4-1: BET surface area (S_{BET}) and vanadium content of the calcined V_xO_y/SBA-15 samples: (*) sample prepared via the ion exchange method in ***Figure 4-1***, (**) sample prepared by wet impregnation with a NH_4VO_3 solution, (***) sample prepared by incipient wetness using a $(NH_4)_6V_{10}O_{28}$ solution. The values in brackets refer to the V content determined by RFA).

Sample	S_{BET} [m^2g^{-1}]	wt% ICP (RFA)	mmol V/ g	$V_{density}$ / nm^2
3.0 wt% V_xO_y/SBA-15***	522	3.0 (3.1)	0.59	0.7
5.7 wt% V_xO_y/SBA-15**	403	5.7 (5.7)	1.12	1.7
5.0 wt% V_xO_y/SBA-15*	270	-- (5.0)	(0.98)	(2.2)
7.7 wt% V_xO_y/SBA-15*	386	7.7 (7.3)	1.51 (1.43)	2.4 (2.2)
4.1 wt% V_xO_y/SBA-15*	427	4.1 (4.1)	0.81	1.1
1.4 wt% V_xO_y/SBA-15*	542	1.4 (1.4)	0.28	0.3

4.2.2 Structural characterization of the uncalcined V_xO_y/SBA-15 samples

In ***Figure 4-2*** the Raman and UV-Vis-DR spectra of the uncalcined vanadium containing SBA-15 samples are depicted. The Raman spectrum of the SBA-15 support exhibited a broad band at 490 cm^{-1} (cyclic tetrasiloxane rings, D1 defect mode) and less intense bands at ~ 600, 800 and 977 cm^{-1} (cyclic trisiloxane rings, D2 defect mode) [23,32]. In the spectrum of the uncalcined 5.7 wt% V_xO_y/SBA-15 sample (wet impregnation) additional bands at 930, 899, 648, 496, 261, and 212 cm^{-1} were detected (***Figure 4-2, left, D***). These were assigned to crystalline NH_4VO_3, which may be a residual from the preparation process. A broad background in the region 870-1000 cm^{-1} indicates the presence of a second vanadium oxide species. V-O stretching vibrations of vanadium V^{5+} compounds are typically located in this spectral range [109]. In the Raman spectrum of the 3.0 wt% V_xO_y/SBA-15 sample (incipient wetness) in ***Figure 4-2 (left, B)*** two ranges of additional Raman bands were detected (~ 970 cm^{-1}, 622-850 cm^{-1}). Thus, a mixture of different vanadium oxide phases may be present on the SBA-15 support. The Raman spectra of the samples prepared by the ion exchange method are shown in ***Figure 4-2 (middle)*** together with the spectra of the SBA-15 support and APTES modified SBA-15. Characteristic Raman bands for APTES modified SBA-15 (***Figure 4-2, middle, F***) were detected (~ 950 and ~ 1050 cm^{-1}, assigned to C-C stretching vibrations of the propylammonium group in the grafted APTES group [32]). Hess *et al.* [32] reported that the decavanadate ion is preserved during the grafting process. Indeed, characteristic Raman bands of the decavanadate precursor were detected at 992, 658, 321, 253, 221, and 184 cm^{-1} (***Figure 4-2, middle, G***) for the high loaded uncalcined 5.0 wt% V_xO_y/SBA-15 sample (2.2 V/nm^2, similar to sample 7.7 wt% V_xO_y/SBA-15). Compared to the spectrum of the bulk $V_{10}O_{28}^{6-}$ reference the Raman band at 958 cm^{-1} was broadened and increased relative to the band at 992 cm^{-1}. With decreasing vanadium loading the low frequency bands < 700 cm^{-1} were not observed in the Raman spectra and the Raman band at 992 cm^{-1} decreased significantly. For all samples a band around 1040-1050 cm^{-1} was observed in the spectra which was assigned to the grafted APTES. Due to the broad Raman signal at 960 cm^{-1} in the Raman spectra of all uncalcined V_xO_y/SBA-15 samples (ion exchange method) more than one vanadium oxide species may be present.

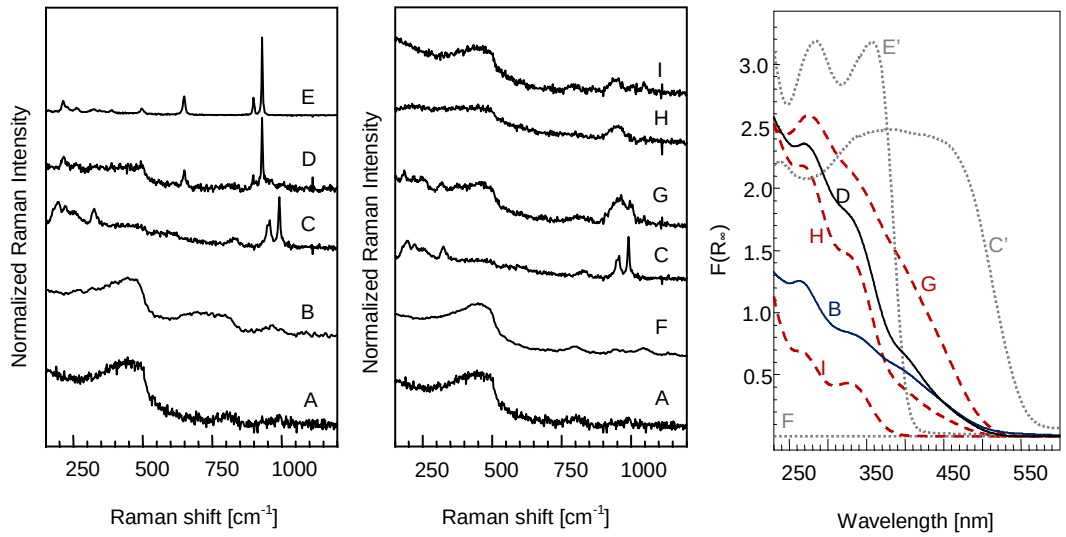

Figure 4-2: Raman spectra (left, middle) and UV-Vis-DRS spectra (right) of the uncalcined V_xO_y/SBA-15 samples and selected vanadate references: (A) SBA-15, (B) 3.0 wt% V_xO_y/SBA-15, incipient wetness (C) 8 wt% V, $(NH_4)_6V_{10}O_{28}{\cdot}xH_2O$ mixed with SBA-15, (C') $(NH_4)_6V_{10}O_{28}{\cdot}H_2O$, (D) 5.7 wt% V_xO_y/SBA-15, wet impregnation, (E) 8 wt% V, NH_4VO_3 mixed with SBA-15, (E') NH_4VO_3, (F) APTES functionalized SBA-15, (G) 5.0 wt% V_xO_y/SBA-15, ion exchange, (H) 4.1 wt% V_xO_y/SBA-15, ion exchange, (I) 1.4 wt% V_xO_y/SBA-15, ion exchange.

The UV-Vis-DR spectra of the uncalcined samples together with the spectra of the bulk references NH_4VO_3 and $(NH_4)_6V_{10}O_{28}{\cdot}xH_2O$ are depicted in ***Figure 4-2 (right)***. For all samples no similarity with the spectra of the bulk vanadate references was observed. Independent of the preparation method similar absorption bands were recorded in the spectra of all uncalcined V_xO_y/SBA-15 samples. These absorption bands were located at 405 nm, 335 nm, and 264-274 nm. The low energy absorption band matches the maximum in the absorption spectrum of $(NH_4)_6V_{10}O_{28}{\cdot}xH_2O$. For the 1.4 wt% V_xO_y/SBA-15 sample prepared via the ion exchange method the band at 405 nm was hardly detectable. The UV-Vis edge energy was determined for the uncalcined V_xO_y/SBA-15 samples according to a method described by Gao and Wachs [100]. The UV-Vis edge energy can provide information about the coordination and the degree of polymerization of the absorbing vanadium species. A more detailed introduction and discussion will be provided in ***Chapter 5***. UV-Vis edge energies in the range of 2.7-2.9 eV were determined for the high loaded sample (5.0 wt% V_xO_y/SBA-15) prepared via the ion exchange method and for the samples prepared via the incipient wetness method. For the low loaded 4.1 and 1.4 wt% V_xO_y/SBA-15 samples prepared via the ion exchange method UV-Vis edge energies in the range of 3.3-3.4 eV were determined. In the UV-Vis-DR spectrum of uncalcined 5.7 wt% V_xO_y/SBA-15 prepared by wet impregnation (***Figure 4-2, right, D***) two regions of the absorption spectrum could be used to determine the UV-Vis edge energy. UV-Vis edge energies at 2.8 and 3.2 eV may be derived from the UV-Vis-DR spectrum. Considering the presence of NH_4VO_3 in the Raman spectra of this sample the second band may indicate a NH_4VO_3 species (UV-Vis edge energy 3.2 eV) on the support. Values in the range of 2.7-2.9 eV were an indicator for a higher polymerized species present on the support exhibiting at least a 5-fold or higher coordination. Values between 3.2-3.4 eV were assigned to less polymerized vanadium oxide centers (small chains or dimers) which exhibit a tetrahedral rather than a square pyramidal coordination of the absorbing vanadium species.

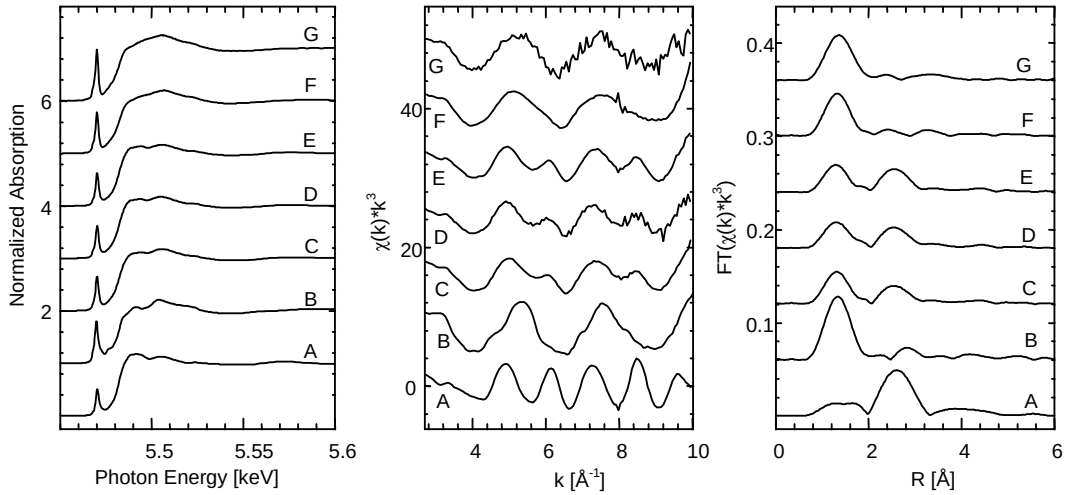

Figure 4-3: V K edge XANES spectra (left), $\chi(k)*k^3$ (middle), and FT($\chi(k)*k^3$) (right) of the uncalcined V_xO_y/SBA-15 samples and selected vanadate references: (A) $(NH_4)_6V_{10}O_{28}\cdot xH_2O$, (B) NH_4VO_3, (C) 5.7 wt% V_xO_y/SBA-15, wet impregnation, (D) 3.0 wt% V_xO_y/SBA-15, incipient wetness (E) 5.0 wt% V_xO_y/SBA-15, ion exchange, (F) 4.1 wt% V_xO_y/SBA-15, ion exchange, (G) 1.4 wt% V_xO_y/SBA-15, ion exchange.

XAFS measurements were conducted to obtain information about the structure of the main vanadium oxide phase of the uncalcined V_xO_y/SBA-15 sample. The V K edge XANES spectra, the derived $\chi(k)*k^3$, and the Fourier transformed $\chi(k)*k^3$ are depicted in ***Figure 4-3***. The XANES spectra of the uncalcined 5.7 wt% (wet impregnation), 3.0 wt% (incipient wetness), and 7.7 wt% (ion exchange) V_xO_y/SBA-15 samples were comparable to that of the $(NH_4)_6V_{10}O_{28}\cdot xH_2O$ reference sample (***Figure 4-3, left***). In contrast to the decavanadate reference sample the pre-edge peak was enhanced in the XANES spectra of the uncalcined V_xO_y/SBA-15 samples. The $\chi(k)*k^3$ of the uncalcined 5.7 wt% (wet impregnation), 3.0 wt% (incipient wetness), and 7.7 wt% (ion exchange) V_xO_y/SBA-15 samples showed oscillations similar to the $\chi(k)*k^3$ of the $(NH_4)_6V_{10}O_{28}\cdot xH_2O$ reference. The amplitude of these oscillations was decreased (***Figure 4-3, middle***). After the Fourier transformation of the $\chi(k)*k^3$ of the uncalcined 5.7 wt% (wet impregnation), 3.0 wt% (incipient wetness), and 7.7 wt% (ion exchange) V_xO_y/SBA-15 samples mainly two signals in the range of 1-2 Å and 3-4 Å were detected in the envelope of the FT($\chi(k)*k^3$) (***Figure 4-3, right***, not phase shift corrected). The first signal was assigned to V-O scattering contributions and the second signal was assigned to V-V scattering paths. Comparing the FT($\chi(k)*k^3$) of the high loaded uncalcined V_xO_y/SBA-15 samples with that of the $(NH_4)_6V_{10}O_{28}\cdot xH_2O$ reference no direct similarity was observed. The increased V-O signal (1-2 Å) in the FT($\chi(k)*k^3$) of these samples resembled that of lower coordinated vanadate species like NH_4VO_3. Therefore, a mixture of decavanadate vanadium centers and lower coordinated vanadium centers may be present on the SBA-15 support. With decreasing vanadium loading the signal at higher distances (3-4 Å) decreased in the FT($\chi(k)*k^3$) of the uncalcined V_xO_y/SBA-15 samples prepared by the ion exchange method. The first signal (1-2 Å) in the FT($\chi(k)*k^3$) of the uncalcined 1.4 wt% and 4.1 wt% V_xO_y/SBA-15 samples (ion exchange) was slightly enhanced compared to the 5.7 wt% and 7.7 wt% V_xO_y/SBA-15 samples. Nevertheless, it was still smaller than in the FT($\chi(k)*k^3$) of most tetrahedral vanadate reference compounds (***Chapter 5.2.5***) like NH_4VO_3. Thus vanadium centers exhibiting a strong structural disorder may be present. The rather high pre-edge peak in

the XANES spectra of the uncalcined 1.4 wt% and 4.1 wt% V_xO_y/SBA-15 (ion exchange) suggested that these vanadium centers may have a tetrahedral coordination (***Chapter 5.2.4***).

4.2.3 Vanadium dispersion in the calcined V_xO_y/SBA-15 samples

XRD measurements were conducted to exclude the presence of crystalline vanadium oxide phases on the support after calcination of the V_xO_y/SBA-15 samples. The resulting powder patterns are depicted in ***Figure 4-4***. A physical mixture of ball milled V_2O_5 and SBA-15 was prepared (8 wt% V) for reference. The domain size of the V_2O_5 crystallites was estimated from the integral breadth using the Debye-Scherrer equation. It was approximately 170 Å ((200) diffraction line, 15.38 °2θ). The powder pattern in ***Figure 4-4*** shows that a mixture of these V_2O_5 crystallites and SBA-15 still exhibited well resolved and characteristic diffraction lines of V_2O_5. Only the 5.7 wt% V_xO_y/SBA-15 sample (wet impregnation) showed characteristic diffraction lines of V_2O_5. The V_2O_5 in the sample prepared via wet impregnation was probably formed by decomposition of NH_4VO_3 residuals that were detected in the Raman spectra of the uncalcined 5.7 wt% V_xO_y/SBA-15 sample (wet impregnation) (***Figure 4-2, left***).

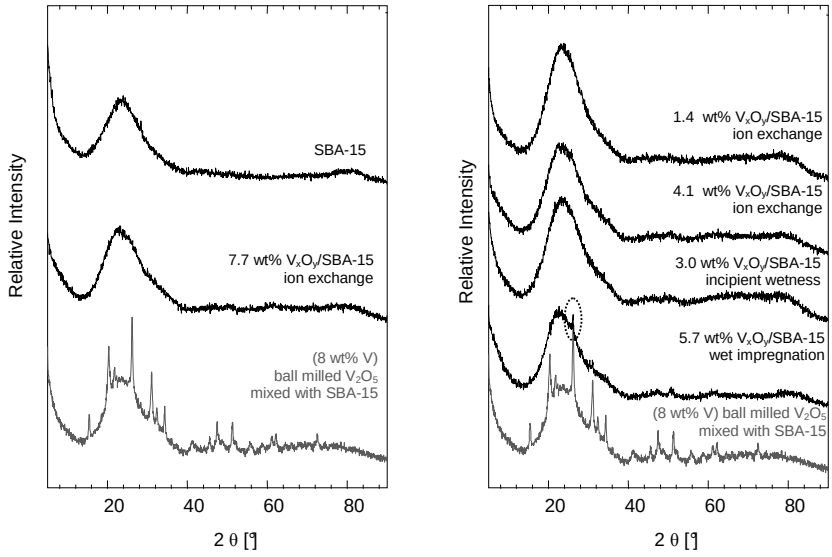

Figure 4-4: XRD powder patterns (Cu K_α) of the calcined V_xO_y/SBA-15 samples, bare SBA-15, and a physical mixture of ball milled V_2O_5 and SBA-15 (8 wt% V).

XRD is not sensitive to minority phases of less than 5% phase fraction. Therefore, Raman spectra of the calcined V_xO_y/SBA-15 samples were recorded. In ***Figure 4-5 (left and middle)*** the Raman spectra of the hydrated (as prepared) and the dehydrated (air/ 673 K/ 12 h) state of the calcined V_xO_y/SBA-15 samples are depicted together with the Raman spectrum of a physical mixture of V_2O_5 and SBA-15 (3 wt% V). The spectra of all calcined V_xO_y/SBA-15 samples showed characteristic bands for the hydrated state (1028, 706, 270, 160 cm^{-1}) and dehydrated state (~ 1040 cm^{-1}) of dispersed vanadium oxide centers on silica supported samples as reported in the literature [23,32]. Therefore, after calcination a disperse vanadium oxide species may have formed as the majority phase on the SBA-15 support in all samples. Characteristic Raman bands of V_2O_5 were only detected for the 5.7 wt% V_xO_y/SBA-15 sample prepared via wet impregnation.

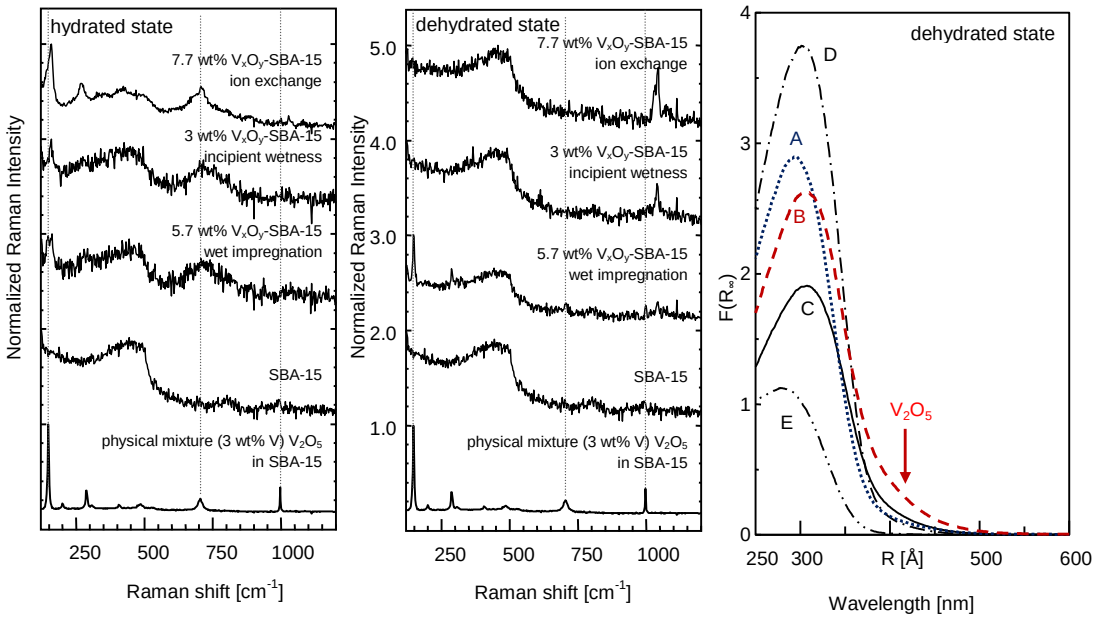

Figure 4-5: Raman (left, middle) and UV-Vis-DRS spectra (right) of the calcined V_xO_y/SBA-15 samples and selected vanadium oxide references: (A) 3.0 wt% V_xO_y/SBA-15 incipient wetness, (B) 5.7 wt% V_xO_y/SBA-15 wet impregnation, (C) 7.7 wt% V_xO_y/SBA-15 ion exchange, (D) 4.1 wt% V_xO_y/SBA-15 ion exchange, (E) 1.4 wt% V_xO_y/SBA-15 ion exchange. (samples diluted 1:1 or 1:2 with SBA-15 for UV-Vis-DRS measurments).

The characteristic Raman bands of V_2O_5 were present in the hydrated and dehydrated state of the calcined 5.7 wt% V_xO_y/SBA-15 (wet impregnation). Crystalline vanadium oxide phases (determined by Raman spectroscopy) originating from the preparation method were excluded for samples prepared by the incipient wetness and ion exchange procedures in the range of V loading employed.

UV-Vis-DRS and XAFS play a pronounced role for the structural characterization of the V_xO_y/SBA-15 model catalysts as will be discussed in more detail in the following chapters. In order to show that for all preparation methods used similar spectra and thus similar dispersed vanadium oxide species were obtained all samples were dehydrated and investigated *in situ* using UV-Vis-DRS and XAFS. ***Figure 4-5 (right)*** shows the UV-Vis-DR spectra of all calcined V_xO_y/SBA-15 samples after dehydration at 554 K (20% O_2 in He). The spectra of all V_xO_y/SBA-15 samples exhibited absorption bands with a maximum in the range of 280 nm (dehydrated 1.4 wt% and 3.0 wt% V_xO_y/SBA-15) and 310 nm (dehydrated 4.1 wt%, 5.7 wt%, and 7.7 wt% V_xO_y/SBA-15). These absorption bands were assigned to a highly dispersed tetrahedral vanadium oxide species (***Chapter 5.2.1***). Furthermore, in the spectra of the calcined and dehydrated V_xO_y/SBA-15 samples (except for the 1.4 wt% V_xO_y/SBA-15 sample) a small absorption band at approximately 405 nm was observed. This absorption band was significantly pronounced in the spectrum of the 5.7 wt% V_xO_y/SBA-15 sample (wet impregnation). Considering the presence of V_2O_5 in the Raman spectrum and XRD pattern of this sample the absorption band at 405 nm was assigned to a V_2O_5 phase. The absence of characteristic V_2O_5 Raman bands in the Raman spectra of all other samples indicate that the slight increase at 405 nm in the UV-Vis-DR spectra was caused by very small amounts of crystalline V_2O_5.

XAFS measurements of dehydrated V_xO_y/SBA-15 samples corroborated that the majority vanadium oxide phase on SBA-15 was a dispersed tetrahedral phase (dehydrated samples, ***Figure 4-6***, 623 K, 20% O_2 in He). For all dehydrated V_xO_y/SBA-15 samples similar V K edge XANES, $\chi(k)*k^3$ and Fourier transformed $\chi(k)*k^3$ were obtained. The V_2O_5 phase present in the 5.7 wt% V_xO_y/SBA-15 sample (wet impregnation) was not visible in the XAFS spectra. Therefore, the fraction of crystalline V_2O_5 in 5.7 wt% V_xO_y/SBA-15 was less than 5-10% of the vanadium oxide species present on the (SBA-15) support in this sample. The FT($\chi(k)*k^3$) of the dehydrated 5.7 wt% V_xO_y/SBA-15 sample prepared by wet impregnation resembled that of the dehydrated 4.1 wt% and 7.7 wt% V_xO_y/SBA-15 samples (***Figure 4-6, right***). All three samples showed an increased amplitude at higher distances (3-4 Å) in the FT($\chi(k)*k^3$). The low loaded 1.4 wt% (ion exchange) and 3.0 wt% (incipient wetness) dehydrated V_xO_y/SBA-15 samples exhibited a comparable envelope of the FT($\chi(k)*k^3$). At higher distances (3-4 Å) the amplitude was reduced. In the UV-Vis-DR spectra (***Figure 4-5, right***) of these samples the absorption maximum was shifted from ~ 300 nm to ~ 280 nm compared to the spectra obtained for the higher loaded dehydrated V_xO_y/SBA-15 samples. Hence, minor differences in the structure of the supported dehydrated vanadium oxide species may be present in the spectra of the low (1.4 and 3.0 wt% V) and higher loaded (4.1-7.7 wt% V) dehydrated V_xO_y/SBA-15 samples. A more detailed discussion of these results is given in ***Chapter 5***.

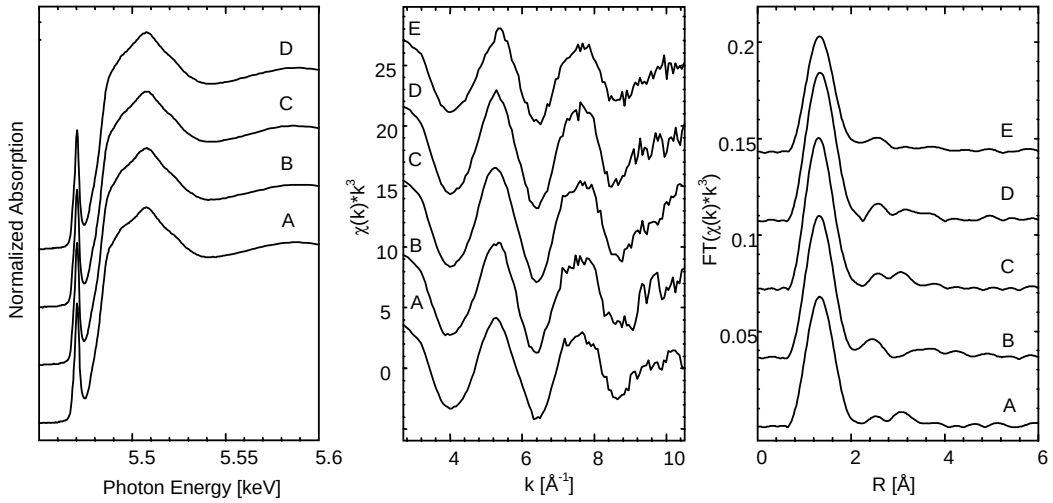

Figure 4-6: V K edge XANES spectra (left), $\chi(k)*k^3$ (middle), and FT($\chi(k)*k^3$) (right) of the calcined and dehydrated V_xO_y/SBA-15 samples (20% O_2 in He, 623 K): (A) 5.7 wt% V_xO_y/SBA-15 wet impregnation, (B) 3.0 wt% V_xO_y/SBA-15 incipient wetness, (C) 7.7 wt% V_xO_y/SBA-15 ion exchange, (D) 4.1 wt% V_xO_y/SBA-15 ion exchange, (E) 1.4 wt% V_xO_y/SBA-15 ion exchange.

4.2.4 Characterization of the SBA-15 support of the V_xO_y/SBA-15 samples prepared by the ion exchange method

The grafting/ion exchange method allowed the preparation of V_xO_y/SBA-15 samples exhibiting a disperse vanadium oxide species even at high vanadium loadings. In contrast to the wet impregnation method, no crystalline V_2O_5 species were present after preparation of a high loaded sample with a vanadium dispersion of 2.4 V/nm^2. Therefore, samples prepared by this method were used for further investigations.

In order to ensure that the mesoporous SBA-15 support was not affected by the preparation process, physisorption, small angle XRD, and electron microscopy measurements were conducted before and after vanadium anchoring.

In ***Figure 4-7*** the N_2 adsorption and desorption isotherms of SBA-15 and the calcined V_xO_y/SBA-15 samples (ion exchange) are depicted. A detailed table of the physisorption and small angle XRD results for all samples is given in the appendix (***Table 10-1***). The SBA-15 samples exhibited a type IV physisorption isotherm according to the IUPAC classification [110]. This is characteristic for mesoporous samples (pore diameter (d_p) 2-50 nm). The significant decrease at lower p/p_0 values indicated that micropores (d_p < 2 nm) were present in all SBA-15 samples (***Figure 4-7, left***). The BET surface areas determined for the bare SBA-15 samples ranged from 607 and 818 m^2/g. For all samples a significant decrease of the BET surface area (30-50%) was observed for the calcined V_xO_y/SBA-15 samples compared to the initial SBA-15 samples. The characteristic diffractions of the hexagonal SBA-15 structure were detected in the small angle XRD patterns ((100), (110), (200) diffraction) of all samples (***Figure 4-7, left, inset***). Hence, the mesoporous SBA-15 structure remained unaffected by the preparation. The cell parameter determined from the (100) diffraction was slightly decreased (0.1-0.4 nm, 1-4 %) in the calcined V_xO_y/SBA-15 samples compared to the initial SBA-15 material. This was interpreted as a shrinking of the SBA-15 pore structure of the supported samples compared to the initial SBA-15 samples. Herbert [111] showed that a shrinking of ~ 30 % of the mesoporous SBA-15 structure was not an unusual observation. This was observed by Herbert for thermal (calcination, 923 K, 24 h) and hydrothermal (water, 373 K, 24 h, autoclave) treatment of SBA-15 samples [111]. The shrinking did not affect the shape of the hysteresis of the sorption isotherms of the SBA-15 samples. For the 1.4 wt% and the 4.1 wt% V_xO_y/SBA-15 sample the type IV physisorption isotherm was still present.

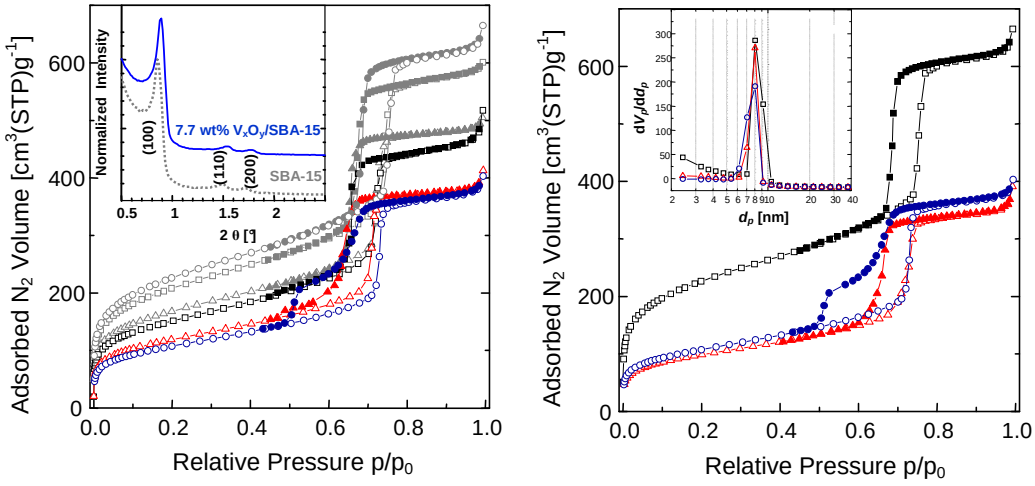

Figure 4-7: N_2 adsorption (open symbols) and desorption (filled symbols) isotherms. Left: initial SBA-15 (grey, same symbols as V_xO_y/SBA-15 samples) and calcined V_xO_y/SBA-15 samples prepared via the grafting/ion exchange method (colored: squares 1.4 wt% V; triangles 4.1 wt% V; circles 7.7 wt% V). The inset depicts the small angle XRD powder patterns of the calcined 7.7 wt% V_xO_y/SBA-15 sample and the initial SBA-15. Right: initial SBA-15 (black, squares), SBA-15-APTES after calcination (blue, circles), and calcined 7.7 wt% V_xO_y/SBA-15 (red, triangles). The inset depicts the respective pore size distributions obtained from the adsorption isotherm (BJH model).

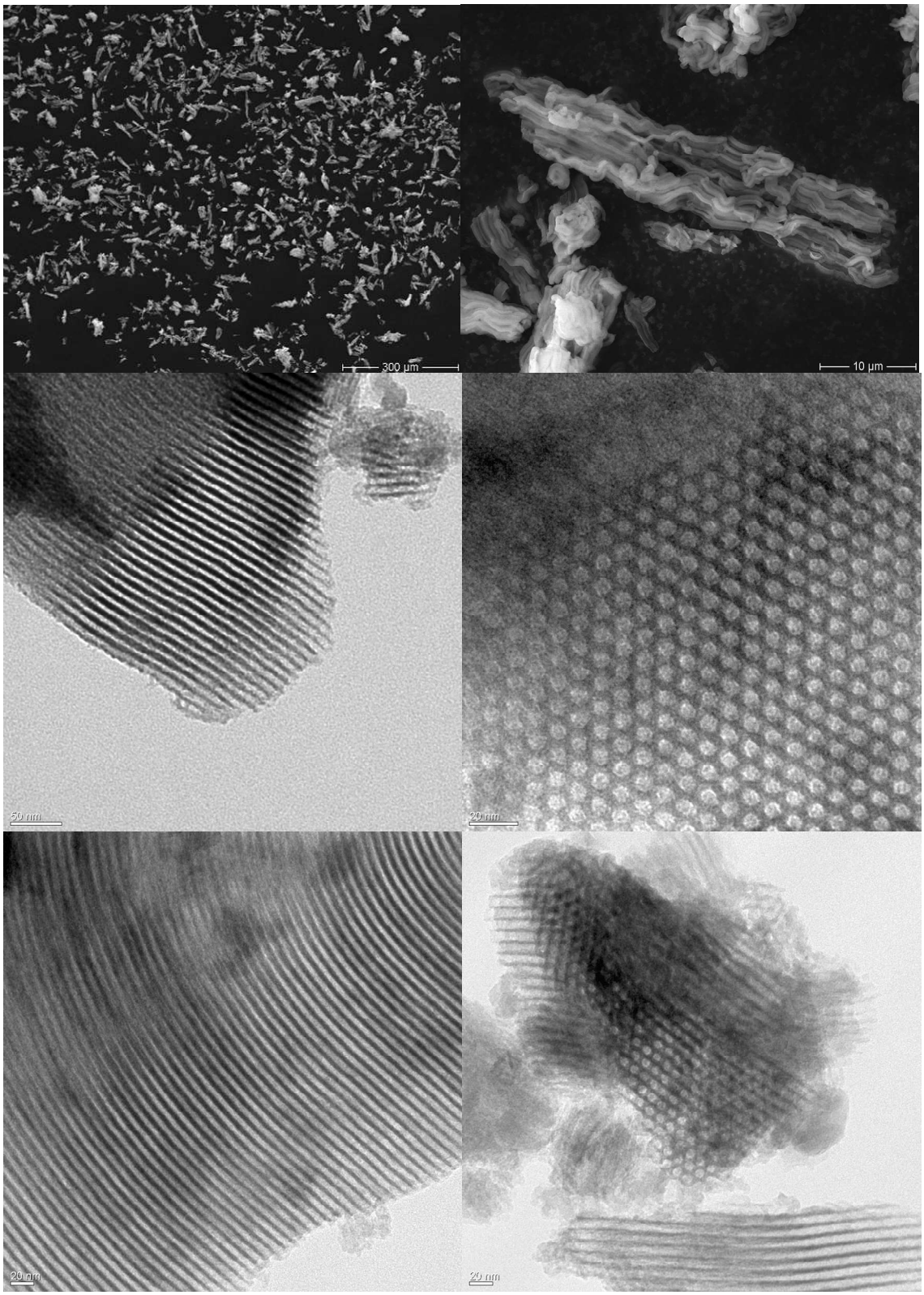

Figure 4-8 top: REM images of the calcined 7.7 wt% V_xO_y/SBA-15 sample; middle: TEM images of the initial SBA-15; bottom: TEM images of the calcined 7.7 wt% V_xO_y/SBA-15 sample.

For the high loaded 7.7 wt% V_xO_y/SBA-15 a second step ($p/p_0 \sim 0.5$) was visible in the desorption isotherm (***Figure 4-7, right***). Two different interpretations of this step are feasible. A possible origin for the additional step in the desorption isotherm may be a change of the SBA-15 mesoporous structure during the ATPES grafting step in the preparation of this sample. This argument was excluded because the shape of the desorption isotherms did not change for the lower loaded 4.1 wt% and 1.4 wt% V_xO_y/SBA-15 samples, which were prepared in the same way (***Figure 4-7, left***). Moreover, the desorption isotherm exhibited only one step, if the functionalized SBA-15-APTES sample was calcined before the ion exchange step. For such a sample a decrease of the BET surface area of ~ 53% was observed. Thus, the APTES functionalization step decreased the BET surface area but did not change the SBA-15 pore structure. Another explanation for the second step in the desorption isotherm of 7.7 wt% V_xO_y/SBA-15 may be a pore plugging of some of the SBA-15 mesoporous channels by the supported vanadium oxide phase. Similar plugging effects on desorption isotherms were reported by Van der Voort *et al.* for PHTS SBA-15 materials [112] and Meyen *et al.* for SBA-VS-15 materials [113]. The fact that the vanadium oxide phase at higher loading may plug some of the SBA-15 channels indicated that it was possible to disperse the vanadium oxide phase into the pores of the SBA-15 using the grafting/ion exchange method.

That the SBA-15 channel structure was preserved during the preparation process was visible in the electron microscopy images of the samples (***Figure 4-8***). In the TEM images of the initial SBA-15 and the calcined V_xO_y/SBA-15 samples a channel structure was detected. Some of the TEM images showed the hexagonal orientation of these channels which is characteristic for SBA-15 (***Figure 4-8, middle and bottom***). The wall thickness between the channels was estimated to be 3 nm and the channel diameter was approximately 6-7 nm for bare SBA-15. For the calcined 7.7 wt% V_xO_y/SBA-15 the wall thickness was estimated to be 3-5 nm and the channel diameter was approximately 5-7 nm. The slight decrease of the channel diameter and the increase of the wall thickness indicates that either Si of the APTES reactant or vanadium oxide were attached to the channel walls. Due to the low element contrast of V and Si this could not be discriminated. However, EDX measurements showed that a high vanadium dispersion was present on the 7.7 wt% V_xO_y/SBA-15 sample. No areas of higher V content than 11 wt% were identified (3 measurements, spot size ~ 30 nm). In order to determine the particle size and morphology, SEM images (***Figure 4-8, top***) were recorded of 7.7 wt% V_xO_y/SBA-15. The main fraction of particles was typically 30-70 µm long and 10 µm wide.

4.3 Summary

V_xO_y/SBA-15 samples were prepared by incipient wetness, wet impregnation, and a grafting/ion exchange method. *In situ* UV-Vis-DRS, XAFS, and Raman measurements were conducted to determine the nature of the vanadium oxide species present on SBA-15. Spectroscopic measurements of the uncalcined V_xO_y/SBA-15 samples suggested that mixtures of different vanadium centers were present on SBA-15. Features corresponding to vanadium oxide centers with higher (5-fold or 6-fold coordination)

and lower (4-fold or 5-fold coordination) degree of polymerization were observed in the spectra of the uncalcined 3.0 wt% -7.7 wt% V_xO_y/SBA-15 samples. From Raman and XAFS measurements it seems likely that the higher polymerized vanadium centers may exhibit a structure similar to that of the decavanadate ion. With decreasing vanadium loading the amount of the less polymerized (4-fold or 5-fold coordination) vanadium oxide centers increased. In the spectra of uncalcined 1.4 wt% V_xO_y/SBA-15 no higher polymerized vanadium oxide phases were observed. The probability that the lower polymerized vanadium oxide centers were formed during the preparation was higher for the grafting/ion exchange process. In addition, residuals of crystalline NH_4VO_3 were detected in the Raman spectrum of the uncalcined sample prepared via wet impregnation (5.7 wt% V_xO_y/SBA-15).

Calcination of the V_xO_y/SBA-15 samples yielded well dispersed vanadium oxide centers on SBA-15. Raman spectra of as prepared and thermally treated samples (dehydrated in 20% O_2 in He, 673 K) showed characteristic bands for the hydrated and the highly dispersed dehydrated state of supported vanadium oxides, respectively. These Raman bands matched those of V_xO_y/SiO_2 samples reported in the literature [23,32]. Therefore, the V_xO_y/SBA-15 samples investigated here were comparable to highly disperse V_xO_y/SiO_2 samples reported in the literature [23,32].

No distinct differences resulted from the preparation method employed, as observed in the Raman, UV-Vis-DR, and XAFS spectra of the V_xO_y/SBA-15 samples in the dehydrated state. For all samples, the majority phase in the dehydrated state was a highly dispersed tetrahedral vanadium oxide species. For the sample prepared by wet impregnation with an aqueous NH_4VO_3 solution, small amounts of crystalline V_2O_5 were detected. Therefore, samples prepared by this method were not used for further structural characterization and catalytic reactivity tests. Samples prepared by the incipient wetness method were also not used as model catalysts although only a dispersed vanadium oxide species was detected. The preparation of larger sample batches (5-10 g SBA-15) using this method is impractical and may cause an inhomogeneous vanadium distribution on the SBA-15 support during the drying process of the uncalcined samples. Therefore, the ion exchange method was preferred for sample preparation. The calcined 1.4 wt%, 4.1 wt%, and 7.7 wt% V_xO_y/SBA-15 (ion exchange) samples shown in this chapter were used for structural characterization of the dispersed vanadium oxide species and for catalytic testing.

The mesoporous structure of SBA-15 was not affected by the preparation method chosen. A decrease of the BET surface area was observed for all V_xO_y/SBA-15 samples. Except for the 7.7 wt% V_xO_y/SBA-15 sample the characteristic type IV physisorption isotherms were still present after anchoring the vanadium oxide phase and calcination. A second step in the desorption isotherm occurred for the calcined 7.7 wt% V_xO_y/SBA-15 sample. Hence, the supported vanadium oxide phase may be present inside the SBA-15 channels, which causes plugging of some pores on the high loaded sample. TEM and small angle XRD measurements showed that the hexagonal channel structure of SBA-15 was maintained in this sample.

5 *Structural characterization of hydrated and dehydrated V_xO_y/SBA-15*

5.1 Introduction

Structural characterization of V_xO_y supported on SiO_2 has been subject of many spectroscopic studies including IR [44,114,115], XPS [116,117,118], Raman [23,32,40,117,118,119], UV-VIS [23,32,40,100,118] and EXAFS [21-23,37,108,120,121,122,]. A recent review of spectroscopic investigations and structural characteristics of various supported vanadium oxides has been presented by Weckhuysen and Keller [18]. It is assumed, that the structure of supported vanadium oxide depends on both amount of vanadium and degree of hydration [32]. Hence, most studies were performed on V_xO_y/SiO_2 samples exhibiting low vanadium loading (< 2.5 V/nm^2). At these loadings a monolayer of supported V_xO_y species is assumed and crystalline V_2O_5 is not detectable [30,31,32]. Under ambient conditions the structure of hydrated vanadium oxide supported on SiO_2 resembles that of V_2O_5 [23,117,108]. Thermal treatment in oxygen results in dehydration of the vanadium oxide species, which will be discussed in detail in ***Chapter 6***. The dehydrated state has been proposed to consist of isolated "VO_4" tetrahedrons bound to the SiO_2 support [21,23,123,124]. However, V_2O_7 dimers or further extended structures supported on SiO_2 have not been excluded [40]. In total, the structure of dehydrated vanadium oxide species supported on SiO_2 remains under debate.

Here, the combination of the spectroscopic methods UV-Vis-DRS and XAFS was used to elucidate the structure of hydrated and dehydrated V_xO_y/SBA-15. Both methods provide information about the electronic and geometric structure, and they are particularly suitable to study supported catalysts under reaction conditions.

UV-Vis-DR spectroscopy allows the investigation of electronic transitions of valence electrons. From the nature of the observed transitions (CT, intervalence, d-d) information about the oxidation state and the geometric configuration can be derived [95,125]. An example of how UV-Vis-DRS can be used to identify the oxidation states of supported transition metal oxides like, for instance, Cr_xO_y/SiO_2 is given by Weckhuysen *et al.* [126]. For the vanadium oxide on SiO_2 model system investigated here the vanadium oxidation state of V^{5+} can be distinguished from the lower vanadium oxidation states (V^{3+},V^{4+}) by UV-Vis-DRS. Furthermore, in the last decade a simple approach for deriving information about the geometric structure and the degree of polymerization of transition metal oxides (d^0 configuration) from UV-Vis-DR spectra was described by several authors [100,127]. They observed that the edge energy E_g of d^0 metal oxides is influenced by the coordination of the metal oxide structure and the degree of polymerization. Wachs *et al.* correlated the number of covalent M-O-M bonds around the central transition metal cation (d^0: V, Mo, W) with the position of the UV-Vis edge energy E_g [100,128,129]. A

linear correlation was observed that allowed distinguishing MO_5/MO_6 polymers from MO_4 polymers and isolated MO_4 metal oxide structures. From this kind of plot Wachs *et al.* [100] concluded that V_xO_y is present as an isolated [VO_4] tetrahedron in the dehydrated state of VO_x on the silica support.

Comparable to UV-Vis-DRS it is possible to derive information about the local geometric and electronic structure from XAFS. The average valence, for instance, can be obtained by comparison with known reference compounds [130]. Moreover, Wong *et al.* and Chaurand *et al.* [94,131] described how the V pre-edge peak in the XANES region can be used for deriving information about coordination and valence of the vanadium oxide species.

Elucidating the geometric structure in more detail from XAFS, however, is often difficult. In the conventional approach theoretical XAFS scattering amplitudes and phases are calculated for a suitable model structure. Subsequently, a sum of theoretical XAFS functions is refined to the experimental data. Structural parameters like coordination numbers, nearest neighbor distances, and disorder parameters may be determined. However, more often than not, the number of potential parameters exceeds the number of "independent" parameters. The upper limit may be calculated from Fourier theory and must not be exceeded. Nonetheless, it appears that even refinements employing a much smaller number of freely varied parameters may yield ambiguous structural results. The often used Nyquist criteria may not be sufficient to evaluate a fitting procedure. Basically, one pair of strongly correlated parameters suffices to render a seemingly good agreement between experimental data and theoretical model structure meaningless. While this case may be clearly indicated by the correlation matrix of the refinement, other pitfalls may be less obvious. Hence, procedures are sought that enable evaluating the significance of each fit parameter individually.

This chapter focuses on elucidating the local structure around the vanadium centers in the hydrated and dehydrated state of V_xO_y/SBA-15 model catalysts with different vanadium loadings. The UV-Vis-DR and XANES spectra of the V_xO_y/SBA-15 model catalysts and suitable vanadium oxide references were investigated. In addition, a detailed XAFS data analysis, in particular of higher V-V distances, was performed together with a detailed evaluation of the significance of the fit parameters employed.

5.2 Results and discussion

5.2.1 UV-Vis-DR spectra of V_xO_y/SBA-15 compared to those of V^{5+} references

In a first approach the UV-Vis-DR spectra of V_xO_y/SBA-15 were compared to the spectra of selected vanadium oxide references (***Figure 5-1***). All spectra shown were measured in the *in situ* cell. Apparently, both hydrated and dehydrated V_xO_y/SBA-15 exhibited only LMCT charge transfer bands, which are located at wavelengths shorter than 500 nm. Absorption bands which are due to lower vanadium valences (V^{4+}, V^{3+}), such as d-d or intervalence transitions, were absent. Hence, the average valence of V_xO_y/SBA-15 is assumed to be +5.

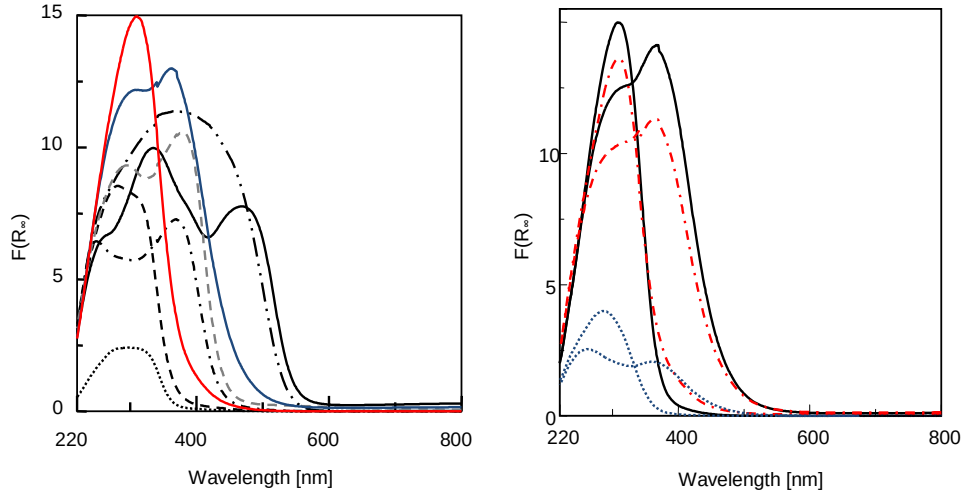

Figure 5-1 Left: UV-Vis-DR spectra of vanadium reference compounds ($Mg_3V_2O_8$ (.....), m-$Mg_2V_2O_7$ (- - -), t-$Mg_2V_2O_7$ (- - -), MgV_2O_6 (— · —), $Mg_3V_{10}O_{28}{\cdot}xH_2O$ (— · · —), V_2O_5 (——)) and 7.7 wt% V_xO_y/SBA-15 in the hydrated (——) and dehydrated (——) state. Right: UV-Vis-DR spectra of V_xO_y/SBA-15 with different loading in the hydrated and dehydrated state (1.4 wt% (.....), 4.1 wt% (— · —), 7.7 wt% (——)).

In ***Table 5-1*** the positions of observed absorption bands for V^{5+} vanadium oxide compounds measured in a standard integration sphere are listed. The values in brackets refer to the positions obtained in the *in situ* cell. The error for each absorption band position was estimated to be ± 5- 10 nm. Compared to the spectra measured in the standard cell the spectra recorded in the *in situ* cell were less well resolved. The positions of absorption bands at wavelengths longer than 270 nm were similar for both measurement cells. However, for wavelengths shorter than 260 nm the positions of the absorption bands were shifted to longer wavelengths in the *in situ* cell. This may be caused by the significantly lower intensity of the incident light below 260 nm (***Figure 10-1*** and ***Figure 10-2, Appendix***). Therefore, the insufficient resolution in the *in situ* cell has to be considered if the absorption band position in this region is compared to that of V_xO_y/SBA-15 samples. Dilution of the samples did not significantly change position and type of the absorption bands (***Table 5-2***). The position of the low energy charge transfer band in the UV-Vis-DR spectra of hydrated V_xO_y/SBA-15 was located around 365 nm for all loadings (***Figure 5-1, right, Table 5-2***).

Table 5-1: Absorption band position and UV-Vis edge energy determined from UV-Vis-DR spectra of vanadium oxide reference compounds (***Figure 5-1, left***) together with the assumed covalent V-O-V bond (CVB) number (reference of the theoretical structure which matched the experimental XRD powder pattern, ***Table 10-3***, ***appendix***). Values in brackets refer to measurements in *in situ* cell.

Sample	Absorption Band [nm]	E_g [eV]	CVB No.
Na_3VO_4	230, 255, 290	3.91	0
K_3VO_4	272, 313	3.54	0
$Ca_3V_2O_8$	225, 250, 297	3.77	0
$Mg_3V_2O_8$	271, 336 (280-320 plateau)	3.44 (3.51)	0
m-$Mg_2V_2O_7$	273, 315 (276, 311)	3.47 (3.53)	1
$Ca_2V_2O_7$	261, 326	3.14	2
t-$Mg_2V_2O_7$	285, 385 (293, 382)	2.85 (2.94)	> 1
$NaVO_3$	225, 281, 347	3.14	2
NH_4VO_3	225, 284, 357	3.17	2
KVO_3	248, 295, 371	3.11	2
CaV_2O_6	250, 272, 344	2.90	3
MgV_2O_6	240, 376 (248, 370)	2.90 (2.97)	3
$Mg_3V_{10}O_{28}\cdot xH_2O$	250, broad ~ 400 nm (broad ~ 400 nm)	2.35	5
$(NH_4)_6V_{10}O_{28}\cdot xH_2O$	240, 370, 440 (broad ~ 400 nm)	2.35	5
V_2O_5	241, 334, 390, 460 (264, 334, 390h, 468)	2.35	5

A second absorption band located at ~ 300 nm for the 7.7 V_xO_y/SBA-15 sample was blue shifted with decreasing V density (~ 293 nm 4.1wt% V, 260 nm 1.4 wt% V). A weak shoulder at 460 nm may be present (***Figure 5-1, right***). Similar bands were found for references with square pyramidal coordination (pseudo octahedral) such as V_2O_5 and MgV_2O_6 (***Table 5-1***). An interpretation of the observed bands was given by Centi *et al.* [132]. They reported that the charge transfer band due to the V=O double bond is observed at ~ 380 nm. It can be calculated from the differences in electronegativity between the metal and the ligand for an octahedral coordination of vanadium oxo compounds [133]. However, this does not explain the band at 460 nm. According to Centi this charge transfer band is due to "delocalized donor acceptor sites" originating from higher "conjugated sites like octahedral VO_6 chains" [132]. The absorption band at 460 nm in the spectra of hydrated V_xO_y/SBA-15 was rather weak. Thus, the structure of hydrated V_xO_y/SBA-15 seems to have a square pyramidal coordination, but, in contrast to V_2O_5, it seems to be less extended.

During thermal treatment of hydrated V_xO_y/SBA-15 in oxygen (20% O_2 in He, 554-626 K) a loss of water and a distinct change in structure were observed ***(Figure 5-1, Table 5-2***). For dehydrated 7.7 wt% V_xO_y/SBA-15 the low energy LMCT band is located at ~ 309 nm and was blue shifted with decreasing loading of V (~ 285 nm, 1.4 wt% V on SiO_2). The bands of undiluted crystalline vanadate references with tetrahedral coordination are located in these regions, for instance Na_3VO_4, NH_4VO_3, m-$Mg_2V_2O_7$, and $Mg_3V_2O_8$ (***Table 5-1***). Referring to Centi *et al.* [132] the charge transfer bands of tetrahedral vanadium oxo compounds are located below 333 nm. Therefore, a tetrahedral structure of dehydrated V_xO_y/SBA-15 is assumed. A more distinct determination of the degree of polymerization of the tetrahedral vanadium oxide species seemed not feasible from comparing only the absorption band positions of the V_xO_y/SBA-15 samples with those of the references. The interpretation of the charge transfer bands of solid compounds remains challenging. The interpretation by Centi *et al.* [132] considers the vanadium oxide as solely molecular a cluster similar to the common interpretation of molecular coordination complexes.

Table 5-2: Absorption band position and UV-Vis edge energy determined from the UV-Vis-DR spectra of hydrated and dehydrated V_xO_y/SBA-15 samples (***Figure 5-1, right***) together with the calculated covalent V-O-V bond (CVB) number. Values in brackets refer to diluted samples ($F(R_\infty)_{max}$~ 1-2).

Sample	Absorption Band [nm]	E_g [eV]	CVB No.
7.7 wt% V hydrated	300, 368 (300, 368)	2.76 (2.74)	3.5
4.1 wt% V hydrated	293, 364 (283, 363)	2.80 (2.79)	3.4
1.4 wt% V hydrated	260, 365 (260, 368)	2.88 (2.80)	3.0
7.7 wt% V dehydrated	309 (302)	3.43 (3.37)	1.0
4.1 wt% V dehydrated	309 (305)	3.42 (3.44)	1.0
1.4 wt% V dehydrated	286 (280)	3.59 (3.60)	0.4

Moreover, if this interpretation was sufficient to describe the LMCT absorption bands even though more than a single transition would occur for an isolated free VO_4^{3-} ion [134]. Calculations may provide more detailed information about the type and intensity of the absorption bands that can be expected. For V_2O_5 monocrystals Lazukova *et al.* received a good agreement between the experimental and the theoretically calculated electroreflectivity spectra [135]. Ronde *et al.* [134] calculated the position of the charge transfer band for isolated tetrahedral compounds. The range obtained (240-330 nm) agrees well with the values of tetrahedral vanadate references found here. However, these results do not allow us to distinguish unambiguously between different connectivities of tetrahedral vanadium oxide compounds such as isolated, dimeric or chain-like structures. One attempt to distinguish different arrangements of supported vandium oxide clusters was reported by Avdeev *et al.* [136]. They concluded that for isolated [VO_4] structures on SiO_2 two absorption bands at 238 and 263 nm are present. These bands are red shifted to 250-260 nm and 270-290 nm if dimeric tetrahedral compounds are present (V-O-V linkage). These results match with the absorption bands of dehydrated V_xO_x/SBA-15 with the maximum at 286 and 309 nm found here (***Table 5-2***). Therefore, for all loadings a dimeric tetrahedral structure is present. Avdeev *et al.* [136] attributed an increase in coordination from 4-fold to 5-fold to absorption bands located at 340 nm in the spectra of hydrated V_xO_y/SiO_2 samples (here 365 nm, ***Table 5-2***). Identifying the contributions of these transitions in the experimental UV-Vis-DR spectra would provide more detailed information. However, considering the broad absorption bands and the insufficient resolution in the UV range (*in situ* cell) a reasonable refinement seems not very likely and thus was not performed here.

5.2.2 Correlation of the UV-Vis-DRS edge energy E_g with the local structure of vanadium oxide references

To gain more insight into the nature of the dispersed vanadium oxide species present on the support, the UV-Vis edge energy E_g of the LMCT band was correlated with the number of V-O-V bonds in the measured crystalline vanadium oxide references as reported by Wachs *et al.* [100]. The E_g values obtained are summarized in ***Table 5-1*** and the resulting plot is depicted in ***Figure 5-2 (left)***. For clarity, all references were measured undiluted in the integration sphere cell. Samples measured in the *in situ* Praying Mantis™ cell, as shown in ***Figure 5-2 (left),*** are depicted as grey symbols. The linear correlation of the V-O-V bond number (CVB) with E_g was almost linear (grey line). The t-$Mg_2V_2O_7$ reference was not considered in this correlation. As discussed in ***Chapter 2.3.6***, the connectivity of $[V_2O_7]_x$ polyhedrons

may be higher than that of dimers and thus the V-O-V number is larger than one. The linear function obtained here was

$$CVB = 13.74 - 3.72 \cdot E_g \ (\pm 5\%, R^2=0.98). \quad (5.1)$$

Deviations from the equation found by Wachs *et al.* (CVB = 14.03 – 3.95·E_g (± 0.34)) [100] can be explained by the larger number of reference compounds used here. A second reason was that all samples were measured undiluted here. Compounds like Na_3VO_4 or K_3VO_4 tend to dehydrate when they are diluted, which causes significantly lower values for E_g (~ 0.5 eV) as observed by Wachs *et al.* [100]. Dilution of all other samples with the white reflectance standard caused a shift of E_g in the range of ± 0.01-0.08 eV.

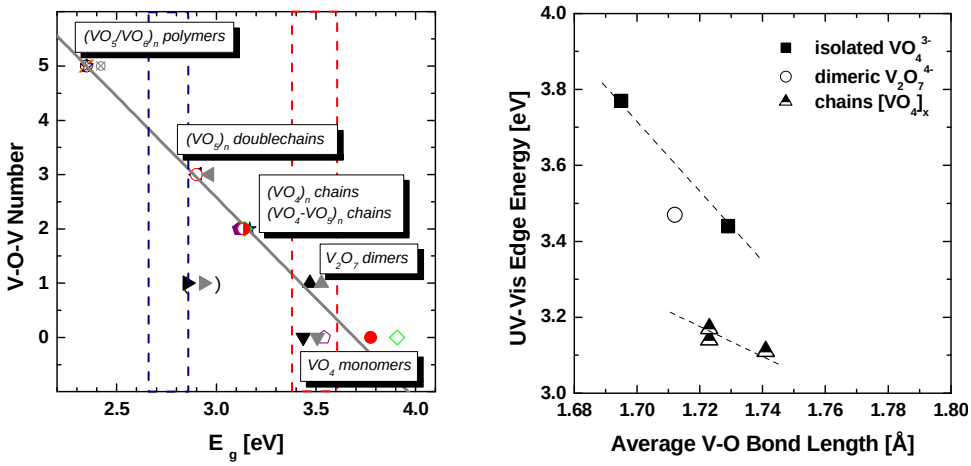

Figure 5-2 Left: Covalent V-O-V bond number (CVB) versus UV-Vis edge energy (E_g) of vanadium oxide reference compounds (Na_3VO_4 (◇), K_3VO_4 (⬠), $Ca_3V_2O_8$ (●), $Mg_3V_2O_8$ (▼), m-$Mg_2V_2O_7$ (▲), $Ca_2V_2O_7$ (◑), t-$Mg_2V_2O_7$ (▶), $NaVO_3$ (♦), NH_4VO_3 (★), KVO_3 (⬟), CaV_2O_6 (○), MgV_2O_6 (◀), $Mg_3V_{10}O_{28}\cdot xH_2O$ (⊠), $(NH_4)_6V_{10}O_{28}\cdot xH_2O$ (☆), V_2O_5 (✳), grey symbols refer to measurements in *in situ* cell), right: UV-Vis edge energy versus average V-O bond length in the first coordination sphere of vanadium references exhibiting a tetrahedral coordination.

The linear correlation (***Figure 5-2, left)*** can be explained according to Weber *et al.* [127]. They concluded, in a simplified, assumption that "the edge energies of moleculary sized clusters should track with the extent of spatial delocalization of the molecular orbitals involved in the electronic transition associated with the UV-visible edge" [127]. Hence, the energy needed for an electronic transition is lowered with increasing number of participating molecular orbitals. Accordingly, the determination of the UV-Vis edge energy allowed an estimation of the size of the vanadium oxide clusters present in the V_xO_y/SBA-15 samples. Relatively high errors (± 5%) were obtained for this linear correlation. These are mainly due to the wide range of E_g values determined for isolated tetrahedral compounds (CVB = 1). Similar spreading of E_g with decreasing CVB number was observed by Wachs *et al.* for W and Mo based d^0 transition metal oxide systems [128,129]. They concluded that not only the CVB number influences the E_g position but also the distortion of the coordination polyhedron [128]. The effect of the distortion of the coordination polyhedron seems to be stronger for less polymerized vanadium oxide structures. This effect cannot be explained by the delocalization of molecular orbitals. It seems more likely that the average V-O bond length in the first coordination sphere, as indicator for the distortion, influences the energy of the

LMCT transitions. A similar trend was proposed by Ronde *et al.* for the absorption band maxima [134]. ***Figure 5-2, right*** shows the edge energy versus the average V-O bond length for several vanadates exhibiting tetrahedral coordination. A decrease of E_g with increasing distortion (average R_{V-O}) was obtained. Moreover, the slope of the linear correlation decreased with increasing V-O-V number from orthovanadate to metavanadate structures. For higher coordinated structures exhibiting a V-O-V number of 3 or 5 no comparable correlation was found. Hence, only the effect of delocalization determines the electronic structure of higher polymerized vanadium centers. Conversely, in lower coordinated tetrahedral compounds the electronic structure of the vanadium centers is rather described with molecular orbitals, which are present in molecular coordination complexes. Moreover, it is possible that the electronic structure of the absorbing vanadium centers is more sensitive towards disturbances of the surrounding cations than the electronic structure of the vanadium centers in the higher clustered vanadium oxide anions like $V_2O_6^{2-}$ or $V_{10}O_{28}^{6-}$. A more detailed explanation was not possible because of the limited data set of isolated and dimeric tetrahedral vanadium oxide references or missing calculations of the electronic structure of model compounds. However, as a result of these contributions (delocalization and distortion) to the electronic structure of vanadium oxides in tetrahedral coordination, an unambiguous discrimination between dimeric and isolated structures is hardly feasible.

5.2.3 UV-Vis E_g- indicator for the local structure of hydrated and dehydrated V_xO_y/SBA-15

Accordingly, the linear correlation of the V-O-V number and the UV-Vis edge energy was used only as an indicator for the structure of the V_xO_y/SBA-15 structures. In ***Table 5-2*** the values obtained for hydrated and dehydrated V_xO_y/SBA-15 are listed for all loadings employed. The values in brackets refer to diluted samples. No distinct changes were observed with dilution. Hence, undiluted samples were used for further reaction experiments as described in the following chapters. For the hydrated V_xO_y/SBA-15 samples UV-Vis edge energies from 2.76 to 2.88 eV were obtained, which increased with higher dispersion of vanadium oxide on the SBA-15 support. The CVB numbers were determined to be between 3.0 and 3.5. These values supported the observation above that hydrated V_xO_y/SBA-15 exhibits a square pyramidal coordination. For dehydrated V_xO_y/SBA-15 V-O-V numbers of 1.0 were obtained for the 4.1 wt% and the 7.7 wt% V on V_xO_y/SBA-15 sample which confirmed the dimeric tetrahedral structure that was indicated by the position of the absorption bands. The low loaded 1.4 wt% V_xO_y/SBA-15 sample exhibited a reduced V-O-V number of 0.3 which suugests an isolated [VO_4] structure. According to Weber *et al.* [127] the value of 0.3 may also indicate a mixture of isolated and dimeric structures on the support. Similar results were recently observed for low loaded Mo_xO_y on SBA-15 samples [137].

The absorption band positions and UV-Vis-DRS edge energies detected here were comparable to those reported by other authors for vanadium oxides supported on SiO_2 in a monolayer coverage [23,100]. However, mostly an isolated structure was assumed for low loaded dehydrated V_xO_y/SBA-15, which is in contrast to the dimeric structures discussed here. Therefore, a detailed XAFS analysis was performed on hydrated and dehydrated V_xO_y/SBA-15 to obtain additional information about the local structure around the V atoms.

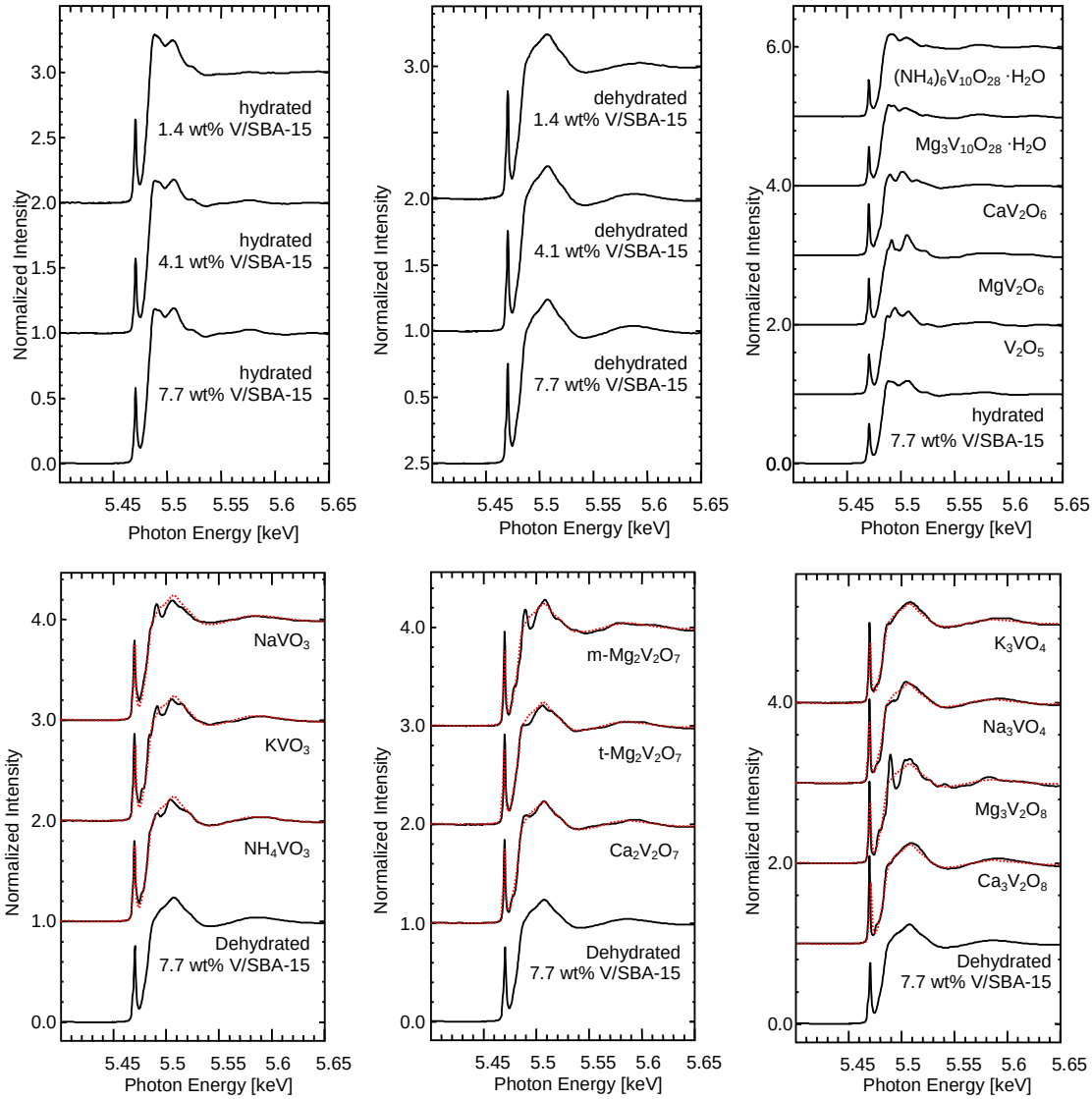

Figure 5-3: V K edge XANES spectra of hydrated and dehydrated V_xO_y/SBA-15 samples with different vanadium loadings (1.4 wt%, 4.1 wt%, and 7.7 wt%). V K edge compared to the spectra of various V^{5+} reference compounds (dotted line refers to 7.7 wt% dehydrated V_xO_y/SBA-15).

5.2.4 XANES analysis – coordination and distortion of V species in V_xO_y/SBA-15

The XANES spectra of hydrated V_xO_y/SBA-15 are depicted in ***Figure 5-3 (top left)***. The spectra resembled those of vanadium oxide references where the vanadium centers exhibit a distorted octahedral or distorted square pyramidal coordination (***Figure 5-3, top right***). The XANES spectra of hydrated V_xO_y/SBA-15, V_2O_5, MgV_2O_6, CaV_2O_6, $(NH_4)_6V_{10}O_{28}{\cdot}xH_2O$, and $Mg_3V_{10}O_{28}{\cdot}xH_2O$ all had a pre-edge peak of similar height. Because the pre-edge peak height is determined by the coordination of the vanadium centers, as discussed in more detail below, hydrated V_xO_y/SBA-15 also appeared to exhibit a distorted square pyramidal coordination of the V centers. During thermal treatment of as-prepared hydrated V_xO_y/SBA-15 in oxygen (20% O_2 in He) a loss of water and a distinct change in structure were observed (discussed in ***Chapter 6***). After thermal treatment dehydrated V_xO_y/SBA-15 was cooled to 293 K (20% O_2 in He) without exposure to air or water (***Figure 5-3 top middle***). No changes in the XAFS

spectra were observed during cooling. Compared to the vanadium oxide references, the overall XANES region of dehydrated V_xO_y/SBA-15 resembled those of metavanadate references like NH_4VO_3, KVO_3, and Na_3VO_4 and distorted pyrovanadate references like t-$Mg_2V_2O_7$ and $Ca_2V_2O_7$ (***Figure 5-3 bottom***). In the local structure of these references the vanadium centers are tetrahedrally coordinated by four oxygen atoms. Compared to the XANES spectrum of dehydrated V_xO_y/SBA-15, NH_4VO_3, KVO_3, and $NaVO_3$ exhibit very similar pre-edge peak heights in their XANES spectra. Conversely, the pre-edge peaks in the XANES of $Ca_3V_2O_8$, K_3VO_4, Na_3VO_4, and $Mg_3V_2O_8$ are much higher than that of dehydrated V_xO_y/SBA-15 (***Figure 5-3, bottom right***).

More detailed correlations of the position and height of the pre-edge peak with the average valence and coordination of the vanadium center were described by Wong *et al.* [131] and Chaurand *et al.* [94]. Here, a method referring to a report by Wong *et al.* was chosen to investigate the coordination of the absorbing vanadium centers in the V_xO_y/SBA-15 samples. Wong *et al.* [131] showed that a plot of the intensity of the pre-edge peak feature versus a "molecular cage-size parameter" such as the average V-O bond length results in a linear correlation. With increasing distortion in the same coordination and with increasing coordination number (tetrahedral to octahedral) a decrease of the intensity was observed. Thus, an identification of different coordinations of the absorbing vanadium center is possible. In contrast to Wong *et al.* the intensity of the pre-edge peak was not determined by the product of its height and its width at half height. Due to the asymmetry of the observed pre-edge peaks the area was determined by a method described by Chaurand *et al.* [94]. For the analysis the energy range around the pre-edge peak was extracted from the normalized spectra. The increase of the absorption edge was eliminated by using an empirical background as shown in ***Figure 5-4 (right)***. The resulting background corrected signal was fitted using three pseudo Voigt functions. The resulting product of the area and the pre-edge peak height at peak maximum (PHA) was plotted versus the average bond length ($R_{V\text{-}O}$) of the measured reference compounds (structure confirmed by XRD refinement, ***Table 10-3***, ***appendix***). As shown in ***Figure 5-4 (left)*** a linear correlation was obtained. The different coordinations (4,5,6-fold) are separated by a shift of the average $R_{V\text{-}O}$ of 0.08-0.10 Å. The signals of tetrahedral references range from 1.70 -1.74 Å, those of distorted square pyramidal references from 1.82-1.83 Å and that of octahedral references are found at 1.92 Å. Interestingly, the $Ca_2V_2O_7$ sample, which consists of a mixture of distorted square pyramidal and tetrahedral VO_x units (average coordination number 4.67), fits very well in the linear correlation. Compared to the UV-Vis edge energy, no influence of the delocalization of the orbitals involved was found. In contrast to the UV-Vis edge energy, it is possible to identify the coordination of the vanadium centers in the oxide cluster. Moreover, information about the degree of distortion around the absorbing vanadium center can be derived.

Compared to references, the coordination of the vanadium centers in hydrated V_xO_y/SBA-15 may be distorted square pyramidal similar to compounds such as V_2O_5 and MgV_2O_6. This has also been observed by Bell *et al.* [108]. Dehydrated V_xO_y/SBA-15 seemed to exhibit a coordination and distortion more similar to references like NH_4VO_3 and KVO_3.

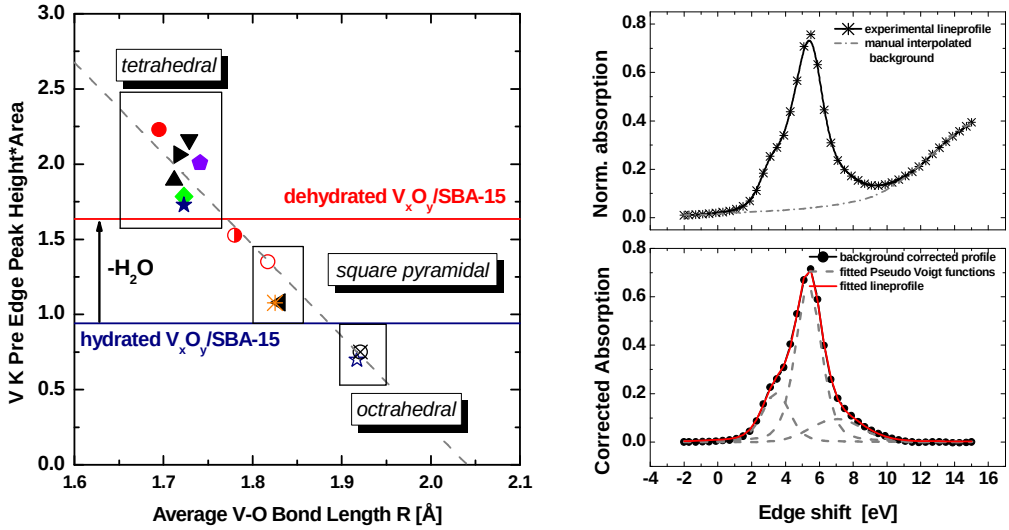

Figure 5-4 Left: Correlation of the product of the V K edge pre-edge peak intensity and area versus average V-O bond length R in the first coordination sphere ($Ca_3V_2O_8$ (●), $Mg_3V_2O_8$ (▼), m-$Mg_2V_2O_7$ (▲), $Ca_2V_2O_7$ (◑), t-$Mg_2V_2O_7$ (►), $NaVO_3$ (♦), NH_4VO_3 (★), KVO_3 (⬟), CaV_2O_6 (○), MgV_2O_6 (◄), $Mg_3V_{10}O_{28}{\cdot}xH_2O$ (⊗), $(NH_4)_6V_{10}O_{28}{\cdot}xH_2O$ (☆), V_2O_5 (✳)), right: subtraction of the background from V K edge pre-edge peak of 7.7 wt% V_xO_y/SBA-15 (top) and an example of the peak fit to the background corrected signal (bottom). The pre-edge peak heights for V_xO_y/SBA-15 are indicated as lines. (Refer to text and ***Table 10-4*** for details).

The average V-O bond length around the absorbing vanadium centers was estimated by using the linear correlation:

$$PHA = 13.28 - 6.58 \cdot R_{V\text{-}O} \ (\pm\ 7\text{-}9\%,\ R^2=0.96). \qquad (5.2)$$

For the hydrated V_xO_y/SBA-15 samples $R_{V\text{-}O}$ was 1.88 Å and for dehydrated V_xO_y/SBA-15 $R_{V\text{-}O}$ was 1.77 Å. The latter value suggests the presence of a strongly distorted VO_x tetrahedron in the vanadium oxide structure of dehydrated V_xO_y/SBA-15. Both $R_{V\text{-}O}$ values were increased compared to the bulk vanadium oxide references. This may be an influence of the high dispersion of the supported vanadium oxide, which may cause a higher distortion.

5.2.5 Local structure of dehydrated V_xO_y/SBA-15 – Comparison to V oxide references

In addition to the UV-Vis-DRS experiments and the investigations of the XANES structure a detailed EXAFS investigation of samples with different V loadings in the hydrated and dehydrated state was performed. In particular, the contribution of higher scattering shells to the XAFS signal was analyzed to possibly reveal the presence of V nearest neighbors in the local structure of vanadium oxide species supported on SiO_2. In the corresponding literature only a few authors present XAFS refinements of supported vanadium oxide samples [21,22,37,114,120-122, 124]. Typically the first V-O coordination sphere was analyzed by XAFS refinement [22,94]. A detailed XAFS analysis of higher shells in the FT(χ(k)*k^3) has been largely neglected. Only Keller *et al.* [37,114,120-122,124] discussed contributions of higher V-O and V-Si shells located at distances > 2 Å. They excluded higher V-O-V contributions to the FT(χ(k)*k^3) of highly dispersed dehydrated V_xO_y samples supported on SiO_2 or Al_2O_3.

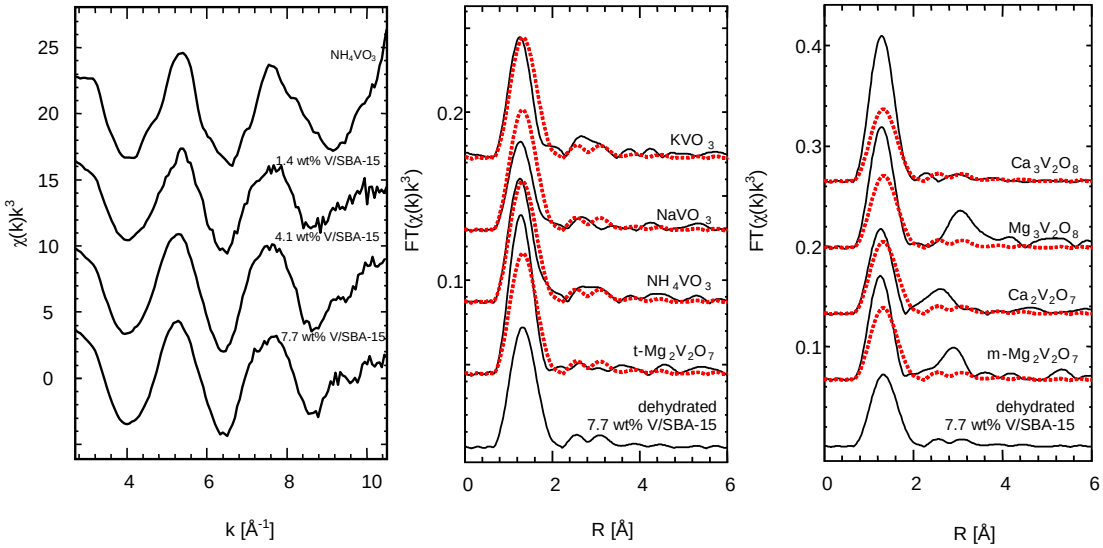

Figure 5-5 left: V K edge χ(k) of dehydrated V_xO_y/SBA-15 with different vanadium loadings (1.4 wt%, 4.1 wt %, and 7.7wt %) and NH_4VO_3. middle, right: V K edge FT(χ(k)*k^3) of dehydrated V_xO_y/SBA-15 (7.7 wt %, dotted) compared to those of various references.

The EXAFS χ(k)*k^3 of dehydrated V_xO_y/SBA-15 with different V loadings are depicted in ***Figure 5-5 (left)***. The usable range extended from 2.7 to 10.5 $Å^{-1}$. The V K edge FT(χ(k)*k^3) of the dehydrated V_xO_y/SBA-15 sample (7.7 wt%) measured at 293 K are shown in ***Figure 5-5***. FT(χ(k)*k^3) and χ(k)*k^3 are not phase shift corrected. Thus, the distances in the FT(χ(k)*k^3) are shifted to lower values by ~ 0.4 Å compared to crystallographic distances.

The FT(χ(k)*k^3) of various vanadium oxide references exhibiting a tetrahedral coordination are compared to that of dehydrated V_xO_y/SBA-15 (***Figure 5-5, middle and right)***. In contrast to the XANES spectra the FT(χ(k)*k^3) of Na_3VO_4 and K_3VO_4 are not shown. The high tendency for dehydration of these compounds caused a high level of noise in the resulting χ(k)*k^3. The first V-O peak in the FT(χ(k)*k^3) at ~ 1.4 Å (not phase shift corrected) for all references shown corresponds to a [VO_4] tetrahedron in the respective structures. The spectra of the metavanadate structures like NH_4VO_3 and KVO_3 resembled that of dehydrated V_xO_y/SBA-15 most closely. In the FT(χ(k)*k^3) of the pyrovanadate structures like $Mg_2V_2O_7$ and $Ca_2V_2O_7$ and the orthovanadate structures like $Ca_3V_2O_8$ and $Mg_3V_2O_8$ the first V-O peak is significantly higher than in the FT(χ(k)*k^3) of dehydrated V_xO_y/SBA-15. In contrast to the FT(χ(k)*k^3) of $Mg_3V_2O_8$ and the pyrovanadates, $Ca_2V_2O_7$ and monoclinic $Mg_2V_2O_7$, which exhibit a significant amplitude at distances above 2 Å, the FT(χ(k)*k^3) of $Ca_3V_2O_8$, KVO_3, NH_4VO_3, triclinic $Mg_2V_2O_7$, and dehydrated V_xO_y/SBA-15 show little amplitude at higher distances. Moreover, looking at the differences between the FT(χ(k)*k^3) of $Ca_3V_2O_8$, KVO_3, NH_4VO_3, and triclinic $Mg_2V_2O_7$, the latter two appear to yield the best agreement with that of dehydrated V_xO_y/SBA-15. In all references the low amplitude of the FT(χ(k)*k^3) at R > 2 Å is characteristic of the local structure around the tetrahedral V centers. In conclusion, based on comparing the XANES and FT(χ(k)*k^3) of dehydrated V_xO_y/SBA-15 to those of potential references, NH_4VO_3 and triclinic $Mg_2V_2O_7$ have been identified as suitable references to serve as model systems for a more detailed structural analysis.

5.2.6 *Local structure of higher connected tetrahedral vanadium oxide cluster - XAFS refinement of a reference based model structure*

Before we discuss the details of analyzing the XAFS data of dehydrated V_xO_y/SBA-15, a suitable analysis procedure for the higher V-V contributions in the XAFS spectra of the references NH_4VO_3 and triclinic $Mg_2V_2O_7$ was sought. As an example, and to reduce the number of tables here, the application of confidence limits and F parameter to distinguish analysis fitting procedures is described below for three refinements of a suitable model structure to the experimental FT(χ(k)*k^3) of dehydrated V_xO_y/SBA-15.

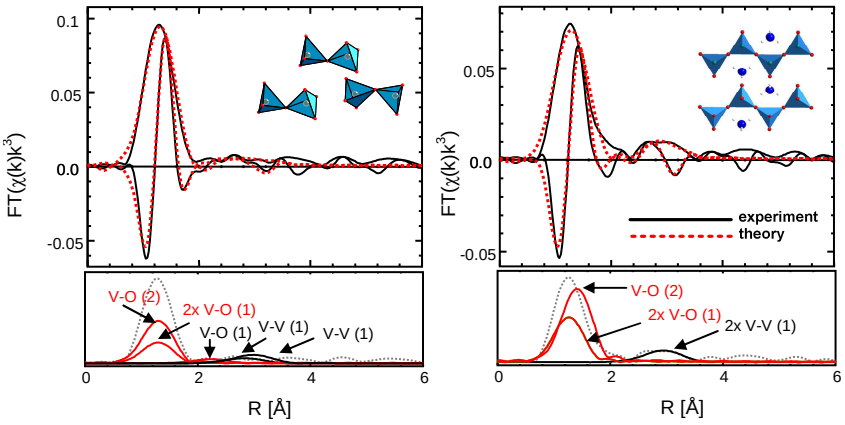

Figure 5-6: Experimental (solid) V K edge FT(χ(k)*k^3) of the NH_4VO_3 (right) and the $Mg_2V_2O_7$ (left) reference together with a theoretical XAFS function (fitting results are given in ***Table 5-3***). Also shown are the Fourier transformed χ(k)*k^3 of the individual scattering paths together with the corresponding coordination number in brackets.

The model structure consisted of a tetrahedral coordination of the V center with four oxygen atoms at ~1.7 Å (NH_4VO_3), two vanadium atoms at ~3.4 Å (NH_4VO_3) and 3.6 Å (triclinic $Mg_2V_2O_7$), one oxygen atom at ~2.9 Å (triclinic $Mg_2V_2O_7$), and one Si atom at ~2.8 Å (***Table 5-3***). Experimental FT(χ(k)*k^3) of triclinic $Mg_2V_2O_7$ and NH_4VO_3 and the corresponding XAFS refinements are shown in ***Figure 5-6***. Deviations between the theoretical and experimental spectra of triclinic $Mg_2V_2O_7$ in the range from 2-4 Å are caused by several Mg neighbors and nearly linear multiple-scattering paths in triclinic $Mg_2V_2O_7$ that contribute in this range. These are not sufficiently accounted for by the simplified refinement procedure used here. Similar arguments hold for NH_4VO_3. The results of the XAFS refinement for dehydrated V_xO_y/SBA-15, NH_4VO_3, and triclinic $Mg_2V_2O_7$ are summarized in ***Table 5-3***. Apparently, the distorted [VO_4] tetrahedron in NH_4VO_3 required two different V-O distances to be included in the refinement, while triclinic $Mg_2V_2O_7$ and dehydrated V_xO_y/SBA-15 exhibited a single V-O distance. It seems that the distortion in the [VO_4] units of the crystalline reference triclinic $Mg_2V_2O_7$ could not be resolved by the XAFS analysis procedure employed. Accordingly, a lower σ^2 was obtained (0.0013 $Å^2$) for NH_4VO_3 compared to those of dehydrated V_xO_y/SBA-15 and triclinic $Mg_2V_2O_7$ (0.0079 $Å^2$ and 0.0058 $Å^2$, respectively). In contrast, a single V-V distance at 3.47 Å (CN = 2) sufficed for NH_4VO_3 (consisting of chains of [VO_4] units), while two V-V distances had to be included for triclinic $Mg_2V_2O_7$ (consisting of adjacent [V_2O_7] units) and dehydrated V_xO_y/SBA-15.

Table 5-3: Type and number (N) of atoms at distance R from the absorbing V atom in a model system assuming an ordered arrangement of V_2O_7 units (***Figure 5-9, right***) compared to experimental distances and XAFS disorder parameters (σ^2). The parameters were obtained from the refinement of this model structure to the experimental V K edge XAFS FT(χ(k)*k^3) of dehydrated V_xO_y/SBA-15 (7.7 wt%), t-$Mg_2V_2O_7$, and NH_4VO_3 (k range from 2.7-10.5 $Å^{-1}$, R range 0.84-3.62 Å, N_{ind} = 16, E_0 = 0 eV in all cases, fit residual 3.9 (dehydrated V_xO_y/SBA-15) (N_{free} = 8), 10.7 (t-$Mg_2V_2O_7$) (N_{free} = 7), 14.7 (NH_4VO_3) (N_{free} = 5)) (subscript c indicates parameters that were correlated in the refinement, subscript f indicates parameters that were fixed in the refinement). Confidence limits and significance to the fit parameters are given in ***Table 5-4***.

Type	N	R_{model} [Å]	deh. 7.7 wt%		t-$Mg_2V_2O_7$		NH_4VO_3	
			R [Å]	σ^2 [$Å^2$]	R [Å]	σ^2 [$Å^2$]	R [Å]	σ^2 [$Å^2$]
V - O	1	1.63	1.78	0.0079	1.74	0.0058	1.69	0.0013
V - O	1	1.70	1.78 $_c$	0.0079 $_c$	1.74 $_c$	0.0058 $_c$	1.69	0.0013 $_c$
V - O	2	1.76	1.78 $_c$	0.0079 $_c$	1.74 $_c$	0.0058 $_c$	1.84	0.0013 $_c$
V - O	1	2.87	2.89	0.0012 $_f$	2.77	0.0113	--	--
V - V	1	3.42	3.29	0.0116	3.33	0.0148	3.47	0.0143
V - V	1	3.62	3.60	0.0116 $_c$	3.52	0.0148	3.47	0.0143 $_c$
V - Si	1	2.80	2.54	0.013	--	--	--	--

In the cases of the references, a similar σ^2 parameter for the V-V contributions of about 0.014 $Å^2$ was obtained. For dehydrated V_xO_y/SBA-15 it was slightly decreased (0.012 $Å^2$). The corresponding confidence limits and significance parameters F are given in ***Table 5-4***. In fitting procedure #1 two V-O distances in the first V-O shell were allowed to vary independently (both with a CN of 2 and the same σ^2). Moreover, E_0 was also allowed to vary in fitting procedure #1. Because N_{ind} = 16 and N_{free} = 11 the refinement procedure #1 would be taken as reliable according to the Nyquist criteria. However, F parameter of 0.6 and 0.9 were obtained with procedure #1 for R and σ^2 of the V-O distances. Moreover, E_0 exhibited a confidence limit of ± 0.25 and F = 0.4. Apparently, fitting procedure #1 already exceeded the number of meaningful parameters and yielded ambiguous structural parameters. On the one hand, the reduced amplitude of the FT(χ(k)*k^3) of dehydrated V_xO_y/SBA-15 compared to that of references consisting of undistorted [VO_4] units (***Figure 5-5***) suggested the presence of more than one V-O distance, including a short "vanadyl" V=O distance. On the other hand, however, the resolution in the experimental FT(χ(k)*k^3) and the available degree of freedom did not permit refining more than one V-O distance in the procedure used. Therefore, the fitting procedure was modified: E_0 was kept invariant in the refinement and only one V-O distance at ~1.75 Å was used. In contrast to procedure #1, procedure #2 yielded reasonable confidence limits and acceptable F parameters. Conversely, the σ^2 parameter of the V-Si at 2.5 Å and the V-O contribution at 2.9 Å exhibited rather high confidence limits. Apparently, both V-O and V-Si neighbors in the distance range from 2.5 Å to 2.9 Å are required for a good refinement of the model structure to the experimental data. This is indicated by the confidence limits and F parameters calculated for the corresponding distances (***Table 5-4***). Nevertheless, the high σ^2 obtained for the V-Si contribution and the rather low σ^2 obtained for the V-O at 2.9 Å indicate a certain ambiguity of the corresponding fit results.

Table 5-4: V K edge XAFS parameters (Z for distances R and disorder parameter σ^2) obtained from three different procedures of fitting a model structure (i.e. "ordered V_2O_7 dimers" on SiO_2 support) to the experimental XAFS FT(χ(k)*k^3) of dehydrated V_xO_y/SBA-15 (7.7 wt %) (details of fit given in ***Table 5-3***) together with confidence limits (± z, referring to 95 % of fit residual) and significance parameters F (details given in text).

		Procedure #1			Procedure #2			Procedure #3		
Pair	N	Z	±z	F	Z	±z	F	Z	±z	F
R(V - O)	2(4)	1.75	0.008	0.6	1.78	0.001	--	1.78	0.001	--
σ^2(V - O)	4	0.0072	0.0001	--	0.0080	0.0001	--	0.0079	0.0001	--
R(V - O)	2(--)	1.80	0.002	--	--	--	--	--	--	--
R(V - O)	1	2.89	0.01		2.89	0.01	--	2.89	0.01	--
σ^2(V - O)	1	0.0001	0.0006	0.9	0.0001	0.0008	--	0.0012_f	--	--
R(V - V)	1	3.27	0.02	--	3.28	0.02	--	3.29	0.01	--
σ^2(V - V)	1	0.0125	0.0006	--	0.0128	0.0007	--	0.0116	0.0007	--
R(V - V)	1	3.60	0.02	--	3.60	0.02	--	3.60	0.02	--
R(V - Si)	1	2.53	0.01	--	2.54	0.01	--	2.54	0.01	--
σ^2(V - Si)	1	0.0114	0.002	0.4	0.0120	0.0013	0.3	0.0130	0.0008	--
E_0		- 0.9	0.25	0.4	0_f	--	--	0_f	--	--
Residual		4.1			3.8			3.9		

The reason may be a considerable static disorder and, thus, a broadened V-Si distance distribution. Therefore, the σ^2 parameter was fixed in the final procedure #3 to a reasonable value, which was obtained empirically. This constraint yielded a more reliable confidence limit for the σ^2 parameter (± 0.0008 $Å^2$) of the V-Si contribution at 2.5 Å (***Table 5-4***). Calculating and evaluating confidence limits and F tests permitted us to arrive at a meaningful and reliable fitting procedure. Moreover, the approach employed appears to be superior to calculating only the Nyquist criteria. In total, procedures #2 and #3 worked very well for the XAFS data analysis of dehydrated V_xO_y/SBA-15 and triclinic $Mg_2V_2O_7$. In contrast, the local structure around V centers in NH_4VO_3 was best described by assuming two different V-O distances in the first coordination shell and only one V-V distance at 3.47 Å (CN = 2) (***Table 5-4***). A V-O distance at 2.8 Å was found to be insignificant.

5.2.7 Local structure of dehydrated V_xO_y/SBA-15 – XAFS refinement of "VO_4" based model structures

After having identified two suitable references as model structures for XAFS refinements to the experimental FT(χ(k)*k^3) of dehydrated V_xO_y/SBA-15 (***Figure 5-5, middle and right***), the XAFS analysis approach chosen shall be described in more detail. In addition to using confidence limits and F tests as introduced above, the suitable XAFS fitting procedure was developed stepwise as outlined in the following.

First, we started with a common assumption from the literature. UV-Vis-DRS or Raman measurements reported in the literature revealed that dehydration of V_xO_y/SBA-15 resulted in a characteristic change from a distorted square pyramidal to a distorted tetrahedral coordination [23,117,100]. The local structure of vanadium oxide species supported on SiO_2 was assumed to correspond to isolated [VO_4] units. Hence, in a first tetrahedron approach the theoretical XAFS function of a [VO_4] tetrahedron consisting of two

slightly different V-O distances was refined to the FT(χ(k)*k^3) of dehydrated V_xO_y/SBA-15 (***Figure 5-7 left***). Because of the similar height of the pre-edge peak in the XANES (***Figure 5-3 bottom left***) and the first V-O peak in the FT(χ(k)*k^3), phases and amplitudes employed in the refinement were calculated using the model structure of NH_4VO_3 (ICSD 1487 [138]). ***Figure 5-7 (left)*** shows a good agreement between theoretical and experimental FT(χ(k)*k^3) of dehydrated V_xO_y/SBA-15 for the first V-O peak below 2 Å. Naturally, the amplitude between 2 Å and 4 Å in the FT(χ(k)*k^3) could not be accounted for. Hence, a structural model assuming only isolated [VO_4] species cannot adequately describe the local structure around the V centers in dehydrated V_xO_y/SBA-15. Therefore, we assumed that higher coordination shells around the vanadium centers significantly contribute to the FT(χ(k)*k^3) of dehydrated V_xO_y /SBA-15. These shells have to be included in the refinement. A seemingly expected contribution may arise from silicon backscatterers in the SiO_2 support at distances of less than 3.0 Å. This has been proposed previously by Keller *et al.* [120]. Thus, in extension of the tetrahedron approach a silicon atom at a V-Si distance of 2.8 Å was included in the theoretical model. In the corresponding "O_3V-O-Si" unit a Si-O distance of 1.62 Å is assumed (***Figure 5-7, middle***), as it is found in various silicates. The result of the XAFS refinement of the "O_3V-O-Si" model to the FT(χ(k)*k^3) of dehydrated V_xO_y/SBA-15 is depicted in ***Figure 5-7 (middle)***. The additional Si backscatterer resulted in a better agreement between theoretical and experimental FT(χ(k)*k^3) at distances of about 2.4 Å (not phase shift corrected). The resulting V-Si distance amounted to 2.54 Å, comparable to the distance obtained by Keller *et al.* (2.61 Å [120]). However, it can be seen easily from ***Figure 5-7 (middle***) that the amplitude in the FT(χ(k)*k^3) of dehydrated V_xO_y/SBA-15 between 2.4 and 4.0 Å is still not accounted for. In addition to the V-Si contributions in the range of 2-3 Å Keller *et al.* [114] proposed the presence of V-O contributions at 2.7 Å, which are caused by the oxygen atoms of the SiO_2 support.

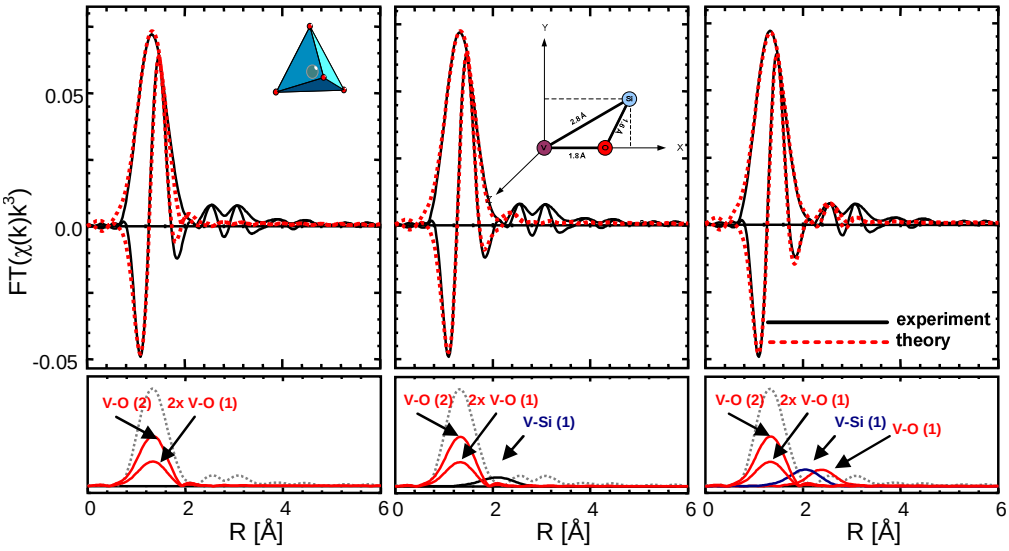

Figure 5-7: Experimental (solid) V K edge FT(χ(k)*k^3) of dehydrated V_xO_y/SBA-15 (7.7 wt%) together with theoretical XAFS functions (left: "isolated VO_4" model, middle: addition of a V-Si path to the "isolated VO_4" model, right: addition of support oxygen to "isolated VO_4" model). Insets show the [VO_4] tetrahedron (left) and a schematic representation of the V-Si path employed (middle). Also shown are the Fourier transformed χ(k)*k^3 of the individual scattering paths together with the corresponding coordination number in brackets.

Thus, to simulate this contribution a V-O distance originating from the triclinic $Mg_2V_2O_7$ [139] at 2.8 Å was added to the refinement. The result of the XAFS refinement is shown in ***Figure 5-7 (right)***. The extended refinement procedure resulted in a better agreement between the theoretical XAFS function of the model structure and the FT(χ(k)*k^3) of dehydrated V_xO_y/SBA-15. However, for distances higher than 3 Å the refinement of the FT(χ(k)*k^3) of dehydrated V_xO_y/SBA-15 was still not sufficient.

5.2.8 Local structure of dehydrated V_xO_y/SBA-15 – XAFS refinement of "V_2O_7" based model structures

Figure 5-7 shows that an "isolated VO_4" model did not properly describe the local structure between 2 Å and 4 Å around vanadium centers in dehydrated V_xO_y/SBA-15. Hence, considering the results from UV-Vis-DRS it was assumed that at least "V_2O_7 dimers" would be needed to achieve a good agreement between theoretical and experimental XAFS FT(χ(k)*k^3). [V_2O_7] units are present in the structures of the references NH_4VO_3 and triclinic $Mg_2V_2O_7$ whose spectra resembled the XANES and EXAFS spectra of dehydrated V_xO_y/SBA-15 (***Figure 3 and Figure 5-5***). Therefore, a V-V scattering path at 3.4 Å was included in the model used for the XAFS refinement. This distance corresponds to the V-V distance between two corner-sharing [VO_4] tetrahedrons in "V_2O_7 dimers" of NH_4VO_3 and $Mg_2V_2O_7$. The result of the corresponding XAFS refinement is shown in ***Figure 5-8***. Apparently, a structural model based on isolated [V_2O_7] dimers was equally unsuited to describe the local structure around V centers in dehydrated V_xO_y/SBA-15. The agreement between theoretical and experimental FT(χ(k)*k^3) in the range from 2 to 4 Å is still not sufficient (***Figure 5-8, left***). Also, adding a V-Si distance to this "isolated V_2O_7 dimer model" only resulted in a minor improvement of the refinement (not shown).

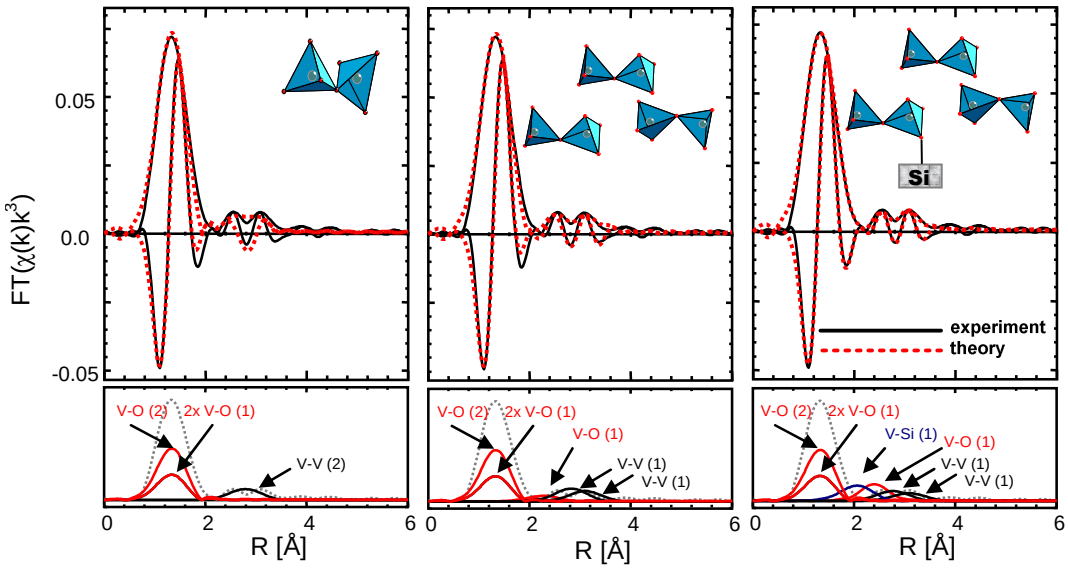

Figure 5-8: Experimental (solid) V K edge FT(χ(k)*k^3) of dehydrated V_xO_y/SBA-15 (7.7 wt%) together with a theoretical XAFS function (i.e. "ordered arrangement of V_2O_7" model). Fit results are given in ***Table 5-3***. The inset shows a schematic representation of the arrangement of V_2O_7 units in $Mg_2V_2O_7$. Also shown are the Fourier transformed χ(k)*k^3 of the individual scattering paths together with corresponding coordination number in brackets.

Figure 5-7 and ***Figure 5-8 (left)*** clearly show that neither an "isolated VO_4" model nor an "isolated V_2O_7" model describe the local structure of the majority of V centers in dehydrated V_xO_y/SBA-15 properly. Hence, in the next step an ordered arrangement of neighboring $[V_2O_7]$ units was assumed. Because of their similar XANES and EXAFS spectra, we again referred to NH_4VO_3 and triclinic $Mg_2V_2O_7$ as references. $[V_2O_7]$ units form chains in NH_4VO_3 with one V-V distance. Conversely, $[V_2O_7]$ units are neighboring but more separated in t-$Mg_2V_2O_7$ resulting in two distinct V-V distances (ICSD 2321 [139]). Accordingly, two additional scattering paths were added to the previous "isolated V_2O_7" model. These two paths correspond to V-O (2.8 Å) and V-V (3.6 Å) distances between two neighboring $[V_2O_7]$ units in the structure of t-$Mg_2V_2O_7$. The result of the corresponding XAFS refinement to the FT(χ(k)*k^3) of dehydrated V_xO_y/SBA-15 is shown in ***Figure 5-8 (middle)*** together with the various V-O and V-V distances used. Apparently, assuming neighboring $[V_2O_7]$ units in an ordered arrangement supported on SBA-15 yielded a good agreement between theoretical and experimental FT(χ(k)*k^3) of dehydrated V_xO_y/SBA-15 over the extended R range from 1 Å to 4 Å. The structural and fitting parameters obtained from the XAFS refinement to the experimental FT(χ(k)*k^3) of dehydrated V_xO_y/SBA-15 and triclinic $Mg_2V_2O_7$ are given in ***Table 5-3*** and ***Table 5-4***. The similar V-O distances, V-V distances, and σ^2 parameters of dehydrated V_xO_y/SBA-15 and t-$Mg_2V_2O_7$ corroborated our choice of model system to describe the local structure around V centers in dehydrated V_xO_y/SBA-15.

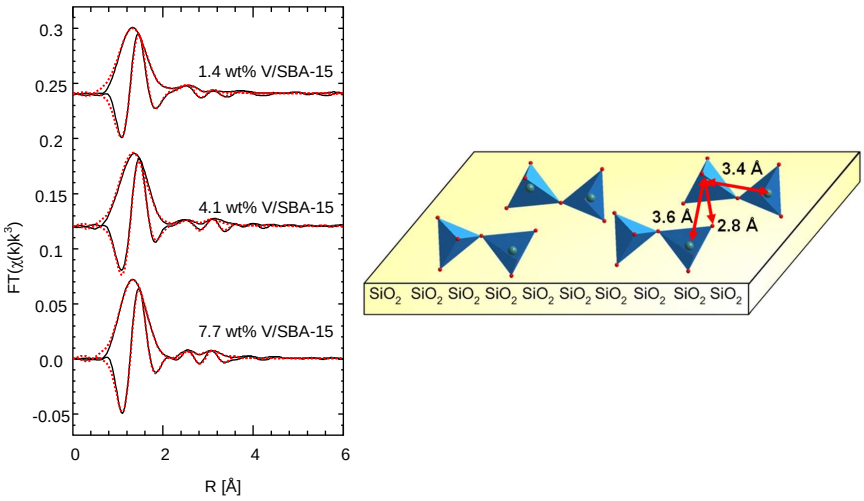

Figure 5-9 left: Experimental (solid) V K edge FT(χ(k)*k^3) of dehydrated V_xO_y/SBA-15 (1.4 wt%, 4.1 wt%, and 7.7 wt%) together with a theoretical XAFS function. The fit results are given in ***Table 5-5***. right: Schematic structural representation of dehydrated V_xO_y/SBA-15. The most prominent distances employed in the XAFS refinement procedure are indicated.

5.2.9 Schematic structural representation of dehydrated V_xO_y/SBA-15

A schematic structural representation of the ordered arrangement of $[V_2O_7]$ units in dehydrated V_xO_y/SBA-15 is depicted in ***Figure 5-9 (right)***. In contrast to previous results on low loaded (< 1 V/nm^2) V_xO_y/SiO_2 samples [21,121] it is concluded that isolated $[VO_4]$ units are not the major vanadium oxide species present in the dehydrated V_xO_y/SBA-15 samples studied here. Of the different loadings studied,

only the 1.4 wt% V_xO_y/SBA-15 sample possessed a vanadium content of less than 0.5 V/nm^2. The three dehydrated V_xO_y/SBA-15 samples exhibited only minor differences in their XANES spectra (***Figure 5-3***), FT(χ(k)*k^3) (***Figure 5-9***), and XAFS fit results (***Table 5-5***). Similar results were obtained for a 2.8 wt% sample prepared by Hess *et al*. [41]. Hence, in the range of 2.8– 7.7 wt% V on SiO_2 the local structure of the majority of V centers in dehydrated V_xO_y/SBA-15 is best described by an ordered arrangement of neighboring [V_2O_7] units (***Table 5-5, Figure 9***). The presence of non-monomeric V_xO_y species in dehydrated V_xO_y/SBA-15 samples was concluded recently based on NEXAFS studies combined with theoretical calculations [42,43]. However, the highly dispersed 1.4 wt% V_xO_y/SBA-15 sample leaves some ambiguity. Concerning the low CVB number of 0.4 determined from the UV-Vis edge energy, it may be possible that a lower connectivity of V_xO_y or even isolated [VO_4] tetrahedrons were present on the SiO_2 support. In the corresponding refinement (***Table 5-5***) higher σ^2 were obtained for the V-O and V-V distances and a decreased σ^2 for the V-Si distance was obtained for the dehydrated 1.4 wt% V_xO_y/SBA-15 sample compared to samples with higher loadings. Thus, the low vanadium loading caused an increased disorder of the V_xO_y structure motifs on the support. Comparing the V-O distances no significant change was obtained for the different loadings. Thus, a change of the distortion of the [VO_4] tetrahedrons and the primary structure of dehydrated V_xO_y/SBA-15 was not observed with increasing dispersion. Furthermore, a decreased amplitude in the FT(χ(k)*k^3) was observed for the second feature at higher distances (~ 3-4 Å).This indicates that the influence of higher V-V distances is less pronounced. Moreover, it may be possible that isolated [VO_4] tetrahedrons are present on the support together with a dimeric tetrahedral species.

Oxygen and silicon atoms of the SiO_2 support are not depicted in the schematic representation shown in ***Figure 5-9 (right)***. In particular Si atoms in the topmost layer of SiO_2 belong to the second coordination sphere of the V centers.

Table 5-5: Type and number (N) of atoms at distance R from the absorbing V atom in a model system assuming an ordered arrangement of [V_2O_7] units (***Figure 5-9, right***) compared to experimental distances and XAFS disorder parameters (σ^2). The parameters were obtained from the refinement of this model structure to the experimental V K edge XAFS FT(χ(k)*k^3) of dehydrated V_xO_y/SBA-15 with different V loadings (i.e. 7.7 wt %, 4.1 wt %, 1.4 wt %) (***Figure 5-9, left***) (k range from 2.7-10.5 Å^{-1}, R range 0.84-3.62 Å, N_{ind} = 16, N_{free} = 8, E_0 = 0 eV in all cases, fit residual 3.8 (7.7 wt%), 7.0 (4.1 wt%), 5.6 (1.4 wt%)) (subscript c indicates parameters that were correlated in the refinement, subscript f indicates parameters that were fixed in the refinement). Confidence limits and significance of fit parameters correspond to those given in ***Table 5-4*** for the 7.7 wt % sample.

Type	N	R_{model} [Å]	dehyd. 7.7 wt% R [Å]	σ^2 [Å^2]	dehyd. 4.1 wt% R [Å]	σ^2 [Å^2]	dehyd. 1.4 wt% R [Å]	σ^2 [Å^2]
V - O	1	1.63	1.78	0.0079	1.78	0.0088	1.78	0.01
V - O	1	1.70	1.78$_c$	0.0079$_c$	1.78	0.0088$_c$	1.78$_c$	0.01$_c$
V - O	2	1.76	1.78$_c$	0.0079$_c$	1.78	0.0088$_c$	1.78$_c$	0.01$_c$
V - O	1	2.87	2.89	0.0012$_f$	2.90	0.003$_f$	2.87	0.003$_f$
V - V	1	3.42	3.29	0.0116	3.30	0.0119	3.35	0.0129
V - V	1	3.62	3.60	0.0116$_c$	3.61	0.0119$_c$	3.61	0.0129$_c$
V - Si	1	2.80	2.54	0.013	2.55	0.0118	2.51	0.0109

Previous reports have indicated that V-Si distances may contribute to the experimental FT(χ(k)*k^3) of dehydrated V_xO_y/SBA-15 [37]. Therefore, a single V-Si scattering path was included in the refinement of the "neighboring V_2O_7" model described above (***Figure 5-8, right***). The structural parameters and refinement details are given in ***Table 5-3*** and ***Table 5-4***. Comparing fit residuals, confidence limits, and F parameters, a significant improvement was observed. Concerning the low distance of the V-Si contribution an angle between V and Si (V-O-Si) of about 90 ° has to be present. This may explain the high average V-O bond length and the distortion of the dehydrated V_xO_y/SBA-15 structure as concluded from the XANES analysis (1.77 Å) and XAFS refinement (1.78 Å). Apparently, both the local structure in V_xO_y species and the interaction with the SiO_2 support are required to describe the FT(χ(k)*k^3) of dehydrated V_xO_y/SBA-15 samples.

5.2.10 Limitations of the XAFS analysis of dehydrated V_xO_y/SBA-15

Eventually, the limitations of the XAFS analysis of dehydrated V_xO_y/SBA-15 presented here should be discussed. XAFS is not a very sensitive technique with respect to distinguishing and identifying additional minority species. Experimental XAFS spectra are clearly dominated by the signal of the majority phase. Hence, the presence of minority vanadium oxide species in dehydrated V_xO_y/SBA-15 with concentrations of less than ~5% cannot be excluded. Only if the contribution of additional phases amounts to more than ~5-10%, will the distortion of the FT(χ(k)*k^3) and the deviation from the model structure assumed be detectable. In particular, this holds, if these minority species happen to be less ordered than the majority phase.

Moreover, XAFS is an averaging technique. Certainly, higher shells should be taken into account properly and various references should be measured for comparison. Even then, however, it may remain difficult to distinguish unambiguously between mixtures of various species or structures. Hence, a more detailed discussion concerning the vicinity of different vanadium oxide species needs to be performed.

Some constraints have to be made when an equal mixture of isolated [VO_4] and neighboring [V_2O_7] units is assumed for the high dispersion sample. First, the V-O distances in the first "VO_4" shell of the two species would have to be the same, which was obtained by the refinement (***Table 5-5***). Otherwise a strong reduction in amplitude of the first V-O peak in the FT(χ(k)*k^3) caused by destructive interference would be discernible. Secondly, isolated [VO_4] would not contribute to the FT(χ(k)*k^3) in the range from 2 Å to 4 Å. Thus, reduction in amplitude and much higher σ^2 parameters compared to the t-$Mg_2V_2O_7$ reference would be detectable. This was not observed in the EXAFS analysis of the dehydrated V_xO_y/SBA-15 presented here (***Table 5-3*** and ***Table 5-5***). A similar statement holds for isolated [V_2O_7] units or a less ordered arrangement of neighboring [V_2O_7] units. Both would result in a reduction in the FT(χ(k)*k^3) amplitude because of missing contributions in the 2-4 Å range or destructive interference caused by a broadened distribution of distances, respectively. Moreover, for isolated or less ordered [V_2O_7] units a single V-V distance would suffice to describe the experimental XAFS spectrum. However, a partial reduction in amplitude in the range of 2-4 Å was observed for the low loaded 1.4 wt% dehydrated

V_xO_y/SBA-15 sample (***Figure 5-9, left***). Furthermore, the refinement procedure employed did not allow the variation of the σ^2 of both vanadium distances independently. Thus, it cannot be excluded that isolated V_xO_y species (besides dimeric) were also present on the dehydrated 1.4 wt% V_xO_y/SBA-15 sample, especially if the low CVB number of 0.3 is taken into account. For higher loadings the fitting procedure has shown that an ordered arrangement of "ordered" dimeric V_xO_y clusters without the presence of isolated species is more likely than a mixture of isolated and dimeric vanadium centers. This is supported by an average CVB number of 1.0 obtained from the UV-Vis edge energy together with the position of the absorption band at 309 nm (***Table 5-2***). Eventually, higher V-Si distances may have to be considered in addition to the V-Si distance of ~2.5 Å (***Table 5-3***). However, a significant contribution of V-Si distances in the range above 3.0 Å in the FT(χ(k)*k^3) would require a highly ordered arrangement of V_xO_y species on the SiO_2 support and a very narrow distance distribution. This seems to be unlikely.

In summmary, assuming a structural arrangement of vanadium centers in dehydrated V_xO_y/SBA-15 that has already been established for reference vanadium oxides (i.e. t-$Mg_2V_2O_7$) is simple and results in a good agreement with experimental data. More complex and artificially constructed arrangements of V_xO_y species supported on SiO_2 may be conceivable but appear to be less likely. Both UV-Vis-DRS and XAFS analysis corroborate a local structure around the majority of V centers in dehydrated V_xO_y/SBA-15 similar to the ordered arrangement of neighboring [V_2O_7] dimers in the structure of t-$Mg_2V_2O_7$ for loadings in the range of 2.8-7.7 wt% dehydrated V_xO_y/SBA-15. With increasing dispersion (< 0.5 V/nm^2) isolated centers may be present.

5.2.11 Local structure of hydrated V_xO_y/SBA-15 - Comparison to V oxide references

The EXAFS χ(k)*k^3 of hydrated V_xO_y/SBA-15 (as-prepared) with different V loadings are depicted in ***Figure 5-10, left***. The usable spectral range extended from 2.7 Å through 11 $Å^{-1}$ for the 7.7 wt% sample. The EXAFS χ(k)*k^3 of the lower loaded samples was limited to 2.7 to 10.5 $Å^{-1}$ because of the high noise level. The V K edge FT(χ(k)*k^3) of hydrated V_xO_y/SBA-15 are shown in ***Figure 5-10 (middle)***. The Fourier transformed χ(k)*k^3 and the V K near edge spectra of hydrated V_xO_y/SBA-15 are compared to those of vanadium oxide references in ***Figure 5-10 (right)***. The range of potential model structures describing the local structure of hydrated V_xO_y/SBA-15 can be narrowed down by comparing the corresponding FT(χ(k)*k^3). Considering peak positions and relative peak heights in the FT(χ(k)*k^3), it appears that from the references available the FT(χ(k)*k^3) of V_2O_5 and CaV_2O_6 resemble that of hydrated V_xO_y/SBA-15. However, from the detailed comparison, the corresponding XANES spectrum of V_2O_5 seemed to be more suitable than that of CaV_2O_6. Compared to V_2O_5, hydrated V_xO_y/SBA-15 may possess a more disordered structure, because of the lower intensity in the FT(χ(k)*k^3). On the one hand, the positions of the various peaks in the XANES of hydrated V_xO_y/SBA-15 are similar to that of V_2O_5 (***Figure 5-3, top right***). On the other hand, the lower peak intensities the FT(χ(k)*k^3) are indicative of a disordered V_2O_5 like structure of the vanadium oxide species in hydrated VxOy/SBA-15 (***Figure 5-10, right)***. Therefore, the local structure of V_2O_5 was used for further structure refinement.

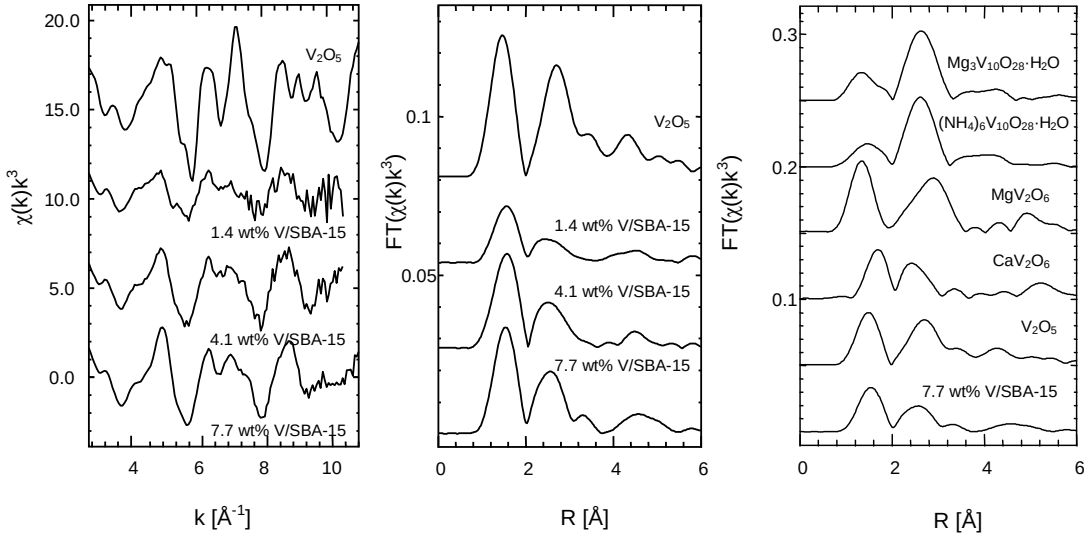

Figure 5-10: V K edge FT(χ(k)*k^3) of hydrated V_xO_y/SBA-15 (7.7 wt%) compared to those of various references (*e.g.* V_2O_5 and MgV_2O_6) and the FT(χ(k)*k^3) and χ(k)*k^3 of hydrated V_xO_y/SBA-15 samples with different vanadium loadings (1.4 wt%, 4.1 wt%, and 7.7 wt%).

5.2.12 Local structure of a square pyramidal vanadium oxide cluster - XAFS refinement of a "V_2O_5" model structure

Comparison of the XANES and FT(χ(k)*k^3) of hydrated V_xO_y/SBA-15 with those of various references identified V_2O_5 as the most suitable model structure for a detailed EXAFS analysis. Therefore, a theoretical XAFS function calculated on the basis of a V_2O_5 model structure (ICSD 60767 [140]) was refined to the experimental FT(χ(k)*k^3) of hydrated V_xO_y/SBA-15. Before the "local V_2O_5" model was applied to hydrated V_xO_y/SBA-15, the V_2O_5 model structure was refined to the FT(χ(k)*k^3) of V_2O_5 to validate the procedure chosen. Good agreement between the theoretical XAFS function of a V_2O_5 model structure and the FT(χ(k)*k^3) of V_2O_5 was obtained (***Figure 5-11***). As described above, the validity of the XAFS analysis approach chosen was evaluated by calculating confidence limits and F parameters (***Table 5-6***). The model structure employed corresponds to the local structure around V centers in bulk V_2O_5 (***Figure 5-11, right***). In fitting procedure #1 three V-O distances (1.6 Å, 1.8 Å, and 2.0 Å) and two σ^2 (one for R = 1.6 Å and one for all other V-O distances) in the first V-O shell were allowed to vary independently. Additionally, three V-V distances (3.1 Å, 3.4 Å, and 3.6 Å) with the same σ^2 were refined. Moreover, E_0 was also allowed to vary in fitting procedure #1. Again because of N_{ind} = 17 and N_{free} = 10 the refinement procedure #1 would be considered reliable according to the Nyquist criteria. Reasonable F values (F < 0.2) were calculated for the V-V distances and the σ^2 (V-V) parameter. However, rather high confidence limits of the V-O and V-V distances of ± 0.3 Å and a F parameter of 0.8 for the first σ^2 (V-O) parameter were obtained with procedure #1. Moreover, E_0 exhibited a confidence limit of ± 0.5 and F = 0.6. Hence, fitting procedure #1 clearly exceeds the number of meaningful parameters. Therefore, the fitting procedure was modified and the number of free parameters was reduced. E_0 was kept invariant again in the refinement and only one σ^2 (V-O) parameter was used.

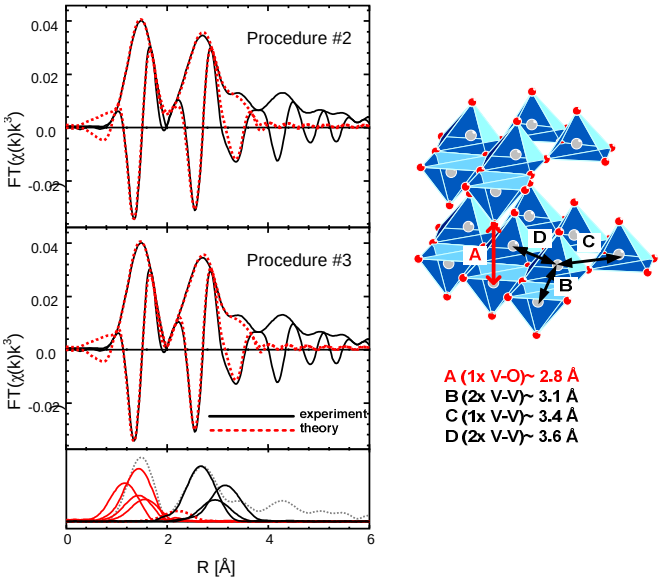

Figure 5-11: Experimental (solid) V K edge FT(χ(k)*k3) of V_2O_5 (left) together with theoretical XAFS functions (V_2O_5 model, red lines refer to the V-O scattering path, black lines refer to the V-V scattering paths) and a representation of the structural V_2O_5 model (right). Prominent distances employed in the XAFS refinement procedure are indicated.

In contrast to procedure #1, procedure #2 yielded reasonable confidence limits (*e.g.* ± 0.01 for V-O distances) and acceptable F parameters (mostly F=0). The theoretical local structure of V_2O_5 from refinement procedure #1 and #2 represents the local structure motif of connected square pyramids in V_2O_5. These square pyramids are connected via edges and are within the layers of the V_2O_5 structure (***Figure 5-11, right***). In order to test if it is necessary to assume a layered structure to fully describe the local structure of crystalline V_2O_5, the refinement procedure was extended by a fourth V-O distance at ~ 2.8 Å (procedure #3). From ***Table 5-6*** it is obvious that a reasonable refinement with low confidence limits and acceptable F parameters (all F=0) was obtained.

Table 5-6: V K edge XAFS parameters (Z for distances R and disorder parameter σ^2) obtained from two different procedures of fitting a model structure (*i.e.* V_2O_5) to the experimental XAFS FT(χ(k)*k^3) of the V_2O_5 reference together with confidence limits (± z, referring to 95% of fit residual) and significance parameter F (details given in text).

		Procedure #1			Procedure #2			Procedure #3		
Pair	N	Z	±z	F	Z	±z	F	Z	±z	F
R(V - O)	1	1.58	0.327	--	1.59	0.009	--	1.59	0.008	--
σ^2(V - O)		0.0076	0.08	0.8	0.0077	0.0004	--	0.0081	0.0003	--
R(V - O)	3	1.87	0.13	--	1.88	0.003	--	1.88	0.003	--
σ^2(V - O)		0.0087	0.0004	--	--	--	--	--	--	--
R(V - O)	1	2.01	0.13	--	2.03	0.02	0.1	2.02	0.02	--
R(V - O)	1	--	--	--	--	--	--	2.72	0.02	--
R(V - V)	2	3.13	0.05	--	3.13	0.01	--	3.13	0.005	--
σ^2(V - V)		0.0056	0.0003	--	0.0057	0.0003	--	0.0058	0.0003	--
R(V - V)	2	3.42	0.10	0.2	3.42	0.02	--	3.42	0.02	--
R(V - V)	1	3.64	0.08	--	3.64	0.01	--	3.63	0.01	--
E_0		2.8	0.5	0.6	2.8_f	--	--	2.8_f	--	--
Residual		8.8			8.7			7.1		

Moreover, ***Figure 5-11*** shows that the resulting theoretical FT(χ(k)*k^3) of V_2O_5 from procedure #3 was more similar to the experimental one for intermediate distances (2-3 Å) than the one obtained from procedure #2. Evidently, the assumption of a layered structure is necessary for a good description of the local structure of the V centers in crystalline V_2O_5.

5.2.13 Local structure of hydrated V_xO_y/SBA-15 – XAFS refinement of a "V_2O_5" based model structure

Applying the refinement procedure introduced above to hydrated V_xO_y/SBA-15 resulted in good agreement between the theoretical XAFS function of a V_2O_5 model structure and the FT(χ(k)*k^3) of hydrated V_xO_y/SBA-15 (***Figure 5-12, left***). However, an increased F parameter and a strongly shifted V-O distance at 3.1 Å with a rather high confidence limit was obtained (***Table 5-7, procedure #SBA1***). Therefore, this distance was not seen as meaningful for describing the local structure of hydrated V_xO_y/SBA-15. The structure of hydrated V_xO_y/SBA-15 seems to be less extended than the layered V_2O_5 structure.

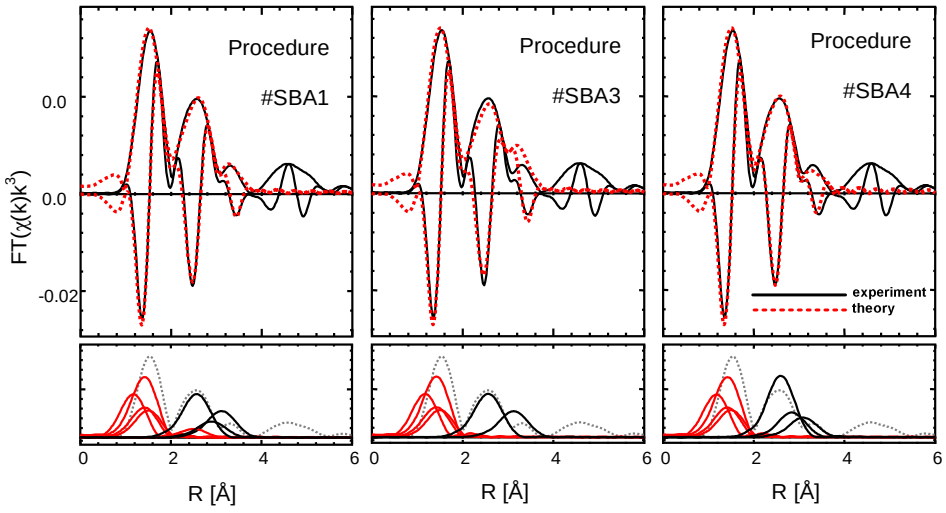

Figure 5-12: Experimental (solid) V K edge FT(χ(k)*k^3) of hydrated V_xO_y/SBA-15 (7.7 wt%) together with theoretical XAFS functions. The procedures refer to the subsequent reduction of the theoretical V_2O_5 model. Details are provided in the text and the fit results are given in ***Table 5-7***. Also shown are the Fourier transformed χ(k)*k^3 of the individual scattering paths together with the corresponding coordination number in brackets.

Removing the V-O contribution at 2.8 Å from the V_2O_5 model structure resulted in a higher R value of the refinement (***Table 5-7, procedure #SBA2***). Apparently, the local structure of hydrated V_xO_y/SBA-15 is similar to that of V_2O_5 but not identical. To improve the structure model used for the refinement of hydrated V_xO_y/SBA-15 the number of V-V distances was reduced. In procedure #SBA3 the V-V distance of 3.42 Å was neglected. This distance is found between two V centers in the V_2O_5 structure which are only connected to each other via the corner of $[VO_5]_x$ square pyramids (***Figure 5-11, right***). This V-V distance is not found in the structure of ternary vanadates such as CaV_2O_6, which are also built from square pyramidal units like V_2O_5.

Table 5-7: V K edge XAFS parameters (Z for distances R and disorder parameter σ^2) obtained from four different procedures of fitting a model structure (*i.e.* V_2O_5) to the experimental XAFS FT(χ(k)*k^3) of hydrated V_xO_y/SBA-15 (7.7 wt%) (details of fit given in ***Table 5-8***) together with the confidence limits (± z, referring to 95% of fit residual) and the significance parameter F (details given in text).

		Procedure #SBA1			Procedure #SBA2			Procedure #SBA3			Procedure #SBA4		
Pair	N	Z	±z	F	Z	±z	F	Z	±z	F	Z	±z	F
R(V - O)	1	1.62	0.01	--	1.63	0.01	--	1.62	0.02	--	1.63	0.01	--
σ^2(V - O)		0.0105	0.0003	--	0.0106	0.0003	--	0.0104	0.0005	--	0.0105	0.0003	--
R(V - O)	3	1.88	0.003	--	1.88	0.003	--	1.88	0.004	--	1.88	0.003	--
R(V - O)	1	1.97	0.02	0.3	1.97	0.02	0.4	1.98	0.03	--	1.98	0.02	0.3
R(V - O)	1(-)	3.07	0.06	0.6	--	--	--	--	--	--	--	--	--
R(V - V)	2	3.07	0.01	--	3.07	0.006	--	3.06	0.01	--	3.08	0.006	--
σ^2(V - V)		0.0121	0.0005	--	0.0114	0.0005	--	0.0114	0.0005	--	0.0087	0.0004	--
R(V - V)	1(-)	3.42	0.03	0.1	3.43	0.03	0.2	--	--	--	3.33	0.02	--
R(V - V)	2(1)	3.66	0.02	--	3.66	0.02	--	3.66	0.02	--	3.60	0.02	--
E_0		0_f	--	--	0_f	--	--	0_f	--	--	0_f	--	--
Residual		8.5			10.0			14.7			8.6		

As shown in figure ***Figure 5-12 (middle)*** and ***Table 5-7*** the reduced refinement procedure #SBA3 resulted in a rather weak agreement between the theoretical XAFS function of the model structure and the FT(χ(k)*k^3) of hydrated V_xO_y/SBA-15. This was expected from the lower similarity found in the XANES spectra of hydrated 7.7 wt% V_xO_y/SBA-15 and CaV_2O_6 (***Figure 5-3, top right***). Moreover, from the UV-Vis-DR spectra (***Figure 5-2, left***) an average V-O-V number of 3.0-3.5 was determined for the hydrated V_xO_y/SBA-15 samples. This indicated that the local structure of hydrated V_xO_y/SBA-15 was more similar to square pyramidal $[VO_5]_x$ chains than to a layered structure of square pyramidal vanadium centers like in V_2O_5 (V-O-V number = 5). Therefore, the refinement #SBA3 was modified by separating the single V-V distance at ~ 3.6 Å with a coordination number of 2 into two individual distances of 3.4 and 3.6 Å, each exhibiting a coordination number of 1. As shown in ***Figure 5-12 (right)*** and ***Table 5-7***, this refinement procedure (#SBA4) resulted in a better residual, low confidence limits, and mostly zero F parameters. Hence, it is assumed that the local structure of hydrated V_xO_y/SBA-15 can be described by a chain-like square pyramidal $[VO_5]_x$ structure. However, the differences between model structures assumed for the local structure of V_2O_5 and hydrated V_xO_y/SBA-15 are small. As shown in ***Figure 5-13*** (***bottom left)*** it was possible to describe V_2O_5 with the reduced structure model applied to hydrated V_xO_y/SBA-15 (***Figure 5-13***, ***right)***. Details of the resulting parameters are given in ***Table 5-8***. Higher R values and increased F parameters (F=0.6) for the refinement of V_2O_5 indicate that procedure #SBA4 is not sufficient for describing the V_2O_5 structure. Nevertheless, the disorder parameters σ^2 for the V-O and V-V scattering paths used in the XAFS refinement increased for hydrated V_xO_y/SBA-15 compared to the V_2O_5 reference (***Table 5-8***). This indicates an increased disorder in the local structure of hydrated V_xO_y species supported on SBA-15 compared to bulk V_2O_5. The structural similarity between hydrated vanadium oxide species supported on SiO_2 and V_2O_5 has previously been observed by Raman spectroscopy [117]. Evidently, the local structure of hydrated V_xO_y/SBA-15 used here is very similar to other materials described previously in the literature [23,117].

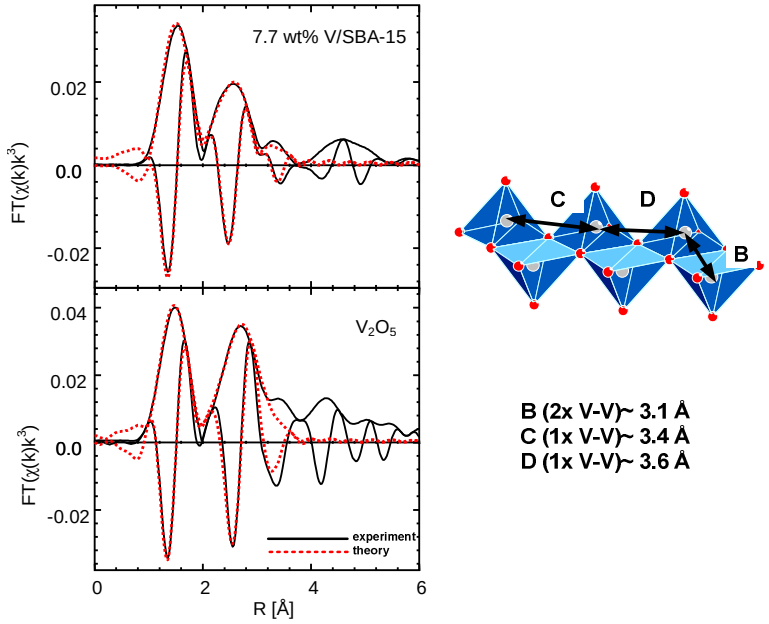

Figure 5-13: left: Experimental (solid) V K edge FT(χ(k)*k^3) of hydrated V_xO_y/SBA-15 (7.7 wt%) (top) and of V_2O_5 (bottom) together with the theoretical XAFS functions. Right: A representation of the reduced V_2O_5 model structure used for the refinement. The most prominent distances employed in the XAFS refinement procedure are indicated.

In addition to the 7.7 wt % V_xO_y/SBA-15, samples with lower loadings of 1.4 wt% and 4.1 wt% V were measured (***Figure 5-10***). The amplitude of the FT(χ(k)*k^3) decreased with increasing dispersion. Especially in the range of 2-4 Å a strong decrease of the amplitude was visible. Hence, the disorder increased with decreasing V loading. Similar trends were observed in UV-Vis-DR spectra (***Table 5-2***) where the average CVB number decreased from 3.5 to 3.0 with decreasing loading. Therefore, a lower degree of "hydration" was assumed for low loaded 1.4 wt% V_xO_y/SBA-15. Apparently, the degree of hydration (V-V contribution) in the hydrated state depends on the vanadium dispersion. Conversely, in the range of V loadings from ~ 1.4 to 7.7 wt% the local structure of dehydrated V_xO_y/SBA-15 was largely independent of the amount of vanadium oxide supported on SBA-15.

Table 5-8: Type and number (N) of atoms at distance R from the V atoms in a V_2O_5 system compared to the experimental distances and the XAFS disorder parameter (σ^2). The parameters were obtained from the refinement of a reduced V_2O_5 model structure (ICSD 60767 [140]) to the experimental V K edge XAFS FT(χ(k)*k^3) of hydrated V_xO_y/SBA-15 (7.7 wt%) and bulk V_2O_5. (k range from 2.7 - 11.0 $Å^{-1}$, R range 0.9 - 3.8 Å, E_0 (V_xO_y/SBA-15) = 0.0 eV, E_0 (V_2O_5) = 0.0, fit residual 8.6 (V_xO_y/SBA-15) and 12.5 (V_2O_5), N_{ind} = 17, N_{free} = 8) (subscript c indicates parameters that were correlated in the refinement). Confidence limits and significance of the fit parameters are given in ***Table 5-7***.

			V_2O_5		hydrated 7.7 wt% V_xO_y/SBA-15	
Type	N	R_{model} [Å]	R [Å]	σ^2 [$Å^2$]	R [Å]	σ^2 [$Å^2$]
V - O	1	1.58	1.59	0.0073	1.63	0.0105
V - O	1	1.78	1.86	0.0073_c	1.88	0.0105_c
V - O	2	1.88	1.86_c	0.0073_c	1.88_c	0.0105_c
V - O	1	2.02	2.01 (F=0.6)	0.0073_c	1.98 (F=0.3)	0.0105_c
V - V	2	3.08	3.11	0.0075	3.08	0.0087
V - V	1	3.42	3.53 (F=0.2)	0.0075_c	3.34	0.0087_c
V - V	1	3.56	3.64	0.0075_c	3.61	0.0087_c

5.3 Summary

Both UV-Vis and X-ray absorption spectroscopy are very suitable techniques for studying the local structure of dispersed metals or metal oxides on various support materials. Here, the local structure of vanadium oxide supported on nanostructured SiO_2 (SBA-15) was investigated. Three samples with different vanadium loadings (1.4 wt%, 4.1 wt%, and 7.7 wt% V on SBA-15) were employed.

For hydrated V_xO_y/SBA-15 a square pyramidal structure similar to V_2O_5 was assumed to be present. Compared to bulk V_2O_5 a lower degree of extension and higher distortion of the [VO_5] vanadium centers was inferred from the UV-Vis edge energy position and the XAFS refinement. Thermal treatment in air at 623 K resulted in characteristic structural changes of the V oxide species. UV-Vis-DRS and XAFS measurements of dehydrated V_xO_y/SBA-15 showed that the local structure could be described by a model structure consisting of an ordered arrangement of neighboring [V_2O_7] units in the range of 0.5-2.5 V/nm^2. This is in good agreement with NEXAFS studies and theoretical calculations that also concluded the presence of V-O-V bonds in the V_xO_y species supported on SBA-15 [42,43]. However, at lower loadings (< 0.5 V/nm^2) isolated [VO_4] tetrahedrons, besides dimeric tetrahedral structures, may also be present. A similar trend was recently observed for low loaded Mo_xO_y/SBA-15 samples [137]. The influence of the SiO_2 support was not negligible and caused a high distortion of the tetrahedral vanadium oxide cluster in dehydrated V_xO_y/SBA-15.

The local structures of dehydrated V_xO_y/SBA-15 were found to be mainly independent of the V loading over the range employed. Conversely, in hydrated V_xO_y/SBA-15 a decrease of the number of V-O-V contributions in FT(χ(k)*k^3) and of the structural disorder of the hydrated square pyramidal vanadium centers with increasing vanadium dispersion was observed. A more detailed discussion about the formation processes of hydrated and dehydrated V_xO_y/SBA-15 as a function of time and atmosphere will be given in the next chapter.

In contrast to conventional XAFS analysis, an extended approach to evaluate the significance of structural fitting parameters in XAS data analysis was employed. After fitting the theoretical XAFS functions of a suitable model structure to the experimental data, confidence limits and F parameters were calculated to identify suitable analysis procedures. Because the number of parameters often exceeds the number of "independent" parameters, evaluating the reliability and significance of a particular fitting procedure is mandatory. It was shown that the number of independent parameters (Nyquist) alone was not sufficient to verify a reliable refinement procedure.

6 *Dynamic changes in the local structure of V_xO_y/SBA-15 model catalysts in oxidative and water saturated atmospheres*

6.1 Introduction

In the previous chapter the structure of dehydrated and hydrated vanadium oxide supported on SBA-15 was discussed. The hydrated structure was proposed to consist of chainlike square pyramidal vanadium oxide centers. The dehydrated vanadium oxide supported on SBA-15 was described by dimeric vanadium oxide units with tetrahedral coordination of the vanadium centers. For lower vanadium loadings (< 0.3 V/nm^2) these centers may be present together with isolated tetrahedral centers. However, these results represent only a picture of the vanadium oxide structure present on SBA-15 under static conditions. Because these samples were introduced as model catalysts it is crucial to know how the transformation between the hydrated and dehydrated state proceeds under reaction conditions.

In situ investigations of structural changes during thermal treatment have been subject of only a few reports. *In situ* IR and NIR measurements reported [23,27,40,114,141,142] a decrease of the isolated Si-OH bonds with increasing vanadium loading. The presence of V-OH bands (3660 cm^{-1}) was reported for hydrated and dehydrated V_xO_y/SiO_2 samples. *In situ* Raman [32,34,143] and UV-Vis-DRS [24,144] measurements showed that at temperatures above 473 K characteristic Raman bands and UV-Vis-DRS absorption bands of the dehydrated state were present independent of the presence of water in the reaction atmosphere. Furthermore, it was reported that hydration and dehydration processes were reversible [24,35,145]. In contrast, Xie *et al.* [34] reported the formation of V_2O_5 crystallites after repeated hydration and dehydration of samples with dispersed vanadium oxide species below the monolayer coverage (2.5 V/nm^2). They assumed that $V_2O_5 \cdot nH_2O$ gels were formed during the hydration process, which decomposed to V_2O_5 clusters and served as "nuclei" for the growth of crystalline V_2O_5. Raman [23], IR [23,115,141], and MAS NMR [146] measurements indicated that some of the silanol groups of SiO_2 are consumed during formation of the dehydrated state and that the respective tetrahedral vanadium oxide species is linked via V-O-Si bonds to the support.

Given these diverse results on the dehydration process found in the literature, it was intended to investigate the dehydration process of V_xO_y/SBA-15 in more detail here. Therefore, the evolution of the vanadium oxide structure on SBA-15 was investigated during temperature programmed reaction in oxygen containing atmospheres using UV-Vis-DRS, XAS, and Raman spectroscopy. Furthermore, the impact of the vanadium loading and the influence of water vapor on the hydration and dehydration process were investigated.

6.2 Results and discussion

6.2.1 Impact of pretreatment temperature on dehydrated V_xO_y/SBA-15 phase

Various temperatures for the oxygen pretreatment process (dehydration process) were reported in the literature. They range from rather low temperatures of 573 K [35,146] and 623 K [32] up to 773 K [23], 853 K [141], and 1073 K [40]. Therefore, various pretreatment temperatures were tested for dehydration of the V_xO_y/SBA-15 samples. In ***Figure 6-1*** the FT(χ(k)*k^3) and UV-Vis-DR spectra of 7.7 wt% V_xO_y/SBA-15, dehydrated at different temperatures in the range of 554-773 K are shown (20% O_2 in He). The UV-Vis-DR spectra of 7.7 wt% V_xO_y/SBA-15 treated at 554 K and 626 K showed only a small blue shift of a few nm of the UV-Vis absorption edge with increasing temperature (***Figure 6-1, left***). The blue shift in the UV-Vis-DR spectra did not affect the average V-O-V number of ~ 1 (dimeric tetrahedrons) determined from the UV-Vis edge energy. The experimental FT(χ(k)*k^3) of 7.7 wt% V_xO_y/SBA-15 treated at 623 K, 723 K, and 770 K (***Figure 6-1, right***) showed only minimal differences, and they were simulated successfully using the model structure of dehydrated V_xO_y (ordered arrangement of $[V_2O_7]$ units, introduced in ***Chapter 5***). The amplitude of the fist V-O shell at 1.78 Å in the FT(χ(k)*k^3) of 7.7 wt% V_xO_y/SBA-15 increased after calcination at 770 K for 8 h compared to dehydration at 623 K for 30 min. The disorder parameter σ^2 of the V-O scattering path decreased from 0.0071 $Å^2$ to 0.0063 $Å^2$ with increasing dehydration temperature (***Table 6-3, Table 6-4, page 104 and 106***). This indicates a wider V-O distance distribution and, thus, a slightly increased structural order of the first V-O coordination sphere. Apparently, above a certain temperature the dehydrated state of vanadium oxide on mesoporous SiO_2 is present with only small changes in average V-O bond length and structural order. Higher temperatures than 773 K were not investigated because of the upper temperature limits of the *in situ* cells used.

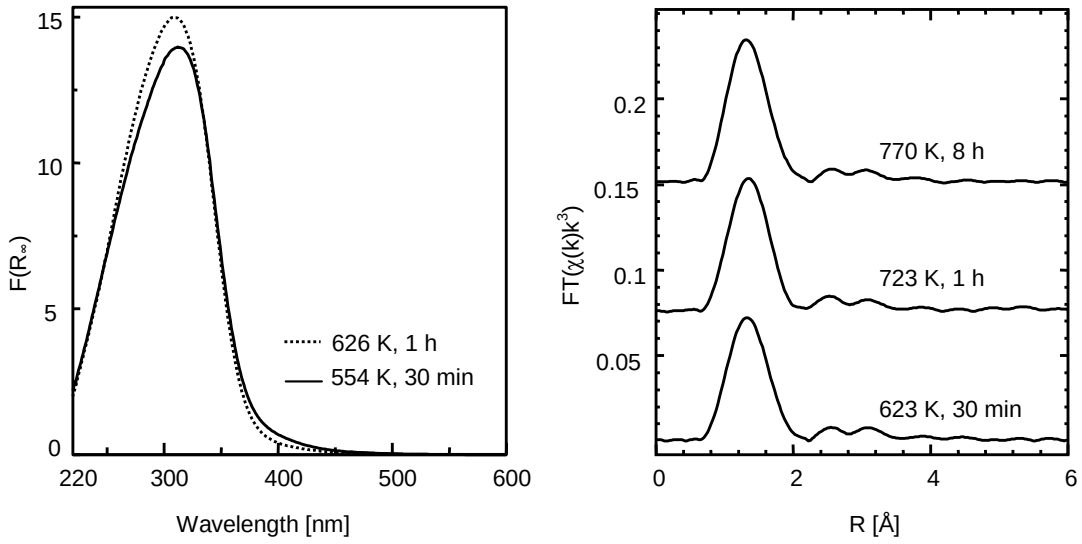

Figure 6-1 Left: UV-Vis-DR spectra of 7.7 wt% V_xO_y/SBA-15 dehydrated at different temperatures. All spectra were recorded at 298 K. Right: V K edge FT(χ(k)*k^3) of 7.7 wt% V_xO_y/SBA-15 after different dehydration procedures. The dehydration was performed in 20% O_2 in He.

A more detailed knowledge of the dehydration process was obtained from *in situ* XAS and UV-Vis-DR spectra recorded during temperature treatment. The UV-Vis-DRS measurements are depicted only for 1.4 wt% V_xO_y/SBA-15 and the XAS results only for 7.7 wt% V_xO_y/SBA-15. Dehydration experiments were conducted for all loadings (1.4, 4.1, 7.7 wt% V on SiO_2) using both spectroscopic methods. The results were similar for all loadings employed (***Figure* 6-2**).

6.2.2 Dehydration process investigated by in situ UV-Vis-DRS

In situ UV-Vis-DR spectra of 1.4 wt% V_xO_y/SBA-15 during dehydration and the evolution of the water ion current (m/e 18) are depicted in ***Figure 6-2, left***. Immediately after starting to heat the sample a change in the UV-Vis-DR spectra was visible (294-400 K), which was accompanied by an increased formation of water. The intensity of the absorption maximum at ~ 365 nm decreased, which caused a blue shift of the UV-Vis absorption edge. A direct correlation between UV-Vis edge energy and vanadium structure as discussed in ***Chapter 5.2.3*** was not made because of the temperature broadening of the UV-Vis-DR spectra. Typically a red shift of the UV-Vis edge energy of 0.1- 0.2 eV was observed for V_2O_5 and magnesium vanadate references during heating to 657 K. However, the strong blue shift of the UV-Vis edge energy between 294 K and 400 K indicates that changes in coordination geometry of the absorbing vanadium centers from square pyramidal to tetrahedral proceeded mainly in this temperature range. A red shift to 286 nm and an increase in intensity were observed for the second absorption band at 260 nm in the UV-Vis-DR spectra. At temperatures above 550 K a slight decrease of this band was detected. The increase in intensity of the band at 286 nm was enhanced after the low energy band at 365 nm nearly disappeared. In the temperature range (400-540 K) where the absorption band at 286 nm reached its maximum a second step of water formation was observed.

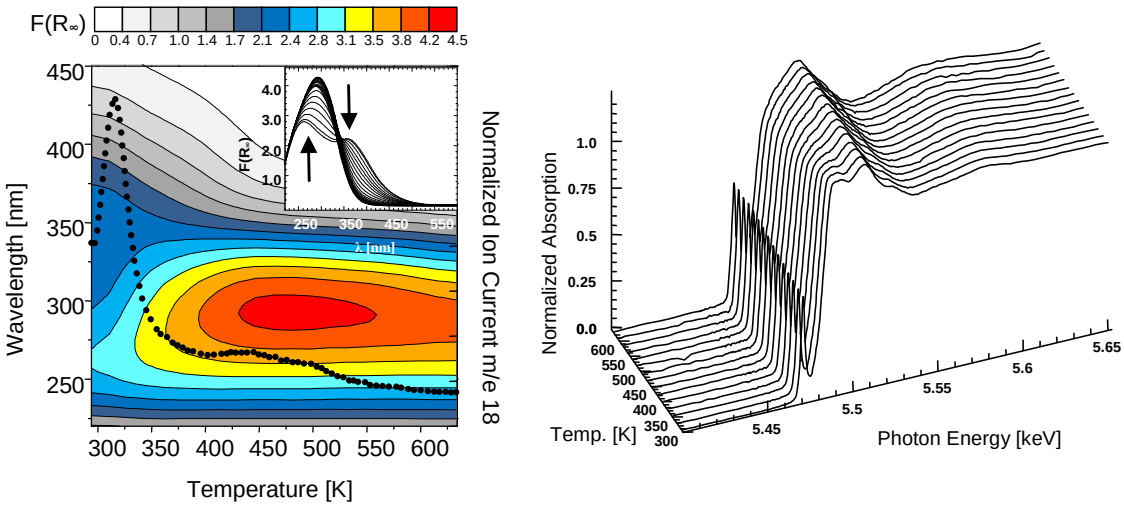

Figure 6-2 Left: *in situ* UV-Vis-DR spectra of the 1.4 wt% V_xO_y/SBA-15 sample and the water ion current m/e 18 (554 K, 4 K/min, 20% O_2 in He) during dehydration. The inset shows the 2D spectra depicted in the 3D color map. Right: V K edge *in situ* XANES spectra during dehydration of the 7.7 wt% V_xO_y/SBA-15 sample (623 K, 5 K/min, 20% O_2 in He, E4 Beamline).

6.2.3 Dehydration process investigated by in situ XAS

The V K edge XANES spectra of 7.7 wt% V_xO_y/SBA-15 recorded during dehydration (298-623 K, 5 K/min, 20% O_2 in He) are shown in ***Figure 6-2, right***. Similar to the changes observed in the UV-Vis-DR spectra of 1.4 wt% V_xO_y/SBA-15 significant changes were observed directly after starting the temperature treatment (298-440 K). Apparently, the characteristic XANES spectra of hydrated V_xO_y/SBA-15 changed rapidly into a XANES spectrum, which was characteristic for the dehydrated state of V_xO_y/SBA-15 (***Chapter 5.2.4***). The strong decrease of the first absorption feature between 5.487 and 5.497 keV in the spectrum of hydrated V_xO_y/SBA-15 was indicative for this transformation. In the temperature range from 298 to 440 K a strong formation of water as reported for the UV-Vis-DRS mesurement was observed (data not shown). At temperatures above 440 K no distinct changes above the V absorption edge were detected in the XANES spectra of 7.7 wt% V_xO_y/SBA-15.

The results of a principal component analysis (PCA) of the XANES spectra are shown ***Figure 6-3***. Two components were identified to be present in the *in situ* XANES spectra recorded during the dehydration. This was inferred from the minimum of the indicator value and the R*CN product (product of residual and component number) of the second component. Hence, dehydration proceeded directly from the hydrated state to the dehydrated state of V_xO_y/SBA-15 and no intermediate phases were formed. Therefore, the XANES spectra of hydrated and dehydrated 7.7 wt% V_xO_y/SBA-15 were assigned to the two phases obtained. Evolution of the resulting phase fractions is depicted in ***Figure 6-3*** together with the V K pre-edge peak height and position (referred to V K edge 5465 eV). The pre-edge peak intensity increased immediately with increasing temperature and reached a constant value at 550 K. The intensity increase seemed to correlate with the increasing fraction of the dehydrated phase during thermal treatment.

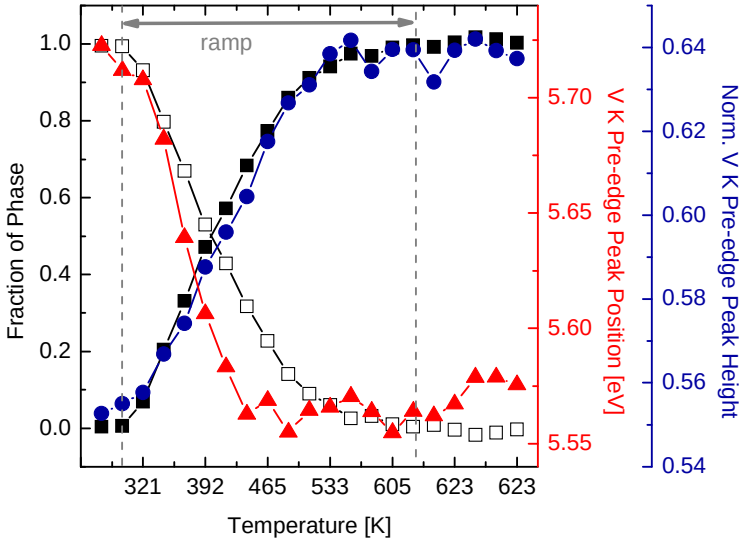

Figure 6-3: Evolution of the V K pre-edge peak height (●) and energy position (▲) together with the resulting concentration of the hydrated (□) and dehydrated (■) phase of 7.7 V_xO_y/SBA-15, derived from the XANES spectra depicted in ***Figure 6-2, right*** (623 K, 5 K/min, 20% O_2 in He, E4 beamline).

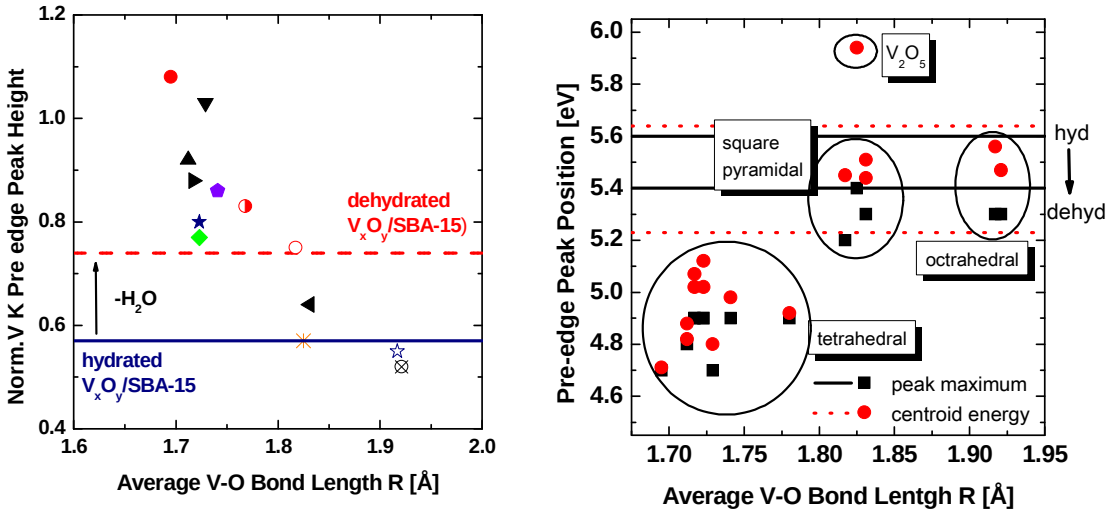

Figure 6-4: V K edge pre-edge peak height as a function of average V-O bond length (left) and relative energy position and centroid energy (right) of vanadium oxide reference compounds measured at A1 beamline. The values determined for dehydrated and hydrated 7.7 wt% V_xO_y/SBA-15 are indicated as lines (symbols as in ***Figure 5-4***, ***Chapter 5.2.4,*** details ***Table 10-4***).

The energy position decreased in the temperature range from 298 K to 440 K and remained constant above 440 K. In contrast to the evolution of the pre-edge peak height no direct correlation of the energy position with the evolution of the V_xO_y/SBA-15 phases was observed.

In ***Chapter 5.2.4*** the linear correlation between the pre-edge peak height and the average length of V-O distances was discussed. Only the pre-edge peak height was used here and not the product of the pre-edge peak area and height (***Figure 6-4, left***). The reason behind this was that the spectra shown in ***Chapter 5.2.4*** were recorded at beamline A1 whereas the spectra shown here were measured at different beamlines (A1, C, E4; Hasylab). Small differences in the resolution of the beamline spectrometer cause small differences in the XANES spectra. For instance the pre-edge peak height of dehydrated 7.7 wt% V_xO_y/SBA-15 was 0.64 at beamline E4 and 0.74 at beamline A1. Due to the fact that not all references shown in ***Figure 6-4*** were available on all beamlines the linear function ***(5.2)*** was not derived for all data sets and applied to the XANES spectra in ***Figure 6-2, right*** (E4 beamline). Nevertheless, the pre-edge peak height showed a linear dependence with the average V-O bond length as depicted in ***Figure 6-4, left*** (beamline A1). Referring to ***Chapter 5.2.4***, the pre-edge peak height represents the average bond length of the V-O distance in the first coordination sphere. Given this relation appears that a continuous decrease of the average bond length took place during the dehydration process. However, the point where the vanadium centers in V_xO_y/SBA-15 changed from a square pyramidal to a tetrahedral coordination could not be determined directly from the pre-edge peak height (average V-O bond length). An estimate was made from the relative energy position of the pre-edge peak. ***Figure 6-4, right*** depicts the relative energy position and centroid energy of the pre-edge peak of vanadium reference compounds as a function of the average V-O bond length. In contrast to the pre-edge peak height no linear correlation was found. A broad range of energy positions between 4.7 eV and 5.1 eV was detected for tetrahedral compounds. Conversely, almost the same energy positions between 5.2 eV and 5.5 eV were determined for square

pyramidal and distorted octahedral compounds. The relative energy position obtained from the maximum of the pre-edge feature and the centroid energy determined according to Chaurand *et al.* [94] showed the same dependence. Only V_2O_5 exhibited an increased centroid energy of 6.0 eV. Thus, the energy position is more sensitive towards the coordination of the absorbing vanadium centers than towards the average bond length.

Apparently, the energy position of hydrated and dehydrated 7.7 wt% V_xO_y/SBA-15 deviated from the energy positions determined for bulk vanadium oxide references (***Figure 6-4, right***). Hence, energy position of the absorption edge is affected by more complex factors than only coordination of the vanadium centers. One factor may be a strong influence of the SiO_2 support that cannot be neglected because of the high dispersion of the vanadium oxide clusters. However, the strong impact of the vanadium coordination on the energy position allowed determining the point where the square pyramidal coordination of vanadium centers changes into a tetrahedral coordination during dehydration. No significant change of the energy position of the pre-edge peak was detected for temperatures above 440 K (***Figure 6-3***). It seems that the transformation from hydrated to dehydrated V_xO_y/SBA-15 was completed at this temperature. This temperature was higher than the transformation temperature determined from the UV-Vis-DR spectra in ***Figure 6-2, left*** (~ 400 K). The increase of the pre-edge peak height at temperatures above 440 K may reflect the decreasing distortion of the tetrahedral V_xO_y species. A temperature of 440 K coincidences with the observation of the characteristic Raman band at 1040 cm^{-1} measured by *in situ* Raman spectroscopy (data shown in ***appendix***, ***10.4*** , Hess *et al.* [32,38,115,117]).

For both methods, UV-Vis-DRS and XAS, the same results were obtained. Moreover, the same dehydration process was inferred for the 1.4 wt% V_xO_y/SBA-15 (UV-Vis-DRS data shown) and the 7.7 wt% V_xO_y/SBA-15 sample (XAS data shown). Apparently, the dehydration process was independent of the vanadium loading on the SBA-15 support.

6.2.4 Dehydration of the silica SBA-15 support

The dehydration process of the vanadium oxide species supported on SBA-15 discussed above cannot be fully understood without knowledge of the processes that occur on the silica support. Dehydration (desorption of physically adsorbed water) and dehydroxylation processes (decomposition of silanol groups) were reported for pure silica samples. Reviews were presented by Zhuravlev *et al.* [147] and Vansant *et al.* [104]. Thermogravimetric (TG) measurements were conducted to compare the dehydration process of V_xO_y/SBA-15 samples with that of bare SBA-15 support. ***Figure 6-5, left*** depicts the thermograms for bare SBA-15, 1.4 wt% and 7.7 wt% V_xO_y/SBA-15. All three curves show the same progression of mass loss in the temperature range employed. Given that a mass loss was already detected at room temperature (303 K), a holding time of 60 min was adhered before starting to heat. After 60 min at 303 K only an insignificant mass loss was detected. After reaching the maximum temperature of 623 K, the temperature was held for 30 min.

Four steps of mass loss were observed in the measured thermograms (***Figure 6-5***). In the case of pure silica samples such as SBA-15 they can be ascribed to different stages of dehydration and dehydroxylation [147]. Zhuravlev reviewed the temperature dependent water desorption processes of various silica samples in vacuum [147]. The first mass loss of SBA-15 occurred already at room temperature (step 1, 303 K). According to Zhuravlev [147] it was ascribed to desorption of physically adsorbed water present in a multilayer coverage on the SiO_2 support. The second step (step 2) was detected between 303 K and 380 K. In this range an increased water evolution was detected in the gas phase by online mass spectrometry. Water formation in this step was ascribed to physically adsorbed water in a coverage below one monolayer. Increasing temperature led to the third step (step 3). It ranged from ~ 380 K up to the maximum temperature of 623 K. It was accompanied by the fourth step (step 4) during hold at 623 K. According to Zhuravlev [147] the dehydration process of physically adsorbed water was accompanied by a dehydroxylation process of the silica where the surface silanol groups decompose to surface siloxane groups (≡ Si – O – Si ≡) and water. A decrease from 4.6 to ~ 1.8 OH – groups/nm^2 was reported for the employed temperature treatment (453-773 K) in vacuum [147]. Furthermore, the temperature of 453-463 K was discussed as the characteristic temperature where dehydration (in vacuum) is complete and a "dry" and fully hydroxylated SiO_2 surface (maximum Si-OH) is present.

Differences in the temperature ranges reported here compared to those reported by Zhuravlev may be due to deviating measurement methods. Here, TG experiments with a constant flow of 50 ml/min 20% O_2 in He were conducted. The similarity of the thermograms of SBA-15 and V_xO_y/SBA-15 did not allow a discussion of the dehydration of hydrated vanadium oxide species and the dehydration of the SBA-15 support independently from each other.

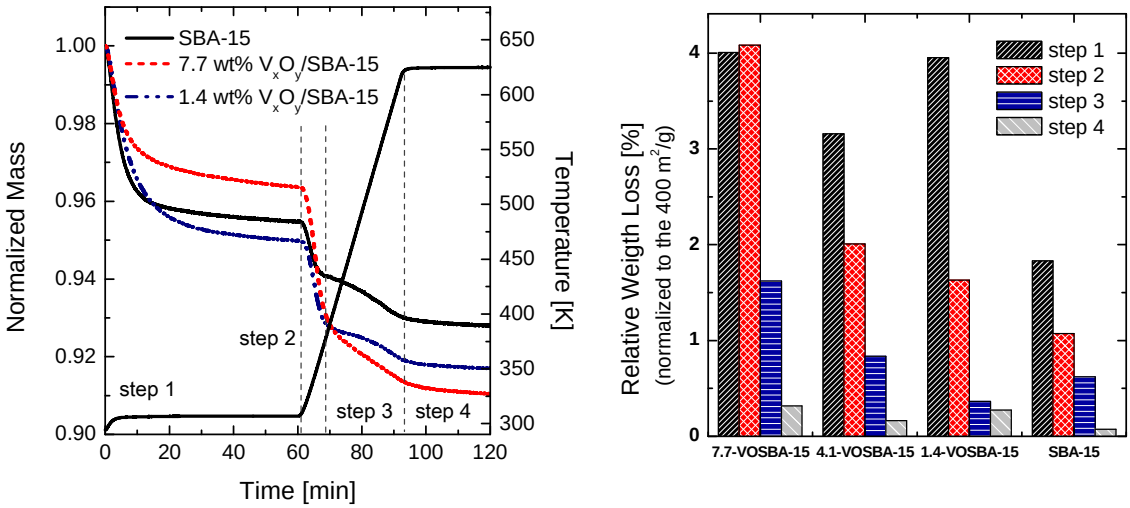

Figure 6-5 Left: Thermograms of bare and V_xO_y/SBA-15 samples. Right normalized relative mass loss detected for the observed steps derived from the thermograms (left side).

A comparison of the relative mass loss is depicted in ***Figure 6-5, right***. The mass loss was referred to a BET surface area of 400 m^2/g. The highest total mass loss of ~ 10.0% (400 m^2/g) was detected for 7.7 wt% V_xO_y/SBA-15. A total mass loss of ~ 6.2% (400 m^2/g) was detected for 4.1 wt% and 1.4 wt% V_xO_y/SBA-15 and a mass loss of 3.6% (400 m^2/g) for bare SBA-15. Thus, the presence of vanadium on the SBA-15 support allows the adsorption of a higher amount of water on the same surface area as on bare SBA-15. Comparing the mass loss of the individual steps showed that step 1 and step 4 seemed to be independent of the vanadium loading on the catalyst. The loss of mass in step 2 and step 3 decreased with decreasing vanadium loading on SBA-15. Thus, in these steps the additional adsorption of water in hydrated V_xO_y/SBA-15 played a pronounced role. The temperature range of step 2 was 303-380 K. In this range the structure transformation from the hydrated to the dehydrated state was observed in the UV-Vis-DR and XANES spectra. Hence, the additional water, compared to bare SBA-15, was adsorbed or bound in the structure of hydrated V_xO_y/SBA-15. The water evolution in step 3 may originate from a further water evolution from the vanadium oxide species or from the dehydroxylating SBA-15 support. Which of these processes is more likely cannot be determined solely from the thermograms. The *in situ* UV-Vis-DRS and XAS measurements indicated that in this temperature range (400-600 K) structural changes were still proceeding. These were ascribed to the formation and ordering of the tetrahedral dehydrated V_xO_y/SBA-15 phase.

6.2.5 Determination of the apparent activation energy of water desorption - E_D

The apparent activation energy for step 2 was determined to reveal the effect of the vanadium oxide on the water desorption process. A method according to Vansant *et al.* [104] was chosen. The maximum of the differential thermogravimetry (DTG signal) was used to determine a maximum rate temperature (T_{max}) as a function of the heating rate (β = 2,4,6,8,10 K/min). By using an Arrhenius type plot the apparent activation energy for water desorption (E_D) was determined from these values, ***Figure 6-6***. In addition to bare SBA-15 a measurement of Kieselgel 60 (reference used by Vansant *et al.* [104]) was conducted. ***Figure 6-6*** depicts the Arrhenius plots for the 7.7 wt% V_xO_y/SBA-15 sample. Desorption energies are listed in ***Table 6-1***. An apparent desorption energy of 40 kJ/mol was determined for Kieselgel 60, in agreement with the values reported by Vansant *et al.* [104].

Table 6-1: Apparent activation energies of water desorption E_d determined from the plot of $\ln(T_{max}^2/\beta)$ as a function of $1/T_{max}$ (***Figure 6-6***), * freshly calcined sample, ** two year old sample.

	E_D [kJ/mol]	
Sample	bare silica support	V_xO_x/SBA-15
7.7 wt% V_xO_y-SBA-15	111 ± 7	83 ± 10* (91 ± 7)**
4.1 wt% V_xO_y-SBA-15	--	72 ± 5
1.4 w% V_xO_y-SBA-15	101 ± 12	75 ± 7
Kieselgel 60	40 ± 9	--

Vansant *et al.* [104] compared this value with "the latent vaporization heat of water (ΔH_v=41 kJ/mol)" and approximated that the "desorption of water can be depicted as vaporization of liquid water out of the silica pores". However, comparing the value obtained for Kieselgel 60 with the one detected for SBA-15 a significantly higher apparent desorption energy was detected for the SBA-15 support (~100-110 kJ/mol). This indicated that a pronounced interaction of physically adsorbed water and SBA-15 was present. One possible explanation may be a "strengthening of the hydrogen bonding" of adjacent hydroxyl groups in small pores [104]. This may result in a higher density of surface silanol groups and an increased interaction of the silanol groups with the physically adsorbed water. Therefore, the pore structure of SBA-15, consisting of meso- and micropores, could cause the higher desorption energy. Vanadium oxide supported on SBA-15 exhibited a lower apparent desorption energy of 72-83 kJ/mol. This lower value may be caused either by a decreased surface area and a changed distribution of pores after APTES functionalization and vanadium grafting or by the pronounced effect of the adsorbed water to the structure of hydrated samples. The comparison of the relative mass losses in ***Figure 6-5*** suggests that the water evolution in step 2 may be more likely explained by the dehydration of the supported hydrated vanadium oxide species than by the dehydration of the silica support. Therefore, the apparent energy of water desorption is mostly due to loss of water from the hydrated V_xO_y/SBA-15 structure.

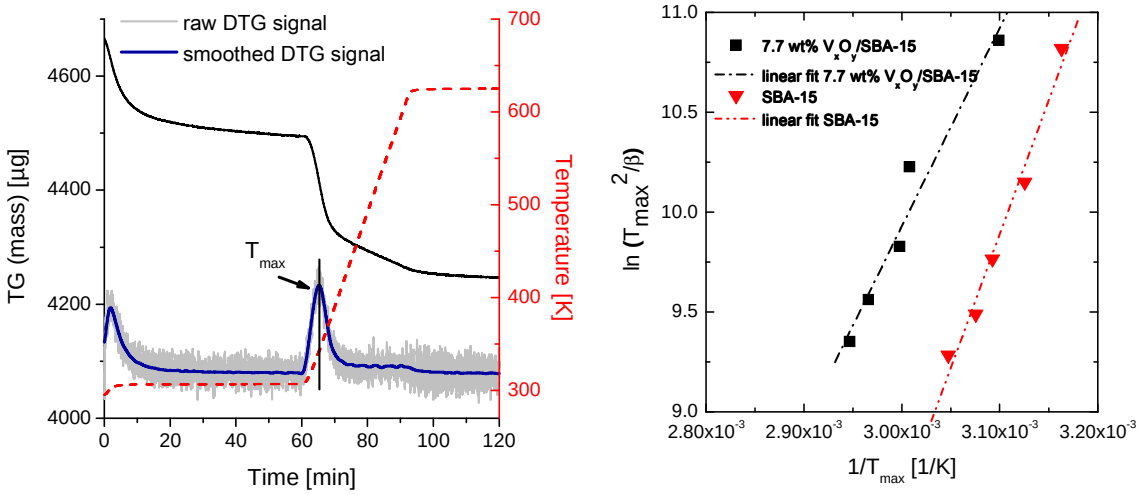

Figure 6-6 Left: TG and DTG signals recorded for 7.7 wt% V_xO_y/SBA-15 (10 K/min, 623 K), location of T_{max} is indicated; right: plot of $\ln(T_{max}^2/\beta)$ as a function of $1/T_{max}$ for bare SBA-15 and 7.7 wt% V_xO_y/SBA-15.

6.2.6 Types of silanol groups on the SiO_2 support – ^{29}Si CP-MAS-NMR

However, no direct information about the changes of the SiO_2 support was obtained from the TG measurements. Hence, ^{29}Si MAS-NMR measurements were conducted for SBA-15 and for hydrated and dehydrated 7.7 wt% V_xO_y/SBA-15. In ***Figure 6-7, left*** the possible types of Si atoms that can be distinguished are depicted schematically. Internal Si atoms that are located in SiO_4 tetrahedrons are denoted as Q^4 centers and have a chemical shift of -110 ppm. Si centers with geminol silanol groups

(HO-SiO_2-OH) are termed as Q^2 centers and they have a chemical shift of -90 ppm. In the case of isolated (HO-SiO_3) or vicinal silanol groups (O_3Si-OH·····HO-SiO_3) a chemical shift of -102 ppm was observed, and the Si centers are denoted as Q^3 centers. The resulting spectra are depicted in ***Figure 6-7, right***. Approximately 35% of the MAS-NMR signal of bare SBA-15 was due to Si centers exhibiting OH groups. In the MAS-NMR spectrum of hydrated 7.7 wt% V_xO_y/SBA-15 the fraction of Si centers with OH groups decreased to 16%. Geminol type Si centers (Q^2) were hardly detectable. This lower amount of Si-OH groups suggests that the missing fraction of Si-OH groups may have formed bonds to the hydrated vanadium centers (Si-O-V). Similar results were reported by Dzwigaj *et al.* [146].

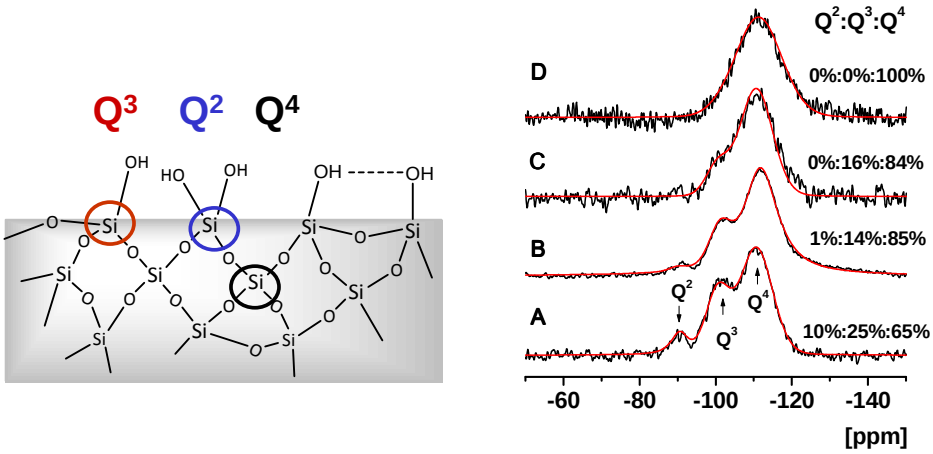

Figure 6-7 Left: A picture of different types of silanol groups of silica materials; right: ^{29}Si CP-MAS-NMR of bare and 7.7 wt% V_xO_y/SBA-15 treated at different temperatures: (A) bare SBA-15, (B) hydrated 7.7 wt% V_xO_y/SBA-15, (C) dehydrated 7.7 wt% V_xO_y/SBA-15 (653 K, 1 h), (D) calcined 7.7 wt% V_xO_y/SBA-15 (843 K, 12 h). The red curve is the envelope of the Gaussian deconvolution.

Thermal treatment according to the standard dehydration procedure at 653 K (1 h hold, 20% O_2 in He) did not significantly change the number of silanol-type Si centers in the sample. Differences compared to the hydrated sample are within the error of the refinement procedure employed. Therefore, the number of Si-O-V bond formed did not change during the dehydration process. Nevertheless, a light yellowish color was observed for dehydrated 7.7 wt% V_xO_y/SBA-15 (653 K, 1 h), which may be explained by aging effects (see below). No signal for Q^3 and Q^2 type Si centers was detected for a higher dehydration temperature of 843 K, as used in the calcination (823 K, 12 h, 20% O_2 in He). Recalcined 7.7 wt% V_xO_y/SBA-15 exhibited a white color after high temperature treatment. A decrease of silanol type Si centers can be explained by a pronounced dehydroxylation of the silica SBA-15. However, this did not explain the total absence of any silanol type Si centers. According to Zhuravlev [147], the number of silanol groups could be reduced by a thermal treatment at 843 K but a complete dehydroxlation of silica would only be achieved at temperatures higher than 1173 K (vacuum). Hence, in addition to the dehydroxylation of the SBA-15 support, a certain fraction of silanol groups formed Si-O-V bonds with the vanadium oxides species.

6.2.7 The hydration process

Typically, freshly calcined samples changed their color from white to yellow and orange after exposure to air under ambient conditions. This process is denoted as hydration. To investigate the hydration process a rehydration of the dehydrated V_xO_y/SBA-15 samples was conducted at room temperature. The gases used were saturated with water for rehydration. A water content of 1.3-1.6 Vol% in the gas phase was achieved, which equals the humidity of ambient air. ***Figure 6-8, left*** depicts the V K pre-edge peak height and the water in the gas phase (m/e 18) as a function of time. The inset shows the corresponding XANES spectra. ***Figure 6-8, right*** shows the evolution of the UV-Vis edge energy and the water detected in the gas phase (m/e 18). Apparently, hydration of the vanadium oxide species of dehydrated V_xO_y/SBA-15 started immediately after water was detectable in the gas phase. During the hydration process a decrease of the pre-edge peak height and an increase in intensity in the XANES spectra (5.48-5.49 keV) was observed. Furthermore, after exposure to water, a decrease of the UV-Vis edge energy from 3.4 eV to 2.8 eV was detected. Both, the decrease of the V K edge pre-edge peak height and the decreasing UV-Vis edge energy showed that the hydrated phase of V_xO_y/SBA-15 was formed immediately after exposure to water. The transformation was completed after approximately 2-3 minutes, indicated by a constant pre-edge peak height in the XANES spectra. The main decrease in the UV-Vis edge energy was reached after 2 min. After a longer period of time (60 min) only a small decrease (< 0.1 eV) was detected compared to the value after 2 minutes. This rapid transformation during rehydration is explained by the strong distortion of the vanadium oxide tetrahedrons formed on the SBA-15 support. An average V-O distance of 1.78 Å was determined for the V_xO_y/SBA-15 samples investigated here. Typical average V-O bond lengths of bulk vanadates are shorter, in the range of 1.70 Å ($Ca_3V_2O_8$) to 1.74 Å (KVO_3). Furthermore, a small Si-O-V distance (2.53 Å) was determined by XAFS refinement, which may explain the strong distortion. Coordination of an additional ligand (H_2O) may cause a decrease in the tension present in the distorted tetrahdral structure of dehydrated V_xO_y/SBA-15 and, thus, explain the rapid hydration of dehydrated vanadium centers in V_xO_y/SBA-15.

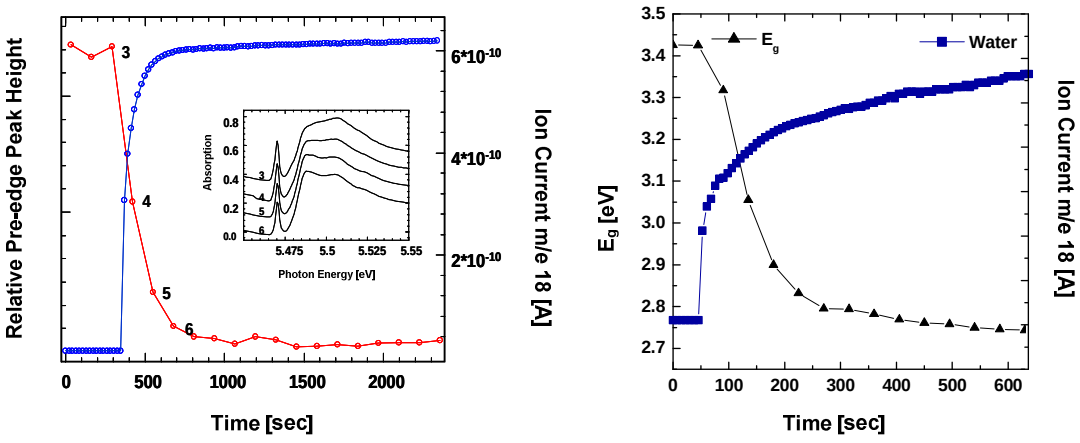

Figure 6-8 Left: V K edge XANES spectra (inset), pre-edge peak height and water ion current during rehydration of dehydrated 7.7 wt% V_xO_y/SBA-15 (298 K, 1.6 Vol% H_2O). Right: UV-Vis edge energy and water ion current during rehydration of dehydrated 7.7 wt% V_xO_y/SBA-15 (298 K, 1.3 Vol% H_2O).

6.2.8 *Reversibility of hydration and dehydration processes*

The reversibility of the structural transformations of hydrated and dehydrated V_xO_y/SBA-15 was investigated in cyclic reaction tests. As prepared V_xO_y/SBA-15 samples were dehydrated in a 20% O_2 in helium atmosphere (623 K for XAS, 554 K for UV-Vis-DRS analysis) and subsequently rehydrated for 0.5-1 h at ~ 298 K using a saturated gas atmosphere (1.3-1.6 Vol% H_2O in He). A second cycle was conducted after this first dehydration/rehydration cycle. The second dehydration was performed at higher temperatures (723 K for XAS, 634 K for UV-Vis-DRS analysis). ***Figure 6-9*** depicts the FT(χ(k)*k^3) of 7.7 wt% V_xO_y/SBA-15 (XAFS) and UV-Vis-DR spectra of 1.4 wt% V_xO_y/SBA-15 measured at ~ 298 K after the respective treatment. Apparently, the spectra of dehydrated 7.7 wt% and 1.4 wt% V_xO_y/SBA-15 showed no differences when comparing the spectra of the first dehydration cycle with those of the second dehydration cycle. Hence, the dehydration process is reversible for the 7.7 wt% and 1.4 wt% V_xO_y/SBA 15. A more detailed discussion will be given below. Comparing the results obtained for hydrated 7.7 wt% and 1.4 wt% V_xO_y/SBA-15, minor deviations were observed after each rehydration cycle. As prepared 1.4 wt% V_xO_y/SBA-15 showed the lowest intensity of the low energy absorption band at ~ 360 nm compared to the more intense absorption band at 280 nm. Thus, a "higher degree of hydration" was present in hydrated 1.4 wt% V_xO_y/SBA-15 after the first and second rehydration cycles. Furthermore, this was corroborated by a decline of the UV-Vis edge energy of the hydrated V_xO_y/SBA-15 samples after each rehydration cycle (***Table 6-2***). A similar trend was observed in the FT(χ(k)*k^3) of 7.7 wt% V_xO_y/SBA-15. The as prepared sample showed a significantly lower amplitude in the range of 2-4 Å. According to ***Chapter 5***, the amplitude in this range is caused by V-V interactions that are found in the structure of hydrated 7.7 wt% V_xO_y/SBA-15. The higher intensity in the range of 2-4 Å after the first rehydration cycle (~ 45 min) may indicate the formation of an increased number of V-O-V bonds.

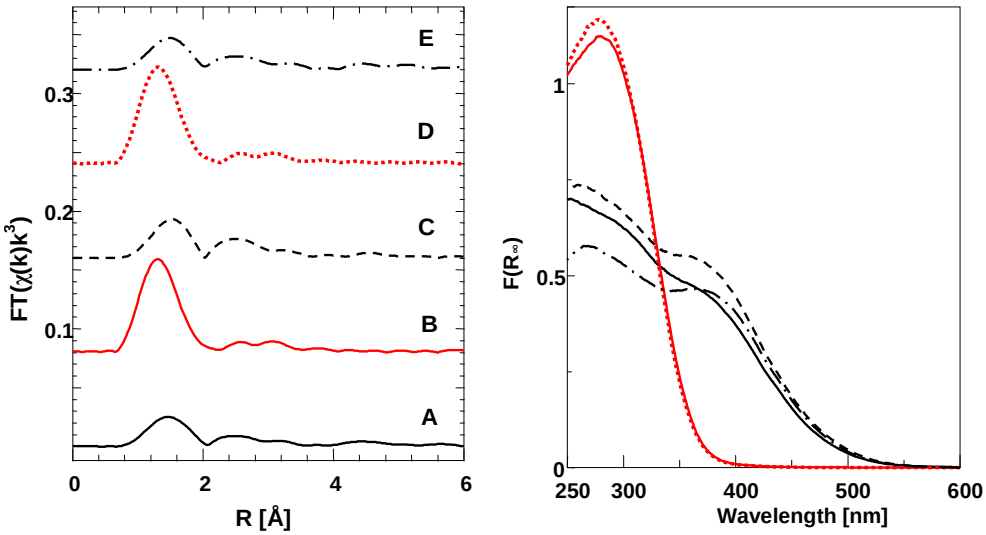

Figure 6-9: FT(χ(k)*k^3) of 7.7 wt% V_xO_y/SBA-15 (left) and UV-Vis-DR spectra of 1.4 wt% V_xO_y/SBA-15 (right) after various hydration and dehydration cycles: as prepared (A); first dehydration at 623 K/ XAS, 554 K/ UV-Vis-DRS, 30 min (B); first rehydration, 1.3-1.6 Vol% 60-90 min (C); second dehydration at 723 K/ XAS, 634 K/ UV-Vis-DRS, 1 h (D); second rehydration, 1.3-1.6 Vol%, 60 min (E). The line types on right side refer to the same procedure as on the left side.

Table 6-2: UV-Vis edge energy E_g of hydrated V_xO_y/SBA-15 samples determined after various rehydration procedures. Dehydration treatments as described in ***Figure 6-9***.

	E_g [eV]		
Sample	as prepared	1. rehydration	2. rehydration
7.7 wt% V_xO_y-SBA-15	2.74	2.71	2.67
4.1 wt% V_xO_y-SBA-15	2.79	2.76	2.73
1.4 wt% V_xO_y-SBA-15	2.80	2.79	2.77

6.2.9 Impact of aging on the structure of V_xO_y/SBA-15

An increasing V-V signal at 2-4 Å in the FT(χ(k)*k^3) was observed in the XAFS spectra of hydrated 7.7 wt% V_xO_y/SBA-15 measured at different times. ***Figure 6-10*** depicts the FT(χ(k)*k^3) of hydrated samples measured after two weeks and after two years following preparation. For comparison, the FT(χ(k)*k^3) of V_2O_5 and the rehydrated samples are also depicted. Rehydration experiments were conducted using the two week old 7.7 wt% V_xO_y/SBA-15. The first signal (V-O tetrahedron) in the FT(χ(k)*k^3) of as-prepared 7.7 wt% V_xO_y/SBA-15 was asymmetric, thus, part of the dehydrated phase was still present. A least-squares XANES refinement was conducted to quantify the remaining fraction of dehydrated phase in the spectrum of the two week old 7.7 wt% V_xO_y/SBA-15. Spectra recorded after the first dehydration and after the first rehydration cycle of 7.7 wt% V_xO_y/SAB-15 were used as references. Approximately 18% of the dehydrated phase was present in the spectrum of two week old as-prepared 7.7 wt% V_xO_y/SBA-15. A similar trend was observed for 4.1 wt% and 1.4 wt% V_xO_y/SBA-15. The presence of dehydrated V_xO_y/SBA-15 two weeks after preparation suggests that hydration of freshly calcined samples is significantly slower (weeks) than rehydration of dehydrated samples (~ 1 hour).

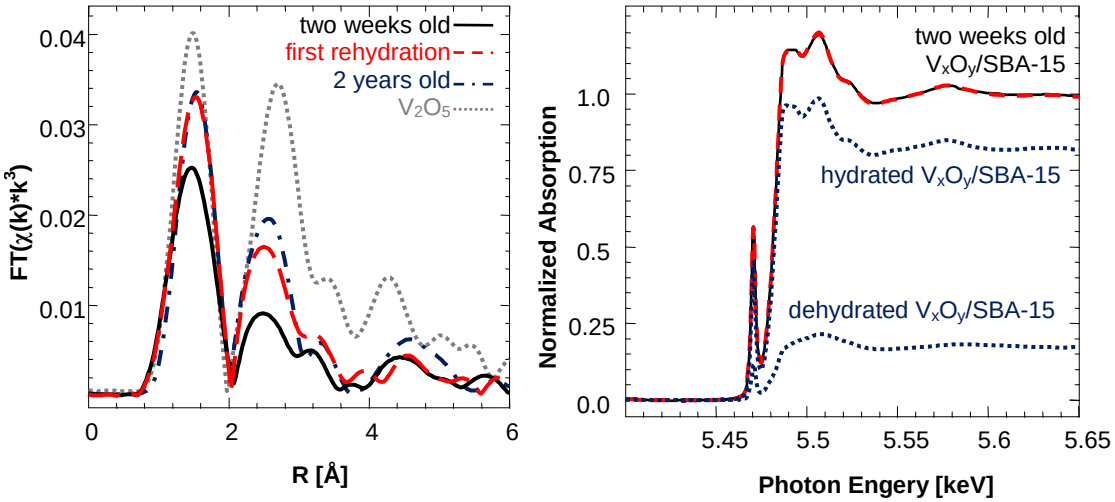

Figure 6-10 Left: FT(χ(k)*k^3) of differently hydrated 7.7 wt% V_xO_y/SBA-15 and V_2O_5. Right: result of the least-squares fit (_ _ _ _) using the V K edge XANES spectra of dehydrated and rehydrated 7.7 wt% V_xO_y/SBA-15 (.....) recorded after the first de-/rehydration cycle (***Figure 6-9, left***) to the experimental XANES spectrum (_____)of two week old as-prepared 7.7 wt% V_xO_y/SBA-15.

Figure 6-11, left shows the UV-Vis-DR spectra of one year old 7.7 wt% V_xO_y/SBA-15 and recalcined 7.7 wt% V_xO_y/SBA-15. On the right side of ***Figure 6-11*** spectra of 1.4 wt% V_xO_y/SBA-15 measured as-prepared and one year later are depicted. (Spectra of 1.4 wt% V_xO_y/SBA-15 were normalized because the as prepared sample was diluted with SBA-15.) An increase of the absorption band at 370 nm in the UV-Vis-DR spectra of the hydrated samples was observed for both loadings. In ***Chapter 5*** this band was assigned to vanadium centers exhibiting a square pyramidal structure. Concidering the intensity increase in the FT(χ(k)*k^3) of 7.7 wt% V_xO_y/SBA-15 at higher distances (2-4 Å), the increase of the band at 370 nm may be caused by an increased number of "hydrated" square pyramidal vanadium centers. This aging effect was interpreted as clustering of hydrated centers on the SBA-15 support. Significant changes of the UV-Vis edge energy in the spectra of hydrated V_xO_y/SBA-15 were not detected. Thus, the average V-O-V number remained three (chains of square pyramidal centers) and the dispersion of hydrated vanadium oxide species remained high. The extension of the hydrated vanadium oxide species on SBA-15 seems to be two-dimensional rather than three-dimensional as in the case of vanadium oxide crystallites.

The "growth" of hydrated V_xO_y species on SBA-15 during storage raised the question whether aging of hydrated V_xO_y/SBA-15 affected the dehydration of V_xO_y/SBA-15. Thermal treatment at 554 K (30 min) of those differently hydrated V_xO_y/SBA-15 samples yielded UV-Vis-DR spectra that were characteristic for dehydrated V_xO_y/SBA-15 (***Figure 6-11***). However, in the case of an one year old 7.7 wt% V_xO_y/SBA-15 a broadening of the absorption band in the UV-Vis-DR spectrum was observed. Such broadening was absent in the UV-Vis-DR spectrum of one year old dehydrated 1.4 wt% V_xO_y/SBA-15.

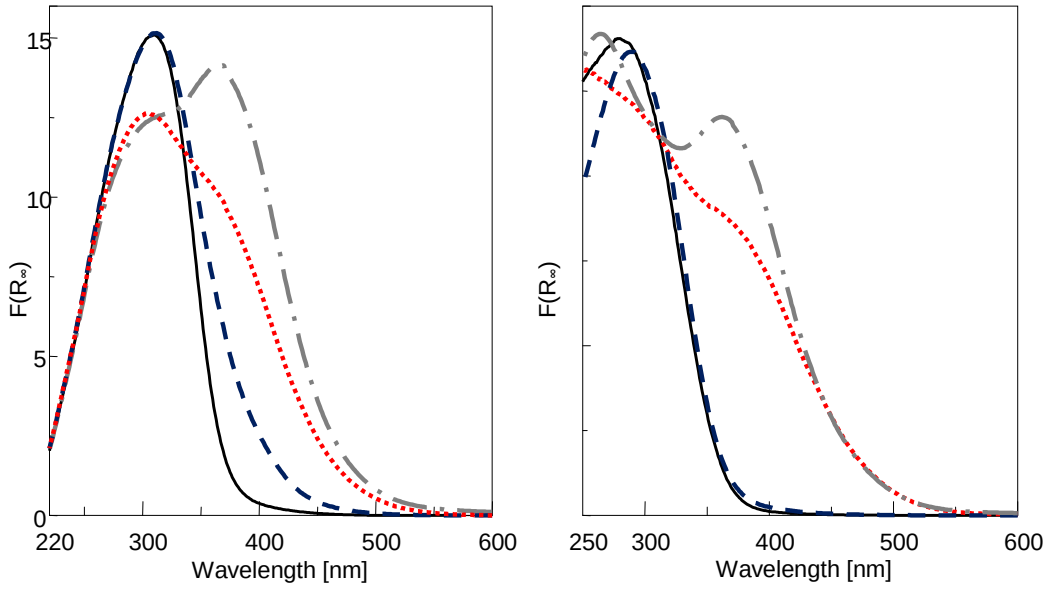

Figure 6-11: UV-Vis-DR spectra of 7.7 wt% V_xO_y/SBA-15 (left) and 1.4 wt% V_xO_y/SBA-15 (right): as-prepared (1.4 wt%)/ hydrated after calcination (7.7 wt%) (.....); dehydrated "as-prepared" sample (_____); hydrated one year old sample (_ . _); dehydrated one year old sample (_ _ _ _); dehydration parameters: 20% O_2 in He, 554 K, 30 min, all spectra recorded at 298 K.

Similar broadening effects in the absorption spectra of dehydrated V_xO_y/SBA-15 were reported by Gruene *et al.* [28]. They assigned the UV-Vis band at 405 nm to small V_2O_5 clusters present on SBA-15 because characteristic bands of V_2O_5 were present in the Raman spectra of these samples (0.6-3.1 V/nm^2 V on SBA-15). These V_2O_5 clusters were not detectable by XRD [28]. Similar results were obtained for 7.7 wt% V_xO_y/SBA-15 (2.5 V/nm^2) here, using *in situ* Raman spectroscopy. The Raman spectrum of dehydrated 7.7 wt% V_xO_y/SBA-15 (723 K, ~ 1 h) is shown in ***Figure 6-12, left***. Apart from a characteristic Raman signal of the dehydrated V_xO_y/SBA-15 species at ~ 1040 cm^{-1} [23,32] several other Raman bands were detected. Comparison with the Raman spectrum of a mechanical mixture of V_2O_5 and SBA-15 (~ 3 wt% V, 298 K) showed that characteristic bands of V_2O_5 (284, 305, 407, 703 and 994 cm^{-1}) were present in the spectrum of the one year old V_xO_y/SBA-15 sample. The amount of V_2O_5 was estimated according to Xie *et al.* [34] assuming a 10 times larger cross section for V_2O_5 compared to the dispersed tetrahedral species. Comparing the intensities of the Raman signal at 995 and 1042 cm^{-1} shows that approximately 3% V_2O_5 have been formed by dehydration of aged 7.7 wt% V_xO_y/SBA-15.

To investigate the impact of a recalcination on "aged" 7.7 wt% V_xO_y/SBA-15 thermal treatment for 12 h at 823 K in a muffle furnace was conducted. After recalcination and dehydration of 7.7 wt% V_xO_y/SBA-15 characteristic V_2O_5 bands were absent in the Raman spectrum. Thus, formation of V_2O_5 clusters on the SBA-15 support during dehydration seems to be a reversible process. To estimate the fraction of V_2O_5 in the UV-Vis-DR spectra a least-squares refinement using three Gaussian curves was performed. Two Gaussian functions were introduced for the dehydrated phase according to the calculation of Avdeev *et al.* [136].The Gaussian curves were allowed to vary between 270 and 290 nm and between 300 and 330 nm. A third Gaussian function in the range of 390-430 nm was introduced to account for V_2O_5.

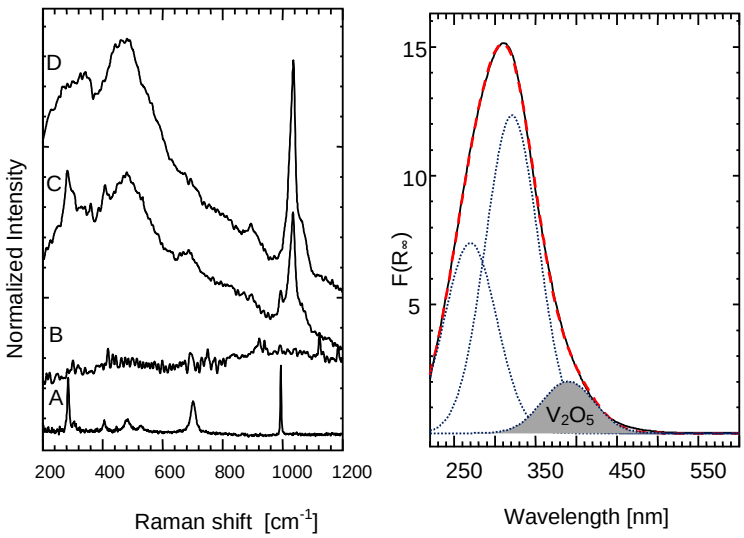

Figure 6-12 left: Raman spectra of (A) a 3 wt% V V_2O_5:SBA-15 mixture (1064 nm, 100 mW) and (B) SBA-15 and *in situ* spectra (514 nm, 6 mW) during dehydration of (C) one year old 7.7 wt% V_xO_y/SBA-15 at 723 K (20% O_2 in N_2) and (D) a 7.7 wt% V_xO_y/SBA-15 sample that is dehydrated at 623 K (20% O_2 in N_2) after recalcination at 823 K for 12 h in a muffle furnace; (spectra C-D, 514 nm, 6 mW); right: least square fit (_ _ _) of three Gaussian functions (.....) to the UV-Vis-DR spectrum (____) of dehydrated one year old 7.7 wt% V_xO_y/SBA-15 (554 K, 30 min, 20% O_2 in He).

Peak heights were allowed to vary between 0 and 20 Kubelka Munk units and the full band width was allowed to vary independently for each Gaussian function. The resulting refinement yielded a good agreement between experimental and refined curves as depicted in ***Figure 6-12, right***. For the one year old sample approximately 10% of the area of the UV-Vis-DR signal was caused by V_2O_5. In dehydrated 7.7 wt% V_xO_y/SBA-15, which was recalcined, this fraction was reduced to below 1% (***Figure 6-11***). However, after storage of the recalcined sample for several days the fraction of V_2O_5 increased again. After 7 days a fraction of 6-7% was determined. The real concentrations will be lower because a strong decrease of intensity was measured below 300 nm in the UV-Vis-DR spectra obtained with the Praying Mantis™ cell. Moreover, the amount of V_2O_5 determined from the Raman spectra was lower.

In XAFS spectra no significant changes with storage time were observed for dehydrated 7.7 wt% V_xO_y/SBA-15. The FT(χ(k)*k^3) exhibited a small decrease of the first V-O signal in the range of 1.6-2.0 Å. The disorder parameter of the V-O distance at 1.78 Å increased from 0.0071 $Å^2$ (***Table 6-3***) to 0.0079 $Å^2$ in two year old dehydrated V_xO_y/SBA-15 (***Table 6-3***). After a treatment of 8 h at 770 K the amplitude in the FT(χ(k)*k^3) of two year old dehydrated 7.7 wt% V_xO_y/SBA-15 increased. The disorder parameter of the V-O distance at 1.78 Å decreased from 0.0079 $Å^2$ to 0.0063 $Å^2$. A similar trend was observed for V-V and V-Si contributions. The overall increase of the disorder parameters of two year old 7.7 wt% V_xO_y/SBA-15 showed that the structure of dehydrated vanadium species was less ordered after dehydration. However, all experimental FT(χ(k)*k^3) of dehydrated 7.7 wt% V_xO_y/SBA-15 were simulated successfully using the dehydrated V_xO_y model structure (ordered arrangement of [V_2O_7], ***Table 6-3***). Hence, the major vanadium oxide phase in dehydrated 7.7 wt% V_xO_y/SBA-15 was still the dimeric tetrahedral species. For the 4.1 wt% V_xO_y/SBA-15 a similar aging effect was observed in the UV-Vis-DR spectra. As a consequence of the aging effect discussed above the presence of V_2O_5 was never fully excluded for dehydrated 4.1 wt% and 7.7 wt% V_xO_y/SBA-15 during further experiments.

Table 6-3: Experimental distances (R) and XAFS disorder parameters (σ^2) for different type and number (N) of atoms at distance R from the absorbing V atom in a model system assuming an ordered arrangement of [V_2O_7] units (***Chapter 5***). Parameters were obtained from the refinement of this model structure to the experimental V K edge XAFS FT(χ(k)*k^3) of dehydrated 7.7 wt% V_xO_y/SBA-15 at various stages of aging (k range from 2.7-10.5 $Å^{-1}$, R range 0.83-3.62 Å, N_{ind} = 16, E_0 = 0 eV in all cases, (subscript c indicates parameters that were correlated in the refinement, subscript f indicates parameters that were fixed in the refinement). Dehydration was conducted in 20% O_2 in He.

Type (N)	2 weeks old 623 K, 30 min		2 years old 623 K, 30 min		recalcined 770 K, 8 h	
	R [Å]	σ^2 [$Å^2$]	R [Å]	σ^2 [$Å^2$]	R [Å]	σ^2 [$Å^2$]
V-O (4)	1.78	0.0071	1.78	0.0079	1.78	0.0063
V-O (1)	2.90	0.0012_f	2.89	0.0012_f	2.89	0.0012_f
V-V (1)	3.29	0.0094	3.29	0.0116	3.30	0.0107
V-V (1)	3.61	0.0094_c	3.60	0.0116_c	3.60	0.0107_c
V-Si (1)	2.55	0.0116	2.54	0.0130	2.53	0.0112
Residual	6.6		3.8		5.9	

6.2.10 Dehydration in water saturated atmospheres

Because water is a common reactant in propene oxidation its influence on the dehydration was investigated. At moderate temperatures (298 K) and in humid atmospheres the hydrated structure of V_xO_y/SBA-15 was the major vanadium oxide phase present on the support. A comparable treatment as used for dehydration (623 K, 20% O_2 in He) was employed to investigate the structure that was present at elevated temperatures in humid atmospheres. In addition, the helium carrier gas was saturated with water to obtain a humidity of 1.3-1.6 Vol% water in the gas phase. The UV-Vis-DRS and XAS measurements were performed after the rehydration/dehydration cycles reported above. After the second rehydration the samples were heated in a water saturated oxygen atmosphere to 623 K (XAS) or 554 K (UV-Vis-DRS). The *in situ* spectra recorded at the respective temperatures are shown in ***Figure 6-13***.

The FT(χ(k)*k^3) of 7.7 wt% V_xO_y/SBA-15 obtained during treatment with water vapor and after switching the water off at 623 K is depicted in ***Figure 6-13 (left)***. Furthermore, the FT(χ(k)*k^3) measured at 298 K after thermal treatment is shown together with the FT(χ(k)*k^3) recorded at 298 K after the first dehydration in dry atmosphere. Apparently, no significant differences were observed. XAFS refinements using the "dimeric V_2O_7" model structure yielded good agreement between the experimental and refined theoretical FT(χ(k)*k^3). The resulting parameters are listed in ***Table 6-4***. The results obtained during the thermal treatment at 623 K in the presence of water (3rd dehydration cycle) and the results obtained after switching the water off at 623 K were similar. Further, no significant differences were observed after cooling the sample down. The σ^2 of the V-O contribution at 1.78 Å was slightly enhanced, which was assigned to thermal disorder effects.

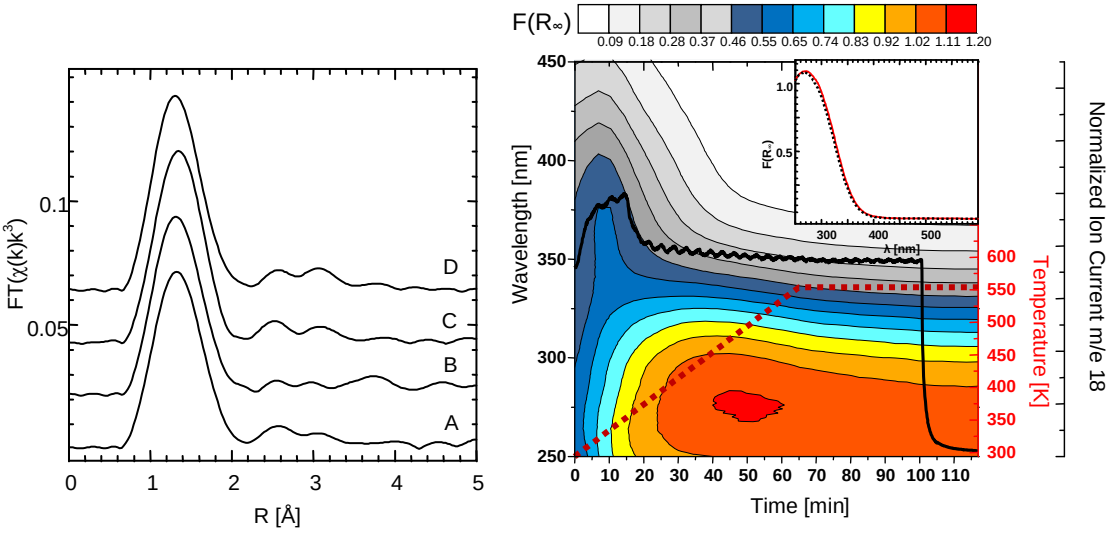

Figure 6-13 Left: V K edge FT(χ(k)*k^3) of 7.7 wt% V_xO_y/SBA-15 after different dehydration procedures: 623 K, 10% O_2/1.6 Vol% H_2O/He (A); 623 K, 10% O_2/He (B); 298 K, 10% O_2/He (C) and 1st dehydration cycle (623 K, 20% O_2/He) 298 K (D). Right: *in situ* UV-Vis-DR spectra of the 1.4 wt% V_xO_y/SBA-15 sample during dehydration together with water ion current m/e 18 (554 K, 4 K/min,1.3 Vol% H_2O, 20% O_2 in He). The inset shows the 2D spectra recorded at 86 min and 113 min.

Table 6-4: Experimental distances and XAFS disorder parameters (σ^2) for different type and number (N) of atoms at distance R from the absorbing V atom in a model system assuming an ordered arrangement of $[V_2O_7]$ units (***Chapter 5***). Parameters were obtained from the refinement of this model structure to the experimental V K edge XAFS FT(χ(k)*k^3) of dehydrated 7.7 wt% V_xO_y/SBA-15 (k range from 2.7-10.5 $Å^{-1}$, R range 0.83-3.62 Å, N_{ind} = 16, E_0 = 0 eV in all cases, (subscript c indicates parameters that were correlated in the refinement, subscript f indicates parameters that were fixed in the refinement). Dehydration in the 1st and 2nd cycle was conducted in 20% O_2 in He and in 10 % O_2 (and 1.6 % H_2O) in He in the 3rd dehydration cycle.

Type (N)	1st dehydration cycle 298K (30min, 623K)		2nd dehydration cycle 298K (60min, 723K)		3rd dehydration cycle 623K (H_2O)		623K (H_2O off)		298K (H_2O off)	
	R [Å]	σ^2 [$Å^2$]	R [Å]	σ^2 [$Å^2$]	R [Å]	σ^2 [$Å^2$]	R [Å]	σ^2 [$Å^2$]	R [Å]	σ^2 [$Å^2$]
V-O (4)	1.78	0.0071	1.78	0.0066	1.79	0.0079	1.78	0.0079	1.78	0.0070
V-O (1)	2.90	0.0012_f	2.89	0.0012_f	2.88	0.0012_f	2.88	0.0012_f	2.88	0.0012_f
V-V (1)	3.29	0.0094	3.30	0.0095	3.31	0.0123	3.27	0.0131	3.30	0.0129
V-V (1)	3.61	0.0094_c	3.61	0.0095_c	3.61_f	0.0123_c	3.58_f	0.0131_c	3.61	0.0129_c
V-Si (1)	2.55	0.0116	2.53	0.0114	2.55	0.0119	2.53	0.0111	2.53	0.0133
Residual	6.6		5.1		5.3		7.8		5.3	

Hence, the dehydrated V_xO_y/SBA-15 phase was present on the SBA-15 support independent of water in the gas phase at elevated temperatures. *In situ* XANES spectra and PCA results were similar to those obtained in the first dehydration cycle in ***Figure 6-3*** (data not shown). In contrast to the XANES spectra, the disorder parameter of the V-V (3.3 and 3.6 Å) and V-Si (2.5 Å) contributions in the FT(χ(k)*k^3) increased slightly during the dehydration in the presence of water. Conversely, the disorder parameter of the V-O contribution at 1.78 Å remained constant (***Table 6-4***).

Figure 6-13 (right) depicts the evolution of the UV-Vis-DR spectra during the dehydration of 1.4 wt% V_xO_y/SBA-15 together with the evolution of the MS ion current of water (m/e 18). Water addition to the gas phase was stopped 35 min after reaching the maximum temperature of 554 K (total time 100 min). Compared to the spectra recorded during dehydration in a dry atmosphere, shown in ***Figure 6-2, left,*** no distinct changes were observed during thermal treatment of hydrated 1.4 wt% V_xO_y/SBA-15. The main transformation between the hydrated and the dehydrated V_xO_y/SBA-15 state was completed between 400 and 440 K. It was accompanied by an increased formation of water. At elevated temperatures the UV-Vis-DR spectra resembled those of dehydrated V_xO_y/SBA-15. The inset in ***Figure 6-13, right*** depicts the spectra recorded at 554 K in a water saturated atmosphere at 86 min (1.3 Vol% H_2O) and in a dry atmosphere at 113 min. After switching the water off only a small blue shift of 3 nm was observed. Compared to the UV-Vis edge energies obtained in the previous dehydration cycles only small changes were observed for all V_xO_y/SBA-15 samples (***Table 6-5***). The UV-Vis edge energy of dehydrated 4.1 wt% and 1.4 wt% V_xO_y/SBA-15 increased after each rehydration/dehydration cycle. This may be caused by a decreasing distortion of the $[VO_4]$ tetrahedron or a decreasing V-O-V number (2 to 1, dimeric to isolated VO tetrahedrons). These two effects cannot be distinguished sufficiently as discussed in ***Chapter 5***. Comparing UV-Vis-DR spectra of dehydrated V_xO_y/SBA-15 recorded at 298 K after several dehydration/rehydration cycles small changes were observed for the various vanadium loadings.

Table 6-5: UV-Vis edge energies E_g determined from the UV-Vis-DR spectra recorded at 298 K after different dehydration cycles (details given in ***Figure 6-14***). The samples were diluted with SBA-15 (1:3 (SBA-15 : 7.7 wt% V_xO_y/SBA-15) and 1:1 (SBA-15 : 1.4 wt% or 4.1 wt% V_xO_y/SBA-15)).

Sample	E_g [eV]		
	623 K 0.5 h 20% O_2/ He	723 K 1 h 20% O_2/ He	723 K 1 h 20% O_2/ He / 1.5 Vol% H_2O
7.7 wt% V_xO_y-SBA-15	3.37	3.40	3.41
4.1 wt% V_xO_y-SBA-15	3.44	3.45	3.52
1.4 w% V_xO_y-SBA-15	3.60	3.62	3.68

Similar spectra were recorded for dehydrated 1.4 wt% V_xO_y/SBA-15 after dehydration at 554 K and 634 K. After dehydration in a humid atmosphere at 554 K the UV-Vis-DR spectrum was blue shifted by several nm. The UV-Vis edge energy increased from 3.60 eV to 3.68 eV and the absorption maximum shifted from 280 nm to 265 nm. This strong blue shift to 265 nm suggests an increased dispersion in the presence of water during the dehydration process. Thus, more isolated vanadium oxide centers may have formed after this treatment. Similar blue shifted UV-Vis-DR spectra were recorded for higher loaded dehydrated V_xO_y/SBA-15. A blue shift from 305 nm to 290 nm was detected for 4.1 wt% dehydrated V_xO_y/SBA-15 and from 308 nm to 296 nm for 7.7 wt% V_xO_y/SBA-15 (***Figure 6-14***). According to the calculation by Avdeev *et al.* [136] the absorption band at 290 nm indicated that the dimeric tetrahedral V_xO_y/SBA-15 species was still present on the support as discussed in ***Chapter 5***. This was also corroborated by the results obtained from XAFS refinement of the FT(χ(k)*k^3) of 7.7 wt% dehydrated V_xO_y/SBA-15. However, for dehydrated 7.7 wt% V_xO_y/SBA-15 a significant increase in absorption intensity at 405 nm was detected during the third dehydration cycle in a humid atmosphere. Hence, V_2O_5 clusters may have formed during this process.

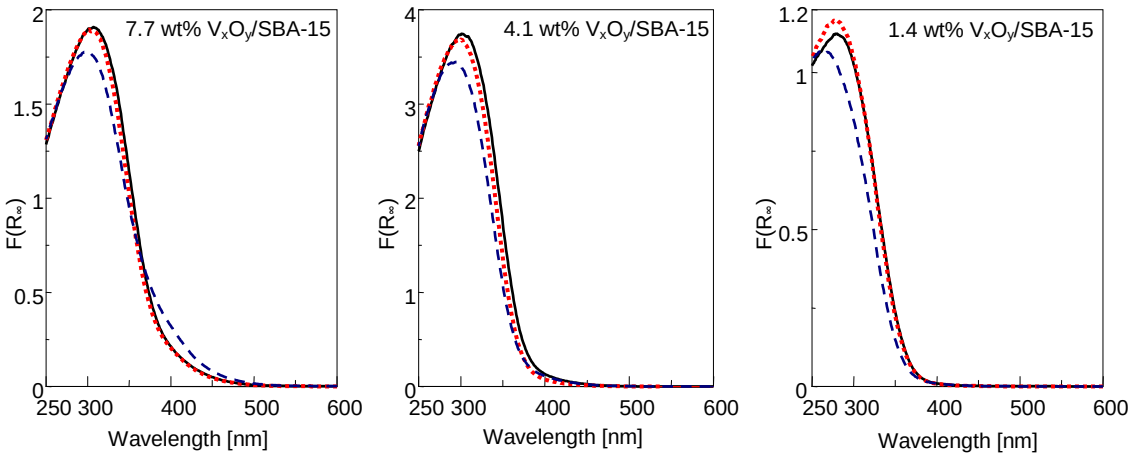

Figure 6-14: UV-Vis-DR spectra recorded at 298 K after different dehydration cycles: 1st dehydration at 554 K for 30 min (——); 2nd dehydration at 634 K for 1 h (.....); 3nd dehydration at 554 K for 30 min (1.3 Vol% H_2O) and 15 min ("dry") (– – –). The samples were diluted with SBA-15 (1:3 (SBA-15 : 7.7 wt% V_xO_y/SBA-15) and 1:1 (SBA-15 : 1.4 or 4.1 wt% V_xO_y/SBA-15)).

6.3 Concluding remarks on the hydration and dehydration of V_xO_y/SBA-15

In situ UV-Vis-DRS and XAFS measurements showed that V_xO_y/SBA-15 samples changed their structure dynamically as a function of temperature, water content in the gas phase, and vanadium loading. Moreover, changes in the silanol distribution of the SiO_2 support played a pronounced role. The scheme depicted in ***Figure 6-15*** is introduced to summarize and discuss the results presented above.

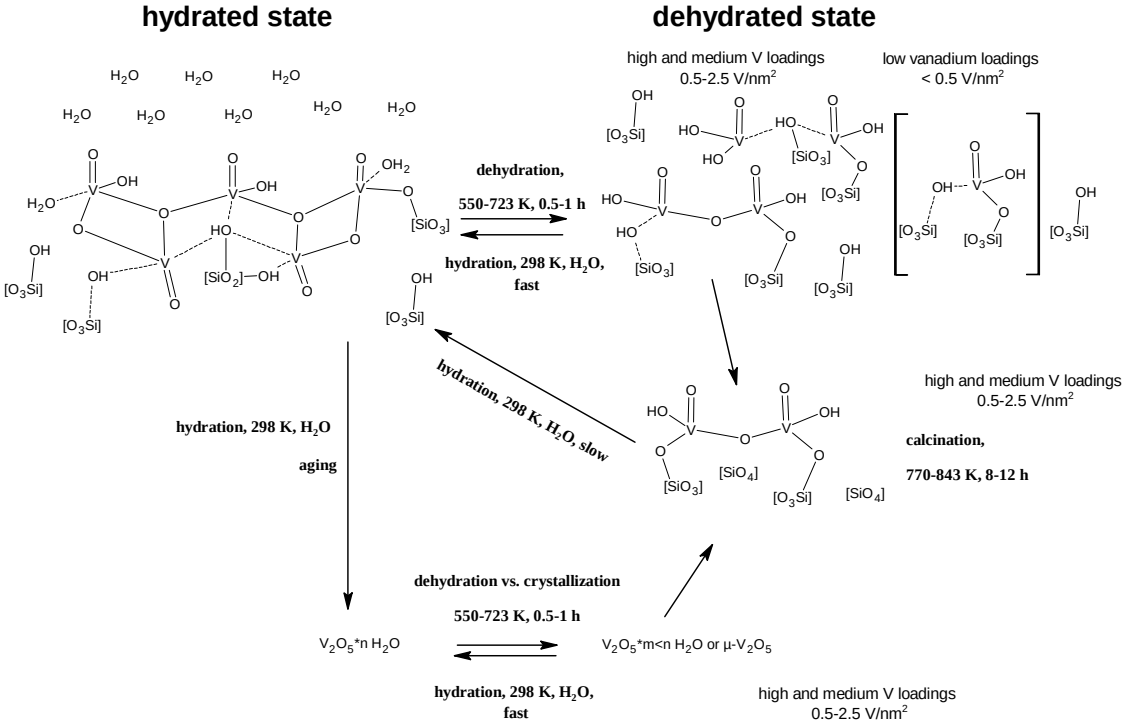

Figure 6-15: Schematic drawing of assumed dynamic structural transformations of supported vanadium oxide phase on SBA-15 during hydration and dehydration.

6.3.1 Coordination of hydrated V_xO_y/SBA-15

Under ambient conditions at 298 K and in a humid atmosphere the hydrated state of V_xO_y/SBA-15 was observed. A vanadium oxide structure with a square pyramidal coordination of the vanadium centers similar to the V_2O_5 and $V_2O_6^{2-}$ vanadate structures was determined from XAFS refinements and the UV-Vis edge energy position (***Chapter 5***). However, no direct evidence about the kind of oxygen groups around the absorbing vanadium centers could be derived in this work. Four types of oxygen containing groups seemed possible according to the literature [35] and the results discussed above: (i) V-OH, (ii) V-O-Si, (iii) V-O-V, and (iv) V←OH_2. Possible configurations are shown in ***Figure 6-15***. First, measurements reported by Schraml-Marth [27] and others [26,40,114] indicated that V-OH stretching modes (~ 3660 cm^{-1}) were present in the FT-IR (DRIFT) spectra of hydrated V_xO_y/SiO_2 samples. Second, ^{29}Si MAS-NMR measurements showed that fractions of the silanol type Si centers present on SBA-15

may have formed bonds (V-O-Si) to the grafted hydrated vanadium oxide centers. The third configuration (iii) involves direct linkages of V-O-V. Such V-V distances were determined from the increased signal at 2-4 Å in the FT(χ(k)*k^3) of the hydrated V_xO_y/SBA-15 samples. Furthermore, the average V-O-V number as determined from the UV-Vis edge energy was 3 (connected square pyramidal double chains). Hence, V-O-V bonds between the vanadium oxide centers may be present in the hydrated state. As a last possible configuration, (iv), a coordination of water seemed likely (V←OH_2). The maximum temperature of water formation was determined from TG experiments to be ~ 323-343 K. This is quite low and suggests weakly bonded water in the structure of hydrated V_xO_y/SBA-15. In addition to coordinated water, layers of physically adsorbed water are depicted in ***Figure 6-15*** because a significant mass loss was observed at 303 K in dry atmospheres.

6.3.2 Impact of coordinated water on hydrated V_xO_y/SBA-15

That water molecules play a key role in the coordination of the hydrated vanadium oxide structure was deduced from *in situ* UV-Vis-DRS and XAFS measurements. The main structural transformation of hydrated V_xO_y/SBA-15 into dehydrated V_xO_y/SBA-15 was observed to be independent of the vanadium loading in a temperature range between 298 K and 440 K. It was accompanied by an increased formation of water. Spectra recorded at higher temperatures resembled those of the dehydrated state of V_xO_y/SBA-15. Therefore, the majority of water is coordinated in the structure of hydrated V_xO_y/SBA-15. The apparent activation energy for water desorption (E_D) in this temperature range was determined from TG experiments to be 70-83 kJ/mol for V_xO_y/SBA-15 (***Table 6-1***). This was lower than for the pure SBA-15 support (~ 110 kJ/mol) and higher than for the Kieselgel 60 silica reference (~ 40 kJ/mol). On the one hand Vansant *et al.* [104] explained the low value for Kieselgel 60 by an evaporation process of physically adsorbed water from the SiO_2 surface. On the other hand, the rather high apparent activation energy for water desorption determined for pure SBA-15 was explained by an increased number of micropores of the untreated SBA-15 samples. However, relating the mass loss observed in this temperature range to the same surface area it was shown that the detected, thus adsorbed, water content on V_xO_y/SBA-15 samples decreased with the decreasing vanadium loading. Therefore, E_D in the range of 70-83 kJ/mol was ascribed to water which was released from the hydrated vanadium oxide structure. The increase in E_D with increasing vanadium loading was explained by a coordinative interaction of water with the vanadium centers on the SBA-15 support. Furthermore, the apparent activation energy of water desorption of hydrated V_xO_y/SBA-15 increased with increasing time of storage in humid atmosphere. Therefore, the coordinative interaction of water with the vanadium centers in hydrated V_xO_y/SBA-15 may increase with "sample age". For "aged" hydrated 7.7 wt% V_xO_y/SBA-15 more V-V interactions were detectable in the FT(χ(k)*k^3). Moreover, the similarity of the FT(χ(k)*k^3) of hydrated V_xO_y/SBA-15 with that of V_2O_5 increased. A V_2O_5·1.2 H_2O gel like structure was proposed by some authors [20,23,34] to be present in the hydrated state of V_xO_y/SiO_2 because the Raman spectra of hydrated V_xO_y/SiO_2 samples resembled that of V_2O_5·nH_2O gels [148]. Thus, the increasing similarity with V_2O_5 indicates that the

vanadium oxide structure of “aged” hydrated 7.7 wt% V_xO_y/SBA-15 may be similar to that of $V_2O_5 \cdot nH_2O$ gels.

In summary, water is important for the formation and coordination of the vanadium oxide structure of hydrated V_xO_y/SBA-15. The fact that water is rather weakly bond to the vanadium centers causes a low thermal stability and dehydration of hydrated V_xO_y/SBA-15 below temperatures of 440 K.

6.3.3 Formation of dehydrated V_xO_y/SBA-15

At elevated temperatures between 440 and 550 K V K edge XANES spectra of V_xO_y/SBA-15 resembled that of dehydrated V_xO_y/SBA-15 (***Figure 6-2***). A principal component analysis showed that the transformation of hydrated to dehydrated V_xO_y/SBA-15 proceeded directly and that no intermediate structures were formed. Hence, only a rearrangement process of the dehydrated vanadium oxide species on the SBA-15 support occurred at temperatures higher than 440 K. The increasing pre-egde peak height in the V K edge XANES spectra indicate a decreasing distortion of the tetrahedral vanadium oxide species. At temperatures above 550 K, only minor changes were observed in the XAFS and UV-Vis-DR spectra of V_xO_y/SBA-15 samples dehydrated in the temperature range from 554 to 723 K. The FT(χ(k)*k^3) of V_xO_y/SBA-15 dehydrated at 723 K showed a slightly decreased disorder parameter σ^2 (0.0066 $Å^2$) of the first V-O coordination sphere than after dehydration at 623 K (0.0070 $Å^2$). This is explained by a narrower distance distribution, which may be a consequence of a slightly enhanced structural order of the dimeric tetrahedrons on the SBA-15 support (***Table 6-4***). In the gas phase, only a minor water formation was observed in the temperature range of 440-550 K. The observed water content may be explained by loss of water due to dehydration of V-OH species. Schraml-Marth *et al.* [40] reported a decrease of the V-OH band (~ 3660 cm^{-1}) in DRIFT spectra of V_xO_y/SBA-15 samples after dehydration (573 K) of a rehydrated sample, which matches this interpretation. In addition to the dehydration of the vanadium oxide phase, a dehydroxylation of the silica support seems possible [104,147]. However, this interpretation is not preferred because no significant changes in the number of silanol groups were observed in the ^{29}Si MAS NMR spectra of 7.7 wt% V_xO_y/SBA-15. Thus, a dehydration of the vanadium oxide species (V-OH) during the formation of the dehydrated vanadium oxide centers was assumed in the temperature range of 440-550 K. Some authors reported that V-OH interactions are detectable by IR measurements for V_xO_y/SiO_2 samples treated at 853 K (12 h, O_2) [141]. Therefore, some of the dehydrated vanadium oxide species may have remained coordinated by hydroxyl groups (V-OH) above 550 K ***(Figure 6-15).***

Apparently, the dehydrated state corresponds to the stable vanadium oxide state of V_xO_y/SBA-15 at elevated temperatures higher than 550 K. Thus, 550 K will be sufficient as pretreatment temperature to obtain dehydrated V_xO_y/SBA-15 samples.

6.3.4 Formation of V_2O_5 crystallites versus dispersion during dehydration

Rehydrated V_xO_y/SBA-15 could be dehydrated again to the same dimeric tetrahedral structure obtained after the first dehydration procedure. Similar observations were reported by Morey *et al.* and Luan *et al.* [35,145]. Conversely, Xie *et al.* [34] observed V_2O_5 formation after repeated hydration/dehydration cycles. They explained this "gradual transformation" [34] of the hydrated state into "V_2O_5" crystals by the formation of $V_2O_5 \cdot nH_2O$ gels that transform into V_2O_5 during dehydration (for samples hydrated longer than 10 min using 3 Vol% H_2O, 298 K). Moreover, Xie *et al.* [34] discussed the reversible hydration of V_2O_5 crystals formed into $V_2O_5 \cdot nH_2O$ gels as long as these V_2O_5 crystallites are small enough so that water can "intercalate" into them [34]. Lager V_2O_5 crystals that were present already after calcination of higher loaded samples were not hydrated [34]. The observation of V_2O_5 after several hydration and dehydration cycles matches the V_2O_5 formation (denoted as μ-V_2O_5 in ***Figure 6-15***) in 7.7 wt% V_xO_y/SBA-15 which was dehydrated in water saturated atmospheres or after longer times of storage. Hence, dehydration of "aged" 7.7 wt% V_xO_y/SBA-15 results in the formation of V_2O_5. Raman bands similar to those detected for V_2O_5 were reported by Abello *et al.* [148] for $V_2O_5 \cdot 0.3H_2O$ gels. Therefore, it seems likely that $V_2O_5 \cdot nH_2O$ gels did not transform completely into V_2O_5, and only a lower amount of water was intercalated into the structure (denoted as $V_2O_5 \cdot m < n\ H_2O$ gels) as depicted in ***Figure 6-15***.

However, recalcination of "aged" 7.7 wt% V_xO_y/SBA-15 prior to dehydration resulted in an apparent redispersion of V_2O_5 (***Figure 6-12***) into dimeric tetrahedral species. Such a redisperion of large V_2O_5 crystallites seems not very likely considering the well accepted assumption in literature that spreading of crystalline V_2O_5 on SiO_2 supports is not possible [149, 150]. Given the low Tammann temperature of V_2O_5 of 482 K [150], V_2O_5, or the vanadium oxide phase in general, may be mobile on the SiO_2 support. The formation of V_2O_5 may be explained by the low amount of reactive silanol groups on the SiO_2 surface that would anchor the vanadium oxide species to the support. Vanadium oxide centers that were not linked to the SiO_2 support will show sintering (V_2O_5 formation). This was shown by Van Der Voort *et al.* [151]. They prepared 2.8 wt% V_xO_y/SiO_2 samples via impregnation of $VO(acac)_2$ on Kieselgel 60 calcined at 473 K and at 973 K. On samples pretreated at 973 K, large amounts of V_2O_5 were detected with Raman spectroscopy. Van Der Voort *et al.* [151] explained this V_2O_5 formation by the decreased number of silanols on the support that induce the dispersion of the vanadium oxide. They detected only a few isolated silanol groups left on the support calcined at 973 K. This explains V_2O_5 formation on 7.7 wt% V_xO_y/SBA-15 but not the redispersion of V_2O_5 formed during the dehydration of aged 7.7 wt% V_xO_y/SBA-15. Following the mechanism discussed above, Si-OH centers have to be present on the support that react with the "mobile" vanadium oxide and thus cause redispersion as it was observed during recalcination. A temperature of 843 K and a holding time of 12 h were chosen for recalcination. It is known from the ^{29}Si NMR results that in the hydrated state and after dehydration at 653 K approximatly 15% of the Si-OH centers were left on 7.7 wt% V_xO_y/SBA-15. After calcination of 7.7 wt% V_xO_y/SBA-15 at 843 K no Si-OH signal was detected in the NMR spectrum. Thus, a reaction of the vanadium centers with the SBA-15 support occurred. The temperature of 843 K used for recalcination is

in the range where isolated Si-OH groups start to dehydroxylate into siloxane groups [147]. Hence, instead of dehydroxylation of isolated silanol groups into siloxane groups, a reaction of these isolated silanol centers with the vanadium oxide may take place resulting in a redispersion. This formation of more V-O-Si bonds with the support after calcination was considered by the depiction of a second V-O-Si bond of the dimeric tetrahedral unit in ***Figure 6-15***.

Apparently, the presence of at least one V-O-Si bond per vanadium center or dimeric unit seems to be a prerequisite for the formation of the dehydrated tetrahedral vanadium species. If the amount of vanadium centers exceeds the number of Si-OH groups that are sterically suitable to form V-O-Si bonds, then the formation of V_2O_5 during dehydration seems likely. In this case a redispersion of hydrated to dehydrated V_xO_y/SBA-15 is not completely reversible.

6.3.5 Number of V-O-Si bonds – Is a O=V[O-Si]$_3$ species possible?

The mechanism discussed above explained the dispersion process of vanadium oxide species on SBA-15. To form the dehydrated state of V_xO_y/SBA-15, the dispersed vanadium oxides species have to form at least one bond (Si-O-V) with the SiO_2 support. Considering the vanadium density of 2.5 V/nm^2 for 7.7 wt% V_xO_y/SBA-15 a linkage of the dispersed species via 3 V-O-Si bonds as claimed by Molinari and Wachs [39] seemed not very likely. Three bonds would be present in an isolated [VO_4] tetrahedron. To link this monovanadate to the support, three Si-OH centers would be required. Assuming a V density of 2.5 V/nm^2, a Si-OH density of 7.5 OH/nm^2 would be required for a full dispersion. However, fully hydrated silica exhibits a silanol density of only 4-5 OH/nm^2 [147]. Moreover, Van der Voort *et al.* [151] showed that a small fraction of silanol groups was detected even on a V_xO_y/SiO_2 sample where V_2O_5 formed. Thus, a O=V[O-Si]$_3$ species seems not very likely. For higher loaded dehydrated V_xO_y/SBA-15 samples, a condensation of the adjacent tetrahedrons to dimeric species that are linked to the silica via one or two Si-O-V bonds is assumed. This suggestion is corroborated by the detection of dimeric [V_2O_7] units with UV-Vis-DRS and XAS. Nevertheless, the high UV-Vis edge energies determined for 1.4 wt% V_xO_y/SBA-15 (> 3.6 eV) indicated that isolated species (VO_4) may have formed. This seems possible considering the low vanadium loading of 1.4 wt% V_xO_y/SBA-15 (0.3 V/nm^2). However, a O=V[O-Si]$_3$ species as proposed by Molinari and Wachs [39] seemed not likely because not all sterically suitable Si-OH groups may be available to form three V-O-Si bonds. Therefore, a coordination by the Si-OH groups of the SBA-15 support is suggested (***Figure 6-15***). The majority of the V-O-Si bonds formed may be conserved during hydration of the vanadium oxide species. This explains the unchanged number of Si-OH centers in the hydrated and dehydrated state of V_xO_y/SBA-15 detected in the NMR measurements (***Figure 6-7***).

6.3.6 Effect of water on the dehydration process

As shown in ***Figure 6-13*** the dehydration process was observed even when water was present in the gas phase. Apparently, water coordinated to the hydrated structure of V_xO_y/SBA-15 was only weakly bound

to the vanadium centers. In contrast to dehydration in "dry" atmospheres, the formation of V_2O_5 was detected for 7.7 wt% V_xO_y/SBA-15. The presence of water may disturb the dehydration/dispersion process. Water may enhance the mobility of vanadium oxide centers on the support and, thus, accelerate the sintering process.

Moreover, a small blue shift of the absorption band was observed for all samples. This shift can be interpreted by different assumptions: (i) reduced V^{4+} centers which exhibit CT absorption bands at lower wavelengths, (ii) stronger distorted VO tetrahedrons, (iii) changed oxygen groups (V-O-Si ↔ V-OH), and (iv) changed connectivity (dimeric → isolated vanadium oxides centers). Assumption (i) seems unlikely considering the high oxygen content in the gas phase (20% O_2) and the fact that no red shift ("reoxidation") was detected after switching the water off. Assumption (ii) seems not likely because the average bond length remained constant during the 3rd dehydration cycle (***Table 6-4***). Referring to assumption (iii) that the oxygen groups around the vanadium centers changed would indicate that V-OH groups changed into (V-O-Si) groups. In this case, O is a stronger ligand than OH. A similar behavior was calculated by Atanasov *et al.* for Cr(IV), Mn(V), and Fe(VI) oxo and hydroxo clusters [152]. The increasing number of V-O-Si bonds suggests that water from the gas phase causes a hydrolysis of the V-OH bond. This assumption was not confirmed by an experimental measurement. The last assumption, (vi), that some of the dimeric $[V_2O_7]$ units transformed into $[VO_4]$ units suggests that the V-O-V bond of the dimeric vanadium species was opened by water in the gas phase. This may be possible but seemed not likely because the low loaded 1.4 wt% sample already consisted of a considerable amount of isolated vanadium oxide centers and also showed a blue shift of the absorption bands. In conclusion, the effect of water on the dehydrated structure remained somewhat ambiguous. Here, assumption (iii) was preferred: V-OH groups transferred into V-O-Si groups. However, the dehydration process of V_xO_y/SBA-15 in humid atmospheres did not change significantly compared to the dehydration process in dry atmospheres. The majority of the vanadium centers remained as dimeric tetrahedral species on SBA-15, which was inferred from the successful XAFS refinements of 7.7 wt% V_xO_y/SBA-15 (***Table 6-4***).

6.4 Summary

In situ UV-Vis-DRS, XAFS, and Raman measurements were conducted to investigate the evolution of the vanadium oxide structure and the gas phase during thermal treatment of V_xO_y/SBA-15 catalysts in 20% O_2 in He. Furthermore, the effect of water vapor on the V_xO_y/SBA-15 structure under ambient conditions and during thermal treatment was determined.

In situ XAFS measurements showed that the hydrated V_xO_y/SBA-15 structure transformed directly into the dehydrated structure during thermal treatment in 20% O_2. No intermediate vanadium oxide phase was detected. Water was released from the hydrated V_xO_y/SBA-15 structure during the dehydration process. In the temperature range between 298 K and 440 K this water loss was accompanied by the transformation from a square pyramidal to a tetrahedral coordination of the vanadium centers. Only minor amounts of water were detected for elevated temperatures (440-550 K). A rearrangement and ordering process of the dimeric tetrahedral vanadium oxide species is suggested in this temperature range. For temperatures higher than 550 K only minor changes were observed in the dehydrated V_xO_y/SBA-15 structure (550-723 K). ^{29}Si MAS NMR measurements indicated that the dehydrated and hydrated vanadium oxide centers are partially linked via Si-O-V bonds to the SBA-15 support.

Exposure to water under ambient (humid) conditions resulted in a hydration of the dehydrated V_xO_y/SBA-15 phase within minutes. After subsequent dehydration of the rehydrated V_xO_y/SBA-15 phase the dehydrated V_xO_y/SBA-15 phase was obtained again. These rehydration/dehydration cycles showed that the observed structural transformations of V_xO_y/SBA-15 were reversible and independent of the amount of vanadium on SBA-15. However, “aging effects” were observed for 7.7 wt% V_xO_y/SBA-15. A clustering of square pyramidal hydrated centers comparable to the formation of $V_2O_5 \cdot nH_2O$ gels was assumed. Dehydration of “aged” 7.7 wt% V_xO_y/SBA-15 resulted in the formation of V_2O_5 crystallites. These crystallites were redispersed successfully under calcination conditions at higher temperatures (843 K, 12 h). For low loaded 1.4 wt% V_xO_y/SBA-15 no sample aging was observed in the UV-Vis-DR spectra.

In general, formation of the dehydrated phase was independent of the presence of water in the reaction atmosphere and resulted in the formation of an ordered [V_2O_7] structure. Small amounts of V_2O_5 formed on 7.7 wt% V_xO_y/SBA-15. Slight changes in the dehydrated V_xO_y/SBA-15 species were detected for all V_xO_y/SBA-15 samples after the addition of water during the dehydration process. These rearrangements indicated a transformation of V-OH/Si-OH into V-O-Si coordination sites. Because water is commonly present in oxidation reactions, like propene oxidation, these changes may play a role for the catalytic performance of V_xO_y/SBA-15.

7 *Structural evolution and reactivity of V_xO_y/SBA-15 catalysts under propene oxidizing conditions*

7.1 Introduction

The V_xO_y/SBA-15 model system was introduced to obtain detailed knowledge on the role of vanadium sites during propene oxidation. Similar investigations were reported for other supported metal oxides model systems, *e.g.* Mo_xO_y/SiO_2 [103,153]. However, reaction product selectivities reported for Mo_xO_y/SiO_2 model catalysts differ from those reported for V_xO_y/SiO_2 catalysts (***Table 7-1***). This suggests different structure-activity correlations during propene oxidation of vanadium in mixed metal oxide catalysts. Structure-reactivity correlations of vanadium oxide catalysts on different supports has been a controversial issue during the past decades, *e.g.* for the oxidative dehydrogenation of propane [28,29,144,154,155,156,157] or for the oxidation of methanol or methane to formaldehyde [20,22,23,141]. However, only few reports discuss the role of vanadium oxide supported on SiO_2 in selective oxidation of propene to acrolein (***Table 7-1***). Recently, Zhao *et al.* [16,158] investigated the catalytic performance in selective propene oxidation and the structure of vanadium oxide phases supported on SiO_2, Al_2O_3, Nb_2O_5, TiO_2, and ZrO_2 in the range of 573-623 K. Compared to vanadium oxide phases on other support oxides, they reported a rather poor activity of the V_xO_y/SiO_2 catalysts for the propene oxidation to acrolein. Furthermore, they concluded that different reaction kinetics and a lower number of active "VO_4" sites [16] were responsible for this poor catalytic activity. The kind of reaction products that are formed during the oxidation of propene over V_xO_y/SiO_2 catalysts depend on the reaction conditions applied (***Table 7-1***). In the presence of high water content in the gas phase, increased amounts of acetone and acetic acid were reported [15,159]. If no water was added to the initial reaction mixture high selectivities towards acetaldehyde, acetone, and acrolein were described [16,160].

Table 7-1: Propene conversion and selectivity for propene oxidation over vanadium and molybdenum oxides supported on SiO_2.

Catalysts	Condition; ratio O_2/propene	Conversion C_3H_6 [%]	Selectivity towards main products	Ref.
5 wt% V_2O_5/SiO_2	473K; ~ 1.2	19	29% acetaldehyde, 7.3% propionaldehyde, 26.8% acrolein	[160]
0.58 V/nm^2 V_2O_5/SiO_2	523 K: 20 % steam; 3	1.8	43.5% acetone, 18% acetic acid, 18.3% CO_x	[15]
1-8 wt% V_2O_5/SiO_2 (0.2-2.7 V/nm^2)	623 K; 8-1	0.2	48-51% acrolein, 47-49% acetone, 6% acrylic acid	[16,158]
10 wt% V_2O_5/SiO_2 (1.17 V/nm^2)	463 K; 25% water vapor; 2	3.5	95% acetone	[159]
5.8 wt% MoO_3/SiO_2 (0.8 V/nm^2)	673 K; 2.3	3	53% propionaldehyde, 10% acrolein, 8% acetaldehyde, 29% CO_x	[103]
6 wt% MoO_3/SiO_2	673 K; 1	2.9	53% propionaldehyde, 18% acrolein, 21% acetaldehyde, 8% CO_x	[153]

Here, *in situ* spectroscopic investigations of vanadium oxides supported on SBA-15 were conducted to deduce reliable structure-reactivity correlations of V_xO_y/SBA-15 under propene oxidizing reaction conditions. These measurements were combined with reaction tests in the *in situ* cells and a laboratory fixed bed reactor. The dehydrated V_xO_y/SBA-15 structure discussed in the previous chapters was used as initial state for structural characterization of V_xO_y/SBA-15 model catalysts under propene oxidizing conditions. In accordance with previous investigations on Mo_xO_y/SBA-15 [8] and $PVMo_{11}O_{40}$/SBA-15 model catalysts [10], similar reaction conditions were employed (573 K and 723 K, 1-7.5% propene and 1-10% O_2 in He).

7.2 Results and discussion

7.2.1 Local structure of V_xO_y/SBA-15 under propene oxidation

Figure 7-1 depicts the room temperature V K edge XANES, the FT(χ(k)*k^3) and the UV-Vis-DR spectra of the dehydrated V_xO_y/SBA-15 samples (554-623 K, 1h, 20% O_2 in He) before and after temperature programmed reaction in propene and oxygen (676-723 K, 1 h, 5% O_2 and 5% propene in He). The V K edge XANES spectra after reaction were similar to the spectra of the initial dehydrated state of V_xO_y/SBA-15. No changes in the characteristic XANES structure, pre-edge peak height, and shape were observed for 4.1 wt% and 7.7 wt% dehydrated V_xO_y/SBA-15 (***Figure 7-1, left***). The spectrum of 1.4 wt% dehydrated V_xO_y/SBA-15 exhibited a slight increase of the amplitude of the XANES after reaction, whereas the pre-edge peak height and shape remained unchanged. The same similarity before and after propene oxidation was observed in the FT(χ(k)*k^3) of the V_xO_y/SBA-15 samples (***Figure 7-1, middle***). Only minor differences in the amplitude of the envelope of the FT(χ(k)*k^3) were detected for all loadings employed. A small decrease of the amplitude at higher distances (2-4 Å), where V-V interactions are located, was observed for dehydrated 7.7 wt% V_xO_y/SBA-15. In contrast, an increase of the amplitude was detected in the same region in the FT(χ(k)*k^3) of dehydrated 1.4 wt% V_xO_y/SBA-15. XAFS refinements were conducted to reveal that the "ordered dimeric tetrahedral model structure" was still sufficient for describing the experimental FT(χ(k)*k^3). The resulting parameters for 7.7 wt% and 1.4 wt% V_xO_y/SBA-15 are listed in ***Table 7-2*** (A detailed description of the refinements is given in ***Chapter 5***). A good agreement of the experimental and theoretical FT(χ(k)*k^3) was obtained for all samples as indicated by residuals lower than 8% (***Table 7-2***).

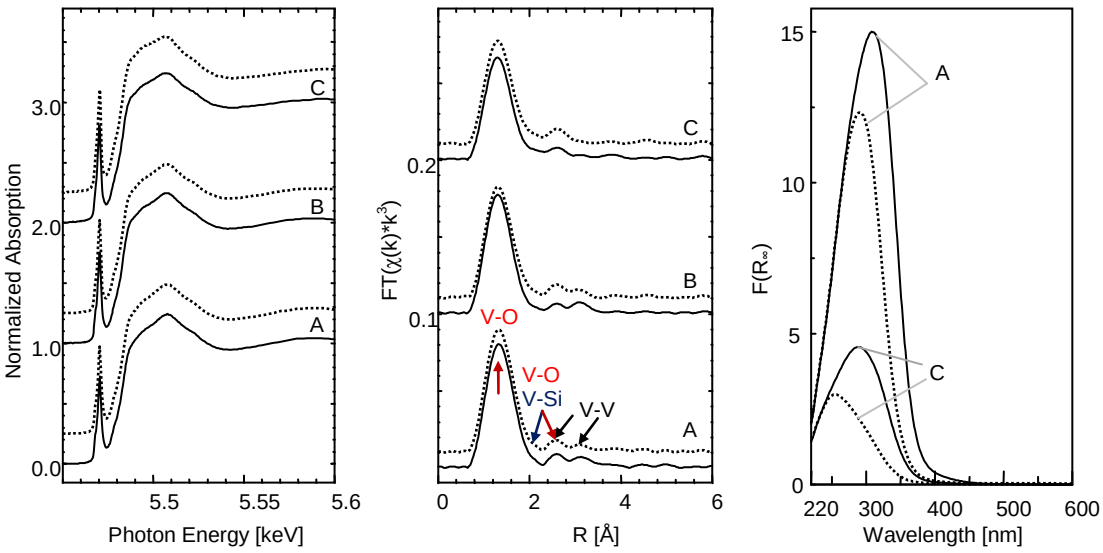

Figure 7-1: V K edge XANES (left), FT(χ(k)*k^3) (middle), and UV-Vis-DR spectra (right) recorded at 298 K after dehydration (solid line, 623 K, 1 h, 20% O_2 in He) and after propene oxidation (dashed line, 673 K (UV-Vis) and 723 K (XAS), 1 h, 5% O_2 and 5% propene in He): (A) 7.7 wt%, (B) 4.1 wt%, and (C) 1.4 wt% V_xO_y/SBA-15.

Table 7-2: Experimental distances (R), XAFS disorder parameters (σ^2), and coordination numbers (N) for different types of atom in a model system assuming an ordered arrangement of $[V_2O_7]$ units (***Chapter 5***). Parameters were obtained from the refinement of this model structure to the experimental V K edge XAFS FT(χ(k)*k^3) of dehydrated 1.4 wt% and 7.7 wt% V_xO_y/SBA-15 (k range from 2.7-10.5 $Å^{-1}$, R range 0.83-3.62 Å, N_{ind} = 16, E_0 = 0 eV in all cases, (subscript c indicates parameters that were correlated in the refinement, subscript f indicates parameters that were fixed in the refinement). Dehydration was conducted in 20% O_2 in He at 623 K for 1 h and propene oxidation at 723 K for 1 h (5% O_2 and 5% propene in He).

	7.7 wt% V_xO_y/SBA-15				1.4 wt% V_xO_y/SBA-15			
	dehydrated		after propene oxidation		dehydrated		after propene oxidation	
Type (N)	R [Å]	σ^2 [$Å^2$]	R [Å]	σ^2 [$Å^2$]	R [Å]	σ^2 [$Å^2$]	R [Å]	σ^2 [$Å^2$]
V – O (1)	1.78	0.0067	1.78	0.0069	1.78	0.01	1.78	0.009
V – O (1)	1.78 $_c$	0.0067 $_c$	1.78 $_c$	0.0069 $_c$	1.78 $_c$	0.01 $_c$	1.78 $_c$	0.009 $_c$
V – O (2)	1.78 $_c$	0.0067 $_c$	1.78 $_c$	0.0069 $_c$	1.78 $_c$	0.01 $_c$	1.78 $_c$	0.009 $_c$
V – O (1)	2.89	0.0012 $_f$	2.89	0.0012 $_f$	2.87	0.003 $_f$	2.87	0.003 $_f$
V – V (1)	3.33	0.0098	3.33	0.0123	3.35	0.0129	3.33	0.0089
V – V (1)	3.61	0.0098 $_c$	3.60	0.0123 $_c$	3.61	0.0129 $_c$	3.56	0.0089 $_c$
V – Si (1)	2.54	0.0088	2.54	0.0923	2.51	0.0109	2.52	0.0103
Residual	4.0		4.0		5.6		7.9	

Accordingly, the dehydrated vanadium oxide structure was still present on the SBA-15 support after propene oxidation. Compared to the parameters obtained from a refinement to the initial FT(χ(k)*k^3) of dehydrated 7.7 wt% V_xO_y/SBA-15, the disorder parameter σ^2 of the V-V distances at 3.3 and 3.6 Å increased during propene oxidation from 0.0098 to 0.0123 $Å^2$. Small rearrangements of the $[V_2O_7]$ dimers, which cause a wider distance distribution as a consequence of a slightly decreased structural disorder, may have occurred during propene oxidation. Another reason for a wider distribution of the V-V distances may be a transformation of small fractions of the dimeric vanadium oxide centers into isolated tetrahedral vanadium oxide centers. In contrast to 7.7 wt% V_xO_y/SBA-15, the V-V disorder parameter σ^2 of 1.4 wt% V_xO_y/SBA-15 was decreased after propene oxidation. The narrower V-V distance distribution and may be explained by an increased structural order. Additionally, it seems possible that the number of V-O or V-Si contributions increased at distances higher than 2 Å. However, the disorder parameters σ^2 of the V-O and V-Si distances showed no significant changes for 1.4 wt% and 7.7 wt% V_xO_y/SBA-15 after propene oxidation (***Table 7-2***).

Distinct changes were detected In the UV-Vis-DR spectra of dehydrated V_xO_y/SBA-15 recorded before and after exposure to catalytic conditions (***Figure 7-1, right***). In the UV-Vis-DR spectra that were measured at 298 K after temperature programmed reaction in propene and oxygen, a blue shift of the absorption maximum and a decrease of the maximum intensity at 300 nm were observed. The UV-Vis edge energy of 7.7 wt% V_xO_y/SBA-15 shifted from 3.41 eV to 3.56 eV (ΔE_g~ ±0.05 eV) and that of 4.1 wt% V_xO_y/SBA-15 from 3.42 eV to 3.62 eV (ΔE_g~ ±0.05 eV). E_g of low loaded 1.4 wt% V_xO_y/SBA-15 shifted from 3.6 eV to 3.9 eV (ΔE_g~ ±0.1 eV). A UV-Vis edge energy of 3.6 eV would be indicative for the presence of isolated and dimeric tetrahedral vanadium centers. For low loaded dehydrated 1.4 wt% V_xO_y/SBA-15, a UV-Vis edge energy of 3.9 eV suggests that isolated centers may be present predominately.

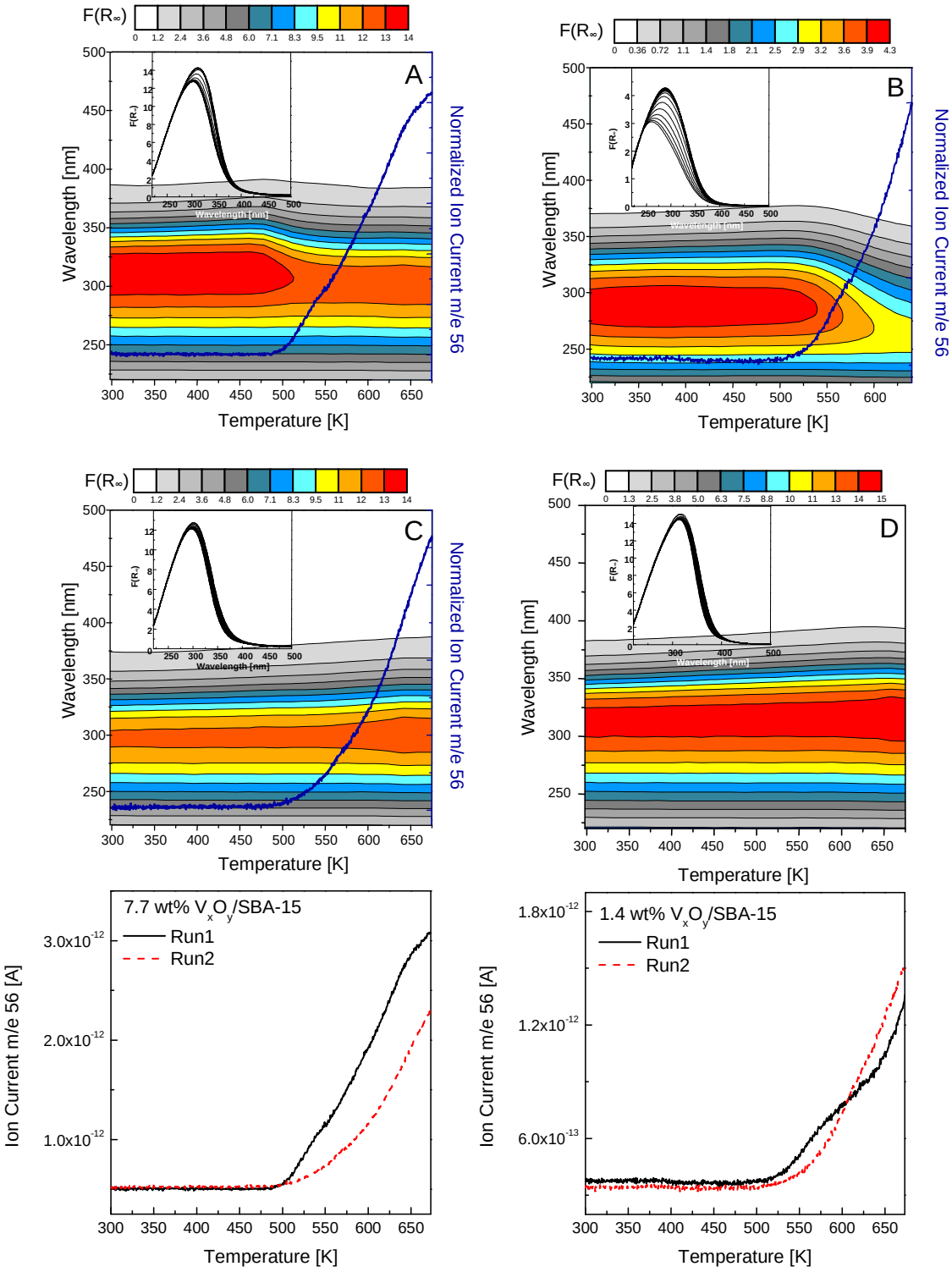

Figure 7-2 Top and middle: *in situ* UV-Vis-DR spectra of dehydrated V_xO_y/SBA-15 (623 K, 1 h, 20% O_2 in He) and the evolution of the ion current m/e 56 (acrolein) during the temperature programmed reaction: (A) 7.7 wt% V_xO_y/SBA-15 (675 K, 5% O_2 and 5% propene in He, 1st run); (B) 1.4 wt% V_xO_y/SBA-15 (634 K, 5% O_2 and 5% propene in He, 1st run), (C) 7.7 wt% V_xO_y/SBA-15 (675 K, 1 h, 5% O_2 and 5% propene in He, 2nd run), (D) 7.7 wt% V_xO_y/SBA-15 (675 K, 5% O_2 in He). Bottom: Evolution of the ion current m/e 56 for the 1st and 2nd measurement run. All measurements were performed with 4 K/min.

In situ UV-Vis-DR spectra were recorded during temperature programmed reaction (298-675 K, 4 K/min, 5% O_2 and 5% propene in He) to determine the temperature where the blue shift occurred. The resulting UV-Vis-DR spectra together with the evolution of the acrolein ion current (m/e 56) are depicted in ***Figure 7-2*** for dehydrated 7.7 wt% and 1.4 wt% V_xO_y/SBA-15. For reference a measurement in 5% O_2 was conducted to ensure that the blue shift occurred only under catalytic conditions (***Figure 7-2, D***). In those spectra, a reversible temperature induced red shift of the UV-Vis edge energy and the absorption maximum was observed. In the spectra recoded in a 5% O_2 and 5% propene atmosphere, the blue shift of the absorption maximum started at 500 K and finished approximately at 550 K for dehydrated 7.7 wt% V_xO_y/SBA-15 (***Figure 7-2, A***). Interestingly, the beginning of the blue shift of the UV-Vis-DR absorption band coincided with the onset of acrolein formation at 500 K (and other aldehydes that are not shown) detected in the online mass spectrometer. The range where the blue shift was mainly observed shifted to 530-600 K for dehydrated 1.4 wt% V_xO_y/SBA-15 (***Figure 7-2, B***). The onset of acrolein formation was at 520 K. A second temperature programmed measurement was conducted subsequently to the first measurement of dehydrated 7.7 wt% V_xO_y/SBA-15 to investigate if the onset of the catalytic activity was reproducible. No change was observed in the *in situ* UV-Vis-DR spectra of 7.7 wt% V_xO_y/SBA-15, except for a temperature induced broadening of the absorption band (***Figure 7-2, C***). The onset temperature of acrolein formation was still at 500 K but the increase of the ion current (m/e 56) was significantly lower than in the first measurement. For a better comparison, the ion currents of the first and second measurement are shown in ***Figure 7-2 (bottom)***. A propene conversion of ~ 8% was detected directly after reaching 675 K for both measurements of 7.7 wt% V_xO_y/SBA-15. Furthermore, the selectivity towards acrolein decreased from 18% in the first measurement to 14% in the second measurement. Such a pronounced difference in the acrolein formation between the initial and a second measurement was not observed for dehydrated 1.4 wt% V_xO_y/SBA-15. The results presented above show that the temperature range where the blue shift in the UV-Vis-DR spectra of dehydrated 7.7 wt% V_xO_y/SBA-15 occurred (500-600 K) coincided with an increased formation and selectivity of acrolein and other aldehydes. Possible explanations for the blue shift observed and of the increased activity of dehydrated 7.7 wt% V_xO_y/SBA-15 will be discussed in ***Section 7.2.3***.

7.2.2 Impact of pretreatment procedure and water vapour on the local structure of V_xO_y/SBA-15 during propene oxidation

In the previous chapter, it was shown that the dehydrated V_xO_y/SBA-15 structure was present at elevated temperatures even in the presence of water in the reaction atmosphere. The influence of different reaction conditions, like pretreatment in oxygen and water vapor, on the local structure of V_xO_y/SBA-15 during propene oxidation were investigated here. Three experiments were performed. First, the sample was dehydrated (554-623 K, 1 h, 20% O_2 in He) prior to the temperature programmed reaction in propene and oxygen (5% propene and 5% O_2 in He). Second, the hydrated V_xO_y/SBA-15 samples were used as initial phase. Third, the hydrated V_xO_y/SBA-15 samples were used as initial phase and water vapor was added to

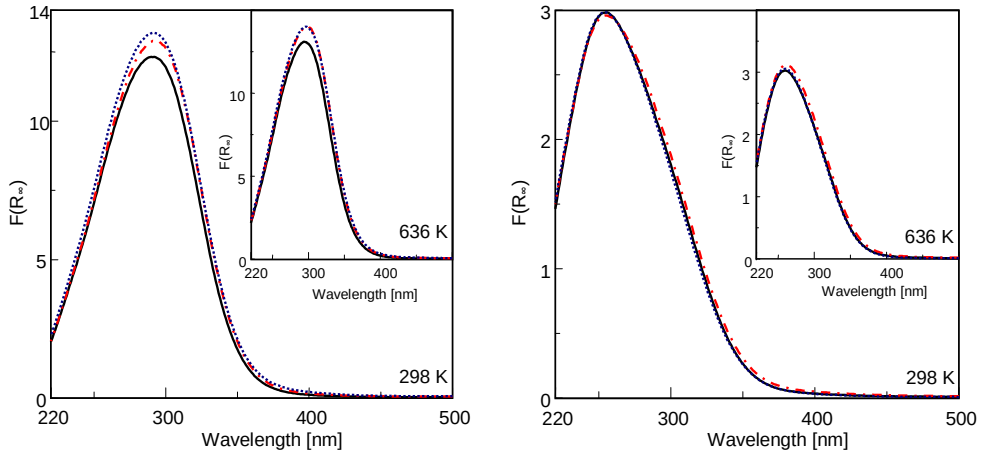

Figure 7-3: *In situ* UV-Vis-DR spectra of 7.7 wt% V_xO_y/SBA-15 (right) and 1.4 wt% V_xO_y/SBA-15 (left) recorded at 636 K and at 298 K after reaction in 5% propene and 5% O_2 in He: dehydrated sample (554 K, 20% O_2) (solid line, black), hydrated sample (dashed and dotted line, red), and hydrated sample with water (0.8 Vol%) in the reaction mixture (dotted line, blue).

the reaction mixture (~ 0.8 Vol%). In this experiment, water vapor was switched off while cooling the samples to 298 K. The UV-Vis-DR spectra of 1.4 wt% and 7.7 wt% V_xO_y/SBA-15 for the different temperature programmed reactions are shown in ***Figure 7-3***. Apparently, no difference can be detected in the UV-Vis-DR spectra recorded *in situ* at 636 K and at 298 K after reaction. The dehydrated V_xO_y/SBA-15 state was present for all three treatments. Similar results were obtained from V K edge XAFS measurements. ***Figure 7-4*** depicts the FT(χ(k)*k^3) of 7.7 wt% V_xO_y/SBA-15 recorded at 723 K and 298 K for the different temperature programmed reactions. Again, no significant difference was observed in the FT(χ(k)*k^3) of 7.7 wt% V_xO_y/SBA-15 for the different treatments employed. ***Figure 7-5*** depicts the *in situ* XAFS spectra for 7.7 wt% V_xO_y/SBA-15 (3rd procedure, hydrated V_xO_y/SBA-15, water) to show that a similar evolution of XAFS spectra was observed as described for the dehydration processes in ***Chapter 6.2.3***.

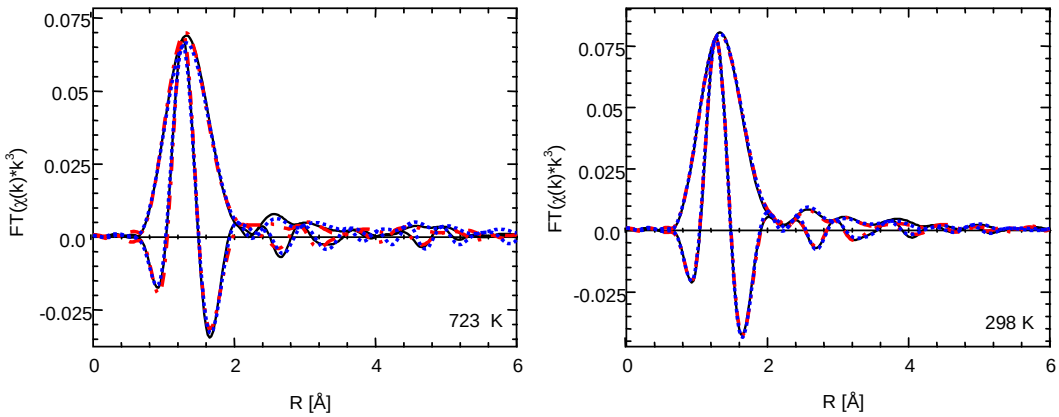

Figure 7-4: *In situ* V K edge FT(χ(k)*k^3) of 7.7 wt% V_xO_y/SBA-15 (right) and 1.4 wt% V_xO_y/SBA-15 (left) recorded at 723 K and at 298 K after reaction in 5% propene and 5% O_2 in He: dehydrated sample (554 K, 20% O_2) (solid line, black), hydrated sample (dashed and dotted line, red), and hydrated sample with water (0.8 Vol%) in the reaction mixture (dotted line, blue).

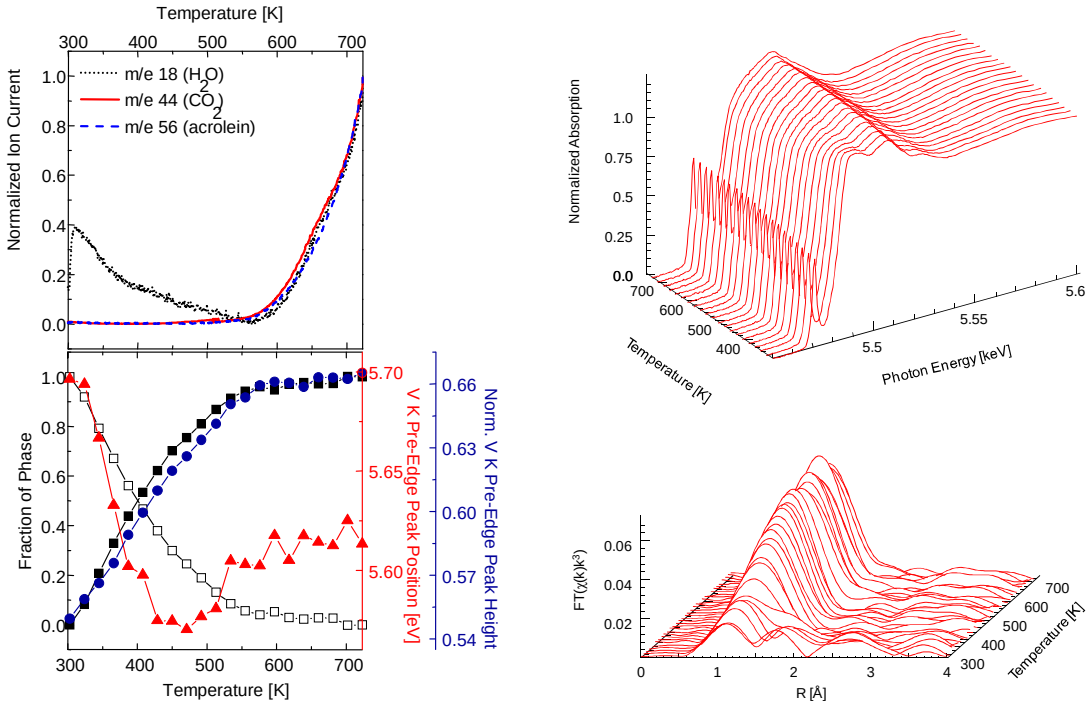

Figure 7-5: Evolution of the recorded MS ion currents (left, top), and the V K edge pre-edge peak height (●) and energy position (▲) (left, bottom, relative to 5.465 keV), and the phase fraction for the hydrated (□) and dehydrated (■) vanadium oxide structure obtained from a PCA (left bottom) of the V K edge XANES spectra (right, top) that were recorded during the temperature programmed reaction (5% O_2 and 5% propene in He, 298-723 K, 5 K/min) of 7.7 wt% hydrated V_xO_y/SBA-15. FT(χ(k)*k^3) (QEXAFS scans) of a comparable measurement are shown on the right side (bottom).

The XANES spectra, the FT(χ(k)*k^3), MS ion currents, and the respective parameters obtained from a PCA analysis and an analysis of the pre-edge peak height and position are depicted in ***Figure 7-5***. XANES scans were recorded in the standard operation mode of the monochromator crystals to gain a better signal to noise ratio. The FT(χ(k)*k^3) was extracted from QEXAFS scans that were recorded in a separate measurement. The usable spectral range of the QEXAFS scans was 2.5-9.0 $Å^{-1}$(***Figure 10-4***, ***appendix***). Similar to dehydration of 7.7 wt% V_xO_y/SBA-15 (***Chapter 6.2.3***, ***Figure 6-3***), two components involved in the structural transformation were determined by a PCA of the V K edge XANES spectra. The amount of hydrated and dehydrated V_xO_y/SBA-15 was determined using the XANES spectrum of the initial hydrated structure and the XANES spectrum recorded at 723 K. The evolution of the hydrated and dehydrated state was comparable to that observed during dehydration in 20% O_2. As depicted in ***Figure 7-5,*** the transformation of the hydrated V_xO_y/SBA-15 structure into the dehydrated V_xO_y/SBA-15 structure occured in the temperature range from 300 K to 440 K. In this temperature range, changes in the XANES were observed, and the pre-edge peak position reached its minimum (***Figure 7-5, left bottom***). In contrast to ***Figure 6-3*** in ***Chapter 6.2.3***, a small increase of the pre-edge peak position was observed above 500 K. The origin of this increase is unclear. It may indicate a change of the coordination sphere (*e.g.* type of ligand) around the absorbing vanadium center during propene oxidation. The increase of the pre-edge peak height coincided with the increasing amount of

dehydrated V_xO_y/SBA-15 phase. This was similar to the dehydration of 7.7 wt% V_xO_y/SBA-15. Below 550 K only the formation of water (m/e 18) was detected with the online mass spectrometer. An increase in the ion currents of the reaction products of propene oxidation was observed for temperatures higher than 550 K. ***Figure 7-5 (left top)*** depicts the ion currents of water (m/e 18), CO_2 (m/e 44), and acrolein (m/e 56). The formation of reaction products was observed at temperatures where the dehydrated phase was already present on the support. Therefore, the dehydrated structure of V_xO_y/SBA-15 was the main vanadium oxide phase present during catalytic propene oxidation. The *in situ* FT(χ(k)*k^3) of 7.7 wt% V_xO_y/SBA-15 resembled that of the dehydrated phase above 440 K. XAFS refinements showed that the "ordered V_2O_7" model structure was sufficient to describe the experimental FT(χ(k)*k^3) of 7.7 wt% V_xO_y/SBA-15 recorded at 723 K for all reaction conditions employed. Low residuals of 8%, acceptable F parameters, and acceptable confidence limits were obtained for all refinements. Compared to the parameters that were obtained after reaction at 298 K, only a small increase of the disorder parameters and small changes of the V-V distances were observed at 723 K. The disorder parameter of the V-V distances increased (~ 0.014 Å^2) compared to that determined at 623 K in a 20% O_2 atmosphere (0.009 Å^2,***Table 6-3***, ***Chapter 6.2.9***). The increased σ^2 suggests a wider V-V distance distribution which may be a consequence of structural rearrangements that occur during the reaction with propene. Nevertheless, for all treatments the ordered dimeric [V_2O_7] model structure was sufficient to describe the experimental FT(χ(k)*k^3) of the 7.7 wt% V_xO_y/SBA-15 sample under reaction conditions.

In conclusion, the pretreatment procedure and the presence of water vapor during catalytic reaction did not affect the local vanadium oxide structure of V_xO_y/SBA-15. The same dehydrated V_xO_y/SBA-15 state was present for all treatments employed.

Table 7-3: Experimental distances (R), XAFS disorder parameters (σ^2), and coordination numbers (N) for different types of atom in a model system assuming an ordered arrangement of [V_2O_7] units (***Chapter 5***). Parameters were obtained from the refinement of this model structure to the experimental V K edge XAFS FT(χ(k)*k^3) of dehydrated 1.4 wt% and 7.7 wt% V_xO_y/SBA-15 (k range from 2.7-10.5 Å^{-1}, R range 0.83-3.62 Å, N_{ind} = 16, E_0 = 0 eV in all cases, (subscript c indicates parameters that were correlated in the refinement, subscript f indicates parameters that were fixed in the refinement). Dehydration was conducted in 20% O_2 in He at 623 K and propene oxidation at 723 K (5% O_2 and 5% propene in He, 0.8% H_2O).

	dehydrated 723 K 5% propene, 5% O_2		hydrated 723 K 5% propene, 5% O_2		hydrated 723 K 5% prop., 5% O_2, 0.8 % H_2O		dehydrated, after reaction 298 K He	
Type (N)	R [Å]	σ^2 [Å^2]	R [Å]	R [Å]	R [Å]	σ^2 [Å^2]	R [Å]	σ^2 [Å^2]
V – O (1)	1.79	0.0084	1.78	0.0084	1.78	0.0088	1.78	0.0069
V – O (1)	1.79$_c$	0.0084$_c$	1.78$_c$	0.0084$_c$	1.78$_c$	0.0088$_c$	1.78$_c$	0.0069$_c$
V – O (2)	1.79$_c$	0.0084$_c$	1.78$_c$	0.0084$_c$	1.78$_c$	0.0088$_c$	1.78$_c$	0.0069$_c$
V – O (1)	2.91	0.0012$_f$	2.88	0.0012$_f$	2.91	0.0012$_f$	2.89	0.0012$_f$
V – V (1)	3.26	0.0146	3.30	0.0165	3.32	0.0140	3.33	0.0123
V – V (1)	3.59	0.0146$_c$	3.63	0.0165$_c$	3.63	0.0140$_c$	3.60	0.0123$_c$
V – Si (1)	2.56	0.0104	2.53	0.0121	2.55	0.0105	2.54	0.0923
Residual	7.3		5.5		4.9		4.1	

7.2.3 Discussion of possible origins of the UV-Vis edge energy shift during propene oxidation

In the previous chapter various reasons were discussed that may explain the UV-Vis edge energy shift observed in the UV-Vis-DR spectra: (i) reduced V^{4+} centers which exhibit CT absorption bands at lower wavelengths, (ii) less distorted VO tetrahedrons, (iii) changed oxygen groups (V-O-Si ↔ V-OH), and (iv) changed connectivity (dimeric → isolated vanadium centers).

A reduction of tetrahedral V^{5+} vanadium centers to tetrahedral V^{4+} or V^{3+} centers (reason (i)) seems not very likely because of the unchanged pre-edge peak in the V K edge XANES spectra (***Figure 7-1***) and the unchanged Raman band at 1040 cm^{-1} (***Figure 7-7***). However, a tetrahedral vanadium oxide species with reduced vanadium centers would exhibit absorption bands in the UV-Vis range with maxima that are blue shifted compared to the maxima that are detected for V^{5+} vanadium centers [132]. Thus, reduced tetrahedral vanadium centers may be one reason for the blue shift observed in the spectra of the dehydrated V_xO_y/SBA-15 samples during propene oxidation (***Figure 7-6***). That no reduction of the tetrahedral vanadium oxide phase occurred during the temperature programmed reaction in propene and oxygen was investigated by an isothermal UV-Vis-DRS experiment at 675 K. Dehydrated 7.7 wt% V_xO_y/SBA-15 was heated to 675 K and held for 15 minutes in 5% O_2 in He. During the thermal treatment in 5% O_2 in He, only a red shift of several nm was detected. The exposure of the sample to the reaction atmosphere at 675 K (5 min, 5% O_2 and 5% propene) caused an immediate blue shift. In order to reveal whether the blue shift was not caused by reduced vanadium phases the atmosphere was switched to 20% O_2 in He to induce a re-oxidation. No change in the absorption spectra was observed. Thus, it was shown that the blue shift was not caused by the formation of reduced (V^{4+}/V^{3+}) tetrahedrally coordinated vanadium centers.

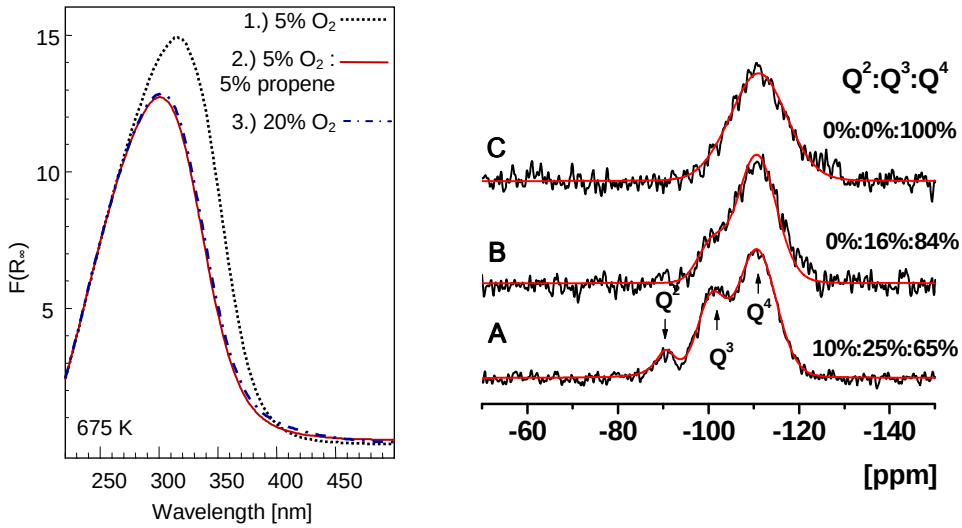

Figure 7-6 Left: *in situ* UV-Vis-DR spectra of dehydrated 7.7 wt% V_xO_y/SBA-15 (623 K, 1 h) after subsequent treatment at 675 K in (1.) oxygen, (2.) propene and oxygen, and (3.) oxygen. Right: ^{29}Si CP-MAS-NMR of SBA-15 and 7.7 wt% V_xO_y/SBA-15 treated at different temperatures: (A) SBA-15, (B) dehydrated 7.7 wt% V_xO_y/SBA-15 (653 K, 1 h), (C) dehydrated 7.7 wt% V_xO_y/SBA-15 (653 K, 1 h) after propene oxidation (5% propene and 5% O_2 in He, 673 K, 1 h). The red curve is the sum of the Gaussian functions used for the profile refinement.

The second reason, (ii), that the distortion of the VO tetrahedron decreased was not corroborated by XAFS refinement results. A blue shift of the UV-Vis edge energy would be observed if the average V-O bond length decreased (***Chapter 5.2.2, Figure 5-2, right***). The parameters in ***Table 7-2*** show clearly that the average V-O distance and the disorder parameters underwent no significant change.

Reason (iii) implies a change of the oxygen ligands induced by the interaction with the propene molecule. In the previous ***Chapter 6***, such an exchange was interpreted by a change of V-OH/Si-OH to V-O-Si groups. This interpretation was corroborated by NMR measurements that allowed determining the Si-OH distribution on the SBA-15 support. As shown in ***Figure 7-7 (right)***, exclusively Q^4 type Si centers and no Si-OH centers were detectable on the SBA-15 support after the catalytic measurement of dehydrated 7.7 wt% V_xO_y/SBA-15. However, Gao *et al.* [23] observed a similar decrease of the number of isolated Si-OH centers with NIR-DR spectroscopy for a 1% V_xO_y/SiO_2 sample under catalytic (methanol oxidizing) conditions. For the same 1% V_xO_y/SiO_2 sample, they observed a comparable blue shift of the UV-Vis edge energy from 3.6 eV to 3.8 eV as observed here for V_xO_y/SBA-15 under catalytic conditions. Gao *et al.* [23] assigned the decrease in Si-OH centers to the formation of Si-O-C_xH_y species. The blue shift in the UV-Vis-DR spectra was assigned to the formation of isolated 4-fold V-methoxy species [23] which is in contrast to the interpretation here. The feasibility of detecting V-O-C_xH_y species formed during propene oxidation at 675 K with UV-Vis-DRS seems not very likely. Even though such V-O-C_xH_y and Si-O-C_xH_y species may form as intermediates, it is expected that these are oxidized in 20% O_2 atmospheres at 675 K and that the blue shift will be reversible. ***Figure 7-7 (left)*** shows that no change in the UV-Vis-DR spectra of 7.7 wt% V_xO_y/SBA-15 was observed after changing the gas phase from catalytic conditions to 20% O_2 at 675 K. Therefore, the transformation of V-OH to V-O-Si bonds seems to be the explanation of the blue shift if it was assumed that the type of oxygen group changed during propene oxidation. Another reason, (vi), for the observed blue shift in the UV-Vis-DR spectra may be a change in the average V-O-V number. In this case, some of the dimeric centers may transform into isolated tetrahedral vanadium centers, and additional V-O-Si bonds are formed. Reason (vi) was corroborated by the decreasing UV-Vis edge energy determined for dehydrated V_xO_y/SBA-15 after the reaction which indicates a lower connectivity of the vanadium centers (V-O-V number, ***Chapter 5.2.2***). In contrast, the XAFS measurements showed no clear trend that would support this interpretation. The increase of the disorder parameter of the V-V distances (3.3 and 3.6 Å) for 4.1 wt% and 7.7 wt% V_xO_y/SBA-15 (***Table 7-2***) may indicate that some of the dimeric tetrahedral vanadium centers transformed into isolated ones. Nevertheless, the opposite trend was observed for 1.4 wt% V_xO_y/SBA-15. The disorder parameter for the V-V distances of 1.4 wt% V_xO_y/SBA-15 decreased after propene oxidation (***Table 7-2***). However, the transformation of V-OH/Si-OH groups to V-O-Si bonds (reason (iii)) rather than the V-O-V bond rupture (reason (iv)) seems to be the more likely explanation of the blue shift observed in the UV-Vis-DR spectra. This suggestion was corroborated by the fact that the blue shift of the UV-Vis edge energy observed was larger for 1.4 wt% V_xO_y/SBA-15 than for 4.1 wt% and 7.7 wt% V_xO_y/SBA-15. 1.4 wt% V_xO_y/SBA-15 already exhibits a considerable amount of isolated vanadium centers and a lower number of V-O-V bonds.

7.2.4 Enhanced reactivity of 7.7 wt% V_xO_y/SBA-15–Impact of V_2O_5 and carbonaceous species

In the temperature range where the blue shift of the UV-Vis absorption bands occurred, an increased acrolein formation was detected in the first measurement run of 1.4 wt% and 7.7 wt% V_xO_y/SBA-15 (***Figure 7-2, A and B***). This was visible as a small shoulder in the acrolein ion current detected in the first measurement run (***Figure 7-2, bottom***). For 1.4 wt% V_xO_y/SBA-15, the ion current at temperatures above 600 K was not higher than in the second run. Therefore, the increased acrolein formation in the lower temperature range of 500-600 K may be correlated with the structural rearrangement of the dehydrated V_xO_y/SBA-15 structure in the initial phase of the reaction. The increased acrolein formation detected for 7.7 wt% V_xO_y/SBA-15 at higher temperatures may be caused by other reasons. The presence of V_2O_5 seems likely for 7.7 wt% V_xO_y/SBA-15 in contrast to 1.4 wt% V_xO_y/SBA-15. These small fractions of V_2O_5 may enhance the reactivity of 7.7 wt% V_xO_y/SBA-15 for propene oxidation. That bulk V_2O_5 is active for the selective oxidation of propene towards acrolein will be discussed in more detail in ***Chapter 2***. The UV-Vis-NIR-DR spectra of 7.7 wt% V_xO_y/SBA-15 showed small absorption bands in the NIR range of the spectra which are indicative for vanadium centers with lower oxidation states. Conversely, in the UV-Vis-NIR-DR spectra of 1.4 wt% V_xO_y/SBA-15 and of freshly calcined and dehydrated 7.7 wt% V_xO_y/SBA-15 (***Figure 7-7, left***), such absorption bands were not detected in the NIR range (0.5-2 eV). Thus, these bands may be caused by V_2O_5 formed during aging that was reduced under reaction conditions. V_2O_5 crystallites can be detected very sensitively by Raman spectroscopy. Conversely, Raman bands of reduced vanadium oxide species are hardly detectable by Raman spectroscopy [18,161].The cross-section for Raman scattering is near zero for reduced vanadium centers [161]. A reversible shift to 1035 cm^{-1} was detected for the Raman band at 1041 cm^{-1}, which was assigned to temperature depended effects.

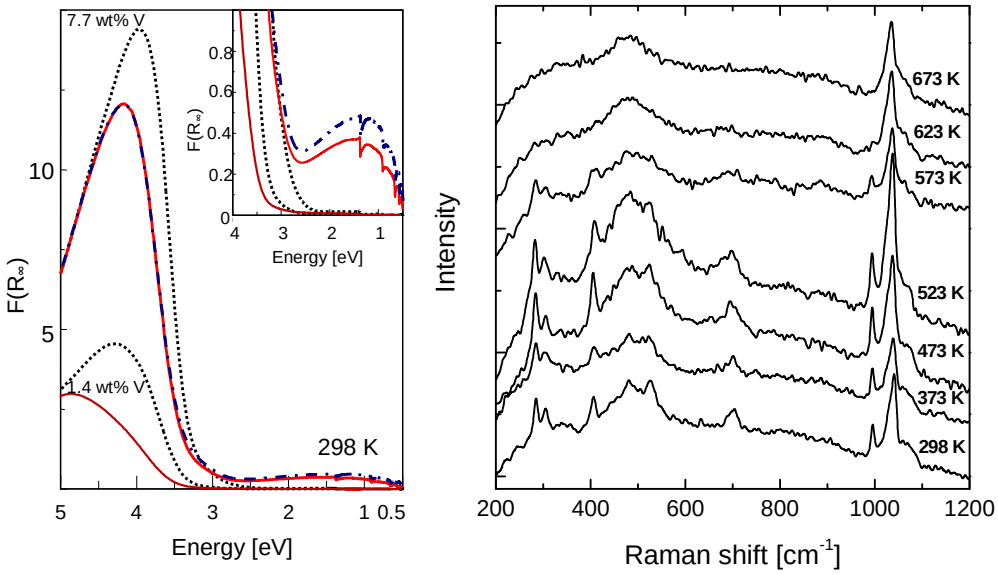

Figure 7-7 Left: *In situ* UV-Vis-NIR-DR spectra of dehydrated (dashed line) 1.4 wt% and 7.7 wt% V_xO_y/SBA-15 (623 K) after 1st (solid line) and 2nd (dashed and dotted line) catalytic measurement (675 K, 5% O_2 and 5% propene in He). Right: *in situ* Raman spectra of dehydrated 7.7 wt% V_xO_y/SBA-15 (723 K, 20% O_2 in N_2) in 5% O_2 and 5% propene in N_2; 514 nm, 6 mW.

Even though (reduced) V_2O_5 was observed for 7.7 wt% V_xO_y/SBA-15 the increased acrolein formation detected was not assigned to such a phase. The amount of V_2O_5 formed on 7.7 wt% V_xO_y/SBA-15 was estimated to be 3-5% of the vanadium oxide phase (***Chapter 6.2.9***). As discussed later on (***Chapter 7.2.6***), it was shown by catalytic testing that this amount is too low to explain the increased activity of 7.7 wt% V_xO_y/SBA-15.

Carbonaceous species formed during reaction may also enhance the catalytic activity of 7.7 wt% V_xO_y/SBA-15 for the propene oxidation. The formation of carbonaceous species in propene atmospheres was reported by Zhao *et al.* [158]. They observed characteristic Raman bands at approximately 1400 cm^{-1} and 1600 cm^{-1} in the *in situ* Raman spectra of 5% and 8% V_xO_y/SiO_2 catalysts (1.2 and 2.7 V/nm^2) recorded at 623 K in 3% propene [158]. Such Raman bands were visible in the *in situ* Raman spectra of hydrated and dehydrated 7.7 wt% V_xO_y/SBA-15 recorded during the temperature programmed reaction in 5% propene and 5% O_2 in the range from 298 K to 523 K (***Figure 7-8).*** These bands were not detected at higher temperatures. The Raman bands of carbonaceous species had a significantly lower intensity for 7.7 wt% V_xO_y/SBA-15 dehydrated prior to reaction in propene and oxygen (***Figure 7-8, right***). Hence, intermediates during the dehydration of hydrated V_xO_y/SBA-15 may enhance formation of carbonaceous species. The carbon formation observed was not caused by residual carbon from the preparation because a carbon amount lower than 0.1 wt% was determined by CHN elemental analysis of hydrated V_xO_y/SBA-15 samples. Hence, the carbon has to be formed by decomposition of propene. Nevertheless, Raman bands of the carbonaceous species were not detectable above 573 K. This temperature is below the temperature (600 K) where 7.7 wt% V_xO_y/SBA-15 showed an increased activity for acrolein formation compared to 1.4 wt% V_xO_y/SBA-15. Apparently, neither V_2O_5 nor carbonaceous species were responsible for the enhanced catalytic activity of 7.7 wt% V_xO_y/SBA-15. Therefore, this effect is assigned to an intrinsic property of the "ordered V_2O_7" structure of dehydrated V_xO_y/SBA-15 present for high vanadium loadings near the maximum vanadium coverage of disperse vanadium oxide species on SBA-15.

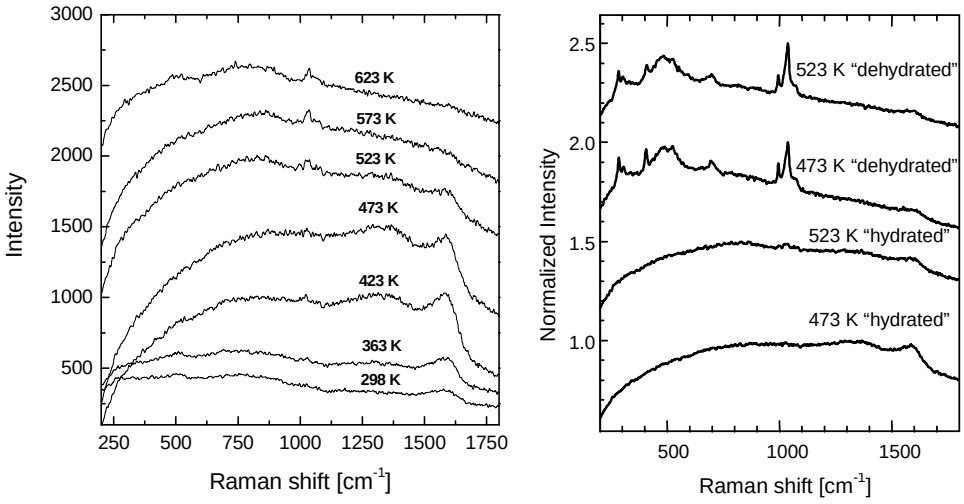

Figure 7-8 Left: *in situ* Raman spectra of hydrated 7.7 wt% V_xO_y/SBA-15 during propene oxidation; 5% O_2 and 5% propene in N_2, 514 nm, 6 mW. Right: Comparison of the *in situ* Raman spectra of hydrated and dehydrated 7.7 wt% V_xO_y/SBA-15 during propene oxidation at 473 K and 523 K.

7.2.5 *Evaluation of the different reactor types for quantitative catalytic measurements*

Prior to the discussion of the results obtained from catalytic reaction tests a short evaluation of the suitability of the reaction cells used for catalytic measurements will be performed. Three different types of reaction cells were used to characterize the V_xO_y/SBA-15 samples under propene oxidizing conditions. Mainly *in situ* XAS and UV-Vis-DRS cells were used for the structural characterization. Catalytic results obtained in the *in situ* cells were compared to measurements conducted in a laboratory fixed bed reactor (SiO_2 tube, "quartz glass"). Therefore, both *in situ* cells and the reactor were connected to the same online mass spectrometer and gas chromatograph to allow qualitative and quantitative determination of the respective gas phase composition. The catalytic propene oxidation (5% O_2 and 5% propene in He) of dehydrated 7.7 wt% V_xO_y/SBA-15 (20% O_2 in He, 554-653 K) is used for comparison. The propene conversion and the sum selectivity towards all oxygenated reaction products as a function of temperature are depicted in ***Figure 7-9*** for all reactors used. A more detailed depiction of the selectivities is given in ***Figure 10-5*** in the appendix. The temperature range where acceptable results were obtained was different for all reactors used. For XAFS measurements reliable quantitative results were obtained for temperatures higher than 673 K. The low propene conversion is due to the low sample mass of 2.4 mg, which was required for the XAFS measurements at the V K edge. In contrast to the *in situ* XAS cell, significantly higher propene conversion was determined in the *in situ* UV-Vis-DR cell for temperatures above 520 K because a higher amount of sample could be introduced into the sample holder (18.9 mg). Temperatures higher than 673 K were not feasible in the *in situ* UV-Vis-DR cell. Moreover, a high deviation of 20% in temperature between the sample and the sample cup was observed. The sample mass in the quartz glass reactor was adjusted to a propene conversion between 5-10% at 673 K. According to the different sample masses used, the rate of propene oxidation and the respective selectivities of the reaction products are compared in ***Figure 7-9 (right)***.

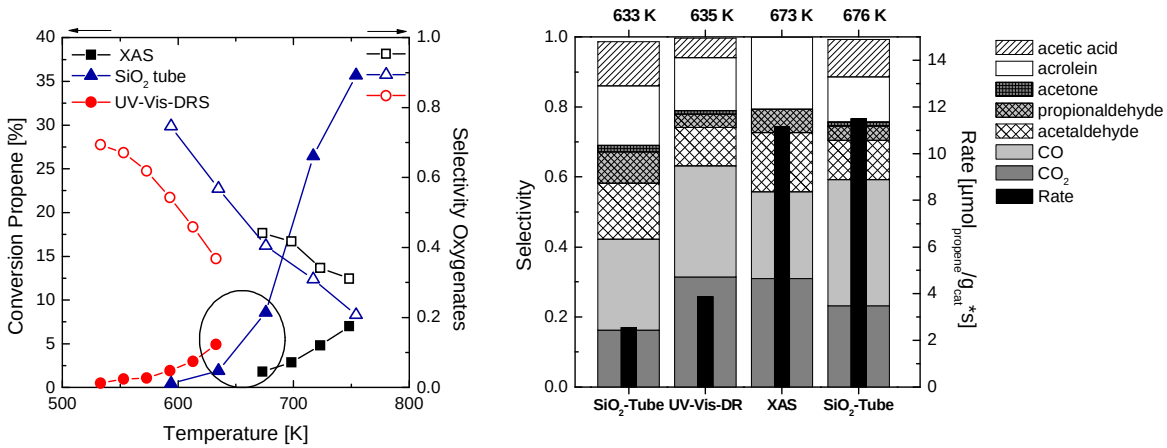

Figure 7-9: Propene conversion and oxygenate selectivity (left). Propene conversion rate referred to the sample mass, and product selectivities determined in the different measurement cells during the temperature programmed propene oxidation using dehydrated 7.7 wt% V_xO_y/SBA-15 (right).

Rates of propene oxidation relative to the mass of the catalyst were comparable for the temperatures employed. The reaction rate was slightly increased for the UV-Vis-DR cell compared to the fixed bed reactor at the same temperature (633 K). Reaction rates determined at 673 K in the XAS cell and in the fixed bed tube reactor were almost the same. Nevertheless, the selectivities of the reaction products formed were different for the various reaction cells. In contrast to the tube reactor and the UV-Vis-DR cell, no acetic acid was observed in the XAS cell. Although the propene conversion of the empty XAS cell (stainless steel) was low (< 0.5% $X_{propene}$, 673 K) compared to the sample measurement (~1.8% $X_{propene}$, 673 K), the cell itself may be active for propene oxidation. Therefore, the XAS cell was not suitable for deriving quantitative catalytic results. Comparing the catalytic results of the tube reactor and the UV-Vis-DR cell, similar selectivities of the reaction products were detected. Compared to the tube reactor, higher selectivities of CO_2 and CO were detected, whereas lower selectivities of acetic acid and acetaldehyde were observed in the UV-Vis-DR cell. Approximately the same selectivity towards acrolein was detected for both reaction cells (17% in SiO_2 tube reactor, 15% in UV-Vis-DR cell). Therefore, some fractions of the partial oxidation products (mainly acetic acid and acetaldehyde) were reacting to form CO and CO_2 in consecutive reactions in the UV-Vis-DR cell. These reactions may take place at the hot sample holder (metal) or at sample locations exhibiting a higher temperature than the average fraction of the sample. In summary, comparable catalytic behavior was detected for propene oxidation conducted in the quartz glass reactor and the UV-Vis-DR cell. For clarity and to reduce the numbers of figures below only the quantitative results obtained in the SiO_2 tube ("quartz glass") reactor are depicted.

7.2.6 Impact of the pretreatment procedure on the catalytic performance of V_xO_y/SBA-15

In situ spectroscopic measurements showed that a similar vanadium oxide structure was present on the SBA-15 support under catalytic conditions independent of thermal pretreatment prior to the catalytic runs or the presence of water vapor. The vanadium oxide structure was proposed to be similar to the dehydrated V_xO_y/SBA-15 structure that consists of an ordered arrangement of $[V_2O_7]$ units and in the case of 1.4 wt% V_xO_y/SBA-15, also of $[VO_4]$ vanadium centers. Exposure to catalytic conditions resulted in an increasing structural disorder of the vanadium centers on the support. This was observed to be independent of the vanadium loading for all pretreatment and reaction conditions. Hence, if a similar structure is present under catalytic conditions, the same catalytic performance will be measured. Evolution of propene conversion as a function of temperature is shown in ***Figure 7-10*** for differently treated 7.7 wt% and 1.4 wt% V_xO_y/SBA-15. The sample mass of V_xO_y/SBA-15 with different loading was adjusted to the same amount of vanadium in the reactor (~ 0.8-0.9 mg V). For clarity SBA-15 (105 mg) and boron nitride (240-290 mg), which was used as diluent, showed propene conversions below ~ 0.2 % (***Table 7-6***).

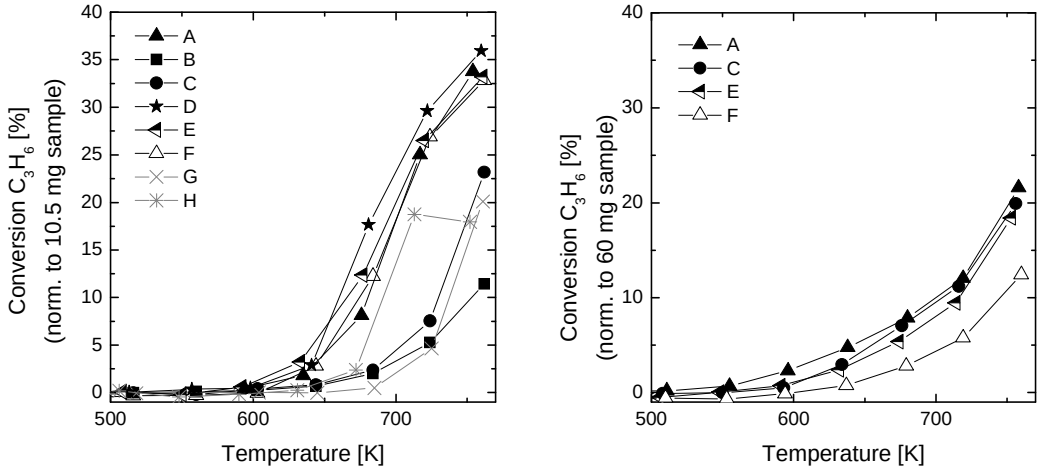

Figure 7-10: Propene conversion during propene oxidation (5% O_2 and 5% propene in He) on 1.4 wt% V_xO_y/SBA-15 (right) and 7.7 wt% V_xO_y/SBA-15 (left): (A) dehydrated sample; 653 K, 1 h, 20% O_2 in He; (B) dehydrated sample, 763 K, 1 h, 20% O_2 in He, (C) "recalcined" sample, 843 K, 12 h, 20% O_2 in He; (D) "multistep" sample: (i) 843 K, 12 h, 20% O_2 in He, (ii) 298 K, 24 h, 20% O_2 and 2% H_2O in He, 653 K, 1 h, 20% O_2 in He; (E) hydrated sample; (F) hydrated sample and 0.8% H_2O in the reaction gas; (G) physical mixture of V_2O_5 and SBA-15 (8 wt% V); (H) physical mixture of "ball milled" V_2O_5 and SBA-15 (8 wt% V). Approximately 0.8-0.9 mg V was used for all measurements.

For the reaction conditions employed in the spectroscopic measurements, the same propene conversions with increasing temperature were observed for differently treated samples (***Figure 7-10, curve A,E,F).*** However, differences were present when 7.7 wt% V_xO_y/SBA-15 was pretreated at 763 K for 1 h (***Figure 7-10 left, curve B***) or recalcined at 843 K for 12 h (***Figure 7-10 left, curve C***). The propene conversion decreased significantly compared to measurements without a pretreatment procedure (***Figure 7-10 left, curve E,F***) or with a thermal treatment at lower temperature (653 K, ***Figure 7-10 left, curve A***). Such a difference was not observed for 1.4 wt% V_xO_y/SBA-15 (***Figure 7-10 right***).

NMR measurements showed that after recalcination of 7.7 wt% V_xO_y/SBA-15 almost no Si-OH centers were detectable (***Chapter 6.2.6, Figure 6-7***). Additionally, XAS measurements showed that the dehydrated vanadium oxide structure was the same as determined for the standard pretreatment procedure (623 K, 0.5-1 h, ***Chapter 6.2.9, Table 6-3***). Furthermore, in the case of "aged" 7.7 wt% V_xO_y/SBA-15 samples, a decrease of the structural disorder of the "aged" dehydrated vanadium oxide structure was observed after recalcination. In contrast to the increased structural order of the vanadium oxide phase after recalcination, a significant change in the XAFS spectra was observed if the "recalcined" sample was treated under reaction conditions. ***Figure 7-11*** depicts the V K edge XANES spectra and the corresponding FT(χ(k)*k^3) of "recalcined" 7.7 wt% V_xO_y/SBA-15 after reaction in propene and oxygen. A decrease of the pre-ege peak height from 0.76 to 0.63 was detected in the XANES spectra. Using the linear correlation introduced in ***Chapter 5.2.4***, an increase of the average V-O distance from 1.77 to 1.84 Å was indicated. A reduction of the valence of the vanadium centers, which may explain a decrease of the pre-edge peak, was excluded because of the unchanged energy position of the pre-edge peak maximum in the V K edge XANES (5.4 eV relative to V K edge at 5465 eV).

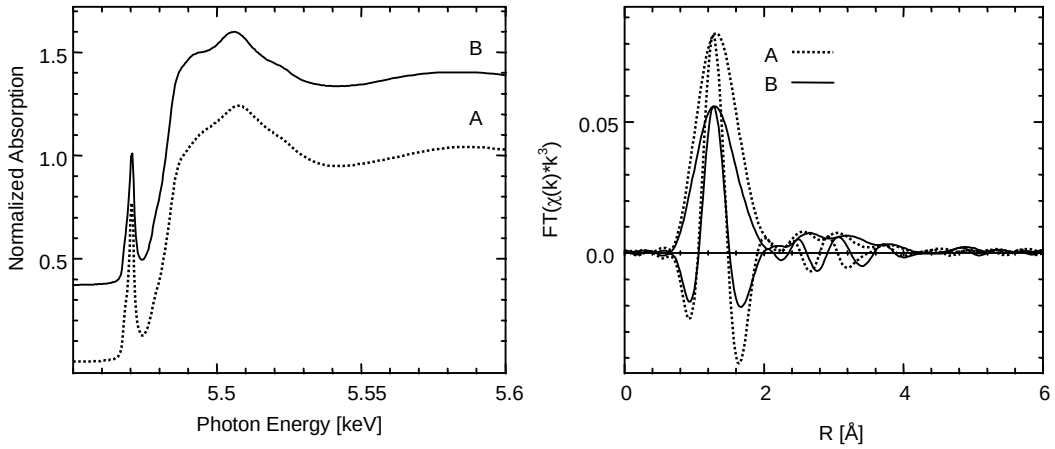

Figure 7-11: V K edge XANES spectra (left) and FT(χ(k)*k^3) (right) of 7.7 wt% V_xO_y/SBA-15 recorded at 298 K after "recalcination" at 768 K for 8 h in 20% O_2 in helium (A) and after a temperature programmed propene oxidation at 723 K, 5% O_2 and 5% propene in He (B).

Moreover, a change in the V-O coordination from 4- to 5-fold seems likely but cannot be distinguished unambiguously from a distorted 4-fold V-O coordination. To show that the dehydrated [V_2O_7] model structure was suitable to describe the experimental FT(χ(k)*k^3) of recalcined 7.7 wt% V_xO_y/SBA-15 after reaction in propene and oxygen, an XAFS refinement was conducted. The results are summarized in ***Table 7-4***. Compared to the refinement conducted to the FT(χ(k)*k^3) after calcination, an increase of the disorder parameters of all scattering paths used was determined. A significant increase of the V-V distances was determined, which was accompanied by an increase of the confidence limits. For the disorder parameters determined for the V-Si distance at 2.5 Å and for the V-V distances, F parameters higher than 0.5 were determined. After propene oxidation that was conducted after a recalcination pretreatment (> 760 K), the vanadium oxide structure was strongly distorted. This is in contrast to samples pretreated below 723 K.

Table 7-4: Experimental distances and XAFS disorder parameters (σ^2) for different types of atom at distance R from the absorbing V atom in a model system assuming an ordered arrangement of [V_2O_7] units (***Chapter 5***). Parameters were obtained from the refinement of this model structure to the experimental V K edge XAFS FT(χ(k)*k^3) of dehydrated 7.7 wt% V_xO_y/SBA-15 (k range from 2.7-10.5 $Å^{-1}$, R range 0.83-3.62 Å, N_{ind} = 16, E_0 = 0 eV in all cases, (subscript c indicates parameters that were correlated in the refinement, subscript f indicates parameters that were fixed in the refinement). Recalcination was conducted in 20% O_2 in He at 768 K for 8 h and propene oxidation at 723 K (5% O_2 and 5% propene in He).

	7.7 wt% V_xO_y/SBA-15			
	dehydrated for 12 h, 768 K		after propene oxidation	
Type (N)	R [Å]	σ^2 [$Å^2$]	R [Å]	σ^2 [$Å^2$]
V – O (1)	1.78	0.0063	1.79	0.0108
V – O (1)	1.78 $_c$	0.0063 $_c$	1.79 $_c$	0.0108 $_c$
V – O (2)	1.78 $_c$	0.0063 $_c$	1.79 $_c$	0.0108 $_c$
V – O (1)	2.89	0.0012 $_f$	2.93	0.003 $_f$
V – V (1)	3.30±0.02	0.0010	3.37±0.04	0.0149 (F=0.6)
V – V (1)	3.60±0.03	0.0010 $_c$	3.73±0.07	0.0149 $_c$
V – Si (1)	2.53	0.0112	2.52	0.0190 (F=0.8)
Residual	5.9		9.5	

Spectroscopic measurement suggested that during the catalytic process V-O-Si bonds were formed. The formation of such bonds to the support would be more likely if Si-OH centers were present. As determined from NMR, these centers were almost absent after recalcination of 7.7 wt% V_xO_y/SBA-15. Thus, the low availability of these centers on recalcined 7.7 wt% V_xO_y/SBA-15 causes the high structural distortion of the vanadium oxide structure because of a lack of binding sites with the support SBA-15. Such a decrease in propene conversion was not observed for low loaded 1.4 wt% V_xO_y/SBA-15. This may be explained by the lower V to surface ratio (0.3 V/nm^2) and the higher surface (40%) of this sample. Thus, the probability that Si-OH centers remained after the recalcination process was higher. Due to the fact that no comparable NMR or XAFS measurements were performed with recalcined 1.4 wt% V_xO_y/SBA-15 this could not be investigated further. That the presence of OH groups, either Si-OH or V-OH, was important for obtaining the higher propene conversion was shown by a rehydration experiment. Curve D in ***Figure 7-10*** shows the propene conversion for 7.7 wt% V_xO_y/SBA-15 that was pretreated in a multistep procedure. The sample was recalcined for 12 h at 843 K and afterwards rehydrated at 298 K for 24 h with 2% H_2O vapor and finally dehydrated for 1 h at 653 K. After this multistep treatment the propene conversion above 600 K was even enhanced compared to 7.7 wt% V_xO_y/SBA-15 that was just dehydrated at 653 K for 1 h.

For 7.7 wt% V_xO_y/SBA-15 V_2O_5 may have formed on the SBA-15 support. Therefore, V_2O_5 may cause the increased activity compared to recalcined 7.7 wt% V_xO_y/SBA-15. To estimate the reactivity of crystalline V_2O_5 compared to 7.7 wt% V_xO_y/SBA-15, two physical mixtures of V_2O_5 and SBA-15 with 8 wt% V were prepared. The first mixture was prepared using well crystalline V_2O_5 (domain size >> 1000 Å) and the second with less crystalline V_2O_5 (Debye-Sherrer domain size ~ 170 Å) that was treated in a ball mill. Both samples showed an increasing propene oxidation above 650 K (***Figure 7-11 left, curve G and H***). In contrast to the well crystalline V_2O_5 sample, the "ball milled" V_2O_5 sample showed a strong increase in the propene conversion above 700 K. For higher temperatures the propene conversion remained constant, whereas the oxygen conversion increased to ~ 100 %. Similar to the results discussed in ***Chapter 2*** for bulk V_2O_5, reduced V^{4+} and V^{3+} phases may be present. Thus, "nano" crystalline" V_2O_5 formed on SBA-15 may have a similar reactivity at lower temperatures as the dehydrated V_xO_y/SBA-15 phase, but it is more likely that this phase is reduced to less reactive V^{4+} and V^{3+} vanadium oxide phases at higher temperatures (> 700 K). Furthermore, the reactivity could only be only comparable to 7.7 wt% V_xO_y/SBA-15 if an equal V mass was used for the catalytic measurements. In ***Chapter 6.2.9*** the amount of V_2O_5 formed on "aged" 7.7 wt% V_xO_y/SBA-15 was estimated by Raman spectroscopy to be 3%. This would mean that only 0.2 wt% of the V was present as crystalline V_2O_5. Such a small amount of crystalline V_2O_5 would not explain the increased reactivity of 7.7 wt% V_xO_y/SBA-15.

A second measurement run was conducted to investigate the reproducibility of the increased propene conversion on 7.7 wt% V_xO_y/SBA-15 with "mild" or no pretreatment procedure. ***Figure 7-12*** depicts the propene conversion during the first and the second measurement of 7.7 wt% V_xO_y/SBA-15 pretreated at 653 K for 1 h or pretreated at 763 K for 1 h.

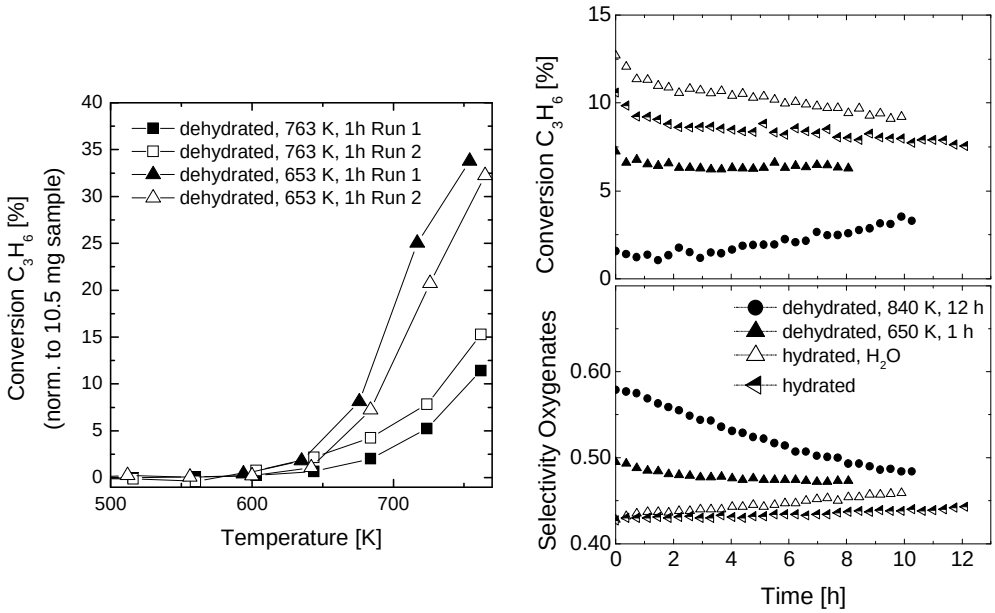

Figure 7-12: Propene conversion and oxygenate selectivity during propene oxidation (5% O_2 and 5% propene in He) of 7.7 wt% V_xO_y/SBA-15 for different treatments. During subsequent temperature programmed reactions (left) and under isothermal conditions at 673 K (right).

Similarly to the UV-Vis-DRS measurements (***Figure 7-2, bottom, left***), the formation of aldehydes increased for the first run of 7.7 wt% V_xO_y/SBA-15 pretreated at 653 K for 1 h (***Figure 10-6***, ***appendix***). For 7.7 wt% V_xO_y/SBA-15 pretreated at 653 K, the conversion of propene was lower in the second run, whereas the conversion increased for 7.7 wt% V_xO_y/SBA-15 pretreated at 763 K for 1 h. It seems that for both pretreatment procedures the conversion of propene approached the same value. In order to further investigate this behavior long-term measurements (8-12 h) at 673 K were performed for selected pretreatment procedures.

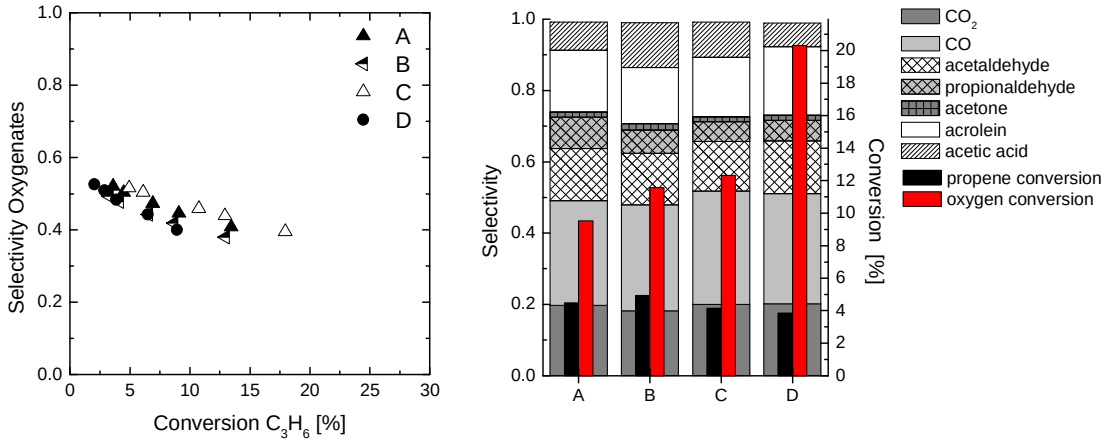

Figure 7-13: Oxygenate selectivity versus propene conversion determined after 8-12 h at 673 K (left) for 7.7 wt% V_xO_y/SBA-15 and comparision of the product selectivities for similar propene conversion (right): (A) dehydrated sample, 653 K, 1 h, 20% O_2 in He; (B) hydrated sample; (C) hydrated sample and 0.8% H_2O in the reaction gas, (D) "recalcined" sample, 843 K, 12 h, 20% O_2 in He. (Details ***Table 7-5***).

In all measurements the propene conversion and the selectivity towards C_2 and C_3 oxygenates approached the same values (***Figure 7-12, right***). These were similar to the values obtained for 7.7 wt% V_xO_y/SBA-15 dehydrated at 653 K for 1 h. After the long-term measurements, the initial flow rate was varied (20-75 ml/min, ~ 0.8 ml reactor volume, 1500-5625 h^{-1} GHSV). The resulting selectivity versus propene conversion is depicted in ***Figure 7-13***. As indicated from the subsequent measurements, the dependence of the selectivity on the propene conversion was similar for all treatment procedures employed. For all treatments of 7.7 wt% V_xO_y/SBA-15, an increase of the CO_x (CO and CO_2) formation was measured with increasing propene conversion. Similar product selectivities were obtained for all treatment procedures for the same propene conversion of 4-5 % (***Table 7-5***). The main difference between the various treatment procedures was the increase of selectivity towards acetic acid from 7 to 10-13% on the samples that were not pretreated in oxygen. The additional water content in the reaction gas mixture of 0.8 Vol% did not change the selectivity towards the products formed. Interestingly, 7.7 wt% V_xO_y/SBA-15 that was recalcined prior to reaction in propene and oxygen showed a significantly enhanced oxygen conversion of 20%. This was more than twice as much as detected for the other treatment procedures. This pretreatment resulted in the lowest propene conversion rate of 7.7 wt% V_xO_y/SBA-15.

The same catalytic performance was observed for all treatment procedures. This matches the observation that the same vanadium oxide species were present on the support. UV-Vis-DR spectra that were recorded after 4 h at 673 K in the reaction mixture showed a blue shift of the characteristic absorption band of the dehydrated tetrahedral V_xO_y/SBA-15 phase. Furthermore, absorption bands below 600 nm (2 eV) that are indicative for d-d transitions of reduced vanadium oxide phases were detected. Some V_2O_5 phases may have formed that were reduced during the reaction. The UV-Vis-DR spectra of subsequent measurements of 7.7 wt% V_xO_y/SBA-15 in propene showed a similar trend (***Figure 7-14***). The amount of reduced V slightly increased after a second temperature programmed reaction in propene and oxygen. Conversely, absorption bands below 600 nm were absent in the UV-Vis-DR spectra for 1.4 wt% V_xO_y/SBA-15 after propene oxidation of 4 h at 673 K. Therefore, the dehydrated tetrahedral species was not reduced.

Table 7-5: Product selectivities and propene conversion of 7.7 wt% V_xO_y/SBA-15 at 673 K after 8-12 h (***Figure 7-13*** (right)): (A) dehydrated sample, 653 K, 1 h, 20% O_2 in He; (B) hydrated sample; (C) hydrated sample and 0.8% H_2O in the reaction gas, (D) "recalcined" sample, 843 K, 12 h, 20% O_2 in He. (*rate [$\mu mol_{propene}/(g \cdot s)$] g=$m_v$ or m_{cat}; **GHSV gas hour space velocity referred to a 0.8 ml reactor volume and a 20-75 ml/min volume flow).

Treat-ment	Mass	GHSV**	Conversion [%]		Rate*		Selectivity [%]								**C** balance
	mg	[h^{-1}]	C_3H_6	O_2	m_v	m_{cat}	CO_2	CO	Aa	Pa	Ac	Ar	AcA	ΣC_{2-3}	[%]
A	10.6	4500	4.4	9.5	118	9	20	29	15	9	1	17	8	50	99.5
B	10.8	5625	4.8	11.6	158	12	18	30	15	7	2	16	13	52	99.7
C	10.6	4500	4.1	12.3	110	8	20	32	14	6	1	17	10	48	100.7
D	11.0	3000	4.0	20.3	69	5	20	31	15	6	1	19	7	48	99.5

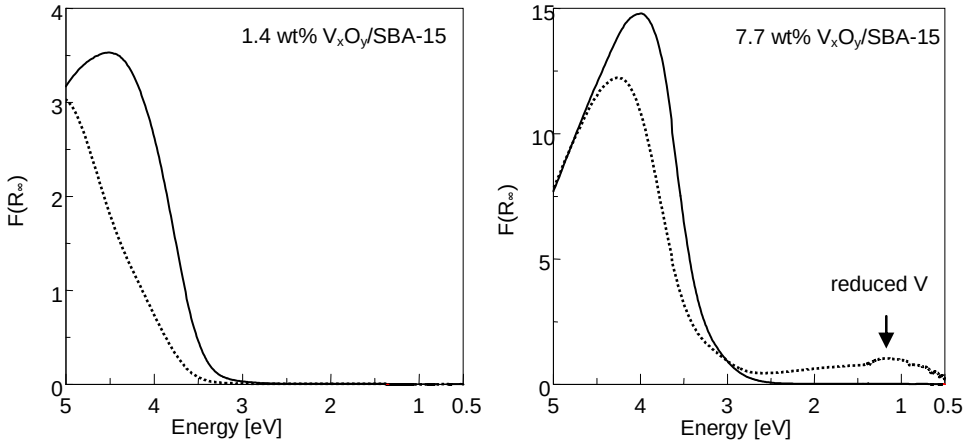

Figure 7-14: UV-Vis-DR spectra of dehydrated (623 K, 20% O_2 in He) 1.4 wt% (right) and 7.7 wt% (left) V_xO_y/SBA-15 recorded at 298 K after dehydration (solid line) and propene oxidation (dotted line) at 675 K for 4 h.

7.2.7 Impact of the vanadium loading on the catalytic performance of V_xO_y/SBA-15

Figure 7-15 depicts the conversion and the selectivities obtained for all V_xO_y/SBA-15 samples during temperature programmed reaction and during isothermal reaction in 5% propene and 5% oxygen at 673 K. The sample mass was adjusted to the same vanadium content in the reactor. All samples were dehydrated in 20% O_2 in helium at 653 K for 1 h before temperature programmed reaction in propene and oxygen. The same increase in propene conversion was detected for 1.4 wt% and 4.1 wt% V_xO_y/SBA-15 (***Figure 7-15, left bottom***). Higher 673 K the propene conversion of 7.7 wt% V_xO_y/SBA-15 was significantly increased compared to the propene conversion of 1.4 wt% and 4.1 wt% V_xO_y/SBA-15. For lower temperatures the increase in propene conversion was similar to that of the lower loaded V_xO_y/SBA-15 samples. The corresponding products selectivities are depicted in ***Figure 7-15 (right)***. For all vanadium loadings an increase in the formation of CO_x products was detected (CO_2 and CO) with increasing temperature. Approximately the same evolution of the CO_2 selectivity was detected for all V_xO_y/SBA-15 samples. Conversely, the selectivity towards CO increased with increasing vanadium loading. Furthermore, mainly acetaldehyde, propionaldehyde, acetone, acrolein and acetic acid (C_2 and C_3 oxygenated products) were detected for all V_xO_y/SBA-15 samples.

In contrast to 4.1 wt% and 7.7 wt% V_xO_y/SBA-15, only minor amounts of acetic acid were detectable for 1.4 wt% V_xO_y/SBA-15. Conversely, higher amounts of propionaldehyde were detected for 1.4 wt% V_xO_y/SBA-15. Except for the selectivity towards acrolein, and acetaldehyde for 1.4 wt% V_xO_y/SBA-15, a significant drop in the C_2 and C_3 selectivity oxygenated products was observed with increasing temperature. For a more precise comparison, the selectivity versus conversion plots were measured by varying the initial flow rate of the sample gas stream (20-75 ml/min total volume flow, ~ 0.8 ml reactor volume, 1500-5625 h^{-1} GHSV). These measurements were conducted after 8-12 h at 673 K to ensure that no fast changes in the gas phase composition occurred. Propene conversion and selectivities determined were constant after that time for all samples (***Figure 7-15, right***).

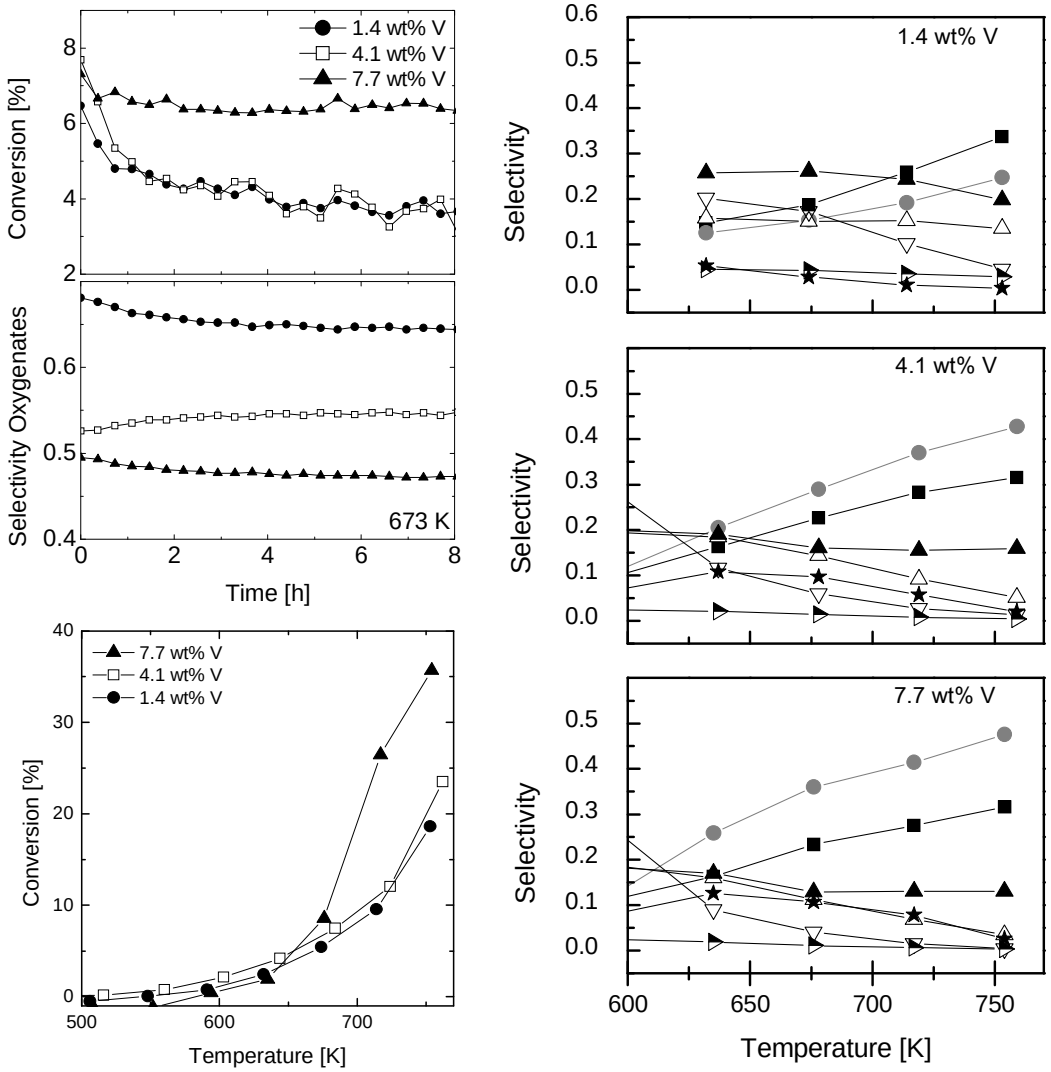

Figure 7-15 Left, top: Propene conversion and oxygenate selectivity during propene oxidation (5% O_2 and 5% propene in He) of dehydrated 1.4-7.7 wt% V_xO_y/SBA-15 under isothermal conditions at 673 K (right). Left, bottom and right: Propene conversion and product selectivity of dehydrated 1.4-7.7 wt% V_xO_y/SBA-15 during the temperature programmed reaction in propene and oxygen (5% O_2 and 5% propene in He). (symbols on right side: circle=CO, square=CO_2, closed triangle up=acrolein, open triangle up=acetaldehyde, open triangle down=propionaldehyde, half filled triangle= acetone, closed star=acetic acid).

A decrease of oxygenate products with increasing propene conversion was observed for all samples (***Figure 7-16, top left***). The sum selectivity towars all oxygenates was approximately 10% higher for 1.4 wt% V_xO_y/SBA-15 than for 4.1 wt% and 7.7 wt% V_xO_y/SBA-15. The single selectivities towards the products formed were compared at the same propene conversion. The detailed results are listed in ***Table 7-6*** and shown ***Figure 7-16***. Interestingly, the ratio of the reacted amount of oxygen and the reacted amount of propene increased from 1.3 to 2.0 and 2.5 with increasing amount of vanadium on SBA-15, respectively. Hence, different reaction mechanism may proceed on the higher loaded V_xO_y/SBA-15 samples.

Table 7-6: Product selectivities and propene conversion of dehydrated 1.4-7.7 wt% V_xO_y/SBA-15 (653 K, 1 h, 20% O_2) at 673 K after 8-12 h. ([1] rate [$\mu mol_{propene}/(g \cdot s)$]; [2] GHSV gas hour space velocity referred to 0.8 ml reactor volume and 20-75 ml/min volume flow,[3] ball milled V_2O_5 + SBA-15, [4] at 643 K, [6] at 684 K).

Sample	Mass	GHSV[2]	Conversion [%]		Rate[1]		Selectivity [%]								C balance
[wt% V]	mg	[h^{-1}]	C_3H_6	O_2	m_v	m_{cat}	CO_2	CO	Aa	Pa	Ac	Ar	AcA	ΣC_{2-3}	[%]
1.4	10.6	3000	3.7	4.5	63	0.9	20	15	12	20	5	25	2	64	99.4
4.1	21.8	3000	3.6	6.5	59	2.4	20	26	17	7	2	23	5	54	99.9
7.7	60	5625	3.6	8.3	121	9.3	19	28	15	10	2	18	7	52	99.7
8[3]	11.5	3000	2.6	6.2	41	3.2	22	29	16	3	1	20	8	49	100.1
V_2O_5[4]	20	3000	2.8	6.0	5	2.8	28	15	13	2	2	20	13	50	99.8
SBA-15[5]	105	3000	-	-	-	-	-	-	-	-	-	-	-	-	-
BN[6]	460	3000	0.2	0.3	-	0.0	33	22	7	-	-	22	-	40	100

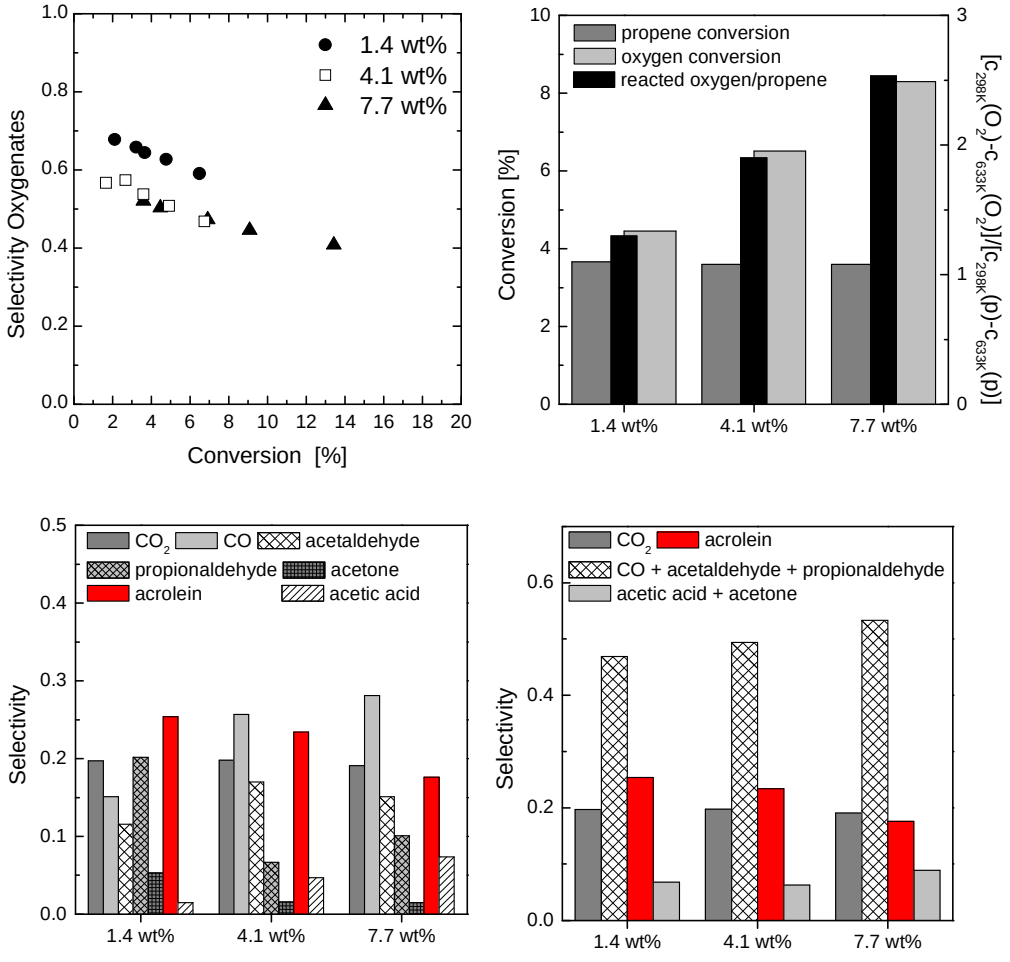

Figure 7-16: Oxygenate selectivity versus propene conversion determined after 8-12 h at 673 K (left, top) for dehydrated 1.4-7.7 wt% V_xO_y/SBA-15. Comparison of propene and oxygen conversions (right, top) and product selectivities corresponding to the conversions shown (bottom). (***Table 7-6***).

The reaction products observed match the reaction products reported in the literature for propene oxidation on V_xO_y/SiO_2 samples (***Table 7-1***). Conversely, the product selectivities detected here deviate from the selectivities reported in the literature (***Table 7-1***). This difference in the product selectivities observed may be explained by the different reaction temperatures used and the absence of a high content of water in the reaction feed. In the presence of a high water content in the gas phase, typically, high amounts of acetone and acetic acid were reported [15,159]. If no additional water is introduced high selectivities towards acetaldehyde, acetone and acrolein were reported [16,158,160]. Moreover, minor amounts of acrylic acid were reported [16]. Comparing the selectivities towards the reaction products formed showed that the same selectivity towards CO_2 (20%) was observed independent of the vanadium content of the V_xO_y/SBA-15 samples. The selectivities towards all other reaction products changed with varying vanadium loading. The selectivity towards C_3 aldehyde oxygenates (acrolein, propionaldehyde, and acetone) was enhanced for 1.4 wt% V_xO_y/SBA-15 compared to higher loaded 4.1 wt% and 7.7 wt% V_xO_y/SBA-15. With increasing vanadium loading the selectivity towards the partial degradation products (C_2 oxygenates and CO) increased. The amounts of product observed may be explained in a similar way to those of the selective oxidation of propane and propylene on bulk mixed metal oxide catalysts (Bettahar *et al.* [5] and Lin *et al.* [3]). A simplified version of the possible reaction pathways (A, B, and C) is given in ***Figure 7-17***. Various reaction pathways for selective propene oxidation were discussed by Bettahar *et al.* [5] and Lin *et al.* [3]. Three types of aldehydes (acrolein (B), propionaldehyde (C), and acetone (A)) seem likely to be formed from the partial oxidation of propene. The corresponding alcohols are possible intermediates [3,5]. The partial degradation products acetaldehyde and acetic acid may form from the consecutive oxidation of propionaldehyde and acetone.

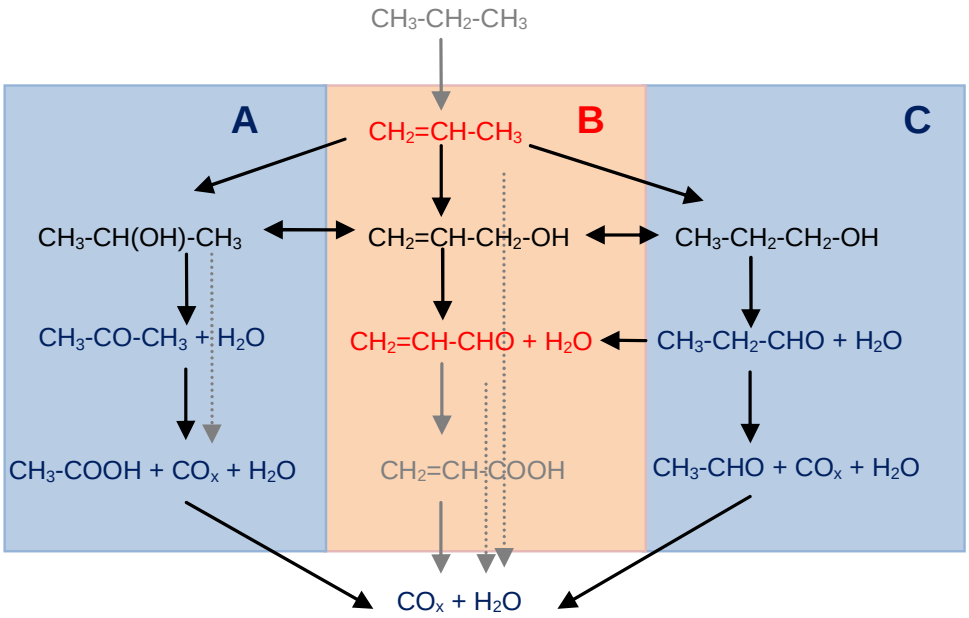

Figure 7-17: Main oxygenate products of the partial oxidation of propane and propene [3,5].

The highest selectivity towards acrolein (25%), propionaldehyde (20%), and acetone (5%) was determined for 1.4 wt% V_xO_y/SBA-15 (***Table 7-6***, ***Figure 7-16***). With the increase of the vanadium content in the V_xO_y/SBA-15 samples, a significant decrease of the propionaldehyde selectivity from 20% to 7-10% was observed. This was accompanied by an increase in CO selectivity from 15% to 26-28% and an increase of the acetaldehyde selectivity from 12% to 15-17%. The other reaction products showed less intense changes in selectivity with increasing vanadium content. The selectivity towards acrolein decreased from 25% to 18% and acetone selectivity decreased from 5% to 2%. Conversely, acetic acid selectivity increased from 2% to 7% with increasing vanadium loading. The proposed reaction scheme was suitable to explain the observed product selectivities because the decreased acetone selectivity was accompanied with an increased formation of acetic acid. Furthermore, a decrease of propionaldehyde selectivity was accompanied by an increased formation of acetaldehyde and CO_x. Only CO increased with the decreasing propionaldehyde selectivity. Therefore, CO may be the major CO_x oxidation product from the consecutive oxidation of propionaldehyde. Additionally, the CO observed may be formed from oxidation of acetone to acetic acid because increase of CO selectivity was stronger than increase of acetaldehyde selectivity. In order to determine which reaction pathway of the propene oxidation was present, the selectivities towards propionaldehyde, CO, and acetaldehyde were combined (***Figure 7-16, right, bottom***). These products represent reaction pathway C. Acetone and acetic acid were selectivity combined to represent reaction pathway A. The combined selectivities towards path A and C together with those towards acrolein (B) and CO_2 are depicted in ***Figure 7-16*** (***right, bottom***). Independent of the vanadium loading, approximately the same selectivity was determined towards CO_2 formation (20%). The combined selectivity towards path A showed a small increase (7-9%). Interestingly, the combined selectivity towards reaction pathway C increased by 6% (47% to 53%), whereas the acrolein selectivity decreased by 7% (25% to 18%) with increasing vanadium content. Thus, the higher vanadium content mainly shifts the propene oxidation to reaction pathway C. Furthermore, the probability of a consecutive reaction of the corresponding C_3 aldehydes, the formation of acetaldehyde and acetic acid, increased with increasing vanadium content of the V_xO_y/SBA-15 samples. This increase in consecutive reactions matches the increased oxygen conversion observed for 4.1 wt% and 7.7 wt% V_xO_y/SBA-15.

Comparing the rates of propene oxidation per gram vanadium showed that no dependence on the surface area was determined (***Table 7-6***) for V_xO_y/SBA-15 samples. The reaction rate per gram vanadium was approximately the same for 1.4 wt% (highest surface area) and 4.1 wt% V_xO_y/SBA-15 and was twice as high for 7.7 wt% V_xO_y/SBA-15 at 673 K (lowest surface area). Similarly to the rate of propene oxidation the rate of acrolein formation increased by approximately 40% for 7.7 wt% V_xO_y/SBA-15 compared to 4.1 wt% and 1.4 wt% V_xO_y/SBA-15. A similar observation was made by Zhao *et al.* [15,158] for V_xO_y/Al_2O_3 but not for V_xO_y/SiO_2. The increased activity of 7.7 wt% V_xO_y/SBA-15 may be an effect of the high density of vanadium centers on the surface or of the presence of small clusters of crystalline vanadium oxide phases. The latter was excluded because reduced vanadium phases were also observed for 4.1 wt% V_xO_y/SBA-15. Thus, the high density of vanadium oxide centers on 7.7 wt% V_xO_y/SBA-15 may explain the enhanced rate of propene oxidation.

Additionally, propene oxidation rate and product selectivities measured for bulk V_2O_5 are listed in ***Table 7-6.*** These values were not determined after several hours of reaction but from the temperature programmed reactions using a constant rate (***Figure 7-10, curve H*** and ***Figure 2-9, Chapter 2***). Apparently, no significant changes in the product selectivities were obtained for V_2O_5 reference compared to 7.7 wt% V_xO_y/SBA-15. Hence, similar reaction mechanisms may proceed on the surfaces of V_2O_5 and of high loaded 4.1 and 7.7 wt% V_xO_y/SBA-15. The reaction rate of propene oxidation per gram vanadium was lower for bulk V_2O_5. This was explained by the higher amount of accessible vanadium surface sites present on V_xO_y/SBA-15 samples.

7.2.8 The influence of the oxygen and propene concentration on the catalytic performance of V_xO_y/SBA-15

The measurements discussed above showed that similarly to propene oxidation on bulk mixed metal oxides, three reaction pathways can be distinguished for the propene oxidation on V_xO_y/SBA-15 catalysts. A second set of experiments intended to investigate the impact of various propene and oxygen concentrations on the catalytic performance of 1.4 wt% and 7.7 wt% V_xO_y/SBA-15. Therefore, the samples were heated with a constant rate to 713 K. Measurements were performed at 593 K, 633 K, 673 K, and 713 K (± 4 K). No pretreatment procedure was conducted prior to the temperature programmed oxidation in propene and oxygen. This resulted in an increase of 6% for the acetic acid selectivity and a slight decrease (3%) of the acrolein and propionaldehyde selectivities compared to the sample pretreated at 653 K (1 h, 20% O_2 in He). The oxygen to propene ratio was varied from 5 to 0.5 by changing the initial propene and oxygen concentrations (Vol% O_2/ Vol% propene ~ 2/5, 5/5, 7.5/5, 10/5, 5/7.5, 5/2.5, and 5/1). The resulting conversions and selectivities (633 K) are depicted in ***Figure 7-18***. For clarity, the reacted ratio of oxygen and propene is also shown. Independent of the initial ratio, the ratio of reacted O_2/propene remained constant between 2.0 and 2.5 for 7.7 wt% V_xO_y/SBA-15 and between 1.4 and 2.1 for 1.4 wt% V_xO_y/SBA-15. Furthermore, no drastic changes of the product selectivity were observed. With decreasing O_2/propene ratio a decrease of the CO selectivity from 33% to 25% was observed. This was accompanied by an increase of the acrolein selectivity from 14% to 18% and a decrease of the propionaldehyde selectivity from 3% to 1%. The change in selectivity for all other products was below 1%. Hence, an excess of oxygen in the gas phase may mainly facilitate the oxidation of acrolein to CO on 7.7 wt% V_xO_y/SBA-15.

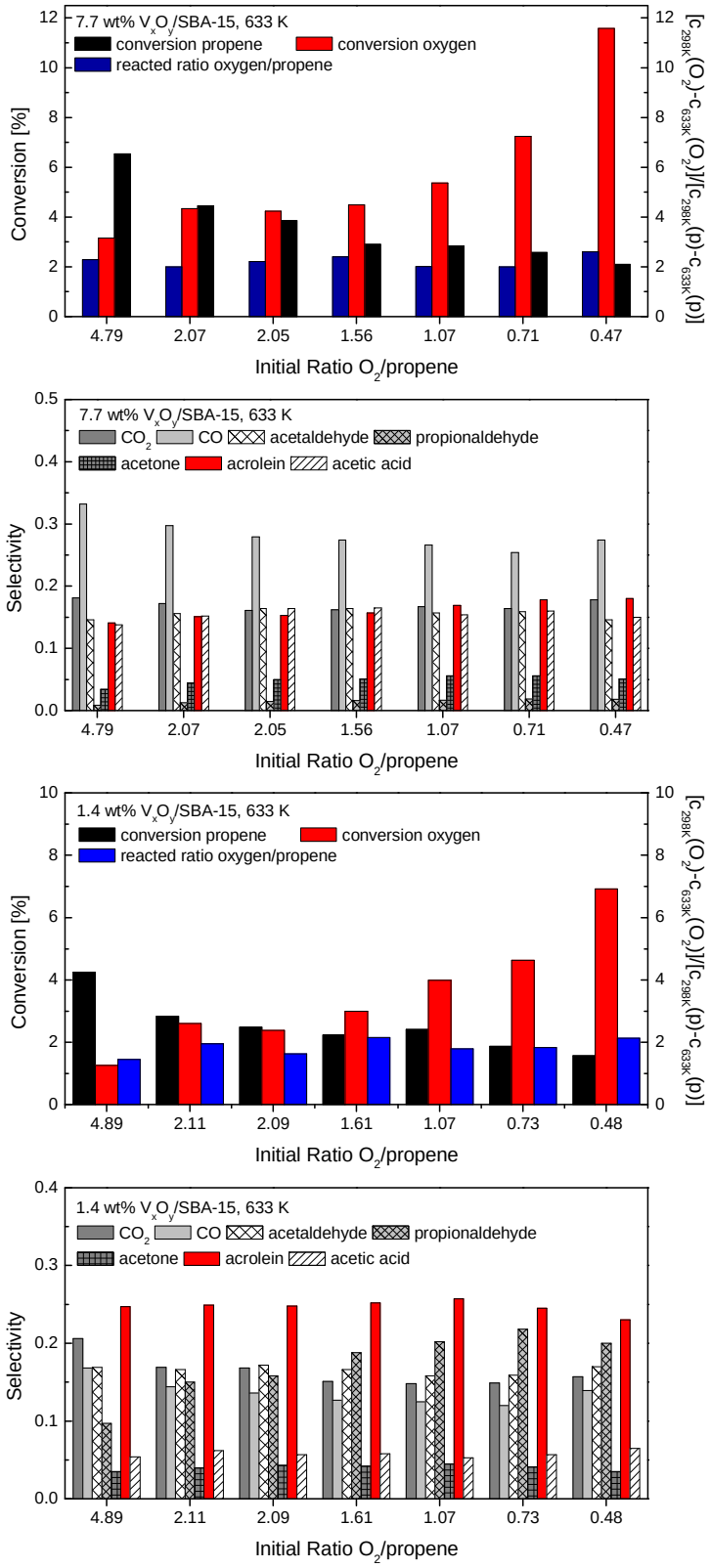

Figure 7-18: Propene and oxygen conversion, reacted ratio of oxygen/propene, and product selectivities for (hydrated) 1.4 wt% and 7.7 wt% V_xO_y/SBA-15 as a function of the initial oxygen to propene ratio in the reaction gas at 633 K. (Vol% O_2/ Vol% propene: ~ 2/5, 5/5, 7.5/5, 10/5, 5/7.5, 5/2.5, and 5/1).

The selectivity towards acrolein (25%) remained constant with decreasing O_2/propene ratio for 1.4 wt% V_xO_y/SBA-15 (***Figure 7-18***). Conversely, the selectivity towards propionaldehyde increased. This increase was accompanied by a decrease of the CO_2 selectivity from 21% to 15% and of the CO selectivity from 17% to 12%. In the case of 1.4 wt% V_xO_y/SBA-15 an oxygen excess may facilitated the deeper oxidation of propionaldehyde to CO and CO_2. These results suggest that an excess of oxygen in the reaction mixture enhances the content of unselective oxygen species. These oxygen species may react with the C_3 aldehydes to form CO_x. The probability that acrolein will be oxidized to CO_x seems to be lower than for the oxidation of propionaldehyde. This would explain that the acrolein selectivity decreases on 7.7 wt% V_xO_y/SBA-15 where only low amounts of propionaldehyde were detected. According to Grzybowska-Świerkosz [162], gaseous or chemisorbed oxygen species (O_2, O_2^-, or O^-) may be responsible for the deep oxidation of propene to CO_x products.

Reaction orders determined for propene and oxygen indicated that the formation of acrolein was mainly independent of the oxygen content. Taking a formal kinetic reaction approach, the reaction orders of propene (m) and oxygen (n) can be obtained from the acrolein reaction rate (***Equation 6.1***). Keeping the concentration of one reactant constant allows determining the reaction order of the other reactant by measuring the reaction rate of acrolein as a function of its concentration.

$$r(acrolein) = k_{eff} c^n(O_2) \cdot c^m(propene) \tag{7.1}$$

$$\rightarrow \quad \ln[r(acrolein)] = \ln[k_{eff}] + n \ln[c(O_2)] + m \ln[c(propene)] \tag{7.2}$$

In the case of a constant oxygen concentration, the reaction order for propene was calculated from the linear function ***6.3*** refined to the experimental data. The corresponding plots depicted in ***Figure 10-7*** and ***Figure 10-8*** in the ***Appendix***.

$$\ln[r(acrolein)] = \ln[k'_{eff}] + m \ln[c(propene)] \tag{7.3}$$

The reaction orders were determined at 633 K to ensure differential conversions below 10% for both V_xO_y/SBA-15 samples. Reactions orders of m ~ 0.5 and n ~ 0 were obtained for 1.4 wt% V_xO_y/SBA-15. A slight increase to n = 0.2 was observed for 7.7 wt% V_xO_y/SBA-15, which may be due to the stronger influence of electrophilic oxygen. Similar reaction orders were determined by Zhao *et al.* for V_xO_y/SiO_2 [158]. They interpreted the reaction order of zero for oxygen as an indicator that only V^{5+} vanadium centers are the active site. Reduced crystalline V_2O_5 phases were excluded as active centers [158]. The reaction order of 0.5 for propene cannot be explained unambiguously. Typically, a reaction order of 0.5 indicates that the molecule dissociates at the catalyst surface. This may be indicative for the necessary H abstraction step that is discussed in the process of the activation of the propene molecule for further oxidation to acrolein. However, this interpretation is highly speculative without further investigating different kinetic models. Nevertheless, the reaction order of zero for oxygen indicates that formation of acrolein was mainly independent of the oxygen content and a fast re-oxidation of the vanadium centers during catalytic propene oxidation.

7.2.9 *The influence of the oxygen to propene ratio on the structure of V_xO_y/SBA-15*

A reaction order of zero for oxygen in the selective oxidation of propene to acrolein indicated a fast reoxidation of the vanadium centers involved. Therefore, the majority of vanadium centers should have an average oxidation state of V^{5+}. Temperature programmed UV-Vis-DRS measurements were conducted with 1.4 wt% and 7.7 wt% V_xO_y/SBA-15 using various oxygen and propene concentrations to investigate the major vanadium oxide phase under these conditions. The samples were dehydrated at 554 K for 1 h in 20% O_2 in He prior to temperature programmed reaction in propene and oxygen. The maximum temperature applied was 626 K. Propene to oxygen ratios of 1/5, 5/5, 5/1, and 5/0 were investigated. The resulting UV-Vis-DR spectra for 1.4 wt% and 7.7 wt% V_xO_y/SBA-15 after reaction are depicted in ***Figure 7-19***. A significant increase in intensity in the range of 0.5-3.0 eV was determined in the UV-Vis-DR spectra without oxygen in the gas phase during the reaction. Absorption bands in this region are indicative of reduced vanadium centers. For all other propene to oxygen ratios, approximately the same UV-Vis-DR spectra were recorded. This was even the case for the 1/5 oxygen to propene ratio. UV-Vis absorption bands below 3.0 eV were absent and characteristic UV-Vis absorption bands of V^{5+} tetrahedral vanadium centers were observed above 3 eV. This corroborated that independently of the vanadium loading, the majority of the vanadium centers are V^{5+} centers. A more detailed discussion about the reduced vanadium oxide state and redox properties of V_xO_y/SBA-15 under reaction conditions will be given in the next chapter.

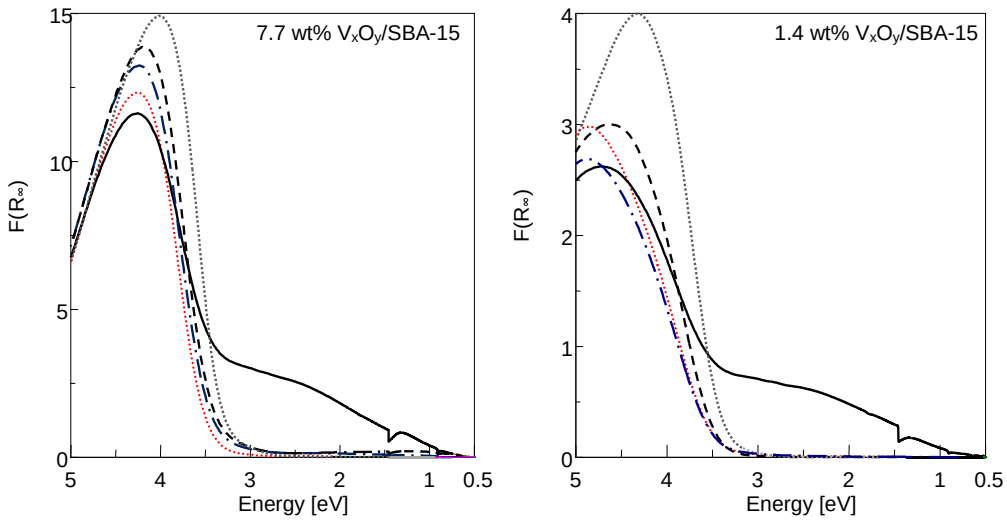

Figure 7-19: UV-Vis-DR spectra of dehydrated 1.4 wt% (right) and 7.7 wt% V_xO_y/SBA-15 (left) recorded at 298 K after temperature programmed reaction in various oxygen:propene mixtures in He at 636 K: after dehydration, 554 K, 20% O_2 (dotted, grey); 5:5 (dotted, red); 1:5 (dashed, black); 5:1 (dashed and dotted, blue); and 0:5 (solid, black).

7.3 Concluding remarks on the catalytic performance and the structural evolution of V_xO_y/SBA-15 during catalytic propene oxidation

7.3.1 Structural evolution of V_xO_y/SBA-15 during propene oxidation

XAFS measurements and Raman experiments showed that mainly the dehydrated V_xO_y/SBA-15 structure was present during propene oxidation. Compared to the structure obtained after dehydration in 20% O_2 a wider V-V distance distribution was determined from XAFS refinements of 4.1 wt% and 7.7 wt% V_xO_y/SBA-15 after propene oxidation. Conversely, XAFS measurements showed that the V-V interaction or V-Si interaction increased for 1.4 wt% V_xO_y/SBA-15. A structural transformation comparable to the dehydration process described in ***Chapter 6*** was observed when hydrated V_xO_y/SBA-15 samples were used for catalytic measurements. Raman measurements showed that carbonaceous species were formed below 573 K during temperature programmed reaction of hydrated V_xO_y/SBA-15 in propene oxidizing conditions. For 7.7 wt% V_xO_y/SBA-15 thermally treated in 20% O_2 at 768 K for 8 h, a significant change compared to the dehydrated state was observed in the XANES spectra and in the FT(χ(k)*k^3) after propene oxidation. This change may be caused by a strong distortion of the dehydrated "ordered V_2O_7" structure. The average vanadium oxidation state was V^{5+} for all treatments employed. NMR measurements showed that on dehydrated 7.7 wt% V_xO_y/SBA-15 (573 K, 1 h, 20% O_2 in He) no Si-OH centers were detected after propene oxidation at 673 K (5% O_2 and 5% propene in He, 1 h).

The characteristic absorption band in the UV-Vis-DR spectra of dehydrated V_xO_y/SBA-15 was blue shifted under propene oxidizing conditions. For 7.7 wt% V_xO_y/SBA-15 small amounts of reduced vanadium oxide phases were present under catalytic conditions. These were ascribed to partially reduced V_2O_5 nano particles present on "aged" V_xO_y/SBA-15 samples. The blue shift observed occurred for all V_xO_y/SBA-15 samples in the range of 500-600 K. In this temperature region an increase of propene conversion, propionaldehyde and acrolein formation was observed compared to a repeated measurement. The onset of catalytic activity (aldehyde formation) was in the range of 500-520 K. The blue shift of the absorption band under propene oxidation conditions (> 550 K) was observed independent of the initial V_xO_y/SBA-15 structure and the vanadium loading. The blue shift may be caused by a reaction of V-OH groups to Si-O-V groups. This reaction would be accompanied by a decrease of Si-OH centers, which matches the decrease of Si-OH centers detected by NMR.

Changes in the V-OH and Si-OH concentration were also reported for other oxidation reactions. A similar decrease of Si-OH centers accompanied with a similar blue shift in the UV-Vis-DR spectra was observed by Gao *et al.* [23] during catalytic methanol oxidation using a 1% V_xO_y/SiO_2 catalyst. Launay *et al.* [26] observed a decrease of the V-OH IR absorption bands at ~3660 cm^{-1} on a 2.1% V_xO_y/SiO_2 catalyst during methane oxidation. Furthermore, Launay *et al.* [26] reported an increased number of V-OH species that may lead to a better catalytic activity in the methane oxidation to formaldehyde. The results reported in

the literature imply that the V-OH bond may be involved in the oxidation of propene. Li *et al.* [159] reported that such V-OH centers (ascribed to Brønstedt acid centers) are the major active site for the oxidation of propene to acetone in the presence of water. They proposed a "V-O-CH-$(CH_3)_2$" as intermediate [159]. Such an intermediate suggests that the V-OH group attacks the C=C double bond of the propene molecule. Moreover, the decrease of the Si-OH groups during propene oxidation indicates reduced vanadium centers left after the desorption of acetone may react with the Si-OH centers to Si-O-V bonds. Another interpretation for the decrease of Si-OH centers may be that not the V-OH bond but the V-O-V bond or a V-(OH)-V bond reacts with the propene molecule. In this case, the blue shift in the UV-Vis-DR spectra would be considerably smaller for low loaded 1.4 wt% V_xO_y/SBA-15 than for higher loaded 4.1 wt% and 7.7 wt% V_xO_y/SBA-15. However, on 1.4 wt% V_xO_y/SBA-15 a lower number of V-O-V bonds was present, and the blue shift increased with decreasing vanadium content. Therefore, V-OH bonds seem to be involved in the formation of V-O-Si bonds during propene oxidation.

7.3.2 Catalytic performance of V_xO_y/SBA-15 during propene oxidation

Nevertheless, more acrolein and propionaldehyde than acetone were detected in the temperature range where the blue shift in the UV-Vis absorption spectra occurred (***Figure 10-6***). The higher concentration of C_3 aldehydes indicates a complex reaction of propene with V_xO_y/SBA-15. The formation of acetone and propionaldehyde may be explained by the attack of electrophilic oxygen on the C=C double bond in propene, which would result in an adsorbed $[OC_3H_6]$ that is negatively charged. In contrast, the formation of acrolein is generally described by a nucleophilic attack of M^{n+}-O^{2-} to the propene molecule. According to Grzybowska-Świerkosz [162], this redox or "Mars van Krevelen mechanism" is started by H abstraction from the methyl group of propene. This results in the formation of a π-allyl species that is positively charged. The π-allyl species is then attacked by the nucleophilic M^{n+}-O^{2-} center. A second H abstraction results in the formation of acrolein. Subsequently, H atoms are transferred to adjacent M^{n+}-O^{2-} centers that form $M^{(n-1)+}$-OH centers. The reduced metal sites are reoxidzied by gaseous oxygen. The formation of propionaldehyde and acetone from propene via a electrophilic mechanism and the formation of acrolein via a nucleophilic mechanism was calculated by Li *et al.* [163,164] for a $V_4O_{11}^-$ cluster. In the case of acrolein and propionaldehyde, two vanadium centers were involved. The fact that the acrolein selectivity remained relatively constant with increasing temperature suggests that acrolein may be formed by the nuclephilic mechanism with π-allyl stabilization (***Figure 7-15, right***). The selectivities towards all other oxygenates decreased significantly with increasing temperature because the impact of electrophilic oxygen from the gas phase increases at elevated temperature.

Nevertheless, acrolein was not the major product of catalytic propene oxidation on V_xO_y/SBA-15. According to ***Figure 7-17*** reaction pathway C, the oxidation to propionaldehyde and acetaldehyde, was enhanced on V_xO_y/SBA-15 samples. Thus, more reactive electrophilic than nuclephilic oxygen species were present. The origin of electrophilic oxygen may be a consequence of the re-oxidation of reduced vanadium centers with molecular oxygen. Recently, Kontratenko *et al.* [165] reported that $V^{n+}\cdots O^{-}$ species are detectable by EPR after the re-oxidation of reduced vanadium centers on VO_x/MCM41. These

$V^{n+}\cdots O^{-}$ oxygen species reacted rapidly with propene [165]. Using highly disperse V_xO_y/SiO_2 and bulk V_xO_y vanadium oxides Kontratenko *et al.* [165,166] showed that the selectivity towards propene was improved by using N_2O instead of oxygen in the reaction of propane to propene. Hence, more nucleophilic oxygen formed during the re-oxidation of reduced V_xO_y/MCM41 with N_2O than with O_2 [165]. Thus, future investigations with other oxidizing agents like N_2O, which may enhance the selectivity of acrolein during propene oxidation on V_xO_y/SBA-15 catalysts, would be desirable.

7.3.3 Impact of vanadium loading on the catalytic performance of V_xO_y/SBA-15

The reaction rate of propene conversion and acrolein formation per gram V was enhanced for 7.7 wt% V_xO_y/SBA-15, in contrast to 1.4 wt% and 4.1 wt% V_xO_y/SBA-15. Conversely, the vanadium oxide structure of the dehydrated 4.1 wt% and 7.7 wt% V_xO_y/SBA-15 samples showed no distinct differences during temperature programmed reaction in propene. However, the arrangement of $[V_2O_7]$ units may be slightly different on 7.7 wt% V_xO_y/SBA-15 from that on 4.1 wt% V_xO_y/SBA-15. This may not be resolved with the spectroscopic methods used. It seems likely that the local vanadium density on 7.7 wt% V_xO_y/SBA-15 may be higher and areas with high and low vanadium dispersion may exist. A higher vanadium density would imply that more disperse vanadium centers than the proposed $[V_2O_7]$ dimers may be involved in the catalytic process. More than two vanadium centers seem likely to facilitate redox mechanism discussed above which may explain the increased acrolein formation on 7.7 wt% V_xO_y/SBA-15. A similar increased acrolein formation was reported by Zhao *et al.* [16] for the oxidation of propene to acrolein over vanadium oxides supported on Al_2O_3 with high vanadium loading but not for vanadium oxides supported on SiO_2. Nevertheless, an increased number of adjacent $[V_2O_7]$ units may explain the increased activity of 7.7 wt% V_xO_y/SBA-15. Furthermore, the decreasing activity in repeated or long term measurements may be explained by a different arrangement of $[V_2O_7]$ units. For instance, V-(OH)-V bonds between the $[V_2O_7]$ units may exist that decrease with time. In contrast to acrolein formation, vanadium loading of V_xO_y/SBA-15 samples had only minor effects on the observed selectivities towards the different reaction pathways (***Figure 7-17***). Increasing the vanadium content on SBA-15 facilitated only the consecutive oxidation of the C_3 aldehydes. Hence, decreasing the vanadium loading of V_xO_y/SBA-15 does not change the basic reaction pathways of propene oxidation on V_xO_y/SBA-15.

7.3.4 Selective oxidation of propene to acrolein on isolated "VO_4" centers

The selective oxidation towards acrolein was observed with 18-25% selectivity independent of the vanadium loading. Regarding the concept of "site isolation" proposed by Grasselli *et al.* [167] at least two available oxygen sites must be present for the stoichiometric reaction of propene to acrolein and water. Moreover, the reaction involves two hydrogen abstraction steps from the methyl group of the propene which requires at least two available"V-O" functionalities. An ordered dimeric $[V_2O_7]$ structure was proposed for higher loaded 4.1 wt% and 7.7 wt% V_xO_y/SBA-15 and thus, the formation of acrolein seems feasible. Conversely, an isolated tetrahedral $[VO_4]$ structure may be present on 1.4 wt% V_xO_y/SBA-15

because of the high UV-Vis edge energy of 3.9 eV. In the case of isolated [VO_4] units, the oxygen sites involved in the reaction must originate from the same vanadium center. Therefore, different "V-O" bonds located at the same vanadium center must be involved. Zhao *et al.* [158] proposed the participation of the V-O-Si bond in the oxidation process of propene. However, the low reducibility of 1.4 wt% V_xO_y/SBA-15 after the catalytic reaction observed in this work (***Chapter 8***) indicates a high strength of the V-O-Si bond. Thus, this bond may not be involved in the reaction process. In consequence of an inactive V-O-Si bond, different sources of "V-O" must be present. No clear evidence about the nature of this source can be given based on the results obtained in this work but two options seem likely. The high UV-Vis edge energy of 3.9 eV after propene oxidation clearly points to isolated vanadium species. In this case the number of V-O-Si bonds must be lower than 3 to explain the reaction without a rupture of V-O-Si bonds in the case of isolated vanadium centers. Therefore other "V-O" sites may be involved in the reaction, *e.g.* V-O^-, V=O or V-OH groups. Another explanation may be that the proposed isolated vanadium tetrahedrons are in spatial proximity, similar to dimeric vanadium centers proposed for 7.7 wt% V_xO_y/SBA-15. This allows a reaction mechanism involving two vanadium sites, *e.g.* two V=O sites. This assumption is corroborated by the fact that the dimeric [V_2O_7] model structure was suitable to describe the experimental Fourier transformed EXAFS obtained for 1.4 wt% V_xO_y/SBA-15 after reaction in propene and oxygen. The latter explanation is preferred here, because more than one vanadium center may enable a better electron transfer during the catalytic reaction.

7.3.5 Elucidation of structure-activity correlations with respect to other model systems

The observed selectivities towards the oxygenated products of 7.7 wt% V_xO_y/SBA-15 were not significantly different from those obtained for bulk V_2O_5. Therefore, similar active centers may be present on the surface of V_xO_y/SBA-15 and of bulk V_2O_5 catalysts. Moreover, a significant influence of the support material was excluded. Compared to other supports (*e.g.* Al_2O_3), SBA-15 exhibits only few weak acidic centers that would interact with the rather basic propene molecule [22,168]. Mostly, an increase of the acetic centers was observed if vanadium oxides were added to the SiO_2 supports. Assuming similar active centers for V_2O_5 and high loaded V_xO_y/SBA-15 may explain the small differencs in the selectivities observed between bulk and supported vanadium oxides. Regarding the structure activity correlations of more complex mixed metal catalysts, *e.g.* MoVTe, this result indicates that structural complexity of vanadium sites in selective propene oxidation may play only a minor role and that chemical complexity may be more important. Hence, the presence of different metal sites will be required to enhance the catalytic performance of vanadium. This is in contrast to results reported for supported molybdenum model catalysts. For Mo_xO_y/SBA-15 [8] and MoO_3/VGCNF [9] catalysts an increased catalytic performance was observed for the oxidation of propene towards acrolein. For these molybdenum systems the structural complexity of the molybdenum oxides was more important than the chemical complexity. In the next stage of model catalysts supported mixed metal oxides systems should be investigated in more detail to reveal the impact of chemical and structural complexity on the catalytic performance. The results obtained for V_xO_y/SBA-15 model catalysts indicate that addition of vanadium

sites to other supported transition metal host structures will only improve acrolein selectivity if the vanadium sites are in cooperation with the transition metal oxide structure during catalytic reaction. Recently heteropolyoxomoybdates containing vanadium supported on SBA-15 were described [10]. These systems seem promising to derive further structure functionality relationships addressing the role of vanadium and molybdenum during selective propene oxidation.

7.4 Summary

In situ UV-Vis-DRS, XAS, and Raman measurements showed that the dehydrated V_xO_y/SBA-15 structure mainly persisted under catalytic propene oxidizing conditions. Moreover, the dehydrated V_xO_y/SBA-15 structure was observed even when hydrated V_xO_y/SBA-15 samples were used for catalytic measurements or when small amounts of water vapor (0.8 Vol%) were added to the reaction mixture. Apparently, the SBA-15 support stabilizes the dehydrated V_xO_y/SBA-15 structure under catalytic conditions. Temperature programmed reaction (5% propene and 5% oxygen in He) on hydrated V_xO_y/SBA-15 samples showed that a structural transformation (dehydration) proceeded similar as observed under dehydrating conditions in 20% O_2 in He. A wider V-V distance distribution was determined for 4.1 wt% and 7.7 wt% V_xO_y/SBA-15 from XAFS measurements after propene oxidation. Hence, a small decrease of the structural order may have occurred during propene oxidation. Conversely, an increase of the V-V contributions or V-Si contributions to the $FT(\chi(k)*k^3)$ was observed for 1.4 wt% V_xO_y/SBA-15.

The onset of catalytic activity was in the range of 500-520 K. The onset was accompanied by a blue shift of the UV-Vis edge energy. The blue shift may be caused by the formation of additional V-O-Si bonds to the SBA-15 support. Therefore, V-OH bonds may have reacted with the propene molecule and residual Si-OH groups may have formed V-O-Si bonds during the re-oxidation of the reduced vanadium centers. The V-O-Si bond formation was an irreversible process. The blue shift of the UV-Vis edge energy in the temperature range of 500-600 K correlated with an increased formation of oxygenated reaction products. A comparable blue shift and increased aldehyde formation was not observed in repeated measurements.

During the catalytic oxidation of propene mainly the following products were observed: acrolein, propionaldehyde, acetaldehyde, acetone, acetic acid, CO, and CO_2. Three parallel reaction pathways were suggested from these reaction products. The main reaction pathway proceeds via the formation of propionaldehyde and acetaldehyde. The second reaction pathway proceeds via the formation of acrolein. A third reaction pathway with low selectivity proceeds via the formation of acetone and acetic acid. CO and CO_2 formed cannot be ascribed to a specific reaction pathway. The different kinds of reaction products formed suggest that nucleophilic and electrophilic oxygen species may be present during catalytic propene oxidation on V_xO_y/SBA-15.

No significant differences in catalytic performance were observed using dehydrated (653 K, 1 h, 20% O_2 in He) and hydrated V_xO_y/SBA-15 samples. Nevertheless, a slight increase of acetone and acetic acid fomation was observed for catalytic measurements that were performed using the hydrated V_xO_y/SBA-15 samples. Hence, more V-OH groups than present on dehydrated V_xO_y/SBA-15 may form during decomposition of hydrated V_xO_y/SBA-15 in propene and oxygen.

The catalytic activity of 7.7 wt% V_xO_y/SBA-15 recalcined for 12 h at 843 K was significantly lower. A strong structural distortion and an increased oxygen conversion were detected for this sample. The structural disorder of recalcined 7.7 wt% V_xO_y/SBA-15 was ascribed to missing HO-Si binding sites for vanadium centers that interacted with the propene molecule

Vanadium loading of V_xO_y/SBA-15 had only a minor effect on the oxygenate selectivities determined. The selectivity towards acrolein and propionaldehyde decreased and the selectivity towards acetaldehyde, acetic acid, and CO increased with increasing vanadium loading on SBA-15. Furthermore, the consecutive oxidation of the C_3 aldehydes increased with increasing vanadium loading. The oxygenate selectivities determined for 7.7 wt% V_xO_y/SBA-15 resembled those of bulk V_2O_5. Therefore, similar active vanadium oxide centers may be present on V_xO_y/SBA-15 and V_2O_5. V_xO_y/SBA-15 showed no reduction under catalytic conditions, in contrast to bulk V_2O_5.

8 Investigation of reducibility and re-oxidation of V_xO_y-SBA-15 catalysts

8.1 Introduction

Catalytic measurements of V_xO_y/SBA-15 showed that the average valence of the vanadium oxide remains V^{5+} under catalytic conditions. Similar observations were reported for Mo_xO_y/SBA-15 catalysts [10]. Mo_xO_y/SBA-15 catalysts showed a low reducibility even under reducing conditions in propene and H_2 (773 K). The low reducibility (Mo^{6+} to $Mo^{5.8+}$) was assigned to a stabilizing effect of the SiO_2 support [10]. However, in the previous chapter absorption bands at wavelengths longer than 500 nm, observed during the temperature programmed reaction with 5% propene at 636 K, give rise to the conclusion that the disperse vanadium oxide phase is reducible with propene at lower temperatures. A reduction of the vanadium oxide phase was observed for high and low loaded V_xO_y/SBA-15, respectively. The observation of reduced disperse vanadium oxide phases on SiO_2 is in contrast to results reported by Zhao [158]. Zhao concluded from Raman and UV-Vis-DR measurements (3% propene, 623 K) that disperse tetrahedral [VO_4] species present on SiO_2 were not reduced with propene. Only a reduction of V_2O_5 nano particles present at higher loadings occurred [158]. Except for the work by Zhao [158], no report was found in the literature that addresses the reduction of V_xO_y/SiO_2 with propene. Ovsitser *et al.* [29] reported for V_xO_y/MCM that under reducing conditions in hydrogen and propane at 773 K absorption bands in the range of 400-800 nm appear in the UV-Vis-DR spectra. These were assigned to reduced vanadium centers. They determined a fast re-oxidation (~ 5 s) of the reduced vanadium centers and a slower (~ 5 min) reduction kinetic from isothermal experiments at 773 K (change of propane and oxygen containing gas atmospheres). Using oxygen as oxidizing agent, they observed fully oxidized vanadium centers under propane oxidizing conditions [29]. Nevertheless, most reports in the literature describe the formation of reduced vanadium centers on V_xO_y/SiO_2 with a disperse vanadium oxide structure. In these investigations the reduction of the vanadium centers was conducted using hydrogen or vacuum [22,24,25,44]. It was proposed from H_2-TPR measurements combined with ESR measurements (up to 1200-1300 K) that the vanadium centers in V_xO_y/SiO_2 can be reduced to V^{4+} and V^{3+} [25]. For samples which were reduced at lower temperatures, Du *et al.* [22] concluded from XAFS measurements that only V^{4+} centers are present after reduction in hydrogen at 773 K. Venkov *et al.* [44] inferred using FTIR investigations with CO and NO as probe molecules that V^{3+} and V^{4+} with two different coordinative vacancies are present after reduction in H_2 and after evacuation. Different types of V^{4+} centers were reported by Berndt *et al.* [24]. They discussed the presence of $V^{4+}O_x$ centers (two different sites in and outside the pores of the MCM material) and acidic $V^{4+/5+}O(OH)_x(OSi{\equiv})_{3-x}$ centers [24].

In summary, no clear picture of the reduced vanadium centers on V_xO_y/SiO_2 was obtained from reports that discuss the role of reduced vanadium centers on silica material. Therefore, it was intended to further elucidate the valence state and the structure of the V_xO_y/SBA-15 model catalysts under changing oxidative (oxygen and propene together with oxygen) and reducing (propene) conditions.

8.2 Results and discussion

8.2.1 Local structure of V_xO_y/SBA-15 under reducing conditions

UV-Vis-DRS investigations (***Chapter 7.2.9, Figure 7-19***) showed that temperature programmed treatment of dehydrated 1.4 wt% and 7.7 wt% V_xO_y/SBA-15 in propene resulted in the formation of reduced vanadium oxide phases on the SBA-15 support. *In situ* XAS measurements were conducted to determine the nature of the reduced vanadium oxide phases. Dehydrated 7.7 wt% V_xO_y/SBA-15 was treated in 5% propene in He at 673 K for 1 h and 723 K for 1 h. The V K edge XANES, $\chi(k)*k^3$, and FT($\chi(k)*k^3$) of 7.7 wt% V_xO_y/SBA-15 and of the bulk vanadium oxide references V_3O_7, VO_2(B), and V_2O_3 are depicted in ***Figure 8-1***. Compared to the XANES spectrum recorded after dehydration, a change of the XANES structure, a shift of the absorption edge, and a significant decrease of the pre-edge peak height from 0.73 to 0.32 (673 K) and 0.20 (723 K) were observed (***Figure 8-1, left***). The XANES features after reduction of dehydrated 7.7 wt% V_xO_y/SBA-15 at 673 K resembled those of the VO_2(B) reference. Thus, indicating a reduction towards V^{4+}. The intensity of the first XANES feature increased with increasing temperature (723 K), and the pre-edge peak height decreased to 0.20. In addition to V^{4+}, V^{3+} centers may have formed. After reduction of 7.7 wt% V_xO_y/SBA-15, no similarity of the $\chi(k)*k^3$ and the FT($\chi(k)*k^3$) with that of bulk references was observed (***Figure 8-1, middle, right***). The oscillation in the $\chi(k)*k^3$ of reduced 7.7 wt% V_xO_y/SBA-15 was strongly damped compared to that of dehydrated 7.7 wt% V_xO_y/SBA-15.

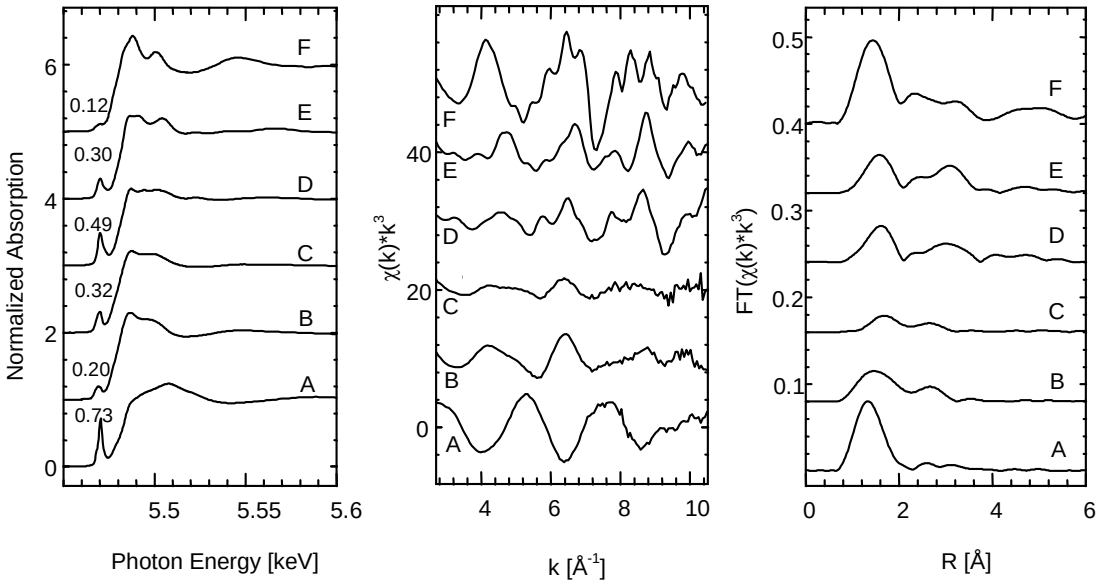

Figure 8-1: V K edge XANES spectra (left), $\chi(k)*k^3$ (middle), and FT($\chi(k)*k^3$) (right) recorded at 298 K: (A) dehydrated 7.7 wt% V_xO_y/SBA-15 (623 K, 20% O_2), (B) dehydrated 7.7 wt% V_xO_y/SBA-15 (623 K, 20% O_2) after reaction in 5% propene in He at 723 K, (C) dehydrated 7.7 wt% V_xO_y/SBA-15 (623 K, 20% O_2) after reaction in 5% propene in He at 673 K, (D) V_3O_7, (E) VO_2(B), (F) V_2O_3.

Variation in the positions of the oscillation in the $\chi(k)*k^3$ of reduced 7.7 wt% V_xO_y/SBA-15 indicate structural transformations compared to the dehydrated 7.7 wt% V_xO_y/SBA-15 structure. This interpretation was corroborated by the damped FT($\chi(k)*k^3$) of 7.7 wt% V_xO_y/SBA-15 after reduction (***Figure 8-1, right***). An overall reduction of the FT($\chi(k)*k^3$) of reduced 7.7 wt% V_xO_y/SBA-15 suggests a strong structural distortion. The maximum of the first signal in the FT($\chi(k)*k^3$), due to V-O interactions, shifted to longer distances. The second signal in the FT($\chi(k)*k^3$) increased with increasing temperature. This signal cannot be assigned unambiguously to a specific contribution (V-V, V-O, V-Si), but the increase implies structural changes in the second coordination sphere of the absorbing vanadium centers during reduction. The low similarity of the $\chi(k)*k^3$, and FT($\chi(k)*k^3$) of 7.7 wt% V_xO_y/SBA-15 after reduction with those of bulk vanadium oxide references with 5- and 6-fold coordination of the vanadium atoms showed that the reduced vanadium centers in 7.7 wt% V_xO_y/SBA-15 maintained their tetrahedral coordination. A XANES analysis using the pre-edge peak area and centroid energy (explained in more detail in ***Chapter 5.2.4***) according to Chaurand *et al.* [94] was employed for a more precise identification of the coordination and the oxidation state of the vanadium centers. The pre-edge peak area of V_2O_5 was normalized to the same value (0.80) as reported by Charaund *et al.* [94]. The pre-edge peak areas of all other samples measured in this work were referred to the normalized V_2O_5 pre-edge peak area (parameters are listed in ***Table 10-4***, ***appendix***). The resulting graph is depicted in ***Figure 8-2***. The parameters reported by Charaund *et al.* [94] were slightly different compared to the parameters determined here. This effect was assigned to lower resolution in the XANES region in this work.

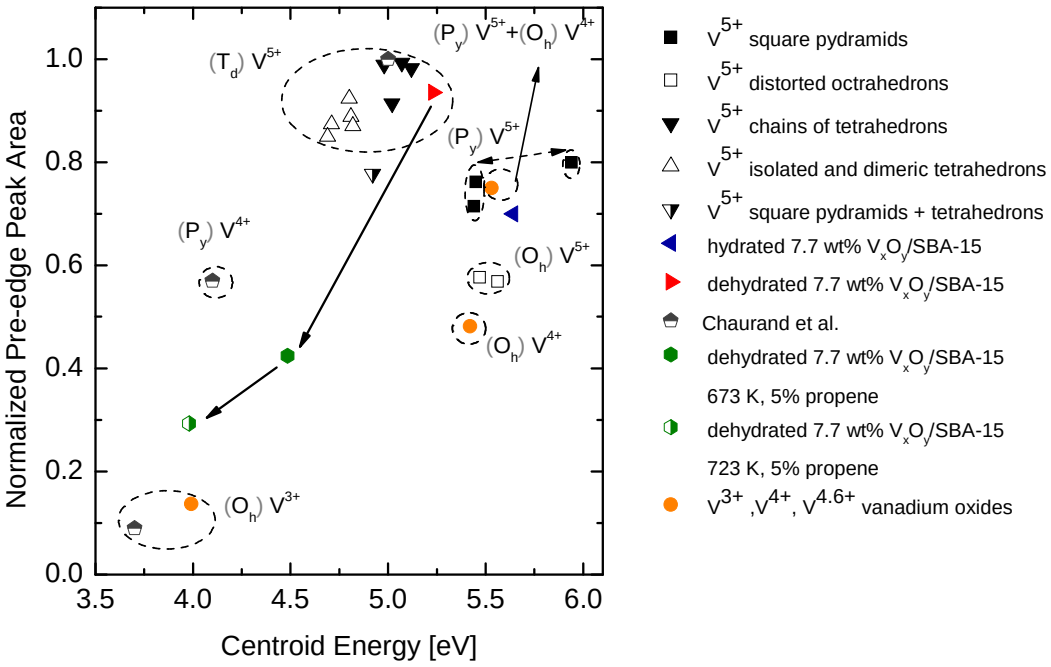

Figure 8-2: Normalized pre-edge peak areas (referred to the area of V_2O_5 that was normalized to 0.80) versus centroid energy of vanadium reference compounds and 7.7 wt% V_xO_y/SBA-15 after various treatments. Additionally, the values reported by Chaurand *et al.* [94] are shown. Dashed rings refer to the coordination of absorbing vanadium centers (O_h = octrahedral, P_y = pyramidal, T_d = tetrahedral). Detailed parameters are listed in ***Table 10-4*** in the ***appendix***.

Comparing the values depicted for V^{5+} references, a good identification of the coordination of the absorbing vanadium centers was possible from the horizontal energy shift of the centroid energy. Even a differentiation of various connectivities was feasible. In the case of tetrahedral V^{5+} references, a shift of 2.5 eV was observed between the centroid energy of references built of isolated and dimeric tetrahedrons and references that are comprised of chainlike tetrahedrons. An energy shift of 0.5 eV was observed between the centroid energy of V_2O_5 (layered arrangement of square pyramids) and $[V_2O_6]$ vanadate references (chains of square pyramids). A decrease of the average valence resulted in a decreasing pre-edge peak area and energy shift. The normalized pre-edge peak areas determined for reduced V_xO_y/SBA-15 were smaller than those of vanadium oxide references with average vanadium valence lower than +5. Hence, mainly V^{4+} centers may be present after reduction at 623 K. After reduction at 723 K, a mixture of V^{4+} and V^{3+} may be present. Tetrahedral V^{4+} references were not available in this work, which made the assignment of coordination and average valence difficult, ***Figure 8-2***. The centroid energies of 4.5 eV and 4.0 eV suggest that no octahedral V^{4+} vanadium oxide centers (5.5 eV) were present in reduced 7.7 wt% V_xO_y/SBA-15.

In situ investigations were employed to determine the temperature range where the reduction of vanadium centers of dehydrated 7.7 wt% V_xO_y/SBA-15 occured. ***Figure 8-3*** depicts the evolution of the V K edge XANES spectra and the evolution of the water ion current (m/e 18) during temperature programmed reduction in 5% propene in He from 298 K to 723 K. A small increase of the ion current, m/e 18, was observed in the range of 300-330 K. In this range, no structural changes were observed in the XANES spectra. A change in the XANES structure and the pre-edge peak height was observed above 520 K. The decrease of the pre-edge peak height was correlated with the formation of water in the gas phase (***Figure 8-3, right***). Therefore, the decreasing pre-edge peak height was due to the reduction of the vanadium oxide phase on SBA-15. The water ion current (m/e 18) remained constant above 650 K indicating that the reduction was not completed. The onset of reduction of 7.7 wt% V_xO_y/SBA-15 at 520 K coincidenced with the onset of catalytic activity during the temperature programmed reaction in 5% propene and 5% O_2 (***Chapter 7***).

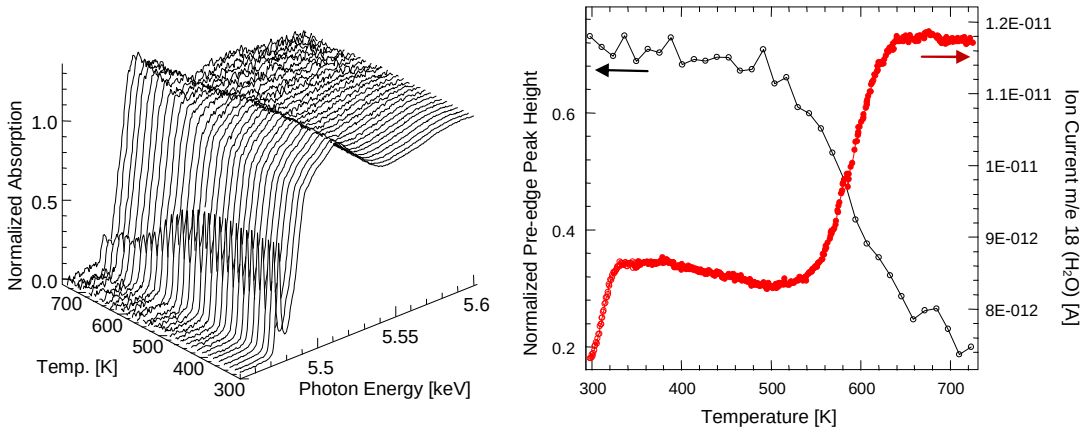

Figure 8-3: V K edge XANES spectra (left) and pre-edge peak height and water ion current m/e 18 (right) during the temperature programmed reaction of dehydrated (623 K, 20% O_2 in He) 7.7 wt% V_xO_y/SBA-15 in 5% propene in He (298-723 K, 5 K/min).

Figure 8-4 (left) depicts the *in situ* UV-Vis-DR spectra of dehydrated 7.7 wt% V_xO_y/SBA-15 during the temperature programmed reaction in 5% propene. With increasing temperature a decrease of the maximum intensity at 310 nm together with a wavelength shift of the absorption maximum to 295 nm was observed. An increase in intensity was observed in the UV-Vis-DR spectra for wavelengths longer than 400 nm. An increase at longer wavelength is indicative of d-d transitions of reduced vanadium species. The blue shift of the absorption band located at ~ 300 nm together with the increasing d-d absorption bands indicated a reduction of the vanadium oxide species. In order to follow the formation of reduced vanadium centers with increasing temperature, the wavelength at 700 nm was chosen for monitoring. For normalization, the intensity at 700 nm was referred to the maximum intensity at approximately 300 nm in the UV-Vis spectra recorded at 298 K after dehydration in 20% O_2. The normalized intensity at 700 nm was denoted as "relative $F(R_\infty)$ at 700 nm". The evolution of relative $F(R_\infty)$ at 700 nm and the water ion current, m/e 18, are shown in ***Figure 8-4 (right)***. An increased water formation was observed between 300 and 340 K similar to the *in situ* XAS measurements. In this temperature range, no change in the UV-Vis-DR spectra was detected. A moderate increase in intensity < 3% at 700 nm occured for temperatures in the range of 340-520 K. At temperatures higher than 520 K, a pronounced increase of up to 15-20% in relative $F(R_\infty)$ at 700 nm was detected in the UV-Vis-DR spectra. This increase was accompanied by an increased formation of water. The rising intensity above 520 K was ascribed to the formation of reduced vanadium centers, considering the results obtained from the XAS measurements. The small increase in intensity at 700 nm below 520 K may be due to the reduction of the residual V_2O_5 phase or the formation of carbonaceous species.

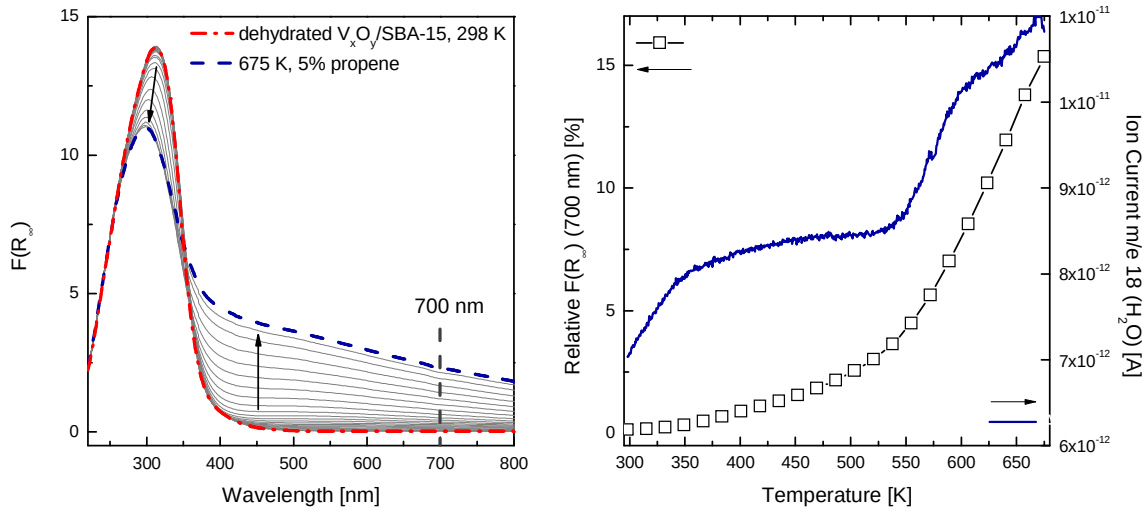

Figure 8-4: *In situ* UV-Vis-DR spectra (left) and absorption at 700 nm (relative to the maximum intensity determined in the absorption spectra at 298 K after dehydration) together with the water ion current m/e 18 (right) during the temperature programmed reaction of dehydrated (623 K, 20% O_2 in He) 7.7 wt% V_xO_y/SBA-15 in 5% propene in He (298-673 K, 4 K/min). The arrows on the left side indicate the evolution of the spectra during temperature treatment.

8.2.2 *Local structure and reactivity of V_xO_y/SBA-15 under changing reaction conditions*

In order to further investigate structure and catalytic performance of 7.7 wt% V_xO_y/SBA-15 under changing reaction conditions, isothermal switching experiments were performed at 673 K. The gas phase was rapidly changed between reducing (5% propene) and oxidizing conditions (5% propene and 5% oxygen). Prior to the switching experiment, 7.7 wt% V_xO_y/SBA-15 was treated for 20 min in 5% propene at 673 K. This treatment caused a reduction of 7.7 wt% V_xO_y/SBA-15 that is visible by an increased intensity at longer wavelengths (> 400 nm, relative $F(R_\infty)$ at 700 nm ~ 20%). After the initial reduction of 7.7 wt% V_xO_y/SBA-15, oxygen was added to the propene feed for ~ 30 min. The structure of 7.7 wt% V_xO_y/SBA-15 during re-oxidation was monitored by fast UV-Vis-DRS scans (~ 26 sec) and the gas phase was monitored by mass spectroscopy. A quantitative gas phase analysis was conducted with a gas chromatograph 1.5 min and 24 min after changing to oxidizing conditions (5% propene and 5% oxygen). At the end of the re-oxidation phase, UV-Vis-DR scans with a better resolution were recorded (~ 4 min scan time). The resulting UV-Vis-DR spectra after three reducing (5% propene) and oxidizing (5% propene and 5% oxygen) reaction cycles (each ~ 30-35 min) are depicted in ***Figure 8-5 (left)***. After the first re-oxidation, the UV-Vis-DR spectrum of 7.7 wt% V_xO_y/SBA-15 resembled those recorded under catalytic conditions at 673 K (***Chapter 7***). Thus, after re-oxidation the vanadium oxide structure of 7.7 wt% V_xO_y/SBA-15 corresponded to the dehydrated V_xO_y/SBA-15 structure ("ordered $[V_2O_7]$"). The average V valence was +5 after re-oxidation. Switching the gas phase back to reducing conditions resulted again in an increase of the intensity of the absorption bands at longer wavelengths and thus a reduction of 7.7 wt% V_xO_y/SBA-15 was observed.

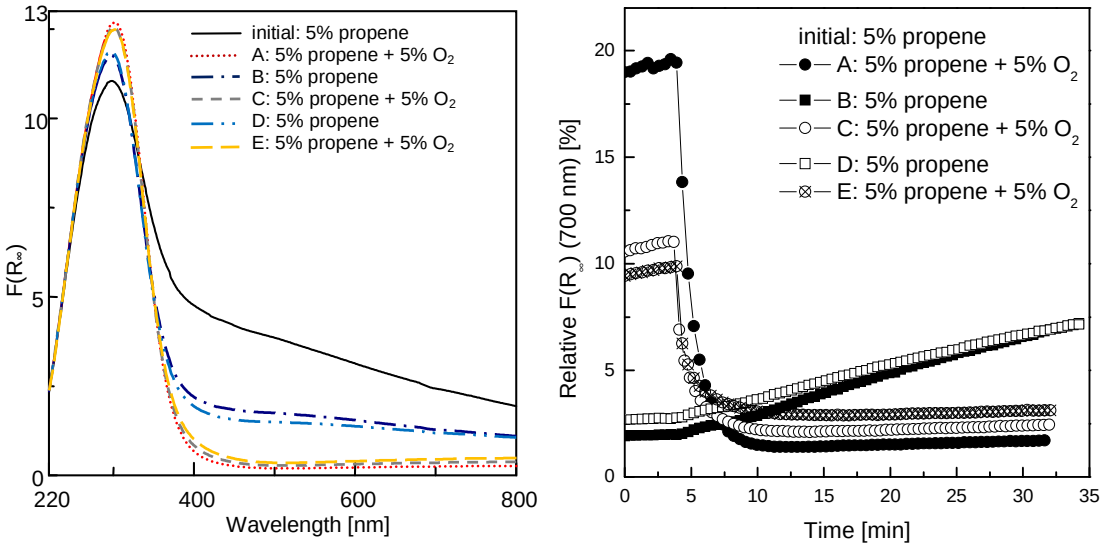

Figure 8-5 Left: UV-Vis-DR spectra of dehydrated (623 K, 20% O_2 in He) 7.7 wt% V_xO_y/SBA-15 recorded at 673 K after several reducing (5% propene) and oxidizing (5% propene and 5% oxygen) reaction cycles. Right: Evolution of the absorption at 700 nm (relative to the maximum intensity determined in the absorption spectra at 298 K after dehydration) during the reducing (5% propene) and oxidizing (5% propene and 5% oxygen) reaction cycles at 673 K. The gas phase was changed after 3.9 min in each reaction cycle.

The relative $F(R_\infty)$ at 700 nm was only 10-12% after 35 min in reducing conditions after the first re-oxidation of 7.7 wt% V_xO_y/SBA-15. This was significantly lower than the relative $F(R_\infty)$ at 700 nm of 20% obtained after the initial reduction. Hence, less centers could be reduced after re-oxidation under catalytic conditions. Repeating the oxidative and reducing treatments resulted in similar UV-Vis-DR spectra of 7.7 wt% V_xO_y/SBA-15. Thus, a reversible re-oxidation and reduction occurred after the initial re-oxidation of 7.7 wt% V_xO_y/SBA-15. In order to follow the reduction and re-oxidation processes, the relative absorption at 700 nm was monitored during the switching experiments (***Figure 8-5, right***). Independent of the initial degree of reduction, the relative intensity at 700 nm decreased rapidly after switching to oxidative catalytic conditions (***Figure 8-5, right, curve A,C,E***). Re-oxidation was completed after approximately 3 min. After each re-oxidation a small increase in the relative intensity at 700 nm of 1.5-3.0% was detected. Therefore, part of the reduced vanadium centers may not be re-oxidized under catalytic conditions. It seemed likely that small fractions of reduced crystalline vanadium oxide phases formed on the SBA-15 support. In contrast to the rapid decay of the relative intensity at 700 nm during the re-oxidation cycle, only a moderate increase of the relative intensity at 700 nm was observed for the second and the third reduction cycle (***Figure 8-5, right, curve B,D***). Moreover, the reduction process seemed not to be finished in the time interval chosen because no maximum or constant value of the relative intensity at 700 nm was observed. Therefore, re-oxidation of reduced vanadium centers on 7.7 wt% V_xO_y/SBA-15 was considerably faster than reduction.

The corresponding concentrations of the major reaction products (CO_2, CO, acrolein and acetaldehyde), determined at the beginning and the end of each re-oxidation in catalytic conditions, are depicted in ***Figure 8-6*** together with the corresponding propene and oxygen conversions. At the beginning of the first re-oxidation cycle, an increased formation of CO_2, acrolein, and acetaldehyde was observed compared to the end of this cycle and the other two reaction cycles.

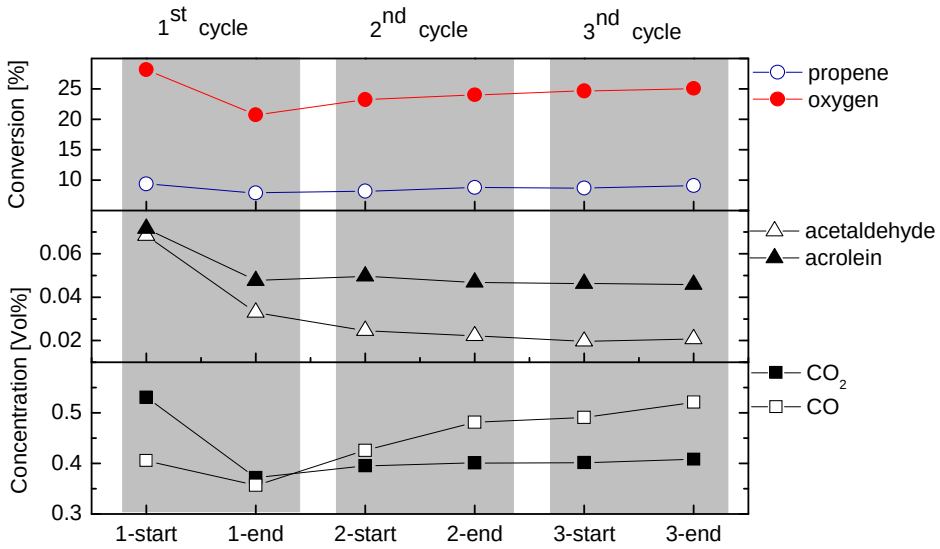

Figure 8-6: Propene and oxygen conversion and concentration of major reaction products after several oxidizing (5% propene and 5% oxygen) reaction cycles (***Figure 8-5***). Refer to text for experimental details.

Conversely, an increase of CO formation was observed after each re-oxidation cycle. In order to elucidate, whether the increased formation of reaction products was correlated with structural changes, a more detailed evolution of the structure and the gas phase composition during the first and the second re-oxidation cycle is depicted in ***Figure 8-7***. Oxygen was added after 3.9 min to the propene feed in each cycle. Adding oxygen to the reaction gas mixture, an increase of the ion currents of the reaction products was observed directly in both re-oxidation cycles (***Figure 8-7, middle***). A pronounced CO_2 formation in both re-oxidation cycles was detected that decreased to a constant level after 2 min. The CO_2 formed in the initial phase was assigned to the combustion of carbonaceous species that may have formed during the reduction. Comparing the evolution of the ion currents of water (m/e 18) and acrolein (m/e 56) during the first and the second re-oxidation cycle, a decrease of the ion currents with increasing time was observed during first re-oxidation cycle. ***Figure 8-7 (bottom, left)*** depicts the *in situ* UV-Vis-DR spectra recorded during re-oxidation. In the initial phase of the first re-oxidation cycle, a decrease of the absorption at longer wavelengths was observed in the UV-Vis-DR spectra. Furthermore, a broadening of the main absorption band around 300 nm and a shift of the maximum from 300 nm to 315 nm were observed in the first minute after switching to catalytic conditions. With increasing time a blue shift of the absorption maximum from 315 nm to 300 nm occurred that was accompanied by a narrowing of the absorption band. This process resembled the blue shift that was observed during temperature programmed reaction of V_xO_y/SBA-15 in 5% propene and 5% oxygen. Apparently, before the final oxidized state under catalytic conditions was reached, an intermediate structure of the vanadium oxide phase was present. The transformation of the vanadium oxide structure was irreversible because similar changes in the UV-VIS-DR spectra were not observed in the second re-oxidation cycle (***Figure 8-7 bottom, right***). Only a decrease of the intensity of the absorption at longer wavelengths was detected in the UV-Vis-DR spectra recorded in the second re-oxidation cycle.

In the previous chapter, it was discussed that during propene oxidation some of the V-O-X (X= OH,Si, or V) bonds changed in the initial phase of the temperature programmed propene oxidation. The structural change, indicated by a blue shift in the UV-Vis-DR spectra, was accompanied by a small increase in catalytic activity. In the first phase of the catalytic reaction, the re-oxidation of the reduced vanadium centers which form during catalytic reaction may be enhanced by the presence of Si-OH groups. Reduced vanadium centers may form Si-O-V bonds with adjacent silanol groups. A similar interpretation may explain the observations during the first re-oxidation of the reduced vanadium centers in 7.7 wt% V_xO_y/SBA-15. Launay *et al.* [26] discussed an exchange of hydroxyl groups between supported vanadium centers and silanol groups during re-oxidation of reduced V_xO_y/SiO_2 samples. Launay *et al*. showed using IR measurements that during reduction (16 h vacuum, $2*10^{-5}$ mbar, 853 K) the number of V-OH bonds decreases [26]. After re-oxidation of the sample in oxygen (853 K, 6 h) they detected again the characteristic IR bands of the V-OH stretching vibration. They proposed that vanadium centers in the proximity of strained D2 defects of the silica surface transfer the OH group from V-OH to the silica surface [26]. Furthermore, Launay *et al.* [26] proposed that some of the previously reacted V-OH groups were restored during re-oxidation of the vanadium oxide phase.

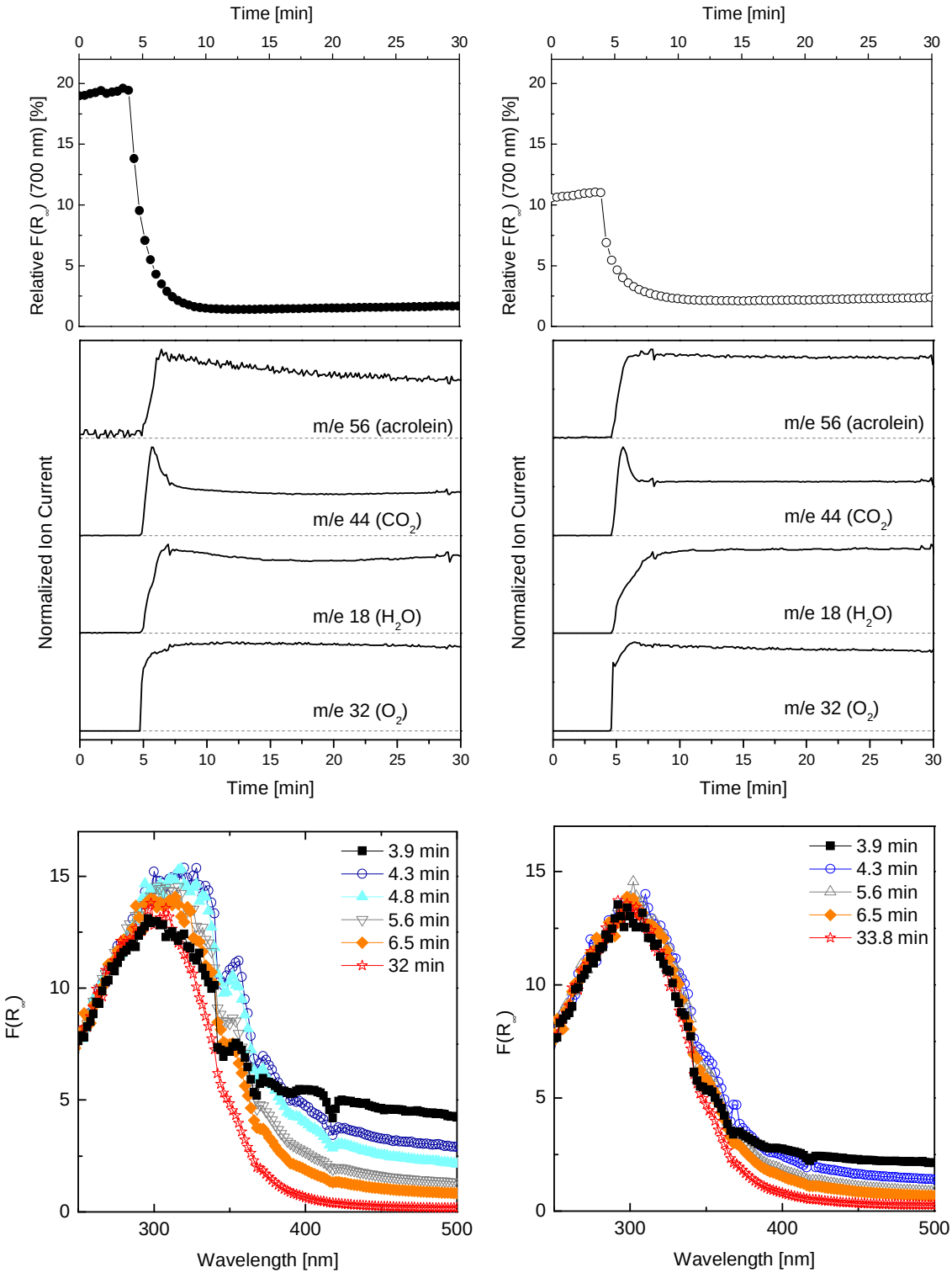

Figure 8-7: UV-Vis-DR spectra of dehydrated 7.7 wt% V_xO_y/SBA-15 (623 K, 20% O_2 in He) recorded during the first (left) and the second (right) re-oxidation (5% propene, 5% O_2) cycle at 673 K. Top: Evolution of the absorption at 700 nm (relative to the maximum intensity determined in the absorption spectra at 298 K after dehydration); Middle: Evolution of MS ion currents; Bottom: *in situ* UV-Vis-DR spectra. The gas phase was changed after 3.9 min in each reaction cycle.

During re-oxidation of the vanadium centers a transfer of a hydroxyl group from a silanol group back to the vanadium oxide center was proposed [26]. Such a mechanism would explain the broadening of the absorption band at 300 nm in the UV-Vis-DR spectra of 7.7 wt% V_xO_y/SBA-15 in the initial phase of the first re-oxidation (***Figure 8-7 (bottom, left)***). The blue shift of the absorption band at 300 nm to lower values after the initial broadening was interpreted to be caused by the reaction of V-OH and Si-OH centers to V-O-Si bonds during the catalytic cycle.

The results reported by Launay *et al.* [26] give rise to the question of which V-O bonds may be involved in the reduction process of the vanadium centers. To decide which V-O bond is involved in the reduction, a comparison of 1.4 wt% and 7.7 wt% V_xO_y/SBA-15 was made. The following bonds, present in the supported vanadium oxide cluster, may be involved in the reduction process: (i) V-OH, (ii) V=O, (iii) V-O-V, and (iv) V-O-Si. First, it seems likely that terminal V-OH bonds, (i), will more readily react than the other bonds because they are easily accessible for the propene molecule. Second, a participation of the V=O bond, (ii), in the reduction process seems not likely because of the high bond strength of this V=O double bond. Another set of bonds are the V-O-V bonds (iii), or V-O-Si bonds (iv). The latter (V-O-Si) were often proposed to participate in the selective methanol oxidation [21,169]. The high UV-Vis-DR edge energy of 1.4 wt% V_xO_y/SBA-15 showed that this sample exhibits more isolated than dimeric vanadium centers, whereas 7.7 wt% V_xO_y/SBA-15 exhibits mainly dimeric tetrahedral [V_2O_7] vanadium centers. Therefore, a higher amount of V-O-V bonds involved in the reduction will result in a higher degree of reduction of 7.7 wt% V_xO_y/SBA-15.

Figure 8-8 (left) depicts the normalized UV-Vis-DR spectra of dehydrated 1.4 and 7.7 wt% V_xO_y/SBA 15 recorded at 298 K after reduction in 5% propene at 636 K. A similar increase of the absorption at longer wavelengths (> 400 nm) was observed for both samples. Apparently, a comparable degree of reduction of the vanadium centers in 1.4 wt% and 7.7 wt% V_xO_y/SBA-15 was present after this treatment. Conversely, a different degree of reduction was observed for a reduction performed in 5% propene after a treatment under catalytic conditions at 673 K (***Figure 8-8, right***). Only a minor increase of the absorption above 400 nm was observed in the UV-Vis-DR spectrum of 1.4 wt% V_xO_y/SBA-15 after 70 min. The increase in absorption above 400 nm determined in the UV-Vis-DR spectrum of 7.7 wt% V_xO_y/SBA-15 was significantly higher. Thus, treatment of V_xO_y/SBA-15 in propene and oxygen changed the reducibility of the vanadium centers present on SBA-15. V-OH and V-O-V bonds may be involved in the reduction of 1.4 and 7.7 wt% dehydrated V_xO_y/SBA-15 because a similar and rather high degree of reduction was observed for both samples after reduction in 5% propene. UV-Vis-DRS measurements indicated that V-OH/Si-OH groups reacted to V-O-Si bonds during catalytic treatment of V_xO_y/SBA-15. It appeared that more V-OH and silanol groups were left on low loaded 1.4 wt% V_xO_y/SBA-15. Therefore, more V-O-Si bonds per vanadium center may be formed in this sample under catalytic conditions. Accordingly, the decreased number of V-OH groups in “reacted” 1.4 wt% V_xO_y/SBA-15 compared to dehydrated 1.4 wt% V_xO_y/SBA-15 may explain its lower reducibility. This interpretation was corroborated by the stronger shift of the UV-Vis edge energy (E_g) observed after catalytic treatment. The blue shift was assigned to the formation of V-O-Si bonds.

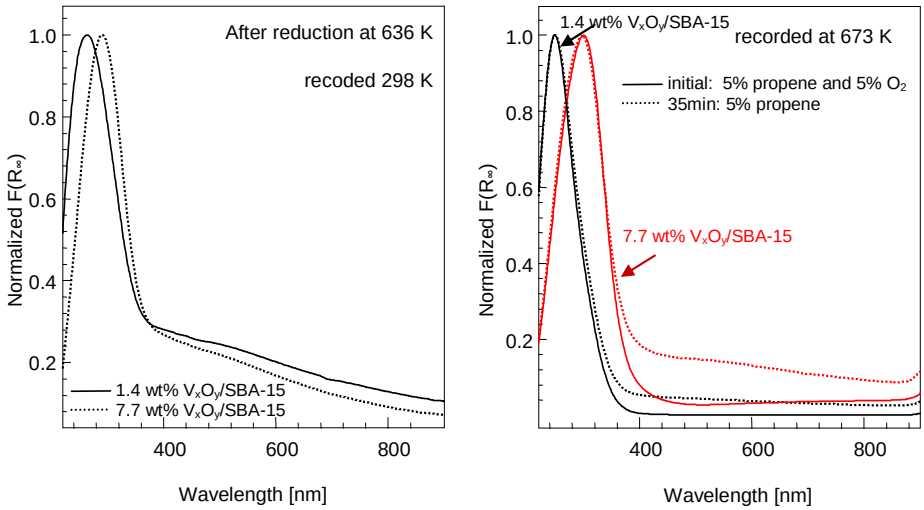

Figure 8-8: UV-Vis-DR spectra recorded at 298 K after reduction of dehydrated V_xO_y/SBA-15 in 5% propene in He at 623 K (left) and UV-Vis-DR spectra recorded at 673 K after reduction in 5% propene at 623 K of V_xO_y/SBA-15 that was treated for 35 min in 5% propene and 5% O_2 in He at 673 K prior to reduction (Right).

The UV-Vis edge energy of 7.7 wt% V_xO_y/SBA-15 shifted from 3.41 eV to 3.56 eV (ΔE_g~ ±0.05 eV), and the E_g of the low loaded 1.4 wt% V_xO_y/SBA-15 shifted from 3.6 eV to 3.9 eV (ΔE_g~ ±0.1 eV). Therefore, the reduction which was observed after catalytic treatment involved mainly the V-O-V bonds. Thus, the degree of reduction observed in the UV-Vis-DR spectra was higher for "reacted" 7.7 wt% V_xO_y/SBA-15 than for "reacted" 1.4 wt% V_xO_y/SBA-15. In order to obtain a more detailed picture of the vanadium oxide structure present on the SBA-15 support, XAFS measurements were conducted after a similar switching experiment as conducted with UV-Vis-DRS (***Figure 8-5)***. The V K edge XANES, $\chi(k)*k^3$, and FT($\chi(k)*k^3$) of 7.7 wt% V_xO_y/SBA-15 after dehydration and of 7.7 wt% V_xO_y/SBA-15 which was reduced for 30 min after the switching experiment are depicted in ***Figure 8-9***. For comparison the V K edge XANES, $\chi(k)*k^3$, and FT($\chi(k)*k^3$) of 7.7 wt% V_xO_y/SBA-15 after reduction at 723 K in 5% propene are shown.

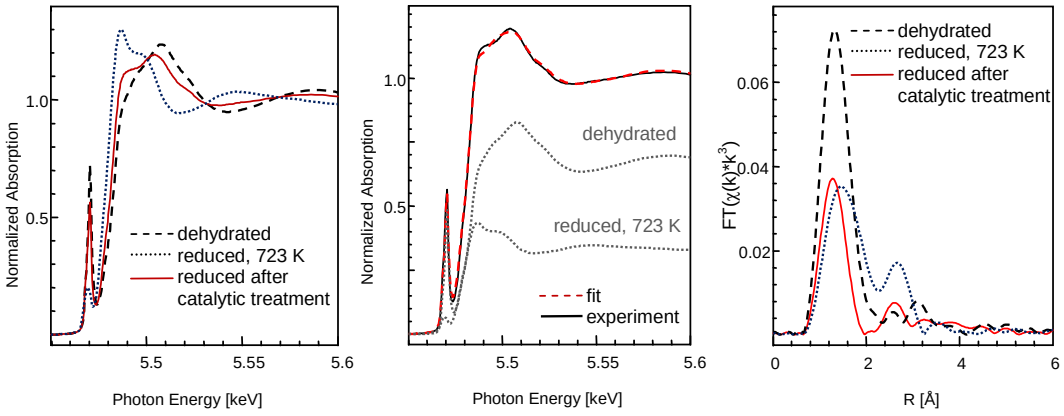

Figure 8-9: V K edge XANES (left), LC XANES fit (middle), and FT($\chi(k)*k^3$) of 7.7 wt% V_xO_y/SBA-15 after dehydration (623 K, 20% O_2 in He), reduction (723 K, 5% propene in He), and after the switching experiment at 673 K under reducing, catalytic, reducing, catalytic and finally reducing conditions (673 K, reducing conditions: 5% propene in He, catalytic conditions: 5% propene and 5% O_2 in He).

The *in situ* spectra at 673 K were omitted because of the high noise level of the spectra. The XANES spectrum of 7.7 wt% V_xO_y/SBA-15 recorded after the switching experiment resembled more the spectrum of dehydrated 7.7 wt% V_xO_y/SBA-15 than the spectrum recorded after reduction at 723 K in 5% propene. Therefore, the majority of the vanadium centers in the dehydrated structure were present as V^{5+} centers. In order to estimate the number of reduced centers, a least square XANES fit was conducted. The XANES spectra of dehydrated and reduced 7.7 wt% V_xO_y/SBA-15 (723 K, 1 h, propene) were used for refinement. A good agreement of the experimental and the theoretical XANES spectrum was obtained (***Figure 8-9, middle***). The residual of the refinement was 1.6%. Accordingly, the refinement employed showed approximately 33% of the vanadium centers were reduced and 67% remained in the dehydrated state. The FT(χ(k)*k^3) of 7.7 wt% V_xO_y/SBA-15, which was reduced after the switching experiment, is depicted in ***Figure 8-9 (right)***. Compared to the FT(χ(k)*k^3) of dehydrated 7.7 wt% V_xO_y/SBA-15, a strong reduction of the FT(χ(k)*k^3) in the range of 1-2 Å was observed. Hence, a strong structural distortion in the first V-O coordination sphere may have occured. The first signal above 2 Å was slightly enhanced and the second signal, which is due to the second V-V coordination sphere, was significantly reduced compared to the FT(χ(k)*k^3) of dehydrated 7.7 wt% V_xO_y/SBA-15. Therefore, a lower number of V-O-V bonds may be present after reduction of the catalytically treated 7.7 wt% V_xO_y/SBA-15 sample. This corroborates that mainly the V-O-V bonds were affected by the reduction of the vanadium centers of "reacted" 7.7 wt% V_xO_y/SBA-15.

Therefore, an increasing number of V-O-Si bonds may change the reducibility of the supported vanadium oxide phase. V_xO_y/SBA-15 samples with an increased number of V-O-Si bonds are, then, less reducible than the initial dehydrated V_xO_y/SBA-15 phase before the catalytic measurements. In order to investigate the reduction at 673 K of dehydrated and "reacted" 7.7 wt% V_xO_y/SBA-15, isothermal experiments with changing gas phase compositions were conducted. In a first experiment the dehydrated 7.7 wt% V_xO_y/SBA-15 sample was heated to 673 K in 20% O_2. Except for a temperature induced broadening of the absorption band, no change was observed. After 1.5 h in 20% O_2, the gas phase was switched to 5% propene for 1 h. This treatment was followed by switching to 20% O_2 for 35 min, 5% propene for 1 h, and finally to 5% propene and 5% oxygen for 35 min. The spectra recorded after each treatment procedure are depicted in ***Figure 8-10 (left)***. In contrast to the temperature programmed reaction shown in ***Figure 8-4,*** the intensity of the absorptions bands of wavelengths longer than 500 nm was smaller (13%) after reduction under isothermal conditions. The maximum of the absorption shifted from 310 nm to 291 nm during the first reduction. After re-oxidation in 20% O_2, the maximum in the UV-Vis-DR spectra shifted to 300 nm, during the second reduction to 293 nm, and finally after switching to catalytic conditions, the absorption maximum in the UV-Vis-DR spectra was detected at 296 nm. The relative intensity at 700 nm, which was assigned to reduced vanadium centers, was approximately 10-13% after the reduction cycles. For the first re-oxidation of 7.7 wt% V_xO_y/SBA-15 in 20% O_2, a reversible transition to the initial absorption maximum at 310 nm was expected. Conversely, only a shift of the absorption band to 300 nm was observed after the first re-oxidation cycle in 20% O_2.

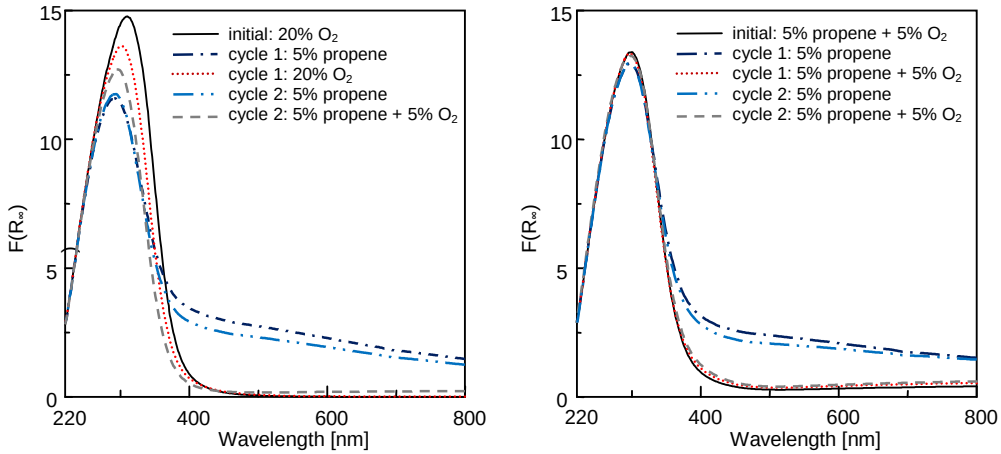

Figure 8-10: *In situ* UV-Vis DR spectra of dehydrated 7.7 wt% V_xO_y/SBA-15 (20% O_2 in He, 623 K) at 673 K after changing the gas phase composition starting with 20% O_2 in He (left), or 5% propene and 5% O_2 in He (right) as the initial gas mixture.

In this time formation of small amounts of propene oxidation products was observed because it took several seconds to purge oxygen out of the *in situ* cell. This short time of catalytic reaction may have inhibited the reversible recovery of V-OH centers. Nevertheless, after re-oxidation in 20% O_2, the absorption band exhibited a lower UV-Vis edge energy (longer wavelength) than the absorption band recoded after re-oxidation under catalytic conditions. Hence, at least some V-OH groups were recovered. In a second switching experiment, dehydrated 7.7 wt% V_xO_y/SBA-15 was heated in 5% O_2 and 5% propene to 673 K. After 30 min under catalytic conditions, the reaction gas was changed to 5% propene for 70 min. This treatment was followed by subsequent changes between reducing and catalytic conditions. The resulting spectra after each treatment are depicted in ***Figure 8-10 (right)***. Comparing the maximum absorption in the UV-Vis-DR spectra, only minor changes were observed after the respective treatments. In the initial UV-Vis-DR spectrum, the absorption maximum was at 300 nm and shifted to 297 nm after switching to propene. Repeated re-oxidation shifted the maximum in the UV-Vis-DR spectra to 298 nm and then to 295 nm after another reductive treatment. After the final re-oxidation it was at 297 nm.

Figure 8-11 depicts the evolution of the relative $F(R_\infty)$ at 700 nm [1] to follow the reduction process during the respective treatments. The gas phase was changed 3.9 min after starting to record the fast UV-Vis-DR spectra. Re-oxidation was finished, independent of the initial degree of reduction, after 3 minutes. Re-oxidation in 20% O_2 resulted in a decrease to almost no intensity of $F(R_\infty)$ at 700 nm, whereas after re-oxidation in 5% propene and 5% oxygen a relative $F(R_\infty)$ at 700 nm of 2-4% was detected. The increase in relative $F(R_\infty)$ at 700 nm during reduction was comparable to the moderate increase observed in the experiment discussed (***Figure 8-5, right***) for samples re-oxidzied prior to the reduction under catalytic conditions. However, for V_xO_y/SBA-15 (re)oxidized in 20% O_2, a different evolution of the relative $F(R_\infty)$ at 700 nm was observed during the reduction in propene (***Figure 8-11, left***).

[1] *"relative $F(R_\infty)$ at 700 nm": The intensity at 700 nm was referred to the maximum intensity at approximately 300 nm in the UV-Vis spectra recorded at 298 K after dehydration of V_xO_y/SBA-1 in 20% O_2.*

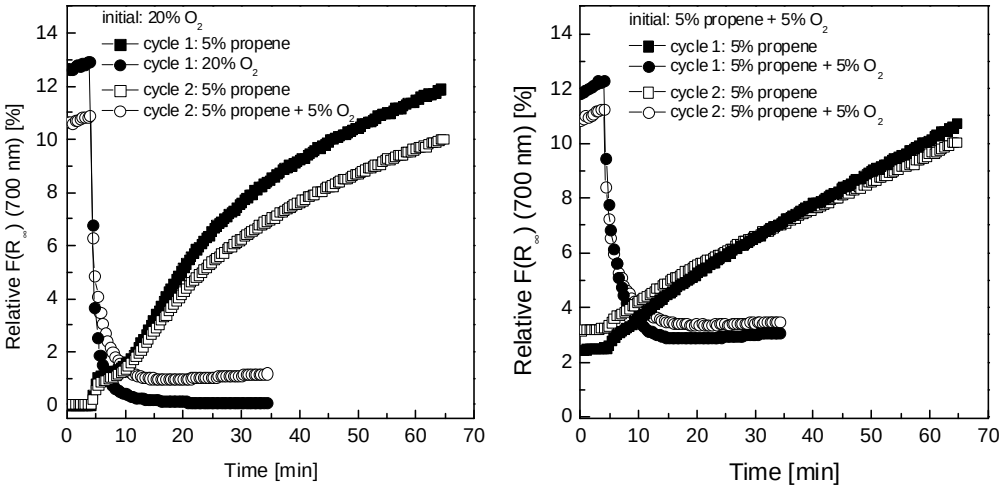

Figure 8-11: Evolution of the relative absorption at 700 nm (relative to the maximum intensity determined in the absorption spectra at 298 K after dehydration) derived from the *in situ* UV-Vis DR spectra of dehydrated 7.7 wt% V_xO_y/SBA-15 (20% O_2 in He, 623 K) at 673 K after changing the gas phase composition starting with 20% O_2 in He (left), or 5% propene and 5% O_2 in He (right) as initial gas mixture.

In the initial time interval (5 min - 10 min) after switching to reducing conditions, only a small increase in relative $F(R_\infty)$ at 700 nm was observed. The relative $F(R_\infty)$ at 700 nm remained constant during the first 5 min. After 5 min (10 min absolute) an increase of the relative absorption at 700 nm was detected which was damped after 15 min (~ 25 min absolute). The increase in relative absorption at 700 nm for the first and the second reduction cycle was comparable during the first 15 min after switching to propene. After 15 min a smaller increase of the relative absorption at 700 nm was observed for the second reduction cycle. Evolution of the structure and gas phase composition during the first reduction cycle of dehydrated and "reacted" 7.7 wt% V_xO_y/SBA-15 is depicted in ***Figure 8-12***. In the first 3 min after switching to propene, a pronounced formation of oxidation products was observed (CO_2, acrolein, water, and C_3H_6O) for dehydrated 7.7 wt% V_xO_y/SBA-15. The ion currents decreased significantly after 3 min (CO_2, acrolein, and C_3H_6O) or reached a constant value in the case of water (***Figure 8-12, middle, left***). Hence, in the initial phase of the reduction oxygen originating from the vanadium oxide phase may have reacted with propene. In the first 5 min after switching to propene, a constant relative $F(R_\infty)$ at 700 nm was observed (***Figure 8-12, top, left***). The *in situ* UV-Vis-DR spectra recorded during the addition of propene are depicted in ***Figure 8-12, bottom, left***. During the first two scans (3.9 min-5.2 min), a blue shift of the absorption maximum from 310 nm to 300 nm was observed in the UV-Vis DR spectra. The UV-Vis-DR spectra recorded during the next 5 min (5.2-10.8 min) remained unchanged. After 10.8 min a slow shift of the absorption maximum from 300 nm to 291 nm was observed in the UV-Vis-DR spectrum. This shift was accompanied by an increase of the absorption at 700 nm. The intermediate absorption spectra (5.2-10.8 min) resembled those recorded under catalytic conditions. Presumably, a similar V coordination sphere must be present. V-O-Si bonds may have formed from reacted V-OH. Interestingly, the V-OH groups were recovered after re-oxidation in 20% O_2, which is in contrast to catalytic conditions. A similar shift of the absorption maximum was not observed in the *in situ* UV-Vis-DR spectra of "reacted" 7.7 wt% V_xO_y/SBA-15 during the first reduction cycle.

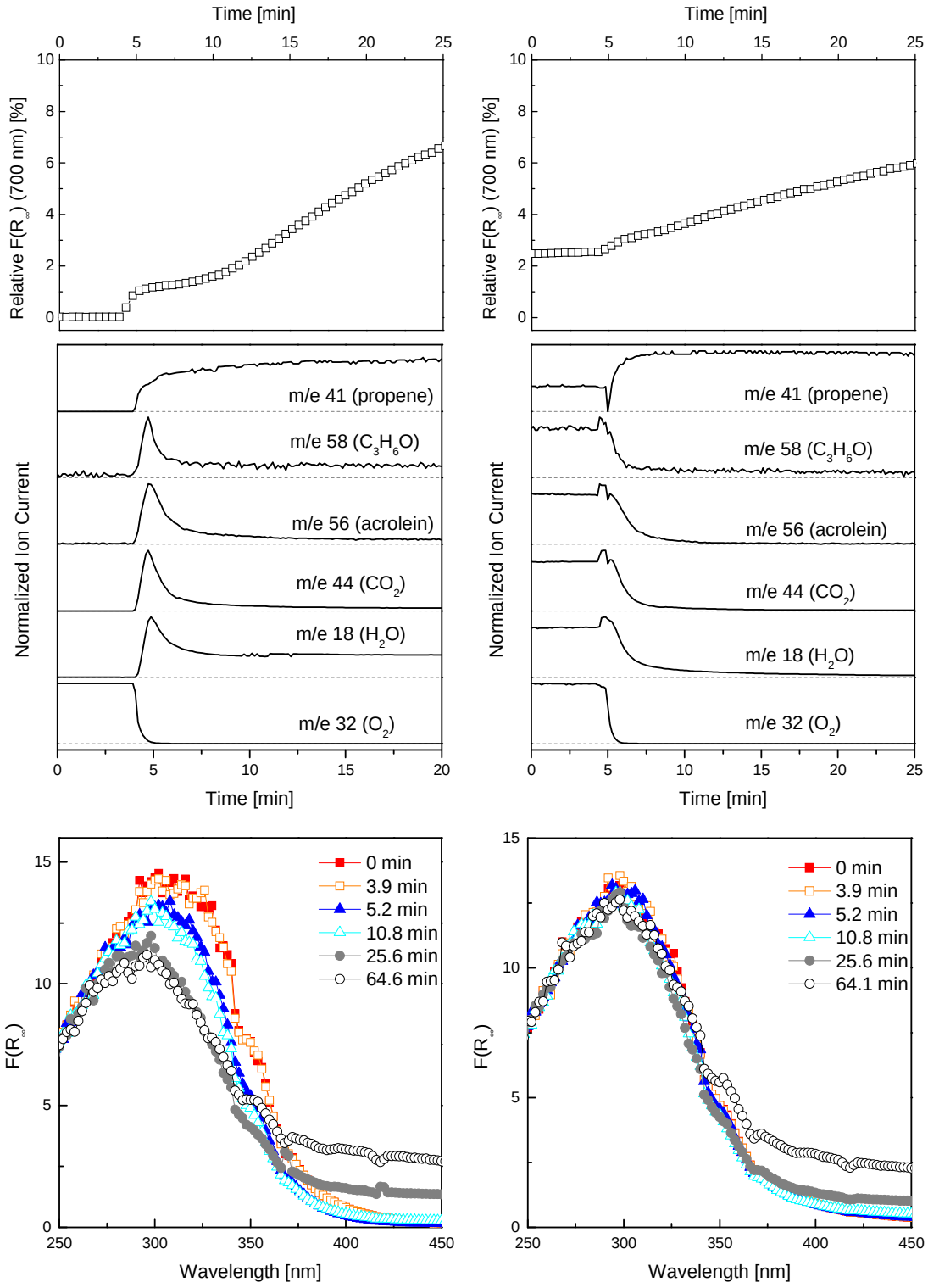

Figure 8-12: UV-Vis-DR spectra of dehydrated 7.7 wt% V_xO_y/SBA-15 (623 K, 20% O_2 in He) recorded during the first reducing (5% propene) cycle at 673 K starting with 20% O_2 in He (left side), or 5% propene and 5% O_2 in He (right side) as the initial gas mixture. Top: Evolution of absorption at the 700 nm (relative to the maximum intensity determined in the absorption spectra at 298 K after dehydration); Middle: Evolution of the MS ion currents; Bottom: *in situ* UV-Vis-DR spectra. The gas phase was changed after 3.9 min in each reaction cycle.

For “reacted” 7.7 wt% V_xO_y/SBA-15 the absorption maximum in the *in situ* UV-Vis-DR spectra remained at 297 nm during the reduction and re-oxidation cycles (***Figure 8-12, bottom, right***). Switching the gas phase from catalytic conditions to propene resulted in a small increase of the ion currents of the reaction products formed in the first minute (~ 5 min. absolute). Between 5 and 7 min, a decay of theses ion currents was observed. The decay was slower than the decreasing ion current of oxygen (m/e 32). Thus, oxygen originating from the sample may have reacted with propene.

8.3 Concluding remarks on the structural evolution of V_xO_y/SBA-15 under dehydrating, catalytic, or reducing conditions

Figure 8-13 shows the proposed structural transformations deduced from the *in situ* UV-Vis-DRS and XAS investigations performed under reducing, oxidizing or catalytic conditions.

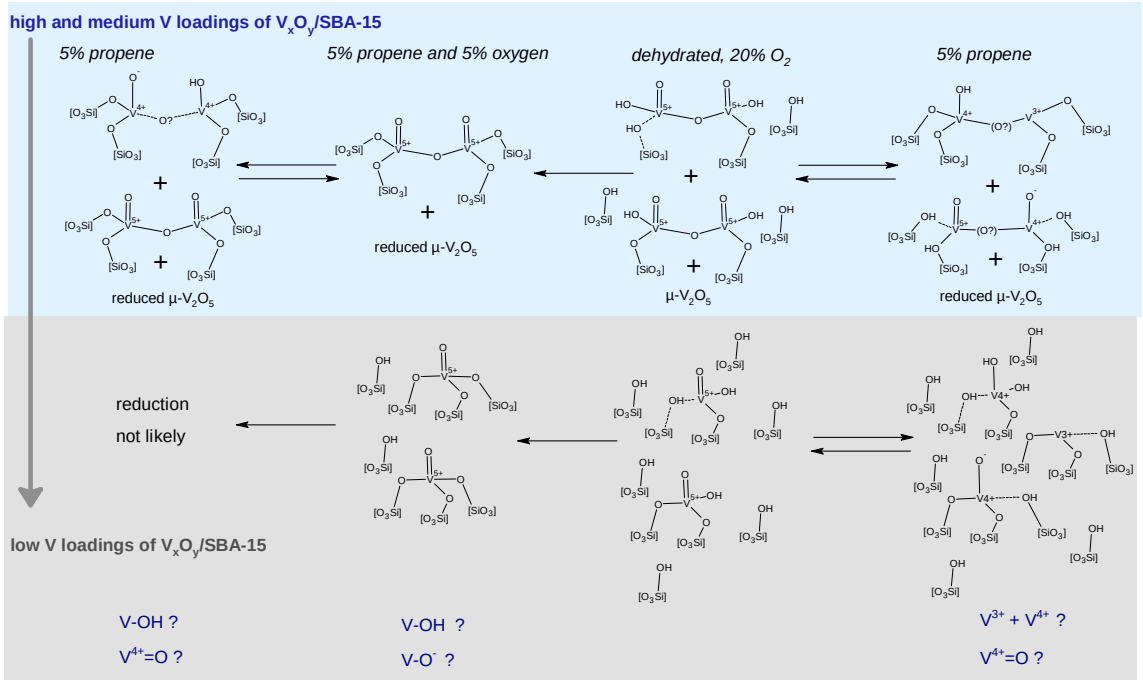

Figure 8-13: Simplified scheme of the structural changes during dehydrating, catalytic or reducing condition.

The dehydrated V_xO_y/SBA-15 structure was obtained from thermal treatment in oxygen containing atmospheres in the temperature range from 550-723 K. The dehydrated structure consists of an ordered arrangement of dimeric tetrahedral [V_2O_7] vanadium oxide units present on the SBA-15 support. The proposed structure is discussed in more detail in ***Chapter 5***. With decreasing vanadium loading isolated tetrahedral [VO_4] units besides dimeric tetrahedral [V_2O_7] vanadium oxide units may be present on the support. Because Si-OH groups were still detectable after dehydration (550-723 K), the number of V-O-Si bonds to the support are presumably one per vanadium center in the case of high loaded V_xO_y/SBA-15 and one or two per vanadium center in the case of low loaded V_xO_y/SBA-15. The remaining vanadium oxygen bonds may be present as V=O or as V-OH referring to IR investigations reported by Launay *et al.* [26,27,141]. The presence of V-OH bonds seems likely because the H^+ ensures the charge compensation of the vanadium oxide clusters.

A reduction of vanadium centers of V_xO_y/SBA-15 was observed for temperatures higher than 520 K after applying reducing conditions to dehydrated V_xO_y/SBA-15 samples. A rather low V K edge pre-egde peak height indicated the formation of V^{4+} and V^{3+} vanadium centers after reduction in propene at 723 K (***Figure 8-2***). A low similarity with the XAS spectra of octahedral vanadium oxide references with an average oxidation state less than +5 was observed (***Figure 8-1***). Hence, the reduced vanadium centers of V_xO_y/SBA-15 may exhibit a 4- or 5-fold V-O coordination symmetry. Whether reduced vanadium centers with double bonds (V^{4+}=O) were present could not be determined. Reduced V^{4+} and V^{3+} vanadium centers require a compensation of the highly negative charge present. A high negative charge of reduced vanadium centers must be present in the reduced dimeric or isolated vanadium oxide clusters with 4- or 5-fold coordinated V-O vanadium centers. Such a negative charge cannot be easily compensated for supported vanadium oxide clusters that are anchored to the support. Conversely, for bulk vanadium oxide references, charge compensation may be given by positively charged cations or by aggregation to larger vanadium oxide clusters resulting typically in a higher coordination (*e.g.* octahedral V^{3+} centers in V_2O_3 or Mg_2VO_4). However, the latter process seems not likely for the vanadium centers linked to the support. The lacking possibilities for charge compensation may explain the fast re-oxidation of the reduced vanadium oxide centers. It still remains unknown how and which oxygen ligands stabilize the vanadium oxide structure of reduced vanadium centers. Formation of V-OH groups may be suited to reduce the negative charge, but Launay *et al.* [26] showed that these centers were removed during reduction in vacuum. Comparable to the results reported by Launay *et al.* [26], a reversible re-oxidation in 20% oxygen was possible together with the recovery of some of the removed V-OH groups (***Figure 8-10, left***). The mechanism behind this process remains unclear because direct observation of the V-OH and Si-OH was not possible with the spectroscopic methods employed. Nevertheless, the reversible exchange of hydroxyl groups with the SBA-15 support indicates a dynamic interaction. Therefore, investigations addressing the reduction in hydrogen and reversibility of the reoxidation of V_xO_y/SBA-15 would be of interest. Unfortunately, the temperature range above 750 K where a reduction in hydrogen proceeds [22], was not feasible with the *in situ* UV-Vis-DR set up used here. The reduction in hydrogen instead of in propene would not be disturbed by catalytic processes with residual oxygen that may change the V-O coordination sphere.

A very different reduction behavior occurred for V_xO_y/SBA-15 treated under catalytic conditions (5% propene and 5% oxygen) prior to reduction in propene. A blue shift of the absorption band in the UV-Vis-DR spectra was detected during this treatment. This change in the UV-Vis-DR spectra was assigned to the formation of V-O-Si bonds. This interpretation was corroborated by the fact that the blue shift was larger in the case of low vanadium loadings (lower number V-O-V bonds), that Si-OH groups were not detectable after such a treatment of dehydrated 7.7 wt% V_xO_y/SBA-15, and that significant changes were not determined in the XAFS refinements. In the case of changes of the V-O-V bonds, it would be expected that almost no blue shift would be observed for 1.4 wt% V_xO_y/SBA-15. Furthermore, a significant change in the V-V interaction in the XAFS refinements would be expected for 7.7 wt% V_xO_y/SBA-15. The unchanged Raman band at ~1040 cm^{-1} that was observed during the temperature programmed reaction in propene and oxygen showed that no change of the V=O bond occurred (***Chapter 7***). The increased number of V-O-Si centers on the support resulted in a lower reducibility of the supported vanadium oxide centers (***Figure 8-8***). This effect was more pronounced for low loaded 1.4 wt% V_xO_y/SBA-15. This corroborated the assumption that on this sample more V-O-Si bonds were formed. The low reduction observed for 1.4 wt% V_xO_y/SBA-15 (***Figure 8-8***) may be due to reduced dimeric centers that may be present besides isolated vanadium centers after dehydration. Hence, $O=V^{5+}$-$(OSi)_x$ centers were not reducible. The observed reduction of 7.7 wt% V_xO_y/SBA-15 was assigned to the reduction at the V-O-V bonds in the $[V_2O_7]$ dimer. It was estimated from a XANES analysis that approximately 33% of the vanadium centers were reduced in "reacted" 7.7 wt% V_xO_y/SBA-15. A similar conclusion that V-O-Si bonds were not reducible (reduction with H_2), in contrast to V-OH or V-O-V bonds, was proposed by Grubert *et al.* [170]. Therefore, mainly the V-O-V bonds are involved in the reduction of the "reacted" V_xO_y/SBA-15 samples.

The nano crystalline V_2O_5 phases on 7.7 wt% V_xO_y/SBA-15 were not responsible for the observed changes in the UV-Vis-DR absorption bands. Similar changes were observed for 1.4 wt% V_xO_y/SBA-15 where no V_2O_5 was detectable. However, an increasing formation of reduced crystalline vanadium oxide centers may explain the increasing formation of CO and the decreasing formation of acetaldehyde during the isothermal switching experiments (***Figure 8-6***).

The results obtained suggest that a different interaction of the vanadium oxide phase with propene proceeds during the catalytic propene oxidation compared to reducing conditions. This may be due to the formation of V-O-C_xH_y or Si-O-C_xH_y intermediate species which change the re-oxidation. The blue shift of the absorption bands in the UV-Vis-DR spectra was irreversible. Hence, adjacent silanol groups may be involved in the initial phase of re-oxidation in propene and oxygen. Surprisingly, a similar irreversible reaction of vanadium centers and silanol groups was not observed during re-oxidation of reduced V_xO_y/SBA-15 catalysts in 20% O_2.

8.4 Summary

In situ UV-Vis-DRS and *in situ* XAS measurements showed that the vanadium oxide phase on V_xO_y/SBA-15 exhibits a dynamic reduction and re-oxidation behavior. Disperse dimeric and isolated vanadium centers present after dehydration of V_xO_y/SBA-15 were reduced to V^{4+} and V^{3+} using propene as the reducing agent. A re-oxidation in 20% O_2 resulted in a reversible oxidation of the reduced vanadium oxide phase to the initial dehydrated V_xO_y/SBA-15 with an average valence of +5. The reduction behavior was independent of the vanadium loading of V_xO_y/SBA-15.

Conversely, a significantly lower reducibility was observed for V_xO_y/SBA-15 treated under catalytic conditions in propene and oxygen. The lower reducibility was ascribed to the formation of additional V-O-Si bonds to the support. V-O-Si bonds were not involved during the reduction in propene. This was corroborated by a lower reducibility of the "reacted" low loaded 1.4 wt% V_xO_y/SBA-15 compared to "reacted" high loaded 7.7 wt% V_xO_y/SBA-15. The higher reducibility of 7.7 wt% V_xO_y/SBA-15 was attributed to the presence of V-O-V bonds in the sample.

The high tendency of partially reduced disperse vanadium oxide phases to re-oxidize rapidly even in the presence of low amounts of oxygen was explained by a missing charge compensation for reduced 4- or 5-fold V^{+4} and V^{3+} centers anchored to SBA-15. Anchoring of disperse dimeric and isolated vanadium oxide clusters to the SBA-15 support inhibits the formation of larger clusters with higher coordination that may stabilize reduced vanadium oxide centers.

9 General conclusions on V_xO_y/SBA-15 model catalysts

9.1 Introduction

The objective of the present work was investigating of V_xO_y/SBA-15 model catalysts for the selective oxidation of propene. Detailed analysis of the preparation, and the hydration and dehydration processes were performed prior to catalytic testing. The grafting anion exchange method chosen allowed the preparation of highly disperse V_xO_y/SBA-15 samples without formation of V_2O_5 during the preparation process. Three different V_xO_y/SBA-15 samples with vanadium loadings in the range of 1.4 wt%-7.7 wt% (0.3 V/nm^2 – 2.4 V/nm^2) were synthesized. *In situ* UV-Vis-DR and XAS measurements were performed to investigate the vanadium oxide structure. Comparison with spectra of vanadium oxide references allowed developing suitable model structures for the hydrated and dehydrated state. The proposed theoretical model structures were refined successfully to the experimental Fourier transformed EXAFS of V_xO_y/SBA-15. Hydration and dehydration processes were studied with various *in situ* methods. Furthermore, the impact of water on the dehydration process was determined. The measurements performed provided a detailed knowledge on the structural properties of V_xO_y/SBA-15 under oxidizing conditions (20% O_2 in He). After characterization under oxidizing conditions the structural evolution under catalytic (5% propene and 5% O_2 in He) and reducing (5% propene in He) conditions was investigated together with monitoring of the gas phase composition. In addition, the catalytic performance (propene conversion, gas phase composition, and selectivity of the reaction products formed) was determined in a laboratory fixed bed reactor. The major results and conclusions obtained are summarized below. The conclusions presented below demonstrate the potential of V_xO_y/SBA-15 as a model catalyst for the selective oxidation of propene to acrolein. The bare SBA-15 support showed no catalytic activity. Therefore, it was possible to deduce structure-activity relations that can be assigned to the role of vanadium oxide during the selective propene oxidation.

9.2 Hydrated state of V_xO_y/SBA-15

The hydrated state of V_xO_y/SBA-15 was observed under ambient conditions in the presence of water. A suitable structural model was developed on the basis of UV-Vis-DRS and XAS experiments. The model structure of the hydrated state consisted of small clusters of vanadium oxide centers exhibiting a square pyramidal coordination. The UV-Vis-edge energy indicated that a two-dimensional and chainlike extension of the vanadium oxide species on the SBA-15 was present, similar to $V_2O_6^{2-}$ vanadate structures. *In situ* spectroscopic experiments showed that the hydrated V_xO_y/SBA-15 structure was not stable at elevated temperatures under oxidizing and under catalytic conditions.

In situ measurements were conducted to obtain a detailed knowledge on the coordination of vanadium centers in hydrated V_xO_y/SBA-15 and on the formation of hydrated V_xO_y/SBA-15. A smaller amount of Si-OH groups in V_xO_y/SBA-15 compared to SBA-15 suggests that V-O-Si bonds were present in the hydrated state of V_xO_y/SBA-15. Various time scales until a fully hydrated state was observed were recorded for freshly prepared (weeks) and for dehydrated V_xO_y/SBA-15 (hours). Hence, more V-O-Si bonds may be present in freshly prepared V_xO_y/SBA-15. The hydrolysis of additional V-O-Si bonds during hydration would explain the larger time scale observed for a full hydration of V_xO_y/SBA-15. The vanadium centers in the hydrated state are coordinated by V-O-V, V-OH, and V··H_2O groups. A decomposition temperature below 440 K of the hydrated state indicates a rather weak bond of the coordinated water species to the vanadium centers. Apparent activation energies in the range of 70-90 kJ/mol were determined for the water desorption. The apparent activation energies for the desorption process of hydrated V_xO_y/SBA-15 increased with vanadium loading and storage time. With increasing time of storage, a "growth" of the hydrated V_xO_y/SBA-15 structure on high loaded 7.7 wt% V_xO_y/SBA-15 was observed. This "growth" was accompanied by an increased formation of V-V interactions and a stronger interaction of coordinated water with the hydrated vanadium oxide species. The formation of $V_2O_5 \cdot nH_2O$ gel like structures seemed likely. In addition to the formation of the dehydrated V_xO_y/SBA-15 structure, the formation of V_2O_5 was observed during thermal decomposition of these $V_2O_5 \cdot nH_2O$ gel like structures.

9.3 Dehydrated state of V_xO_y/SBA-15

The dehydrated V_xO_y/SBA-15 structure formed at temperatures above 440 K during thermal treatment of hydrated V_xO_y/SBA-15 in 20% O_2. The UV-Vis-DRS and XAFS spectra of dehydrated V_xO_y/SBA-15 showed similarity with those of vanadium oxide references exhibiting a dimeric or chainlike structure of VO_x tetrahedrons. Therefore, a model structure based on an ordered arrangement of adjacent $[V_2O_7]$ units was proposed for dehydrated V_xO_y/SBA-15. This theoretical model structure was refined successfully to the experimental Fourier transformed EXAFS of all three V_xO_y/SBA-15 samples employed.

Dehydration of hydrated V_xO_y/SBA-15 was accompanied by an increased amount of water in the gas phase. Structural rearrangement processes to the final structure of dehydrated V_xO_y/SBA-15 were observed between 440 K and 550 K. No intermediate structures were formed. The number of dispersed V_xO_y centers in the dehydrated state correlated significantly with the number of available Si-OH sites. Formation of V_2O_5 will be likely if the amount of vanadium centers exceeds the number of Si-OH groups. Therefore, the presence of at least one V-O-Si bond per vanadium center or dimeric unit seems to be a prerequisite for the formation of dehydrated tetrahedral vanadium centers. Formation of three V-O-Si bonds per vanadium site to the support seemed not likely because even for high vanadium loadings not all Si-OH groups of SBA-15 reacted to V-O-Si bonds during dehydration at moderate temperatures of 723 K. Therefore, V-OH groups may be present in dehydrated V_xO_y/SBA-15. For low V/Si-OH ratios (< 0.5 V/nm^2) the formation of isolated besides dimeric vanadium centers seemed likely. The formation

of the dehydrated state was observed to be independent of the presence of water during the thermal treatment.

Small V_2O_5 aggregates formed on high loaded 7.7 wt% V_xO_y/SBA-15 during dehydration and were able to re-disperse on the support under calcination conditions. The re-dispersion effect was observed for vanadium loadings near the maximum surface coverage in the range of 2.4 V/nm^2.

9.4 Structure of V_xO_y/SBA-15 catalysts under reducing and under catalytic conditions

It was shown from Raman and UV-Vis-DRS measurements that the vanadium oxide structure under propene oxidizing conditions corresponds mainly to the dehydrated V_xO_y/SBA-15 state. Only minor structural changes compared to the dehydrated state were observed in the V K edge XANES and EXAFS spectra of V_xO_y/SBA-15 after reaction in propene and oxygen. The observed changes affected the V-V interactions slightly. XAFS measurements showed that minor structural distortions may be present in the second (V-V) coordination sphere. Changes in the UV-Vis edge energy indicated that V-O-Si bonds formed in the initial phase of the reaction with propene in the presence of oxygen. V-OH groups may have reacted with Si-OH groups to V-O-Si bonds. For high loaded 7.7 wt% V_xO_y/SBA-15, a decrease of the Si-OH groups was detected in the ^{29}Si MAS-NMR spectrum that was not observed under dehydrating conditions. This suggests that Si-OH groups reacted with the vanadium centers. Furthermore, the UV-Vis edge energy shift observed in the UV-Vis-DR spectra was more distinct for 1.4 wt% V_xO_y/SBA-15 than for high loaded 7.7 wt% V_xO_y/SBA-15. More V-O-V bonds were determined for 7.7 wt% V_xO_y/SBA-15. Therefore, V-OH rather than V-O-V bonds may be involved in the V-O-Si bond formation. The formation of V-O-Si bonds should be visible in the Raman spectra. According to the theoretical calculation [171], an increase in the region 873-962 cm^{-1} (Si-O-V out of phase interface mode) and in the region 1020-1080 cm^{-1} (in phase mode) was expected. However, the data quality of the recoded spectra was not sufficient to resolve these changes. More detailed investigations would be desirable. Further measurements of changes of the V-OH groups with IR spectroscopy and of the Si-OH groups with *in situ* NMR spectroscopy may elucidate the reaction observed.

In addition to the structural characterization under catalytic conditions, the reducibility of dehydrated V_xO_y/SBA-15 catalysts was tested using propene as reducing agent. Dehydrated V_xO_y/SBA-15 samples were reducible independent of the vanadium loading. XANES spectra suggest the formation of tetrahedral or square pyramidal V^{4+} and V^{3+} centers. In oxidizing conditions a complete re-oxidation of the reduced vanadium species of V_xO_y/SBA-15 proceeded without formation of additional V-O-Si bonds. In contrast to the reduction of dehydrated V_xO_y/SBA-15, a lower reducibility was observed for V_xO_y/SBA-15 samples treated under propene oxidizing conditions prior to the reduction. The reducibility was lower for "reacted" 1.4 wt% V_xO_y/SBA-15 than for "reacted" 7.7 wt% V_xO_y/SBA-15. Therefore, V-O-Si bonds formed during catalytic reaction might not be involved in the reduction process. Conversely, V-O-V bonds present in 7.7 wt% V_xO_y/SBA-15 may be involved. The changed reducibility of V_xO_y/SBA-15

under catalytic conditions is of great interest, given that TPR experiments are commonly used to elucidate the redox properties of vanadium oxide catalysts. The reducibility cannot be deduced from the initial dehydrated state of V_xO_y/SBA-15. This knowledge has to be considered for further TPR experiments with V_xO_y/SBA-15.

9.5 Catalytic performance of V_xO_y/SBA-15

In addition to elucidating the structure and reducibility of V_xO_y/SBA-15, a functional characterization was performed. The catalytic performance during propene oxidation was investigated using a laboratory reactor. The formation of selective oxidation products like acrolein, propionaldehyde, acetaldehyde, acetone and acetic acid was observed together with the formation of CO_2 and CO. Three major reaction pathways existed for propene oxidation [3,5]. First, propene was selectively oxidized to acrolein with 18-25% selectivity. Second, propene was oxidized to propionaldehyde and acetaldehyde, and, third, propene was oxidized to acetone and acetic acid. The reaction products formed during the selective oxidation of propene suggest that different oxygen species are involved. In accordance with the literature [162] formation of acrolein is ascribed to the presence of nucleophilic oxygen (O^{2-}) that attacks propene at the methyl group. The formation of the other reaction products is ascribed to electrophilic oxygen (O_2, O^-, and O_2) that attack propene at the C=C bond. The origin of electrophilic oxygen may be a consequence of the re-oxidation of reduced vanadium centers with molecular oxygen. Thus, future investigations with other oxidizing agents like N_2O, which may enhance the selectivity for acrolein during propene oxidation on V_xO_y/SBA-15 catalysts, would be desirable. The formation of acetone and acetic acid suggested that V-OH groups were involved in propene oxidation. For temperatures above 500 K the UV-Vis edge energy shift indicated a reaction of V-OH to V-O-Si bonds. Experiments at temperatures below 500 K, therefore, may provide more information about the role of V-OH groups in propene oxidation. Furthermore, the influence of high water content (> 20 Vol%) was not investigated in this work. Increasing the amount of water in the reaction atmosphere to a high content may increase the number of V-OH groups. Thus, investigations with high water content seem promising to investigate the role of V-OH groups in selective propene oxidation.

Higher vanadium loading of V_xO_y/SBA-15 facilitated the consecutive reactions of the primary C_3 aldehydes to C_2 oxygenates and CO. The amount of electrophilic oxygen may increase with higher vanadium loading on SBA-15. However, when combining the selectivities of the oxidation to the C_3 aldehydes and the selectivity of the consecutive reactions of the respective reaction pathway, no significant difference was observed with vanadium loading. Therefore, decreasing the vanadium loading of V_xO_y/SBA-15 does not alter the fundamental reaction pathways of the propene oxidation. Conversely, a twice as high propene conversion rate and 40% higher acrolein formation rate per V site was observed for 7.7 wt% V_xO_y/SBA-15 compared to 4.1 wt% and 1.4 wt% V_xO_y/SBA-15. The same reaction rates were determined for 4.1 wt% and 1.4 wt% V_xO_y/SBA-15. The increase in these reaction rates is attributed to a higher density of adjacent [V_2O_7] units on 7.7 wt% V_xO_y/SBA-15. Thus, either the C-H abstraction

step or the electron transfer process during propene oxidation to acrolein may be facilitated due to the increased number of neighboring vanadium sites.

The reaction orders determined for the formation of acrolein were zero for oxygen and 0.5 for propene. The reaction order of 0.5 for propene could not be assigned unambiguously to a specific reaction mechanism. The zero reaction order for oxygen indicates that a fast re-oxidation of the vanadium centers involved proceeds during the propene oxidation. This interpretation is corroborated by the fact that the average vanadium valance of V_xO_y/SBA-15 remained +5 during propene oxidation. Furthermore, UV-Vis-DRS experiments with alternating reducing and oxidizing conditions showed that the re-oxidation process of V_xO_y/SBA-15 is considerably faster than the reduction.

9.6 Structure-activity correlations deduced from a comparison of V_xO_y/SBA-15 with bulk V_2O_5

Reduced vanadium oxide phases (i.e. V_4O_9 and VO_2 (B)) were observed during the reaction of propene and oxygen on V_2O_5. The formation of reduced vanadium phases may be caused by the participation of mobile bulk oxygen species in the catalytic process (***Chapter 2***). Such mobile bulk oxygen species may be required for the re-oxidation step in selective oxidation reactions (Mars van Krevelen mechanism). However, for V_xO_y/SBA-15 an average valance of V^{5+} was observed during catalytic oxidation of propene although V_xO_y/SBA-15 exhibits no accessible mobile oxygen species. Hence, mobile bulk oxygen species are not required for a fast re-oxidation of reduced vanadium species during the propene oxidation. Therefore, the oxygen mobility in V_2O_5 is a consequence of its bulk structure but not a prerequisite for the catalytic performance of vanadium oxides in selective oxidation reactions.

The observed reaction products and selectivities detected during propene oxidation on V_xO_y/SBA-15 were not significantly different from those observed with bulk V_2O_5 (***Chapter 2***). Therefore, basically the same reaction steps may occur. This suggests that similar active centers are present on the surface of SBA-15 supported and bulk V_2O_5 during propene oxidation. Similar active centers can be explained by similar structural motifs of vanadium oxide clusters on the surface, or they may be assigned to intrinsic properties of the vanadium sites, *e.g.* electronic and redox properties. The latter is corroborated by the fact that even 1.4 wt% V_xO_y/SBA-15, for which isolated [VO_4] units may be present, showed basically the same reaction pathways for the selective oxidation of propene with oxygen as bulk V_2O_5 (V_4O_9). Apparently, no change in the reaction pathways was observed when V_xO_y/SBA-15 model catalysts, consisting of small tetrahedral units with low extension, were compared to structurally more complex bulk V_2O_5. Moreover, even an increase in the structural complexity among the V_xO_y/SBA-15 model catalyst, deduced from the increasing number of adjacent and connected tetrahedral vanadium centers, did not change significantly the reaction pathways for propene oxidation. Only a decrease in acrolein selectivity from 25% to 18% was observed with increasing loading, which was assigned to consecutive reactions of the primary aldehydes. Hence, the selectivity towards acrolein formation of vanadium oxide centers seems to be independent on the vanadium oxide structure for the “binary” V^{5+} catalysts

investigated here. Thus, structural complexity of the vanadium oxide structure seems to have only a minor impact on the propene oxidation reaction over V_xO_y/SBA-15 model catalysts and bulk V_2O_5.

9.7 Structure-activity correlations with respect to complex mixed metal oxide catalysts

The objective of the present work was elucidating structure-activity correlations of V_xO_y/SBA-15 model catalysts for the selective oxidation of propene to acrolein. The results obtained showed that supporting vanadium oxide on SBA-15 enhanced the activity compared to bulk V_2O_5 while selectivity towards the desired product acrolein remained similar. The increase in activity is assigned to an increased number of accessible surface sites on V_xO_y/SBA-15 catalysts. Among the V_xO_y/SBA-15 samples, 7.7 wt% V_xO_y/SBA-15 exhibited a superior activity. Conversely, almost the same selectivity towards acrolein was observed. Hence, a higher density of active vanadium sites, possibly with a higher connectivity than isolated or dimeric vanadium units, may facilitate the acrolein formation.

However, the low changes in acrolein selectivity suggested that the structural complexity of the vanadium oxide phase of V_xO_y/SBA-15 and bulk V_2O_5 had only a minor impact on the propene oxidation. Presumably, metal sites with a different character may be required, which reduce and control the unselective character of the active vanadium sites, *e.g.* Mo, Te, W. Such an interpretation suggests that these metal sites in highly active bulk catalysts, *e.g.* MoVNbTe, may work as moderator for the vanadium sites involved in the reaction. Thus, vanadium sites may increase the activity, but the cooperation of vanadium with other metal sites may be required to obtain a high selectivity. In this case, the chemical complexity must be increased in order to improve the catalytic performance of vanadium sites in the selective oxidation of propene towards acrolein. However, vanadium is mostly the minor component in highly active mixed metal catalyst. Therefore, from the point of view of possible cooperating metal sites, like Mo, it would be of interest whether certain host structures, thus structural complexity, must be present to improve activity and selectivity of mixed metal oxide catalysts. Hence, in the next generation of SBA-15 supported metal oxides, mixed metal oxide systems, *e.g.* Mo and V seem promisingly.

The minor role of structural complexity of the vanadium oxide phase of V_xO_y/SBA-15 and bulk V_2O_5 on selective propene oxidation is interesting and will need further investigation. With respect to the variety of structural configurations that are possible for vanadium oxide structures new model systems which exhibit more complex vanadium oxide structures must be employed. Moreover, the structural complexity of vanadium oxide sites in highly active “MoVTe” catalysts may be higher than the structural complexity provided by the V_xO_y/SBA-15 model system. Changing the support material may be one opportunity to obtain different vanadium oxide structures compared to that observed for V_xO_y/SBA-15. Nevertheless, the support material itself should not be active for propene oxidation, like Nb_2O_5. Non-oxidic materials like carbon or less active oxides like MgO or Ta_2O_5 may be more likely as possible support material.

10 Appendix

10.1 Physisorption, small angle XRD and CHNS results of SBA-15 and V_xO_y/SBA-15 samples

Table 10-1: Lattice plane distance (d_{100}) and cell parameter (a_0) determined from the 100 diffraction in the small angle XRD powder patterns. BET surface area (S_{BET}), C parameter (C_{BET}) and BJH pore size ($d_{pore,BJH}$), pore volume (V_{pore}) and the SBA-15 channel wall thickness (d_{wall}, determined from a_0-$d_{pore,BJH}$) of the initial bare and the functionalized V_xO_y/SBA-15 samples: (*) sample prepared via the ion exchange method in ***Figure 4-1***, (**) sample prepared by wet impregnation with a NH_4VO_3 solution, (***) sample prepared by incipient wetness using a $(NH_4)_6V_{10}O_{28}$ solution.

Sample	d_{100} [nm]		a_0 [nm]		$d_{pore,BJH}$ [nm]		d_{wall} [nm] (BJH)		V_{pore} [ml/g] (BJH)		S_{BET} [m^2g^{-1}]		C_{BET}	
	bare	func.	bare	func.	bare	func.	bare	func.	bare	func.	bare	func.	bare	func.
3.0 wt% V_xO_y/SBA-15***	10.2	10.0	11.8	11.5	8.0	7.1	3.8	4.4	0.78	0.67	751	522	148	186
5.7 wt% V_xO_y/SBA-15**	10.4	10.4	12.0	12.0	8.0	9.2	4	2.8	0.82	0.81	768	403	166	131
5.0 wt% V_xO_y/SBA-15*	10.3	10.2	11.9	11.8	8.0	7.0	3.9	4.8	0.66	0.50	639	270	166	180
7.7 wt% V_xO_y/SBA-15*	10.5	10.2	12.2	11.8	8.0	8.0	4.2	3.8	0.85	0.57	818	386	144	153
4.1 wt% V_xO_y/SBA-15*	10.0	9.9	11.5	11.4	7.0	7.0	4.5	4.4	0.67	0.57	607	427	146	155
1.4 wt% V_xO_y/SBA-15*	10.2	10.0	11.7	11.6	8.0	7.0	3.7	4.6	0.85	0.71	749	542	132	164

Table 10-2: CHN element content of bare SBA-15, SBA-15-APTES, and calcined V_xO_y/SBA-15 samples: (*) samples prepared via the ion exchange method in ***Figure 4-1***, (**) sample prepared by wet impregnation with a NH_4VO_3 solution, (***) sample prepared by incipient wetness using a $(NH_4)_6V_{10}O_{28}$ solution.

Sample	bare SBA-15 [wt%]		V_xO_y/ SBA-15 [wt%]		APTES/SBA-15 [wt%]			APTES/SBA-15	APTES/SBA-15
	C	H	C	H	N	C	H	mmol N / g	N/nm^2 (bare SBA-15)
3.0 wt% V_xO_y/SBA-15***	0.1	1.0	0.2	0.9					
5.7 wt% V_xO_y/SBA-15**	0.1	0.8	0.2	0.7					
5.0 wt% V_xO_y/SBA-15*	2.0	0.6	0.0	0.4	1.6	4.8	1.5	1.14	1.1
7.7 wt% V_xO_y/SBA-15*	0.1	1.0	0.1	0.9	2.7	8.7	2.2	1.93	1.4
4.1 wt% V_xO_y/SBA-15*	0.1	0.0	0.1	1.1	1.9	7.2	1.7	1.36	1.3
1.4 wt% V_xO_y/SBA-15*	0.1	0.5	0.0	0.9	4.9	14.8	3.5	3.50	2.8

10.2 Information: Vanadium oxide and vanadate references

Table 10-3: Origin and theoretical XRD phases that match the experimental XRD powder pattern of the vanadium oxide references used.

Sample	Purchaser / Synthesized	Reference for Theoretical Structure
$Ca_3V_2O_8$	Synthesized (TU Berlin, AK Ressler)	[172]
$Mg_3V_2O_8$	Synthesized (TU Berlin, AK Ressler)	[67]
Na_3VO_4	Aldrich, 99.98%	no explicit phase
m-$Mg_2V_2O_7$	Synthesized (TU Berlin, AK Ressler)	[69]
K_3VO_4	Alfa Aesar, 99.9%	no explicit phase
$Ca_2V_2O_7$	Synthesized (TU Berlin, AK Ressler)	[173]
t-$Mg_2V_2O_7$	Synthesized (TU Berlin, AK Ressler)	[139]
$NaVO_3$	Aldrich, 99.9%	[174]
KVO_3	Alfa Aesar, 99.9%	[175]
NH_4VO_3	Fluka, 99%	[138]
CaV_2O_6	Synthesized (TU Berlin, AK Ressler)	[176]
$(NH_4)_6V_{10}O_{28}$	Synthesized (TU Berlin, AK Ressler)	[177]
$Mg_3V_{10}O_{28} \cdot xH_2O$	Synthesized (TU Berlin, AK Ressler)	[66]
MgV_2O_6	Synthesized (TU Berlin, AK Ressler)	[68]
V_2O_5	Alfa Aesar, 99.8 %	[140]
VO_2(B)	Synthesized (TU-Berlin, AK Lerch)	[71]
V_3O_7	Synthesized (TU-Berlin, AK Lerch)	[178]
V_2O_3	Synthesized (TU-Berlin, AK Lerch)	[179]

10.3 Baselines of white reflectance standard measured in the *in situ* UV-Vis-DR cells used

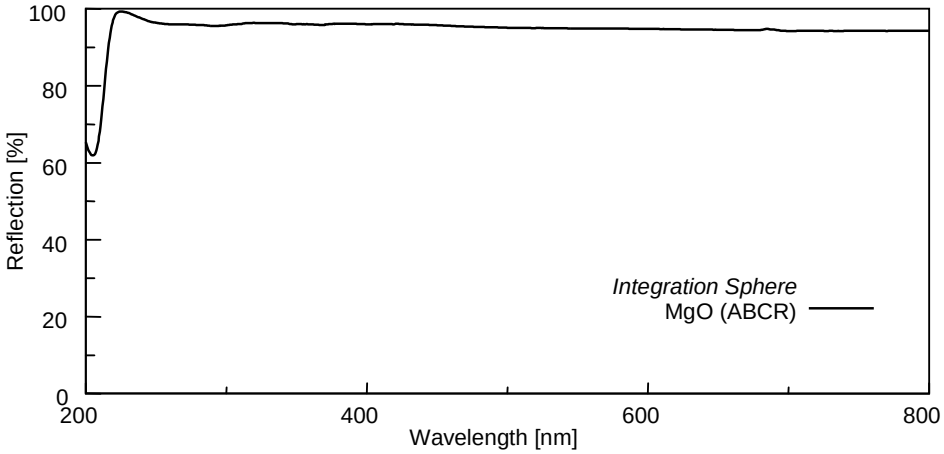

Figure 10-1: Baseline measured in the UV-Vis-DR spectrometer using the standard integration sphere.

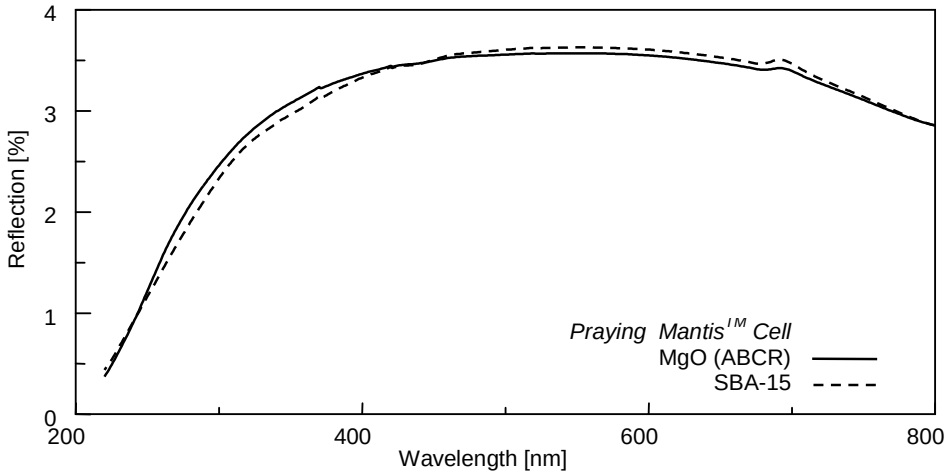

Figure 10-2: Baselines measured in the UV-Vis-DR spectrometer using the Praying Mantis™ cell.

10.4 *In situ* Raman measurements during dehydration

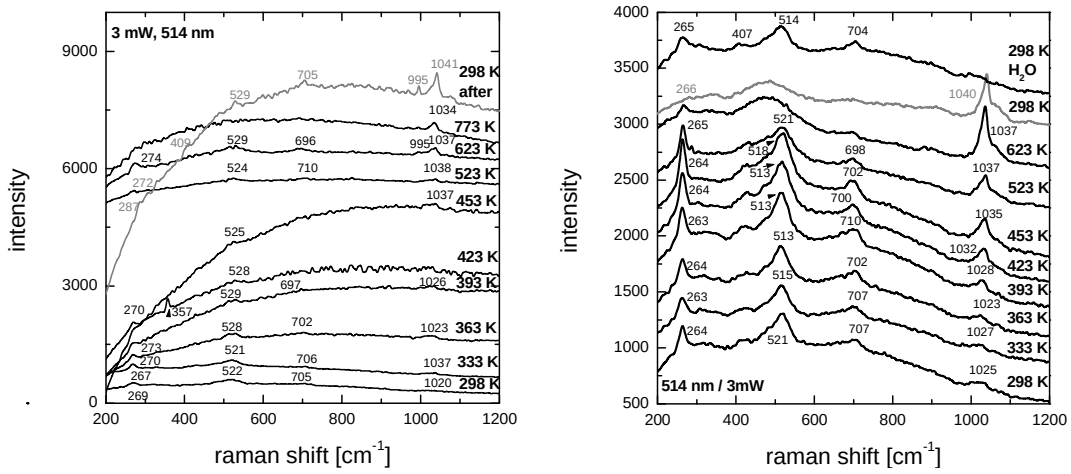

Figure 10-3: *In situ* Raman spectra during dehydration in a "dry" (left) and a water saturated atmosphere (right); 20% O_2 and 80% N_2 (and ~ 45% H_2O), 25 ml/min – 50 ml/min.

10.5 Usable spectral range of the $\chi(k)*k^3$ determined from *in situ* XAFS spectra

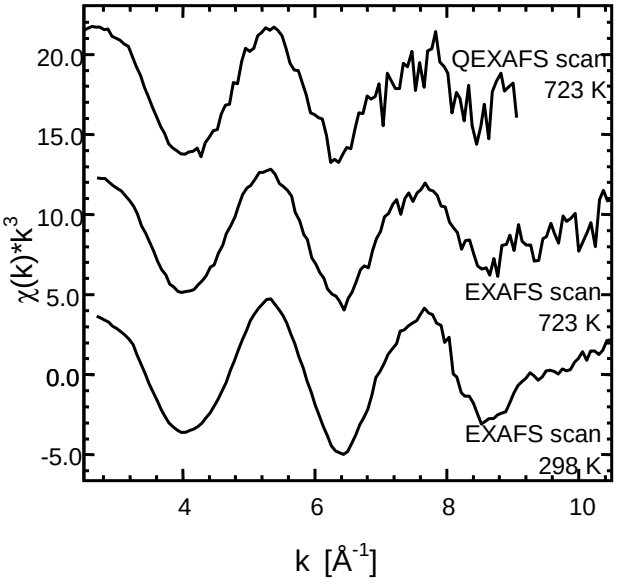

Figure 10-4: Usable spectral range of EXAFS and QEXAFS scans used for measurements of 7.7 wt% V_xO_y/SBA-15 under catalytic conditions (5% propene and 5% O_2 in He, 40 ml/min).

10.6 Supporting data chapter 7

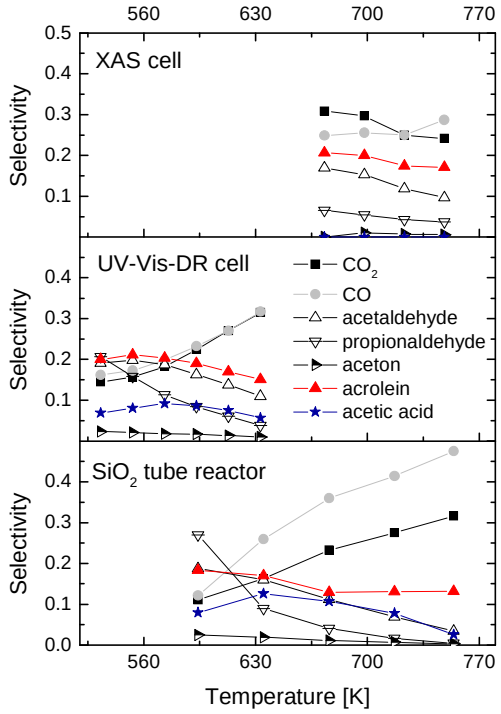

Figure 10-5: Product selectivities determined in the different measurement cells during the temperature programmed propene oxidation using a dehydrated 7.7 wt% V_xO_y/SBA-15.

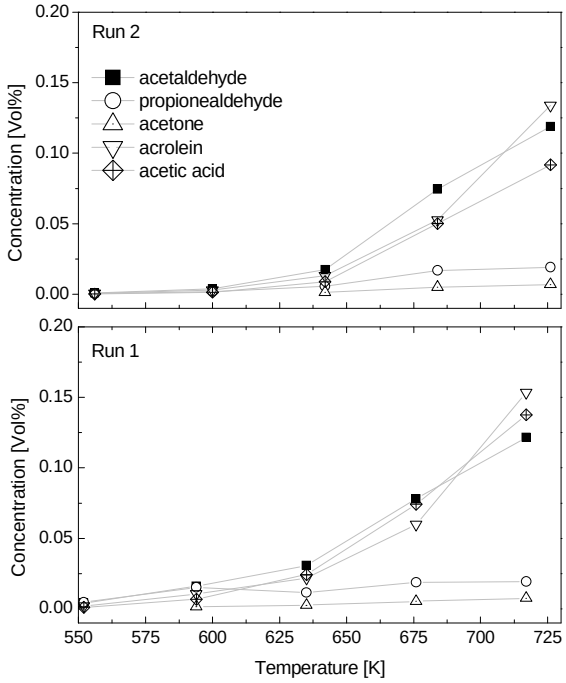

Figure 10-6: Product concentration during propene oxidation (5% O_2 and 5% propene in He) of 7.7 wt% V_xO_y/SBA-15 for subsequent temperature programmed reactions.

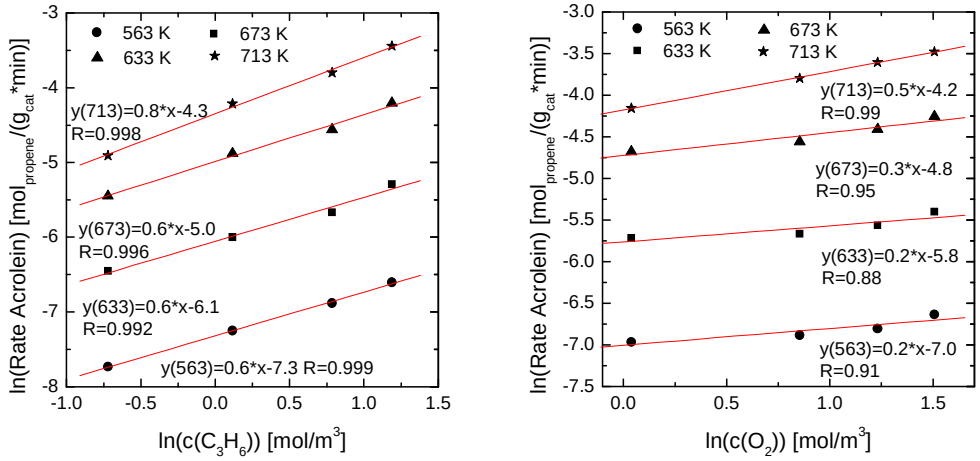

Figure 10-7: Determination of the reaction order for propene (left) and oxygen (right) for the acrolein formation on 7.7 wt% V_xO_y/SBA-15.

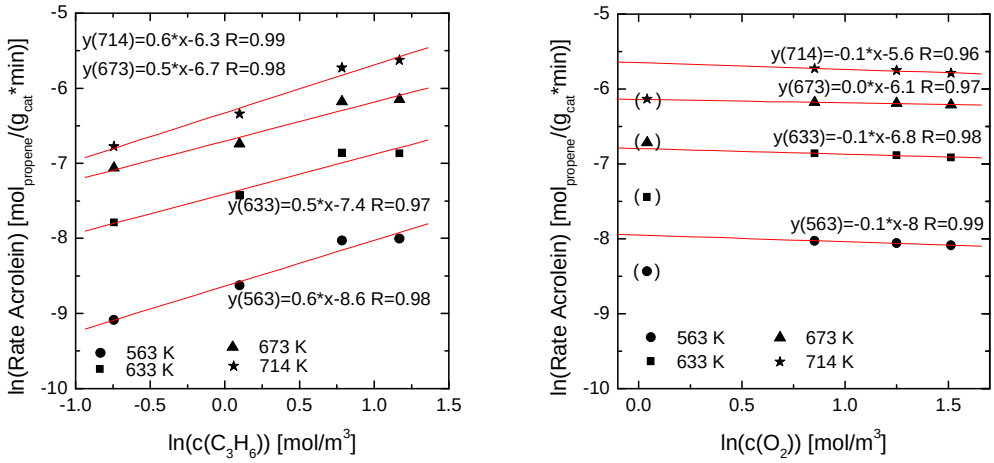

Figure 10-8: Determination of the reaction order for propene (left) and oxygen (right) for the acrolein formation on 1.4 wt% V_xO_y/SBA-15.

10.7 Results of the analysis of the V K edge pre-edge feature

Table 10-4: Results of the analysis of the pre-edge feature determined from the normalized V K edge XANES spectra (* ***Chapter 8, Figure 8-2***): Energy position at maximum intensity relative to V K edge (5.645 keV); height of pre-edge peak at maximum intensity (PH); centroid energy and energy position of the individual components relative to V K edge (5.645 keV) determined and total area of pre-edge peak from peak refinement according to Chaurand *et al.* [94] (***Section 5.2.4, Figure 5-4, right***); product of pre-edge peak height and total area; average V-O bond length from the literature (***Table 10-3***); and beamline used at Hasylab.

Sample	E [eV]	PH	Component positon [eV]			Total Area	Centroid [eV]	R_{V-O} [Å]	PH· Area	Beam-line
			1	2	3					
$Ca_3V_2O_8$	4.70	1.08	4.70	3.31	4.97	2.06	4.71	1.70	2.23	A
$Mg_3V_2O_8$	4.70	1.03	4.74	3.42	5.89	2.10	4.80	1.73	2.16	A
Na_3VO_4	4.70	1.05	4.73	3.42	5.30	2.01	4.69			A
m-$Mg_2V_2O_7$	4.80	0.92	4.83	3.51	6.13	2.06	4.82	1.71	1.89	A
K_3VO_4	4.80	1.00	4.78	3.23	6.98	2.18	4.99			A
$Ca_2V_2O_7$	4.90	0.83	4.83	3.10	6.05	1.84	4.92	1.77	1.52	A
t-$Mg_2V_2O_7$	4.90	0.88	4.92	3.21	7.10	2.34	5.07	1.72	2.06	A
$NaVO_3$	4.90	0.77	4.92	3.33	7.06	2.32	5.12	1.72	1.79	A
KVO_3	4.90	0.86	4.87	3.09	6.99	2.34	4.98	1.74	2.01	A
NH_4VO_3	4.90	0.80	4.86	3.20	6.98	2.16	5.02	1.72	1.73	A
CaV_2O_6	5.20	0.75	5.17	3.59	6.72	1.80	5.45	1.82	1.35	A
$(NH_4)_6V_{10}O_{28}$	5.30	0.52	5.28	3.45	7.29	1.34	5.56	1.92	0.70	A
$Mg_3V_{10}O_{28}$	5.30	0.55	5.25	3.39	7.31	1.36	5.47	1.92	0.75	A
MgV_2O_6	5.30	0.64	5.20	3.35	6.47	1.69	5.44	1.83	1.08	A
V_2O_5	5.40	0.57	3.01	5.32	6.83	1.89	5.94	1.83	1.08	A
hydrated V_xO_y/SBA-15	5.60	0.57	5.55	3.89	7.41	1.65	5.64		0.94	A
dehydrated V_xO_y/SBA-15	5.40	0.74	5.36	3.43	7.05	2.21	5.23		1.64	A
reduced 673 K * V_xO_y/SBA-15	5.17	0.32	5.44	3.88		1.00	4.48		0.32	A
reduced 723 K* V_xO_y/SBA-15	4.24	0.20	3.82	5.37	1.99	0.69	3.98		0.14	A
VO_2(B)	5.26	0.30	3.95	5.50	7.57	1.14	5.42		0.34	C
V_3O_7	5.17	0.49	4.26	5.19	7.28	1.77	5.53		0.86	C
V_2O_3	5.19	0.12	0.87	2.58	4.66	0.32	3.99		0.04	C

10.8 Results from XRD refinements

monoclinic $Mg_2V_2O_7$ (Sample B, *Figure 2-2*)

R-Values [%]:	R_{exp}: 3.49; R_{wp}: 6.22; R_p: 4.71; GOF: 1.78
Quantitative Analysis - Rietveld	
Phase 1 : ICSD 2321	2.82(22) wt%
Phase 2 : ICSD 93603	97.18(22) wt%
Phase 1:	ICSD 2321 [139]
R-Bragg [%]:	2.092
Spacegroup:	$P\bar{1}$
Crystallite Size [nm] (Lorentzian):	26.6(46)
Lattice parameters	
a (Å)	13.968(19)
b (Å)	5.641(12)
c (Å)	4.8838(86)
alpha (°)	81.13(11)
beta (°)	105.83(12)
gamma (°)	130.08(13)
Phase 2:	ICSD 93603 [69]
R-Bragg [%]:	3.255
Spacegroup:	$P12_1/c1$
Crystallite Size [nm] (Lorentzian):	101.69(60)
Lattice parameters:	
a (Å)	6.60368(41)
b (Å)	8.41165(51)
c (Å)	9.48087(57)
beta (°)	100.6372(10)

triclinic $Mg_2V_2O_7$

R-Values[%]:	R_{exp}: 3.82; R_{wp} : 6.80; R_p: 5.12; GOF: 1.78
Quantitative Analysis - Rietveld	
Phase 1 : ICSD 2321"	96.00(35) wt%
Phase 2 : ICSD 93603	4.00(35) wt%
Phase 1:	ICSD 2321 [139]
R-Bragg [%]:	2.703
Spacegroup:	$P\bar{1}$
Crystallite Size [nm] (Lorentzian):	182.1(16)
Lattice parameters:	
a (Å)	13.77974(43)
b (Å)	5.41704(18)
c (Å)	4.92857(16)
alpha (°)	81.37459(73)
beta (°)	106.83011(74)
gamma (°)	130.34723(69)
Phase 2	ICSD 93603 [69]
R-Bragg [%]:	2.059
Spacegroup	$P12_1/c1$
Crystallite Size [nm] (Lorentzian):	19.3(31)
Lattice parameters:	
a (Å)	6.681(10)
b (Å)	8.236(13)
c (Å)	9.472(12)
beta (°)	99.93(16)

MgV_2O_6 (Sample D, *Figure 2-2*)

R-Values [%]:	R_{exp}: 3.51 R_{wp}: 9.53 R_p : 6.39 GOF : 2.71
Phase:	ICSD 10391 [68]
R-Bragg [%]:	7.395
Spacegroup:	*C*12/*m*1
Crystallite Size [nm] (Lorentzian):	148.7(17)
Strain (Gaussian):	0.0815(29)
Lattice parameters:	
a (Å)	9.28049(49)
b (Å)	3.48887(18)
c (Å)	6.72976(36)
beta (°)	111.73192(82)

$Mg_3V_2O_8$

R-Values [%]:	R_{exp} : 2.64 R_{wp} : 5.52 R_p: 4.17 GOF : 2.09
Phase:	ICSD 21085 [67]
R-Bragg [%]:	2.672
Spacegroup:	*Cmca*
Crystallite Size [nm] (Lorentzian):	204.2(27)
Strain (Gaussian):	0.1085(16)
Lattice parameters:	
a (Å)	6.06620(27)
b (Å)	11.44485(50)
c (Å)	8.31868(36)

$Mg_3V_{10}O_{28}{\cdot}x\ H_2O$

R-Values [%]:	R_{exp} : 2.38 R_{wp} : 10.22 R_p : 7.30 GOF : 4.29
Phase:	$Mg_3V_{10}O_{28}{\cdot}28\ H_2O$ [66]
R-Bragg [%]:	6.247
Spacegroup:	$P\bar{1}$
Crystallite Size [nm] (Lorentzian):	90.3(21)
Strain (Gaussian):	0.00(14)
Lattice parameters:	
a (Å)	10.52751(64)
b (Å)	10.74262(71)
c (Å)	21.3503(13)
alpha (°)	89.8932(68)
beta (°)	97.6450(62)
gamma (°)	104.3959(66)

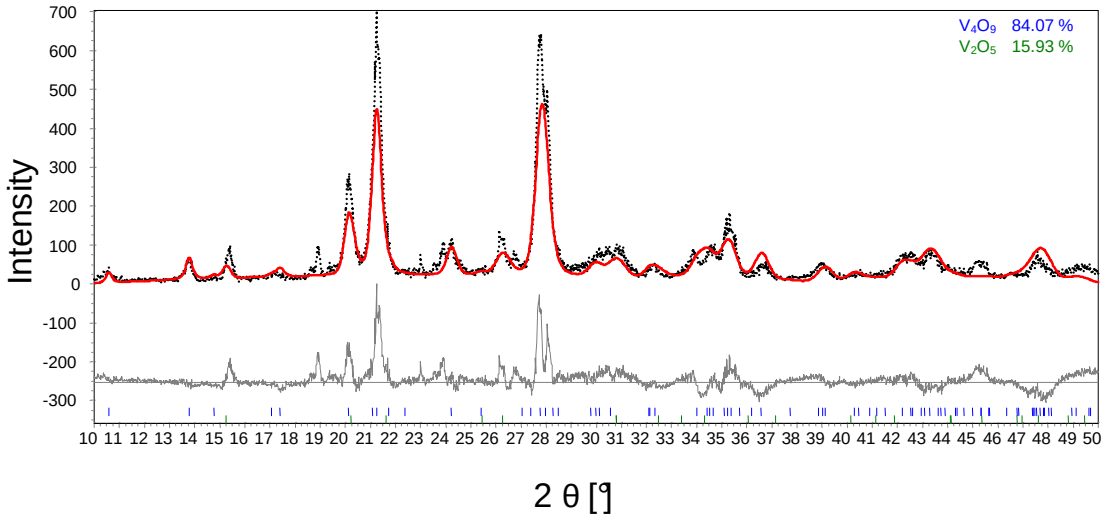

Figure 10-9: Experimental Cu Kα XRD powder pattern of V_4O_9 determined in 5% propene in He (56 ml/min) (dotted black) at 598 K together with the XRD structure refinement of the corresponding phases (solid red) and the differential plot (solid grey).

Experimental XRD pattern of V_4O_9 determined during reduction of V_2O_5 in 5% propene in He (56 ml/min) at 598 K

R-Values [%]:	R_{exp}: 13.35 R_{wp}: 34.34 R_p: 27.42 GOF : 2.57
Quantitative Analysis – Rietveld:	
Phase 1 : V_4O_9 Kijima	84.07(90) wt%
Phase 2 : V_2O_5	15.93(90) wt%
Phase 1:	V_4O_9 Kijima [56]
R-Bragg [%]:	22.440
Spacegroup	*Cmcm*
Crystallite Size [nm] (Lorentzian):	49.4(50)
Strain (Gaussian):	1.652(75)
Lattice parameters:	
a (Å)	10.3877(47)
b (Å)	8.1717(28)
c (Å)	16.7118(21)
Phase 2:	V_2O_5 [140]
R-Bragg [%]:	24.828
Spacegroup	*Pmmn*
Crystallite Size [nm] (Lorentzian):	10000(870000)
Strain (Gaussian):	2.80(29)
Lattice parameters:	
a (Å)	11.598(11)
b (Å)	3.5435(33)
c (Å)	4.3870(46)

Bibliography

[1] Centi, G.; Cavani, F.; Trifirò, F. *Selective Oxidation by Heterogeneous Catalysis;* Kluwer Academic / Plenum Publishers: New York, 2001; p 1.

[2] Arpe, H.-J. *Industrielle Organische Chemie : bedeutende Vor- und Zwischenprodukte*, 6th ed.; Wiley-VCH: Weinheim, Germany, 2007; p 317.

[3] Lin, M. M. Selective oxidation of propane to acrylic acid with molecular oxygen. *Appl. Catal. A* **2001,** *207* (1-2), 1-16.

[4] Kniep, B. L.; Ressler, T.; Rabis, A.; Girgsdies, F.; Baenitz, M.; Steglich, F.; Schlögl, R. Rational Design of Nanostructured Copper–Zinc Oxide Catalysts for the Steam Reforming of Methanol. *Angew. Chem., Int. Ed.* **2004,** *43* (1), 112 –115.

[5] Bettahar, M. M.; Costentin, G.; Savary, L.; Lavalley, J. C. On the partial oxidation of propane and propylene in mixed metal oxide catalysts. *Appl. Catal. A* **1996,** *145* (1-2), 1-48.

[6] Schlögl, R. Active Sites for Propane Oxidation: Some Gerneric Considerations. *Top. Catal.* **2011,** *54* (10-12), 627-638.

[7] Ressler, T. Solid-state kinetics and catalytic behavior of selective oxidation catalysts from time-resolved XAFS investigations. *Catal. Today* **2009**, *145* (3-4), 258–266.

[8] Ressler, T.; Walter, A.; Huang, Z.-D.; Bensch, W. Structure and properties of a supported MoO_3–SBA-15 catalyst for selective oxidation of propene. *J. Catal.* **2008,** *254* (2), 170–179.

[9] Ressler, T.; Walter, A.; Scholz, J.; Tessonnier, J.-P.; Su, D. S. Structure and properties of a Mo oxide catalyst supported on hollow carbon nanofibers in selective oxidation. *J. Catal.* **2010,** *271* (2), 305–314.

[10] Ressler, T.; Dorn, U.; Walter, A.; Schwarz, S.; Hahn, A. H. P. Structure and properties of $PVMo_{11}O_{40}$ heteropolyoxomolybdate supported on silica SBA-15 as selective oxidation catalyst. *J. Catal.* **2010,** *275* (1), 1–10.

[11] Brückner, W.; Oppermann, H.; Reichelt, W.; Terukow, J. I.; Abramowitsch, F.; Wolf, E. *Vanadiumoxide : Darstellung, Eigenschaften, Anwendung*; Akademie-Verlag: Berlin, 1983; pp 13–17.

[12] Dinse, A.; Khennache, S.; Frank, B.; Hess, C.; Herbert, R.; Wrabetz, S.; Schlögl, R.; Schomäcker, R. Oxidative dehydrogenation of propane on silica (SBA-15) supported vanadia catalysts: A kinetic investigation. *J. Mol. Catal. A* **2009,** *307* (1-2), 43–50.

[13] Sugiyama, S; Hirata, Y.; Osaka, T.; Mogria, T.; Nakagawa, K.; Sotowa, K.-I. ^{51}V MAS NMR and XAFS Evidences for Redox of Magnesium *Pyro*- and *Ortho*-Vanadates on the Oxidative Dehydrogenation of Propane. *J. Ceram. Soc. Jpn.* **2007**, 115 (10), 667–671.

[14] Centi, G.; Cavani, F.; Trifirò, F. *Selective Oxidation by Heterogeneous Catalysis;* Kluwer Academic / Plenum Publishers: New York, 2001; pp 203-283.

[15] López Nieto, J. M.; Kremenic, G.; Fierro, J. L. G. Selective Oxidation of Propene over Supported Vanadium Oxide Catalysts. *Appl. Catal., A.* **1990**, *61* (1), 235–251.

[16] Zhao, C.; Wachs, I. E. Selective oxidation of propylene over model supported V_2O_5 catalysts: Influence of surface vanadia coverage and oxide support. *J. Catal.* **2008**, *257* (1), 181–189.

[17] Bauer, G.; Güther, V.; Hess, H.; Otto, A.; Roidl, O.; Roller, H.; Sattelberger, S. Vanadium and Vanadium Compounds. In *Ullmann's Encyclopedia of Industrial Chemistry;* Wiley-VCH: Weinheim, Germany, 2005. doi:10.1002/14356007.a27_367

[18] Weckhuysen, B. M.; Keller, D. E. Chemistry, spectroscopy and the role of supported vanadium oxides in heterogeneous catalysis. *Catal. Today* **2003,** 78 (1-4), 25–46.

[19] Bartholomew, C. H.; Farrauto R. J. *Fundamentals of Industrial Catalytic Processes*, 2nd ed.; Wiley-VCH: Hoboken, NJ, 2006; pp 580–583.

[20] Hess C.; Hoefelmeyer J. D.; Tilley, T. D.; Bell, A. T. Partial oxidation of methanol over highly dispersed vanadia supported on silica SBA-15. *Catal. Lett.* **2005,** *105* (1-2), 1–8.

[21] Bronkema, J. L.; Bell, A. T. Mechanistic Studies of Methanol Oxidation to Formaldehyde on Isolated Vanadate Sites Supported on MCM-48. *J. Phys. Chem. C* **2007,** *111* (1), 420–430.

[22] Du, G.; Lim, S.; Pinault, M.; Wang, C.; Fang F.; Pfefferle L.; Haller G. L. Synthesis, characterization, and catalytic performance of highly dispersed vanadium grafted SBA-15 catalyst. *J. Catal.* **2008,** *253* (1), 74–90.

[23] Gao, X.; Bare, S. R.; Weckhuysen, B. M.; Wachs, I. E. In Situ Spectroscopic Investigation of Molecular Structures of Highly Dispersed Vanadium Oxide on Silica under Various Conditions. *J. Phys. Chem. B* **1998,** *102* (52), 10842–10852.

[24] Berndt, H.; Martin, A.; Brückner, A.; Schreier, E.; Müller, D.; Kosslick, H.; Wolf, G.-U.; Lücke, B. Structure and Catalytic Properties of VO_x/MCM Materials for the Partial Oxidation of Methane to Formaldehyde. *J. Catal.* **2000,** *191* (2), 384–400.

[25] Fornés, V.; López, C.; López, H. H.; Martínez, A. Catalytic performance of mesoporous VO_x/SBA-15 catalysts for the partial oxidation of methane to formaldehyde. *Appl. Catal., A* **2003,** *249* (2), 345–354.

[26] Launay, H.; Loridant, S.; Nguyen, D. L.; Volodin, A. M.; Dubois, J. L.; Millet, J. M. M. Vanadium species in new catalysts for the selective oxidation of methane to formaldehyde: Activation of the catalytic sites. *Catal. Today* **2007,** *128* (3-4), 176–182.

[27] Nguyen, L. D.; Loridant, S.; Launay, H.; Pigamo, A.; Dubois, J. L.; Millet, J. M. M. Study of new catalysts based on vanadium oxide supported on mesoporous silica for the partial oxidation of methane to formaldehyde: Catalytic properties and reaction mechanism. *J. Catal.* **2006,** *237* (1), 38–48.

[28] Gruene, P.; Wolfram, T.; Pelzer, K.; Schlögl, R.; Trunschke, A. Role of dispersion of vanadia on SBA-15 in the oxidative dehydrogenation of propane. *Catal. Today* **2010,** *157* (1-4), 137–142.

[29] Ovsitser, O.; Cherian, M.; Kondratenko, E. V. In-Situ UV/vis and Transient Isotopic Analysis of the Role of Oxidizing Agent in the Oxidative Dehydrogenation of Propane over Silica-Supported Vanadia Catalysts. *J. Phys. Chem. C* **2007,** *111* (24), 8594–8602.

[30] Wachs, I. E.; Weckhuysen, B. M. Structure and reactivity of surface vanadium oxide species on oxide supports. *Appl. Catal., A* **1997,** *157* (1-2), 67–90.

[31] Muylaert, I.; Van Der Voort, P. Supported vanadium oxide in heterogeneous catalysis: elucidating the structure–activity relationship with spectroscopy. *Phys. Chem. Chem. Phys.* **2009,** *11* (16), 2826–2832.

[32] Hess, C.; Hoefelmeyer, J. D.; Tilley, T. D. Spectroscopic Characterization of Highly Dispersed Vanadia Supported on SBA-15. *J. Phys. Chem. B* **2004,** *108* (28), 9703–9709.

[33] Hanke, W.; Bienert, R.; Jerschkewitz, H.-G.; Untersuchungen an katalytisch aktiven Oberflächenverbindungen. Herstellung und Untersuchung von Vanadinoxid-Phasen auf SiO_2. *Z. Anorg. Allg. Chem.* **1975,** *414* (2), 109–129.

[34] Xie, S.; Iglesia, E.; Bell, A. T. Effects of Hydration and Dehydration on the Structure of Silica-Supported Vanadia Species. *Langmuir* **2000,** *16* (18), 7162–7167.

[35] Morey, M.; Davidson, A.; Eckert, H.; Stucky, G. Pseudotetrahedral $O_{3/2}V{=}O$ Centers Immobilized on the Walls of a Mesoporous, Cubic MCM-48 Support: Preparation, Characterization, and Reactivity toward Water As Investigated by ^{51}V NMR and UV–Vis Spectroscopies. *Chem. Mater.* **1996,** *8* (2), 486–492.

[36] Thomson Reuters (formerly ISI) Web of Knowledge database. http://www.isiwebofknowledge.com/ (accessed Jan 2011)

[37] Keller, D. E.; Koningsberger, D. C.; Weckhuysen, B. M. Molecular Structure of a Supported VO_4 Cluster and Its Interfacial Geometry as a Function of the SiO_2, Nb_2O_5, and ZrO_2 Support. *J. Phys. Chem. B* **2006,** *110* (29), 14313–14325.

[38] Chlosta, R.; Tolzov-Müller, G.; Schlögl, R.; Hess. C. Nature of dispersed vanadium oxide: influence of the silica support structure and synthesis methods. *Catal. Sci. Technol.* **2011.** doi: 10.1039/c1cy00062d

[39] Molinari, J. E.; Wachs, I. E. Presence of Surface Vanadium Peroxo-oxo Umbrella Structures in Supported Vanadium Oxide Catalysts: Fact or Fiction? *J. Am. Chem. Soc.* **2010,** *132* (36), 12559–12561.

[40] Schraml-Marth, M.; Wokaun, A.; Pohl, M.; Krauss, H.-L. Spectroscopic Investigation of the Structure of Silica-supported Vanadium Oxide Catalysts at Submonolayer Coverages. *J. Chem. Soc., Faraday Trans.* **1991,** *87* (16), 2635–2646.

[41] Walter, A.; Herbert, R.; Hess, C.; Ressler, T. Structural characterization of vanadium oxide catalysts supported on nanostructured silica SBA-15 using X-ray absorption spectroscopy. *Chem. Cent. J.* **2010,** *4*, 3.

[42] Hävecker, M.; Cavalleri, M.; Herbert, R.; Follath, R.; Knop-Gericke, A.; Hess, C.; Hermann, K.; Schlögl, R. Methodology for the structural characterisation of V_xO_y species supported on silica under reaction conditions by means of in situ O K-edge X-ray absorption spectroscopy. *Phys. Status Solidi B* **2009,** *246* (7), 1459–1469.

[43] Cavalleri, M.; Hermann, K.; Knop-Gericke, A.; Hävecker, M.; Herbert, R.; Hess, C.; Oestereich, A.; Döbler, J.; Schlögl, R. Analysis of silica-supported vanadia by X-ray absorption spectroscopy: Combined theoretical and experimental studies. *J. Catal.* **2009,** *262* (2), 215–223.

[44] Venkov., T. V.; Hess, C.; Jentoft, F. C. Redox Properties of Vanadium Ions in SBA-15-Supported Vanadium Oxide: An FTIR Spectroscopic Study. *Langmuir* **2007,** *23* (4), 1768–1777.

[45] Rozanska, X.; Kondratenko, E. V.; Sauer, J. Oxidative dehydrogenation of propane: Differences between N_2O and O_2 in the reoxidation of reduced vanadia sites and consequences for selectivity. *J. Catal.* **2008,** *256* (1), 84–94.

[46] Novakova, E. K.; Vérdrine, J. C. Propane Selective Oxidation to Propene and Oxygenates on Metal Oxides. In *Metal Oxides : Chemistry and Applications;* Fierro, J. L. G., Ed.; CRC Press: Boca Raton, FL, 2006; pp 413–461.

[47] Ressler, T. Solid-state kinetics and catalytic behavior of selective oxidation catalysts from time-resolved XAFS investigations. *Catal. Today* **2009**, *145* (3-4), 258–266.

[48] López Nieto, J. M.; Kremenic, G.; Fierro, J. L. G. Selective Oxidation of Propene over Supported Vanadium Oxide Catalysts. *Appl. Catal.* **1990**, *61* (1), 235–251.

[49] Centi, G.; Cavani, F.; Trifirò, F. *Selective Oxidation by Heterogeneous Catalysis;* Kluwer Academic / Plenum Publishers: New York, 2001; p 234.

[50] Patel, D.; Andersen, P. J.; Kung, H. H. Oxidative Dehydrogenation of Butane over Orthovanadates. *J. Catal.* **1990**, *125* (1), 132–142.

[51] Solsona, B.; Dejoz, A.; Vázquez, M. I.; Márquez, F.; López Nieto, J. M. SiO_2-supported vanadium magnesium mixed oxides as selective catalysts for the oxydehydrogenation of short chain alkanes. *Appl. Catal., A* **2001**, *208* (1-2), 99–110.

[52] Siew Hew Sam, D.; Soenen, V.; Volta, J. C. Oxidative Dehydrogenation of Propane over V---Mg---O Catalysts. *J. Catal.* **1990**, *123* (2), 417–435.

[53] Cavani, F.; Ballarini, N.; Cericola, A. Oxidative dehydrogenation of ethane and propane: How far from commercial implementation? *Catal. Today* **2007**, *127* (1-4), 113–131.

[54] Kung, H. H.; Kung, M. C. Oxidative dehydrogenation of alkanes over vanadium-magnesium-oxides. *Appl. Catal., A* **1997**, *157* (1-2), 105–116.

[55] Gao, X.; Ruiz, P.; Xin, Q.; Guo, X.; Delmon, B. Preparation and characterization of three pure magnesium vanadate phases as catalysts for selective oxidation of propane to propene. *Catal. Lett.* **1994**, *23* (3-4), 321–337.

[56] Kijima, N.; Toba, M.; Yoshimura, Y. A Chemical Potential Diagram and an In-situ X-ray Diffraction Analysis of a V–Mg–O Catalyst Used in the Oxidative Dehydrogenation of *n*-Butane. *Catal. Lett.* **2009**, *127* (1-2), 63–69.

[57] Sugiyama, S.; Hirata, Y.; Osaka, T.; Mogria, T.; Nakawa, K.; Sotowa, K.-I. ^{51}V MAS NMR and XAFS Evidences for Redox of Magnesium *Pyro*- and *Ortho*-Vanadates on the Oxidative Dehydrogenation of Propane. *J. Ceram. Soc. Jpn.* **2007**, *115* (10), 667–671.

[58] Balderas-Tapia, L.; Hernández-Pérez, I.; Schacht, P.; Córdova, I. R.; Aguilar-Ríos, G. G. Influence of reducibility of vanadium–magnesium mixed oxides on the oxidative dehydrogenation of propane. *Catal. Today* **2005**, *107-108*, 371–376.

[59] Ballarini, N.; Battisti, A.; Cavani, F.; Cericola, A.; Cortelli, C.; Ferrari, M.; Trifirò, F.; Arpentinier, P. The combination of propane partial oxidation and of WGS reaction in a single catalytic bed, and the self-adapting catalytic properties of vanadium oxide catalyst. *Appl. Catal., A* **2006**, *307* (1), 148–155.

[60] Haber, J.; Witko, M.; Tokarz, R. Vanadium pentoxide I. Structures and properties. *Appl. Catal., A* **1997**, *157* (1-2), 3–22.

[61] Colpaert, M. N.; Clauws, P.; Fiermans, L.; Vennik, J. Thermal and low energy electron bombardment induced oxygen loss of V_2O_5 single crystals: Transition into V_6O_{13}. *Surf. Sci.* **1973**, *36* (2), 513–525.

[62] Colpaert, M. N. Exploratory Study of Catalytic Oxidation Reactions on Vanadium Pentoxide Single Crystals. *Z. Phys. Chem. (Frankfurt)* **1973**, *84* (1-4), 150–156.

[63] Andersson, A. An Oxidized Surface State Model of Vanadium Oxides and Its Application to Catalysis. *J. Solid State Chem.* **1982**, *42* (3), 263–275.

[64] Yamazaki, S; Li, C.; Ohoyama, K; Nishi, M.; Ichihara, M.; Ueda, H; Ueda, Y. Synthesis, structure and magnetic properties of V_4O_9 – A missing link in binary vanadium oxides. *J. Solid State Chem.* **2010,** *183* (7), 1496–1503.

[65] Holgado, J. P.; Soriano, M. D.; Jiménez-Jiménez, J.; Concepción, P.; Jiménez-López, A.; Caballero, A.; Rodríguez-Castellón, E.; López Nieto, J. M. Operando XAS and Raman study on the structure of a supported vanadium oxide catalyst during the oxidation of H_2S to sulphur. *Catal. Today* **2010**, *155* (3-4), 296–301.

[66] Iida, A.; Ozeki, T. $Mg_2Na_2V_{10}O_{28}{\cdot}20H_2O$ and $Mg_3V_{10}O_{28}{\cdot}28H_2O$. *Acta Crystallogr., Sect. C* **2004**, *C60*, i43–i46.

[67] Krishnamachari, N.; Calvo, C. Refinement of the Structure of $Mg_3(VO_4)_2$. *Can. J. Chem.* **1971**, *49* (10), 1629–1637.

[68] Ng, H. N.; Calvo, C. Crystal Structure of and Electron Spin Resonance of Mn^{2+} in MgV_2O_6. *Can. J. Chem.* **1972,** *50* (22), 3619–3624.

[69] Nielsen, U. G.; Jakobsen, H. J.; Skibsted, J.; Norby, P. Crystal structure of α-$Mg_2V_2O_7$ from synchrotron X-ray powder diffraction and characterization by ^{51}V MAS NMR spectroscopy. *J. Chem. Soc., Dalton Trans.* **2001**, *21*, 3214–3218.

[70] Uliká, L. Thermal Decomposition of Decavanadates of Bivalent Metals. *J. Therm. Anal. Calorim.* **1980**, *18* (1), 127–136.

[71] Oka, Y.; Yao, T.; Yamamoto, N.; Ueda, Y.; Hayashi, A. Phase Transition and V^{4+}-V^{4+} Pairing in VO_2(B). *J. Solid State Chem.* **1993**, *105* (1), 271–278.

[72] Kim, Y. H.; Lee, H.-I. Redox Property of Vanadium Oxide and Its Behavior in Catalytic Oxidation. *Bull. Korean Chem. Soc.* **1999**, *20* (12), 1457–1463.

[73] Kijima, N.; Toba, M.; Yoshimura, Y. A Chemical Potential Diagram and an In-situ X-ray Diffraction Analysis of a V–Mg–O Catalyst Used in the Oxidative Dehydrogenation of *n*-Butane. *Catal. Lett.* **2009**, *127* (1-2), 63–69.

[74] Brückner, W.; Oppermann, H.; Reichelt, W.; Terukow, J. I.; Abramowitsch, F.; Wolf, E. *Vanadiumoxide : Darstellung, Eigenschaften, Anwendung*; Akademie-Verlag: Berlin, 1983; pp 13–17.

[75] Schiebold, E. Über die Kristallstruktur des Periclas. *Z. Kristallogr.* **1921,** *56*, 430-435.

[76] Rüdorff, W.; Reuter, B. Die Struktur der Magnesium- und Zink-Vanadinspinelle. Beitrag zur Struktur der Spinelle. *Z. Anorg. Allg. Chem.* **1947,** *253* (3-4), 194–208.

[77] Reuter, B.; Aust, R.; Colsmann, G.; Neuwald, Ch. Über Oxidsysteme mit Übergangsmetallionen in verschiedenen Oxydationsstufen. XIX. Darstellung und Eigenschaften Vanadium(II)-haltiger und damit n-leitender Vanadium(III)-Spinelle. *Z. Anorg. Allg. Chem.* **1983,** *500* (5), 188–198.

[78] Bosch, H.; Kip, B. J.; Van Ommen, J. G.; Gellings, P. J. Factors Influencing the Temperature-programmed Reduction Profiles of Vanadium Pentoxide. *J. Chem. Soc., Faraday Trans. 1* **1984**, *80* (9), 2479–2488.

[79] Théobald, F.; Cabala, R.; Bernard, J.; *C. R. Acad. Sci. Paris* **1969**, *269*, 1209–1212.

[80] Burrows, A.; Kiely, C. J.; Perregaard, J.; Højlund-Nielsen, P. E.; Vorbeck, G.; Calvino, J. J.; López-Cartes, C. Structural characterisation of a VMgO catalyst used in the oxidative dehydrogenation of propane. *Catal. Lett.* **1999**, *57* (3), 121–128.

[81] Soenen, V.; Herrmann, J. M.; Volta, J. C. *In Situ* Electrical Characterization of Magnesium Vanadate Reference Phases (meta-MgV_2O_6, pyro-$Mg_2V_2O_7$, and ortho-$Mg_3V_2O_8$) Used in Oxidative Dehydrogenation of Propane to Propene. *J. Catal.* **1996**, *159* (2), 410–417.

[82] Zhao, D.; Feng, J.; Huo, Q.; Melosh, N.; Fredrickson, G. H.; Chmelka, B. F.; Stucky G. D. Triblock Copolymer Syntheses of Mesoporous Silica with Periodic 50 to 300 Angstrom Pores. *Science (Washington, D.C.)* **1998,** *279* (5350), 548–552.

[83] Schreiber, A.; Ketelsen, I.; Findenegg, G. H. Melting and freezing of water in ordered mesoporous silica materials. *Phys. Chem. Chem. Phys.* **2001,** *3* (7), 1185–1195.

[84] Adaptation from: Harris, D. C. *Exploring Chemical Analysis;* Freeman: New York, 1997. Home Page. http://archives.evergreen.edu/webpages/curricular/20002001/MANDM2000/Handouts/Labs/ Chemistry/lab6x.htm (accessed July 2008)

[85] FEFF Home Page. http://leonardo.phys.washington.edu/feff/ (accessed May 2011)

[86] Koningsberger, D. C., Prins, R., Eds. *X-ray Absorption : principles, applications, techniques of EXAFS, SEXAFS and XANES;* Wiley: New York, 1988.

[87] Weckhuysen, B. M., Ed. *In-situ spectroscopy of catalysts;* American Scientific Publishers: California, 2004; Chapters 6, 7, 9.

[88] Rehr, J. J.; Booth, C. H.; Bridges, F.; Zabinsky, S. I. X-ray-absorption fine structure in embedded atoms. *Phys. Rev. B: Condens. Matter* **1994,** *49* (17), 12347–12350.

[89] Rehr, J. J.; Albers, R. C. Theoretical approaches to x-ray absorption fine structure. *Rev. Mod. Phys.* **2000,** *72* (3), 621–654.

[90] Ressler, T.; Jentoft, R. E.; Wienold, J.; Günter, M. M.; Timpe, O. In Situ XAS and XRD Studies on the Formation of Mo Suboxides during Reduction of MoO_3. *J. Phys. Chem. B* **2000,** *104* (27), 6360–6370.

[91] Ressler, T. WinXAS: a program for X-ray absorption spectroscopy data analysis under MS-Windows. *J. Synchrotron Radiat.* **1998,** *5* (2), 118–122.

[92] Ressler, T.; Brock, S. L.; Wong, J.; Suib, S. L. Multiple-Scattering EXAFS Analysis of Tetraalkylammonium Manganese Oxide Colloids. *J. Phys. Chem. B* **1999,** *103* (31), 6407–6420.

[93] Press, W. H.; Teukolsky, S. A.; Vetterling, W. T.; Flannery, B. P. *Numerical Recipes : The Art of Scientific Computing*, 3rd ed.; Cambridge University Press: New York, 2007. (www.nr.com)

[94] Chaurand, P.; Rose, J.; Briois, V.; Salome, M.; Proux, O.; Nassif, V.; Olivi, L.; Susini, J.; Hazemann, J.-L.; Bottero, J.-Y. New Methodological Approach for the Vanadium K-Edge X-ray Absorption Near-Edge Structure Interpretation: Application to the Speciation of Vanadium in Oxide Phases from Steel Slag. *J. Phys. Chem. B* **2007,** *111* (19), 5101–5110.

[95] Weckhuysen, B. M., Van der Voort, P., Catana, G., Eds. *Spectroscopy of transition metal ions on surfaces;* Leuven University Press: Leuven, Belgium, 2000; pp 221–268.

[96] Kober, F. *Grundlagen der Komplexchemie;* Salle: Frankfurt am Main, 1979.

[97] Woodward, P. M.; Mizoguchi, H.; Kim, Y.-I.; Stoltzfus, M. W. The Electronic Structure of Metal Oxides. In *Metal oxides : chemistry and applications;* Fierro, J. L. G., Ed.; Taylor & Francis: Boca Raton, FL, 2006; pp 133–193.

[98] Kortüm, G. *Reflexionsspektroskopie : Grundlagen, Methodik, Anwendungen;* Springer: Berlin, 1969.

[99] Delgass, W. N. Diffuse reflectance and photoacoustic spectroscopies. In *Spectroscopy in heterogeneous catalysis;* Academic Press: New York, 1979; pp 86–131.

[100] Gao, X.; Wachs, I. E. Investigation of Surface Structures of Supported Vanadium Oxide Catalysts by UV-vis-NIR Diffuse Reflectance Spectroscopy. *J. Phys. Chem. B* **2000,** *104* (6), 1261–1268.

[101] Barrett, E. P.; Joyner, L. G.; Halenda, P. P. The Determination of Pore Volume and Area Distributions in Porous Substances. I. Computations from Nitrogen Isotherms. *J. Am. Chem. Soc.* **1951,** *73* (1), 373.

[102] Massiot, D.; Fayon, F.; Capron, M.; King, I.; Le Calvé, S.; Alonso, B.; Durand, J.-O.; Bujoli, B.; Gan, Z.; Hoatson, G. Modelling one- and two-dimensional solid-state NMR spectra. *Magn. Reson. Chem.* **2002,** *40* (1), 70–76.

[103] Thielemann, J. Synthesis, Characterization and *in situ* Catalysis of Silica SBA-15 Supported Molybdenum Oxide Model Catalysts. Dissertation, Technical University, Darmstadt, 2011.

[104] Vansant, E. F.; Van Der Voort, P.; Vrancken, K. C. *Characterization and chemical modification of the silica surface;* studies in surface science and catalysis 93; Elsevier: Amsterdam, 1995; pp 93–126.

[105] Fitzer, E.;. Fritz, W. *Technische Chemie : Einführung in die chemische Reaktionstechnik*, 3rd ed.; Springer: Berlin, 1989; pp 42–49.

[106] NIST chemistry WebBook database. http://webbook.nist.gov/chemistry/ (accessed Aug 2010).

[107] Asatryan, R.; da Silva, G.; Bozzelli, J. W. Quantum Chemical Study of the Acrolein (CH_2CHCHO) + OH + O_2 Reactions. *J. Phys. Chem. A* **2010,** *114* (32), 8302–8311.

[108] Olthof, B.; Khodakov, A.; Bell, A. T.; Iglesia, E. Effects of Support Composition and Pretreatment Conditions on the Structure of Vanadia Dispersed on SiO_2, Al_2O_3, TiO_2, ZrO_2, and HfO_2. *J. Phys. Chem. B* **2000,** *104* (7), 1516–1528.

[109] Hardcastle, F. D.; Wachs, I. E. Determination of Vanadium-Oxygen Bond Distances and Bond Orders by Raman Spectroscopy. *J. Phys. Chem.* **1991,** *95* (13), 5031–5041.

[110] Sing, K. S. W.; Everett, D. H.; Haul, R. A. W.; Moscou, L.; Pierotti, R. A.; Rouquérol, J.; Siemieniewska T. Reporting physisorption data for gas/solid systems with Special Reference to the Determination of Surface Area and Porosity. *Pure Appl. Chem.* **1985,** *57* (4), 603–619.

[111] Herbert, R. Synthesis, Characterization and Catalysis of Nanostructured Vanadia Model Catalysts for Partial Oxidation of Propane. Dissertation, Technical Universiy, Berlin, 2008.

[112] Van Der Voort, P.; Ravikovitch, P. I.; De Jong, K. P.; Benjelloun, M.; Van Bavel, E.; Janssen A. H.; Neimark, A. V.; Weckhuysen, B. M.; Vansant, E. F. A New Templated Ordered Structure with Combined Micro- and Mesopores and Internal Silica Nanocapsules. *J. Phys. Chem. B* **2002,** *106* (23), 5873–5877.

[113] Meyen, V.; Cool, P.; Vansant, E. F.; Kortunov, P.; Grinberg, F.; Kräger, J.; Mertens, M.; Lebedev, O. I.; Van Tendeloo, G. Deposition of vanadium silicalite-1 nanoparticle on SBA-15 materials. Structural and transport characteristics of SBA-VS-15. *Micropor. Mesopor. Mat.* **2007,** *99* (1-2), 14–22.

[114] Keller, D. E.; Visser, T.; Soulimani, F.; Koningsberger, D. C.; Weckhuysen, B. M. Hydration effects on the molecular structure of silica-supported vanadiumoxide catalysts: A combined IR, Raman, UV–vis and EXAFS study. *Vib. Spectrosc.* **2007,** *43* (1), 140–151.

[115] Hess, C.; Wild, U.; Schlögl, R. The mechanism for the controlled synthesis of highly dispersed vanadia supported on silica SBA-15. *Micropor. Mesopor. Mat*. **2006,** *95* (1-3), 339–349.

[116] Liu, W.; Lai, S. Y.; Dai, H.; Wang, S.; Sun, H.; Au, C. T. Oxidative dehydrogenation of *n*-butane over mesoporous VO_x/SBA-15 catalysts. *Catal. Lett.* **2007,** *113* (3-4), 147–154.

[117] Hess, C.; Tzolova-Müller, G.; Herbert, R. The Influence of Water on the Dispersion of Vanadia Supported on Silica SBA-15: A Combined XPS and Raman Study. *J. Phys. Chem. C* **2007,** *111* (26), 9471–9479.

[118] Hess, C. Direct correlation of the dispersion and structure in vanadium oxide supported on silica SBA-15. *J. Catal.* **2007,** *248* (1), 120–123.

[119] Oyama, S. T.; Went, G. T.; Lewis, K. B.; Bell, A. T.; Somorjai, G. A. Oxygen Chemisorption and Laser Raman Spectroscopy of Unsupported and Silica-Supported Vanadium Oxide Catalysts. *J. Phys. Chem. B* **1989,** *93* (18), 6786–6790.

[120] Keller, D. E.; Koningsberger, D. C.; Weckhuysen, B. M. Elucidation of the Molecular structure of Hydrated Vanadium Oxide Species by X-ray Absorption Spectroscopy: Correlation between the V···V coordination number and distance and the point of zero charge of the support oxide. *Phys. Chem. Chem. Phys.* **2006,** *8* (41), 4814–4824.

[121] Keller, D. E.; Airaksinen, S. M. K.; Krause, A. O.; Weckhuysen B. M.; Koningsberger, D. C. Atomic XAFS as a Tool To Probe the Reactivity of Metal Oxide Catalysts: Quantifying Metal Oxide Support Effects. *J. Am. Chem. Soc.* **2007,** *129* (11), 3189–3197.

[122] Keller, D. E.; Weckhuysen, B. M.; Koningsberger, D. C. Application of AXAFS Spectroscopy to Transition-Metal Oxides: Influence of the Nearest and Next Nearest Neighbour Shells in Vanadium Oxides. *Chem. Eur. J.* **2007,** *13* (20), 5845–5856.

[123] Tanaka, T.; Yamashita, H.; Tsuchitani, R.; Funabiki, T.; Yoshida, S. X-Ray absorption (EXAFS/XANES) study of supported vanadium oxide catalysts. Structure of surface vanadium oxide species on silica and γ-alumina at a low level of vanadium loading. *J. Chem. Soc., Faraday Trans. 1* **1988,** *84* (9), 2987–2999.

[124] Keller, D. E.; de Groot, F. M. F.; Koningsberger, D. C.; Weckhuysen, B. M. ΛO_4 Upside Down: A New Molecular Structure for Supported VO_4 Catalysts. *J. Phys. Chem. B* **2005,** *109* (20), 10223–10233.

[125] Sojka, Z.; Bozon-Verduraz, F.; Che, M. UV–Vis–NIR and EPR Spectroscopies. In *Handbook of heterogeneous catalysis*, 2nd ed.; Ertl, G., Knözinger, H., Schüth, F., Weitkamp, J., Eds.; Wiley-VCH: Weinheim, Germany, 2008; Vol. 2, pp 1039–1065.

[126] Weckhuysen, B. M., Van Der Voort, P., Catana, G., Eds. *Spectroscopy of transition metal ions on surfaces;* Leuven University Press: Leuven, Belgium, 2000; Chapter 4, pp 244–254.

[127] Weber, R. S. Effect of Local Structure on the UV-Visible Absorption Edges of Molybdenum Oxide Clusters and Supported Molybdenum Oxides. *J. Catal.* **1995,** *151* (2), 470–474.

[128] Tian, H.; Roberts, C. A.; Wachs, I. E. Molecular Structural Determination of Molybdena in Different Environments: Aqueous Solutions, Bulk Mixed Oxides, and Supported MoO_3 Catalysts. *J. Phys. Chem. C* **2010,** *114* (33), 14110–14120.

[129] Ross-Medgaarden, E. I.; Wachs, I. E. Structural Determination of Bulk and Surface Tungsten Oxides with UV−vis Diffuse Reflectance Spectroscopy and Raman Spectroscopy. *J. Phys. Chem. C* **2007,** *111* (41), 15089–15099.

[130] Haaß, F.; Adams, A. H.; Buhrmester, T.; Schimanke, G.; Martin, M.; Fuess, H. X-Ray absorption and X-ray diffraction studies on molybdenum doped vanadium pentoxide. *Phys. Chem. Chem. Phys.* **2003,** *5* (19), 4317-4324.

[131] Wong, J; Lytle, F. W.; Messmer, R. P., Maylotte, D. H. *K*-edge absorption spectra of selected vanadium compounds. *Phys. Rev. B: Condens. Matter* **1984,** *30* (10), 5596–5610.

[132] Centi, G.; Perathoner, S.; Trifiro, F.; Aboukais, A.; Aissi, C. F.; Guelton, M. Physicochemical characterization of V-silicalite. *J. Phys. Chem.* **1992,** *96* (6), 2617–2629.

[133] So, H.; Pope, M. T. Origin of some charge-transfer spectra. Oxo compounds of vanadium, molybdenum, tungsten, and niobium including heteropoly anions and heteropoly blues. *Inorg. Chem.* **1972,** *11* (6), 1441–1443.

[134] Ronde, H.; Snijder, J. G. The position of the VO^{3-}_4 charge-transfer transition as a function of the V---O distance. *Chem. Phys. Lett.* **1977,** *50* (2), 282–283.

[135] Lazukova, N. I.; Gubanov, V. A.; Mokerov, V. G. Electronic Absorption Spectra of V_2O_5. *Int. J. Quantum Chem.* **1977,** *12* (5), 915-923.

[136] Avdeev, V. I.; Zhidomirov, G. M. Modeling the active centers of V_2O_5/SiO_2 and V_2O_5/TiO_2 supported catalysts. DFT theoretical analysis of optical properties. *J. Struct. Chem.+* **2005,** *46* (4), 577–590.

[137] Thielemann, J. P.; Ressler, T.; Walter, A.; Tzolova-Müller, G.; Hess, C. Structure of molybdenum oxide supported on silica SBA-15 studied by Raman, UV–Vis and X-ray absorption spectroscopy. *Appl. Catal., A* **2011,** *399* (1-2), 28–34.

[138] Hawthorne, F. C.; Calvo, C. The crystal chemistry of the M^+VO_3 (M^+= Li, Na, K, NH_4, Tl, Rb, and Cs) pyroxenes. *J. Solid State Chem.* **1977,** *22* (2), 157–170.

[139] Gopal, R; Calvo, C. Crystal Structure of Magnesium Divanadate, $Mg_2V_2O_7$. *Acta Crystallogr., Sect. B* **1974,** *B30* (10), 2491–2493.

[140] Enjalbert, R; Galy, J. A Refinement of the Structure of V_2O_5. *Acta Crystallogr., Sect. C* **1986,** *C42*, 1467–1469.

[141] Launay, H.; Loridant, S.; Pigamo, A.; Dubois, J. L.; Millet, J. M. M. Vanadium species in new catalysts for the selective oxidation of methane to formaldehyde: Specificity and molecular structure dynamics with water. *J. Catal.* **2007,** *246* (2), 390–398.

[142] Baltes, M.; Cassiers, K.; Van Der Voort, P.; Weckhuysen, B. M.; Schoonheydt, R. A.; Vansant, E. F. MCM-48-Supported Vanadium Oxide Catalysts, Prepared by the Molecular Designed Dispersion of $VO(acac)_2$: A Detailed Study of the Highly Reactive MCM-48 Surface and the Structure and Activity of the Deposited VO_x. *J. Catal.* **2001,** *197* (1), 160–171.

[143] Jehng, J.-M.; Deo, G.; Weckhuysen. B. M.; Wachs, I. E. Effect of water vapor on the molecular structures of supported vanadium oxide catalysts at elevated temperatures. *J. Mol. Catal. A* **1996,** *110* (1), 41–54.

[144] Peña, M. L.; Dejoz, A.; Fornés, V.; Rey, F.; Vázquez, M. I.; López Nieto, J. M. V-containing MCM-41 and MCM-48 catalysts for the selective oxidation of propane in gas phase. *Appl. Catal., A* **2001,** *209* (1-2), 155–164.

[145] Luan, Z.; Bae, J. Y.; Kevan, L. Vanadosilicate Mesoporous SBA-15 Molecular Sieves Incorporated with *N*-Alkylphenothiazines. *Chem. Mater.* **2000,** *12* (10), 3202–3207.

[146] Dzwigaj, S.; El Malki, E. M.; Peltre, M.-J.; Massiani, P.; Davidson, A.; Che, M. Effect of calcination/rehydration treatments on the environment of V in β zeolite. *Top. Catal.* **2000**, *11-12* (1-4), 379–390.

[147] Zhuravlev, L. T. The surface chemistry of amorphous silica. Zhuravlev model. *Colloids Surf., A* **2000,** *173* (1-3), 1–38.

[148] Abello, L.; Husson, E.; Repelin, Y.; Lucazeau, G. Structural Study of Gels of V_2O_5:Vibrational Spectra of Xerogels. *J. Solid State Chem.* **1985,** *56* (3), 379–389.

[149] Knötziger, H.; Taglauer, E. Toward Supported Oxide Catalysts via Solid-Solid Wetting. *Catalysis* **1993,** *10*, 1–40.

[150] Wang, C.-B.; Cai, Y.; Wachs, I. E. Reaction-Induced Spreading of Metal Oxides onto Surfaces of Oxide Supports during Alcohol Oxidation: Phenomenon, Nature, and Mechanisms. *Langmuir* **1999,** *15* (4), 1223–1235.

[151] Van Der Voort, P.; White, M. G.; Mitchell, M. B.; Verberckmoes, A. A.; Vansant, E. F. The effect of water on the structure of supported vanadium oxide structures. An FT-RAMAN, *in situ* DRIFT and *in situ* UV-VIS diffuse reflectance study. *Spectrochim. Acta, Part A* **1997,** *53* (12), 2181–2187.

[152] Atanasov, M.; Adamsky, H.; Eiffert, K. Valence Stabilization, Mixed Crystal Chemistry, and Electronic Transitions in Tetrahedral Oxo and Hydroxo Cr(IV), Mn(V), and Fe(VI) Clusters: A Theoretic Investigation. *J. Solid State Chem.* **1997,** *128* (1), 1–16.

[153] Liu, T.-C.; Forissier, M.; Coudurier, G.; Védrine, J. C. Properties of Molybdate Species Supported on Silica. *J. Chem. Soc., Faraday Trans. 1* **1989,** *85* (7), 1607–1618.

[154] Hess, C. Nanostructured Vanadium Oxide Model Catalysts for Selective Oxidation Reactions. *ChemPhysChem* **2009,** *10* (2), 319–326.

[155] Dinse, A.; Frank, B.; Hess, C.; Habel, D.; Schomäcker, R. Oxidative dehydrogenation of propane over low-loaded vanadia catalysts: Impact of the support material on kinetics and selectivity. *J. Mol. Catal. A* **2008,** *289* (1-2), 28–37.

[156] Liu, Y.-M.; Feng, W.-L.; Li, T.-C.; He, H.-Y.; Dai, W.-L.; Huang, W.; Cao, Y.; Fan, K.-N. Structure and catalytic properties of vanadium oxide supported on mesocellulous silica foams (MCF) for the oxidative dehydrogenation of propane to propylene. *J. Catal.* **2006,** *239* (1), 125–136.

[157] Liu, Y.-M.; Cao, Y.; Yi, N.; Feng, W.-L.; Dai, W.-L.; Yan, S.-R.; He, H.-Y.; Fan, K.-N. Vanadium oxide supported on mesoporous SBA-15 as highly selective catalysts in the oxidative dehydrogenation of propane. *J. Catal.* **2004,** *224* (2), 417–428.

[158] Zhao, C. *Operando spectroscopic and kinetic study of the selective oxidation of propylene to acrolein over well-defined supported vanadium oxide catalysts;* Dissertation; Lehigh University: Pennsylvania, 2007.

http://proquest.umi.com/pqdlink?did=1417810771&Fmt=7&clientId=79356&RQT=309&VName=PQD (accessed 08.07.2011)

[159] Li, M.; Shen, J. Microcalorimetric Adsorption Characterizations of Supported Vanadia Catalysts for Selective Oxidation of Propylene to Acetone. *J. Catal*. **2002,** *205* (2), 248–258.

[160] Yoshida, S.; Magatani, Y.; Noda, S.; Funabiki, T. Partial Oxidation of Propene over U.V.-irradiated Vanadium Oxide supported on Silica. *J. Chem. Soc., Chem. Commun.* **1981,** *12,* 601–602.

[161] Jackson, S. D., Hargreaves, J. S. J., Eds. *Metal oxide catalysis;* Wiley-VCH: Weinheim, Germany, 2009; Vol. 2; pp 178-179.

[162] Grzybowska-Świerkosz, B. Thirty years in selective oxidation on oxides: what have we learned? *Top. Catal.* **2000**, *11/12* (1-4), 23–42.

[163] Li, S.; Mirabal, A.; Demuth, J.; Wöste, L.; Siebert, T. A Complete Reactant–Product Analysis of the Oxygen Transfer Reaction in $[V_4O_{11}{\cdot}C_3H_6]^-$: A Cluster Complex for Modeling Surface Activation and Reactivity. *J. Am. Chem. Soc.* **2008,** *130* (50), 16832–16833.

[164] Li, H.-B.; Tian, S. X.; Yang, J. Propene Oxidation with the Anionic Cluster $V_4O_{11}^-$: Selective Epoxidation. *Chem. Eur. J.* **2009,** *15* (41), 10747-10751.

[165] Kondratenko, E. V.; Brückner, A. On the nature and reactivity of active oxygen species formed from O_2 and N_2O on VO_x/MCM-41 used for oxidative dehydrogenation of propane, *J. Catal.* **2010,** *274* (1), 111–116.

[166] Kondratenko, E. V.; Ovsitser, O.; Radnik, J.; Schneider, M.; Kraehnert, R.; Dingerdissen, U. Influence of reaction conditions on catalyst composition and selective/non-selective reaction pathways of the ODP reaction over V_2O_3, VO_2 and V_2O_5 with O_2 and N_2O. *Appl. Catal., A* **2007,** *319*, 98–110.

[167] Grasselli, R. K. Genesis of site isolation and phase cooperation in selective oxidation catalysis. *Top. Catal*. **2001,** *15* (2-4), 93–101.

[168] Liu, Y.-M.; Cao Y.; Zhu, K.-K.; Yan S.-R.; Dai W.-L.; He H.-Y.; Fan K.-N. Highly efficient VO_x/SBA-15 mesoporous catalysts for oxidative dehydrogenation of propane. *Chem. Commun.*, **2002,** (23), 2832–2833.

[169] Goodrow, A.; Bell, A. T. A Theoretical Investigation of the Selective Oxidation of Methanol to Formaldehyde on Isolated Vanadate Species Supported on Silica. *J. Phys. Chem. C* **2007,** *111* (40), 14753–14761.

[170] Grubert, G.; Rathousky, J.; Schulz-Ekloff, G.; Wark, M.; Zukal, A. Reducibility of vanadium oxide species in MCM-41. *Micropor. Mesopor. Mat.* **1998,** *22* (1-3), 225–236.

[171] Döbler, J.; Pritzsche, M.; Sauer, J. Vibrations of Silica Supported Vanadia: Variation with Particle Size and Local Surface Structure. *J. Phys. Chem. C* **2009**, *113* (28), 12454–12464.

[172] Gopal, R.; Calvo, C. The structure of $Ca_3(VO_4)_2$. *Z. Kristallogr.* **1973,** *137* (1), 67–85.

[173] Trunov, V. K.; Velikodnyi, Yu. A.; Murasheva, E. V.; Zhuravlev, V. D. The crystal structure of calcium pyrovanadate. *Dokl. Akad. Nauk.* **1983,** *270,* 886.

[174] Marumo, F.; Isobe, M.; Iwai, S.; Kondo, Y. α form of sodium metavanadate. *Acta Crystallogr., Sect. B* **1974,** *B30* (6), 1628–1630.

[175] Petrasova, M.; Madar, J.; Hanic, F. Crystal structure of potassium metavanadate. *Chem. Zvesti.* **1958,** *12*, 410–418.

[176] Bouloux, J. C.; Perez, G.; Galy, J. Structure cristalline des metavanadates CaV_2O_6 et CdV_2O_6 alpha. La transformation polymorphique CdV_2O_6 alpha - CdV_2O_6 betha. *Bull. Soc. Fran. Miner, et cristallogr.* **1972,** *V.95,* 130–133.

[177] Eglmeier, C.; Range, K.-J.; Kleynhans, A.; Heyns, A. M. $H_{36}N_6O_{34}V_{10}$. *S. Afr. J. Chem.* **1993,** *46,* 7–13.

[178] Waltersson, K.; Forslund, B.; Wilhelmi, K.-A.; Andersson S.; Galy J. Structural Crystallography and Crystal Chemistry. *Acta Crystallogr., Sec. B* **1974,** *30* (11), 2644-2652.

[179] *Natl. Bur. Stand. (U.S.) Monograph.* **1983**, *25* (20), 108.

Table Captions

Figure Captions